A Fully Actuated Tail Propulsion System for a Biomimetic Autonomous Underwater Vehicle

A Thesis submitted in partial fulfilment of the
requirement for the Degree of Doctor of Philosophy

Aerospace Sciences
School of Engineering
University of Glasgow

By
Ahmad Naddi Ahmad Mazlan
January 2015

Author's Declaration

I declare that this thesis is my own work and that due acknowledgement has been given by means of complete references to all sources from which material has been used for this thesis. I also declare that this thesis has not been presented elsewhere for a higher degree.

Ahmad Naddi Ahmad Mazlan

January 2015

Abstract

In recent years that has been a worldwide increase in the utilisation of Autonomous Underwater Vehicles (AUVs) for many diverse subsea applications. This has given rise to an increase in the research and development of these vehicles, with a particular focus on extending operational capability and longevity. Consequently, this activity has resulted in the design of many different types of AUVs that employ a variety of different propulsion and manoeuvring mechanisms. One particular area that has yielded promising results involves the vehicles designs that are biologically inspired or biomimetic. This class of AUV replicates the anatomical features of aquatic species in order to exploit some of the benefits associated with this type of swimming e.g. higher efficiency at low speeds, improved manoeuvrability. The study presented in this thesis considers the design and performance analysis of a unique biomimetic AUV design based on the physiology of an adult Atlantic salmon. This vehicle, called *RoboSalmon*, is equipped with a multiple jointed, fully actuated tail that is used to replicate the undulatory swimming gait of a real fish. The initial stage of this design process involves the development of a mathematical model to describe the fusion of the dynamics and electro-mechanics of this vehicle. This model provides the design specifications for a prototype vehicle, which has been used in water tank trials to collect data. Forward swimming and manoeuvring experiments, e.g. cruise in turning and turning circle swimming patterns, have been conducted for performance analysis and validation purposes. This part of the study has illustrated the relationship between the vehicle surge velocity, tail amplitude and tail beat frequency. It was found that the maximum surge velocity has been measured at 0.143 ms^{-1}. Also, the vehicle has been shown to accomplish turning circle manoeuvres with turning radius just over the half of its body length. The final stage of this study involved the design of a heading control system, which changes the course of the vehicle by altering the tail centreline. This study allowed the course changing performance of the vehicle to be analysed. Furthermore, a line of sight guidance system has been used to navigate the vehicle through a multiple waypoint course in order to show autonomous operation within a simulated environment. Moreover, the vehicle has demonstrated satisfactory performance in course changing and tracking operations. It is concluded that the *RoboSalmon* biomimetic AUV exhibits higher propulsive efficiency and manoeuvrability than propeller based underwater vehicles at low speeds. Thus the results of this study show that mimicking biology can improve the propulsive and manoeuvring efficiencies of AUVs.

Acknowledgement

First and foremost, my appreciation and thanks go to my supervisor Dr Euan McGookin for his endless guidance, assistance and patience throughout the course of my study. His contribution is highly appreciated particularly in guiding me through this challenging experience not just to complete this research but to be a better researcher.

I am truly and deeply indebted to numerous technical staff in the James Watt and Rankine Building, especially John Kitching and John McCulloch for helping me with the fabrication work as well sharing their technical knowledge. Also, I have to record my deep sense of appreciation to my friends whom had contributed either directly or indirectly to my study and supported me through the difficult times.

Finally and most of all, I would like to thank my parents, Ahmad Mazlan Osman and Zainun Mohamad Yusoff, and both my sisters, Nadiatul Azra and Natrah Amira for the immense amounts of patience, support, encouragement and dua'. Without their contributions this thesis would not have been possible.

Table of Contents

List of Figures

List of Tables

1

Introduction

1.1 Preface

Deep sea exploration is considered to be a challenging task due to the complexity and hazardous nature of the underwater environment. The growing industry in unmanned underwater vehicles has renewed the attention of scientist and researchers to overcome the challenging scientific and engineering problems associated with the unstructured and hazardous underwater environment. This includes the study of vehicle design, actuator specification and development of motion control algorithms which have been reported in the past decades (Molnar, et al., 2007; Zhu & Sun, 2013). The unmanned underwater vehicle (UUV) has been widely used in sea bottom exploration, repairing, surveying, inspection, oil and gas exploration, mine countermeasure, search & rescue and gathering scientific data (Tan, et al., 2007; Akcakaya, et al., 2009; Seto, et al., 2013; Zhu & Sun, 2013).

Nonetheless, the UUV usefulness is not limited to deep sea applications. Numbers of UUV applications can be applied in shallow water environments (e.g. river, lake) for inspection and collecting samples task. This has led to concept designs of much smaller scale of UUVs, low cost fabrication and operation (Bellingham, et al., 1994; Wang, et al., 2008a). Generally, underwater vehicle classification can be divided into two major categories; manned underwater vehicles (MUVs) and unmanned underwater vehicles (UUVs). The remotely operated vehicles (ROVs) and autonomous underwater vehicles (AUVs) fall into the UUV category (Blidberg, 2001; Christ & Wernli Sr, 2014).

One of the most popular category class is the ROV as the name suggests is tethered with umbilical cable and remotely operated by pilot commands from the surface (Christ & Wernli Sr, 2014). Moreover, the power of the vehicle can be on-board, off-board or a hybrid of both. In an off-board condition, the power is supplied to the ROV using a tether. Elvander & Hawkes (2012) stated that ROVs are used to replace divers at depths or within higher risk environments. The human intervention in ROVs operations makes them suitable for operations that require complex manipulations at great depth (Chadwick, 2010; From, et al., 2014)

The unmanned underwater vehicle has been involved in a number of underwater archaeological surveys where ROVs have been used to investigate the wrecks of RMS *Titanic* in 1986 and German battleship *Bismarck* in the summer of 1989 (Ballard, 1993). The Jason Jr., a small ROV developed by the Woods Hole Oceanographic Institution was deployed to explore the interior of the Titanic in conjunction with the deep diving submarine *Alvin* (Yoerger & Slotine, 1991). The *Jason Jr.* operates under the guidance from an operator inside Alvin through fibre optic cables. This capability allow scientists to explore and photograph wreck area that would be too dangerous for *Alvin* and divers to venture (Sellers, 2010).

Another type of UUV is the AUV, an untethered underwater vehicle which Tan, et al. (2007) described as “a free swimming vehicle of high autonomy”. This type of vehicle is capable of performing missions without human intervention. The freedom of movement provide advantages over ROVs where increase the operating range which make the AUVs suitable for inspection and surveying (Akcakaya, et al., 2009; Chadwick, 2010; Roper, et al., 2011) and the operating cost also can be reduced as the support vessel can be operated in multiple sites (Roper, et al., 2011). However, it can be noted that this operating range is limits on board power source. In addition, since it does not need supervision, it is required to be programmed in advance. It returns to a pre-programmed location once the mission is completed where the vehicle and its data are retrieved.

An AUV can also be used to complement the ROV missions and vice versa. One of the most useful applications of ROV and AUV technologies can be seen in search and rescue missions which have involved the recovery of downed aircraft such as the wreckage search of Swissair Flight 111 (Petersen, 2007), Air France 447 (Wise, 2011) and with the recent search for the missing Malaysia Airlines Flight 370 (Smith & Marks, 2014). Smith & Marks (2014) stated that the Bluefin Robotics AUV, named Bluefin-21 is among the tools deployed to hunt for the missing aircraft. Since the exact location of the MH370 crash site is not known, it makes the search process particularly tricky with uncertain measured depths of sea level needed to be covered. The AUV has the capability of mapping the sea floor at a depth of 4500 m below sea level through the use of sonar. However, up until now the search has been unsuccessful which has caused the search to be expanded and new underwater vehicles to be deploy to join the Bluefin-21. One of the suggested vehicles is the REMUS 6000 (Sanchez, 2014) which is similar to Bluefin-21 but can operate at depths of 6000 m. Previously, the REMUS 6000 aided in the search and discovery of the wreckage of Air France Flight AF447 at the bottom of the Atlantic Ocean (Purcell, et al., 2011; Wise, 2011).

1.2 Research Motivation

Nowadays, several abilities such as travel at low and high speed, longer mission duration, manoeuvrability and navigation purpose have become essential to underwater vehicles. Existing AUVs propeller based systems are designed to work efficiently for a mission (e.g. mapping, surveying) that required cruising at high speed. However, in certain applications the propeller based system appears to be inefficient. It has been noted that this system has poor manoeuvring performance (i.e. does not allow it to manoeuvre at low speed and has large turning circle). A large amount of research has been done into optimizing the propeller based system for various applications (e.g. azimuth thruster). This includes configuring multiple thrusters around the vehicle body to allow it to manoeuvre at low speed. Conversely, this configuration increases the vehicle power usage.

Researchers (Liu, et al., 2005; Yu, et al., 2010; Liu, et al., 2014) found that a more efficient propulsion system is necessary to produce better vehicle performance. Researchers have tended to look to nature as an inspiration for their design where the biomimetic propulsion system has been considered as an alternative to propeller based system. The term biomimetic or biomimicry represents the imitation of nature's methods, mechanisms and processes into man-made systems (Bar-Cohen, 2006). In recent years, people have become more focused on the efficient swimming capabilities of fish and the potential benefits that can be transferred to marine vehicle design by mimicking or being inspired by biological based swimming. As examples fish such as pike and yellowfin tuna that can swim at high speed with high level of efficiency and the eel that manoeuvres skilfully within confined spaces (Triantafyllou & Hover, 2003). Moreover, this includes the real fish manoeuvrability ability such as performing a rapid turn for catching prey and avoiding obstructions (Fish, 1997; Guo & Wang, 2008).

This versatile range of swimming abilities has inspired researchers to improve the performance of current autonomous underwater vehicles by implementing biomimetic propulsion systems that replicate the motion of the fish. The investigations into biomimetic systems have provided significant insights into both theory and application of robotics in recent years which can lead to increases in vehicle efficiency and manoeuvrability (Liu, et al., 2005; Yu, et al., 2007; Watts, 2009). Therefore, in the context of this study, the idea is to mimic the nature of real fish swimming to replace the conventional propeller based system that is used extensively in underwater vehicles applications.

1.3 Atlantic Salmon - Subcarangiform

Anderson & Chhabra (2002) indicated that there is trade off existence between speed and manoeuvrability in types of fish where the design choice depends on researchers to select the most desirable attributes to mimic in their designs. In this study, a biomimetic underwater vehicle has been developed with multi jointed tail that imitates Atlantic salmon. The Atlantic salmon has subcarangiform locomotion that approximately 2/3 to 1/2 of their body involved in the propulsive wave for forward motion (Hoar & Randall, 1978). This genus of fish has been chosen because it exhibits several beneficial attributes. The first of these is that salmon swimming performance provides both reasonably fast propulsion and efficient manoeuvring capabilities.

Generally the Atlantic salmon can be found in several locations across Europe, North America and United Kingdom where the majority of the European market is dominated by Norwegian and United Kingdom industries (Mora, et al., 2011). Mora, et al. (2011) stated that about half of total stock is from Norway and another quarter from the United Kingdom i.e. Scottish rivers (Conservation of Atlantic Salmon in Scotland Project, 2010). This indicates the importance of salmon fisheries sector contributions towards the Scottish economy where salmon has become Scotland’s number one food export (Scottish Salmon Producers' Organisation, 2012).

Another key attribute is that salmon have amazing navigation capabilities which is considered to be one of the marvels of nature where they precisely return to their home river even after migrating across thousands of miles of open water (Young, 1962; Verspoor, et al., 2007). Moreover, the size of an Atlantic salmon allows an electronic circuit and sensors to sufficiently occupy the space of a prototype hull. Moreover, it is found the manageable size of the Atlantic salmon enables it to be experimenting in smaller water tank compared to other larger vehicle that require special testing facilities and a team of operators (Watts, 2009).

1.4 Aims & Objectives

The work carried out in this research is aimed to investigate the potential benefits of utilising a biomimetic propulsion system for the underwater vehicles design. In order for this aim to be achieved, several objectives must be met first. The objectives for this research are described below:

1. Develop a mathematical model to assist with the understanding of the dynamics of the biomimetic underwater vehicle and to estimate the performance of the prototype hardware.

2. Develop fishlike motion control algorithms for the biomimetic underwater vehicle.

3. Analyse the biomimetic propulsion system swimming performance by undergo several physical trials.

4. Validate the prototype hardware performance with data obtained from model using qualitative and quantitative measurement.

5. Implement heading and guidance control system for path tracking.

1.5 Contribution of Research

The contributions of this research can be summarized as follows:

1. Development of a fully actuated biomimetic AUV based on fish swimming

2. The hydrodynamics of the biomimetic AUV is analysed using a mathematical model. The model has been developed based on the conventional marine vessels where there is significant difference in technique to represent the propulsion system mimicking real fish undulation motion.

3. Control algorithms altering tail centreline has been presented in order for the vehicle to have manoeuvring capability.

4. Use of a validated model to develop an autonomous guidance control system for the vehicle.

1.6 Thesis Structure

The study of a fully actuated tail propulsion system implemented on an autonomous underwater vehicle is carried out in this thesis as outlined below:

Chapter 2 presents an overview of existing research in areas related to this work. It consists of an overview of conventional underwater vehicles and their applications. This followed by lists of numbers of biomimetic vehicle designs that has been developed in last decade to investigate the performance of fish like swimming motion.

Chapter 3 presents the design and development of a fully actuated version of a *RoboSalmon* prototype. The relevant aspects concerning fish swimming motion are discussed to provide a biological basis for the tail design. The challenges in both mechanical and electronic system design are discussed in detail.

The development of mathematical model describing the dynamic behaviour of a biomimetic underwater vehicle is discussed in Chapter 4. This mathematical model is used to determine the kinematic and dynamic performance of the vehicle. It is modelled using the conventional marine vessel techniques with several modifications taken into accounts especially the way it produces thrust for forward movement. This chapter also includes details of the experimental laboratory setup used to test of the *RoboSalmon* vehicle and collect physical data for validating the mathematical model validation process.

Chapter 5 describes the *RoboSalmon* experimentation and simulation outcomes for the forward motion. It involved varying the tail beat parameters that consist of tail beat amplitude and frequency. The effect of these parameters towards the vehicle surge velocity has been analysed. Followed by the discussion on the characteristic of the recoil motion that affected by varying these tail beat parameters. An attempt to reduce the recoil motion experienced by the vehicle is done by continuously utilizing the head motion is presented. Finally, the vehicle performances in terms of propulsion efficiency and power consumption have been measured.

Manoeuvring experimentation and simulation results are presented in Chapter 6 where the vehicle is tested while performing a turning circle and zig-zag swimming pattern. This involves varying the similar parameters used for forward swimming (i.e. tail beat amplitude and frequency) with the addition of tail deflection angle. The symmetry of vehicle turning is tested by considering tail deflection angle on both sides of the tail centreline.

Chapter 7 presents the design of *RoboSalmon* heading controller based on the Proportional Integral Derivative (PID) and sliding mode control. The PID heading control has been implemented on the vehicle in both simulation and experimentation while the sliding mode only applied in simulation environment. These controllers are implemented in order to control vehicle heading by altering the tail centreline with the heading tracking performance of these heading controllers has been discussed and compared. Next step was to introduce a guidance system in a form of line of sight to provide navigation ability for the *RoboSalmon* vehicle. The vehicle was commanded to navigate through set of paths that were made up from several waypoints.

Finally, Chapter 8 presents the conclusions that have been drawn from this study along with a brief overview of how the results compare with the objectives set out at the start of this thesis. This is followed by a section that discussed lists of suggestions and further improvements that could be made on certain area of *RoboSalmon* in the future.

2

Literature Review

2.1 Introduction

This chapter aims to provide an overview of current AUV/UUV technologies. Propellers thruster and control surface are commonly used for locomotion and manoeuvring for underwater vehicles. The increase in research, commercial or military purposes generates result an interest to develop a more efficient vehicle. As suggested earlier, the biomimetic propulsion has been considered as an alternative to propeller driven propulsion. This system is used to mimic fish tail like undulation motion for forward propulsion. It has been argued that there are several advantages of a fish like propulsion system over a propeller such as less noise, better manoeuvrability (Liu, et al., 2005), and relatively high energy efficiency (Guo, et al., 1998; Rossi, et al., 2011a). Thus, the naturally evolved excellent performance of fish has inspired researchers, engineers and scientists to apply biomimetic technology to the design of underwater vehicles.

The field of biomimetic robotics is multi-disciplinary in nature where numerous different subject areas such as mechanical, naval, electrical and electronics engineering are involved. Therefore, it is important to acquire the relevant knowledge or ideas in modelling and designing a biomimetic vehicle. Nonetheless, it is also necessary to discuss the construction of conventional unmanned underwater vehicles in order to establish the relevant requirements and limitations for the design of underwater vehicles. Therefore, this chapter is divided into four further sections. Firstly, Section 2.2 presents the state of the art in the design and construction of conventional underwater vehicles. Different approaches in selecting types of actuator that involved in realizing the fish like motion are described in Section 2.3. This is followed in Section 2.4 by a list of biomimetic swimming vehicles that have been constructed for academic and commercial purposes. Finally Section 2.5 presents concluding remarks drawn from this review of the current literature in this field of study.

2.2 Conventional Underwater Vehicle

As been mentioned in Chapter 1, UUV can be splits into ROVs and AUVs categories. Both vehicles have demonstrated that they can operate well in underwater environment. According to Christ & Wernli Sr (2014), the main difference between these vehicles is that ROVs are tethered to the ship while AUVs are not. The power and communication is supplies through this tethered cable and the ROV is operated by a pilot. On the other hand, an AUV is a free moving vehicle that carries its own power supply (Blidberg, 2001). Both types of vehicle possess different capabilities and limitation that make them better suited certain applications than the other. However, this section will focus on autonomous underwater vehicles, as this type of platform is most relevant to the research studies.

AUVs are a particular class of unmanned and self-contained UUVs that are able to complete survey/sampling tasks as well as make navigational and tactical decision based on inputs from the on board sensors (Bellingham, 2001; Chadwick, 2010). Thus, it can be operated without supervision and need to be programmed ahead of time. AUVs have been developed by many institutions with several vehicles having demonstrated their wide ranging operational capabilities. They have been used in research, military and offshore industry application where tasks such as surveying, pipe or cable inspection, surveillance or reconnaissance, mine disposal and harbour patrolling are carried out (Lienard, 1990; Corfield & Hillenbrand, 2002; Danson, 2002). Even though the applications and utilisation of the AUV are varied, many have similar configuration and have basic subsystems (Griffiths, 1999). These include subsystems for propulsion, navigation, mission management, user interface, manipulator system and power storage.

The drag is an important element to be considered when designing an AUV hull shape and Wang, et al.(2007) discussed that minimizing the effect of these elements helps to expand the operational range, improve the load capability and increase efficiency. A wide variety of AUV shapes and sizes have been designed (see Table 2.1) and ranging from torpedo shape, laminar flow, streamlined rectangular style and multihull vehicles (Stevenson, et al., 2007, 2009).

Table 2.1. AUV hull shape

Shape	Vehicle
Torpedo	Autosub (Millard, et al., 1997), Bluefin Robotic (Panish, 2009) and Remus (Allen, et al., 2000)
Laminar flow	Early HUGIN vehicles (Marthiniussen, et al., 2004)
Streamlined rectangular	Marius (Pascoal, et al., 1997) and Sea Otter MK-II (see Figure 2.1) (Atlas Elektronik GmbH, 2013)
Multihull vehicles	Autonomous Benthic Explorer (ABE) (see Figure 2.2) (German, et al., 2008)

Figure image has been removed due to Copyright restrictions

Figure 2.1: SeaOtter Mk II AUV with rectangular hull shape (Atlas Elektronik GmbH, 2013)

Figure image has been removed due to Copyright restrictions

Figure 2.2: Autonomous Benthic Explorer (ABE) that has multihull vehicle shape (Blidberg, 2001)

The earliest AUV was developed in 1800s and resemble a torpedo shape (Blidberg, 2001) which is still the most popular choice of AUV shape configuration (Singh, et al., 1997; Bellingham, 2001). Most torpedo shaped AUVs are propelled by single or dual fixed propellers and manoeuvres through a set of actuated rudder and elevator control surfaces (Eskesen, et al., 2009). This shape minimizes drag and as a consequence minimizes the energy required for vehicle propulsion which then contributes to higher cruise efficiency. Budiyono (2009) summarized that most commercially existing torpedo shape AUVs have design speeds on average of 3 m/s.

Bluefin Robotics offers a wide range of AUVs that able to meet the requirement in defence, commercial, and scientific demand (Panish, 2009; Goldberg, 2011). These AUV products consists of Bluefin-9, Bluefin-12S, Bluefin-12D and Bluefin-21 classes of torpedo shaped vehicles with three different diameters (i.e. 9”, 12” (see Figure 2.3), and 21”). According to Panish (2009), by using a core set of building blocks, the length of vehicle can be fully configurable to meet the demands of the specific application, length potentially range from 1 to 5 m.

Figure image has been removed due to Copyright restrictions

Figure 2.3: A 12” diameter Bluefin Robotic AUV (Panish, 2009)

Ducted tailcones propulsion design has been applied to these types of vehicles, it is used to replace the extended dive planes and control fins that are common with many AUVs (Panish, 2009). It is claimed that it provides exceptional propulsive efficiency, dynamic stability, less maintenance, improved directional control in a compact and robust structure (Bluefin Robotics, 2014). The Bluefin AUV can be deployed for shallow and deep water survey applications where it is highly stable with extensively configurable tool, such as side scan sonar, synthetic aperture sonar, and multibeam echo that can be used to produce high quality measurement (Panish, 2009). This has been demonstrated by the high quality imagery produced when integrate the Sonardyne International Ltd.’s Solstice Side Scan Sonar with a Bluefin-12 AUV (Sonardyne, 2014). Finally, the Bluefin’s AUVs are designed to be slightly positive buoyant for safety measure where in the event of any malfunction, the vehicle floats to the surface for easy recovery.

Nereus, a hybrid unmanned autonomous underwater vehicle (HROV) operated by the Woods Hole Oceanographic Institution (WHOI). It is designed to perform scientific survey and sampling to a depth of the ocean of 11,000 m, which is almost twice the depth of any existing operational vehicle (Bowen, et al., 2008; Lee, 2014). Bowen, et al. (2008) stated that *Nereus* is a hybrid remotely operated since it can be configured in two different modes; ROV or AUV mode based on the user's requirement. Whitcomb et al. (2010) reported that the vehicle has successfully demonstrated it is able to reach the deepest ocean depth of 10,903 m in the Challenger Deep of the Mariana Trench in the Western Pacific in May 2009.

Also, the US Navy have identified numbers of AUV military applications in military particularly for shallow water such as surveillance, reconnaissance, mine countermeasures (MCM) and antisubmarine warfare (ASW) missions (Seto, et al., 2013). The REMUS 100 with an operating depth rating of 100 m has been developed for a variety of missions including mine countermeasures (MCM) operations (von Alt, 2003). It maps the seafloor to detect mines by utilizing the side scan-sonar (Freitag, et al., 2005). Utilisation of AUVs for mine hunting is useful since they are able to perform quick surveys for large areas and identify the potential threat thus minimize the human or other asset risk in unknown environment (Nguyen, et al., 2008). In addition, the successful wartime deployment of the REMUS 100 during Operation Iraqi Freedom in 2003, proved to be an invaluable asset for conducting mine clearance operations in the port city of Umm Qasr (Schnoor, 2003; von Alt, 2003).

Although AUVs appear to provide beneficial capabilities, there are some limitations. One of the most important limitations is its on board power source (Yuh, et al., 2011). The operating period and effective operating range of AUVs depends on the power supply it carries on board and the power requirement of the other vehicle systems, e.g. the electric drives for the thrusters. Hasvold, et al. (2006) summarized various AUV power sources, where the selection depends on the AUV size and application. It has been suggested that primary lithium and lithium ion for small AUVs with shallow design depth whereas fuel cell based power sources are suitable for larger AUVs designed for deep water operation. Even though, primary lithium battery provides very high energy density and endurance, its operating costs and safety prove to be an issue that eventually limit its applications

(Størkersen & Hasvold, 2004). Brege (2011) argues another AUV limitation is the high construction costs. However, Brun (2012) reported the potential of having an affordable AUV resulted on the increases in AUV technologies that have a tendency to to produce more efficient power system, functionality and operating time.

Existing torpedo shape AUVs are usually designed for high speed cruising missions, e.g. surveying large areas of the seabed (Steenson, et al., 2011), and are known to be effective for operations in open water and uncluttered conditions (Geder, et al., 2013). On the contrary, it has poor manoeuvring performance due to a large turning circle i.e. typically several body lengths to execute a turn (Anderson & Kerrebrock, 2002; Licht, et al., 2004; Licht, 2012) where it has been measured that MUNExplorer AUV with 4.5 m in length has turning radius of approximately 23 m (Issac, et al., 2007). Also, the torpedo shaped vehicle requires a certain minimum speed in order to maintain flow over the control surfaces in order to remain controllable (Bellingham, 2001; von Alt, et al., 2001; Seto, et al., 2013). Therefore, Singh, et al. (1997) and Bellingham (2001) argue that the torpedo shaped vehicles do not have the ability to keep position at a specified location which suggests they are not suitable for missions that involve operation within in confined spaces or very close to the seabed.

Some torpedo shaped AUVs such as *NPS Aries*, *C-Scout*, *Odyssey IV* and *Redermor* overcome this issue by adding tunnel or cross axis thrusters in order to enable it to keep position or manoeuvre at low speeds (Bellingham, 2001; Saunders & Nahon, 2002). The implementation of multiple thrusters significantly helps to reduce complexity in the control problem and overcome thruster failures. In addition, the introduction of azimuth thrusters as an alternative propulsion system improves the vehicle manoeuvrability. This is due to the elimination of thrust losses since the propeller direction can be rotates to produce thrust in desired direction(Fossen & Johansen, 2006). One AUV that has hovering capability is the *Odyssey IV* which due to its conservative size and weight makes it deployable from small boats. It is equipped with 4 thrusters; two vectored side thrusters at the stern and two fixed cross-body thrusters at the bow. Eskesen, et al.(2009) stated that this configuration allows for vehicle precision in hovering. It has demonstrated its potential in a survey operation on a scientific mission of the George's Bank area of the Gulf of Maine (Eskesen, et al., 2009). It was used for mapping and photographing the presence of Didemnum that was destroying the habitat for local fish.

Nevertheless, the implementation of multiple thrusters results in an increase in power consumption that adversely affects the vehicle operating range. Also, additional thrusters add extra weight which for majority of cruising operations are redundant (Anderson & Chhabra, 2002; Anderson & Kerrebrock, 2002). Another AUV limitation is its inability to adjust to sudden or previously unknown obstacles and threats along the path which can lead to potential collision (Horner, et al., 2005; Engelhardtsen, 2007).

AUVs have demonstrated that they are valuable assets for search and survey missions. This is due to their relatively small size, ease of deployment and unsupervised autonomous operational capabilities (Bellingham, et al., 1994; Langdon, 2010). Singh, et al. (1997) found AUVs for scientific tasks tend to be much smaller than those vehicles being designed for military purposes or for use in the offshore industry. This is mostly due to the financial constraints, ease in deployment and recovery. Working in such a complex and hazardous underwater environment carries a high risk where there have been several incidents has been reported. These include situation such as technical system failure (e.g., instrument failure, loss of communications) and catastrophic implosion that can cause the mission to be abort or even cause the loss of the vehicle (Seto, et al., 2013).

This happened on *Autosub2* which was lost under the Fimbul ice sheet in the Antarctic in February 2005 due to the technical system failure (Strutt, 2006). Also, the loss of the *ABE* AUV at sea off the coast of Chile in March 2010 (Fountain, 2010) and recently, the loss of *Nereus* HROV while exploring the Kermadec Trench in May 2014 (Lee, 2014) suggested that both suffered catastrophic implosion.

As has been mentioned above, the existing designs of AUV hull span torpedo shapes, laminar flow designs, streamlined rectangular styles and multihulls, with torpedo shaped as the most popular choice. Such a hull is designed to minimize drag and maximize vehicle speed. Despite the maturity of this design for deep water missions (for instance surveying work requiring high speed cruising), it lacks intrinsic manoeuvrability. Manoeuvrability is important in any AUV which must perform obstacle avoidance. Several modifications are typically made to torpedo shaped designs to improve their manoeuvrability, including the addition of multiple thrusters around the hull. However, these modifications increase AUV weight, power consumption, and ultimately degrade vehicle operating range. As a result of these problems, researchers have sought for better designs as part of this search have turned their attention to nature. The versatile range of fish swimming abilities and the efficiency of fish propulsion have inspired researchers to include such capabilities into underwater vehicle design by mimicking biological based swimming.

2.3 Biomimetic Underwater Vehicles

Various different approaches have been taken for the development of biomimetic underwater vehicles in the recent years with most research concentrating on the reproduction of fish like propulsion (Morgansen, et al., 2007; Watts, 2009; Liu & Hu, 2010). Most of the research utilised the vehicle posterior side to mimic the different types of real fish locomotion. This configuration also allows the electronic, power and sensor systems to occupy the space within the anterior hull (Wang, et al., 2012). A number of biomimetic underwater vehicles have been designed and the majority of the known vehicles have adopted either carangiform (e.g. herring, jacks, mackarel) or thunniform (e.g. tuna, billfish and lamnid sharks) locomotion due to the high speed swimming and highly efficient thrust production associated with these types of fish (Colgate & Lynch, 2004; Wang, et al., 2011).

Most of the biomimetic underwater vehicle designs use rigid links driven by motors to replicate the undulation motion of real fish (Rossi, et al., 2011a). Liu, et al. (2014) indicate that the complexity of the design and actuation can be varied from a simple rigid rod shaped tail driven by motor actuator to a multi-jointed tail driven separately or jointly by several motor actuators. It has been argued that this type of linkage configuration can be complex, heavy and bulky (Rossi, et al., 2011b). Furthermore, this motor and linkage mechanisms encounter similar issues as a propeller driven system that are low efficiencies and excessive thermal energy generation (Guo, et al., 1998)

Thus, an alternative way to produce fish like swimming motion is by using smart materials, which include ionic polymer-metal composites (IPMC), piezoelectric actuators, and shape memory alloys (SMA) (Shi, et al., 2013; Liu, et al., 2014). Its behaviour where it is flexible and able to produce significant bending deformation under low voltages actuation has attracted the interest from researchers. The development of these materials makes it possible to emulate the biological muscles, several works on smart material have been reported; ionic polymer-metal composites (IPMC) (Guo, et al., 2006; Chen, et al., 2010), shape memory alloys (SMA) (Wang, et al., 2008b; Rossi, et al., 2011a) and piezoelectric actuators (Fukuda, et al., 1994).

According to Chu et al. (2012), the smart material can perform flexible and complex movement of real fish with considerable simpler mechanisms. Therefore, higher possibility for a smaller, less noise and lighter vehicle can be designed compared to the motor based actuator vehicle (Rossi, et al., 2011a; Chu, et al., 2012). However, Cen & Erturk (2013) found that the biomimetic underwater vehicle with motor based actuation outperformed smart material actuation as it capable to provide a high swimming speeds vehicle whereas the smart materials appear to be lacking (Tao, et al., 2006; Nguyen, et al., 2013). Another disadvantages of smart material is due to the leaking electric current causes safety issues to arise when considering operation in water (Guo, et al., 1998).

At present, the fish swimming modes can be classified into two categories; Body and/or Caudal Fin (BCF) and Median and/or Paired Fin (MPF) (see Figure 2.4). The former generate thrust by bending their bodies into a backward moving propulsive wave that extends to the caudal fin (Sfakiotakis, et al., 1999). The changes in proportions of the bodies involve (shaded area) and amplitude envelopes of the propulsive wave are different for each types of locomotion are illustrated in Figure 2.4(a). Meanwhile, the Median and Paired Fin propulsion consists of undulatory fin motion and oscillatory fin motion as shown in Figure 2.4(b). This propulsion relies on the ability of multiple fins (e.g. pectoral, anal, and dorsal) to flap that will result thrust generation (Hoar & Randall, 1978; Korsmeyer, et al., 2002).

Figure image has been removed due to Copyright restrictions

Figure 2.4: Swimming modes associated with (a) BCF propulsion and (b) MPF propulsion. The shaded areas contribute to the thrust generation (Sfakiotakis, et al., 1999)

The BCF has the capability to provide greater thrust, maximum acceleration, useful for high speed swimming and fast start (Moyle & Cech Jr, 2004; Barton, 2007) whereas MPF attain a slower speed but greater precise control manoeuvrability (Hoar & Randall, 1978; Sfakiotakis, et al., 1999; Moyle & Cech Jr, 2004).

2.4 Biomimetic Underwater Vehicle Prototypes

There have been numerous biomimetic studies carried out into alternative ways to replace propeller systems on underwater vehicles for commercial and academic purposes. These studies can range from conceptual studies to development of oscillating foil propulsion systems to full autonomous underwater vehicles or robotic fish (Triantafyllou & Triantafyllou, 1995; Barrett, et al., 1996; Watts, 2009; Liu & Hu, 2010). There are few existing biomimetic underwater vehicles that have the capability to realize both BCF and MPF locomotion; commonly only one type of swimming locomotion is chosen to generate thrust with certain compromises in performance. This is due to the design complexity and time constraint. Since this research focuses on the modelling, simulation and development studies of a BCF based prototype, only vehicles that mimic the BCF swimming are mentioned in this section.

2.4.1 *RoboTuna*

The earliest fish like biomimetic vehicle that has been documented is known as *RoboTuna* where it is developed at Massachusetts Institute of Technology (MIT) in 1994 (Liu & Hu, 2003). Its design is inspired by biological tuna because of the high speeds achieved by this type of fish (Barton, 2007). The *RoboTuna* was built approximately 1.25 m in length and mounted on a carriage at the MIT Testing Tank space (Techet, et al., 2003). Barrett, et al. (1996) stated that it has “flexible Tuna-form shaped hydrodynamic outer hull and is propelled by a single oscillating tail foil”.

Figure image has been removed due to Copyright restrictions

Figure 2.5: *RoboTuna* (Barrett, et al., 1996)

The tail structure consists of an eight link mechanism with a lunate caudal tail fin attached to the last link. It is driven through complex system of pulleys and cable tendons by six brushless DC servo motors (Triantafyllou & Triantafyllou, 1995). These pulleys and cables are the representation of biological fish muscle and tendon. Moreover, the whole body is covered with lycra and foam in order to provide a smooth and flexible tail surface. Barrett, et al. (1996) stated that the *RoboTuna* is suspended from the support structure by a mast in the position of the dorsal fin shown in Figure 2.5 that slides along the tank. Moreover, this mast also acts as an outlet which all the tendons and sensor wires pass through.

The wake characteristic produced by the flapping motion is evaluated by the Strouhal Number. It is a non-dimensional parameter which can be defined as the product of the tail beat frequency and the wake width, divided by the forward velocity (refer to Chapter 5). Triantafyllou & Triantafyllou (1995) indicate that the swimming efficiency peaks when the Strouhal Number lies between 0.25 and 0.35. The development of the robotic mechanism allows *RoboTuna* to replicate closely the swimming motion of biological Tuna (Barrett, et al., 1996).

The control system and data collection technique has been implemented on *RoboTuna* which allow various parameters to be analysed and it has been highlighted the seven key parameters involved the swimming (Barrett, 2002; Roper, et al., 2011). Varying these parameters create wide range of possibility to search for the optimum performance which is not possible due to the time constraint. Thus, Barrett (2002) suggested that a more efficient search technique is needed where a genetic algorithm (GA) technique has been applied to search an optimal set of swimming parameter.

2.4.2 *RoboPike*

Next, MIT developed a robotic vehicle with 0.81 m in length known as *RoboPike* (Triantafyllou, et al., 2000). Its design is based on a pike (carangiform) where the tail structure consists of three independently controlled links. A pike was chosen due to its amazing abilities to turn quickly and fast acceleration from a stop (Roper, et al., 2011). Unlike *RoboTuna*, the *RoboPike* is a free swimming robot fish. However, it is not autonomous, it is equipped with communication module and on board computer (i.e. Motorola 68322) where the latter is used to interpret the navigation commands from the user (Kumph, 2000; Afolayan, et al., 2012).

2.4.3 *GhostSwimmer* & *BIOSwimmer*

Recent developments of a biomimetic swimmer that resemble a tuna fish can be seen in GhostSwimmer (Rufo & Smithers, 2011) and BIOSwimmer (Conry, et al., 2013). Both are developed by Boston Engineering's Advanced Systems Group (ASG) which the latter is funded by The Department of Homeland Security's (DHS) Science and Technology Directorate (S&T) (Conry, et al., 2013). The vehicles have the same profile as a five foot tuna with the posterior part being flexible. The *BIOSwimmer* can be considered as a variant of *GhostSwimmer*. The difference can be seen in its propulsion system where the *GhostSwimmer* propelled forward by motor driven tail whereas the *BIOSwimmer* use a propeller (Rufo & Smithers, 2011; Conry, et al., 2013). It is claimed that it provides a solution for swimming in a challenging underwater environment such as navigating through shallow and cluttered area where it can be used for inspection, surveillance and search & rescue mission (Conry, et al., 2013). However, the propeller system is not biomimetic in nature.

2.4.4 Vorticity Control Unmanned Undersea Vehicle (VCUUV)

Inspired by the work undertake on *Robotuna*, Draper Laboratories developed the Vorticity Controlled Unmanned Underwater Vehicle (VCUUV) where it is claimed as the first biomimetic autonomous underwater vehicle that uses vorticity control propulsion and manoeuvring (Anderson & Chhabra, 2002). It is designed as a 2.4 m flexible-hull UUV that intended to mimic tuna swimming. In addition, the vehicle shape was directly scaled from a casting of a 1 m biological fish in order to have a close approximation of yellowfin tuna.

Figure image has been removed due to Copyright restrictions

Figure 2.6: VCUUV system layout (Anderson & Chhabra, 2002)

The components arrangement in VCUUV is shown in Figure 2.6 where it is fitted with various sensors, actuators and an on board power source. The tail structure is composed of three driven links and a caudal fin where the links independently actuated by double-acting hydraulic cylinders. Anderson & Chhabra (2002) highlighted a precise and robust control of tail linkage is compulsory for The VCUUV is manoeuvred by means of the on board compass which provides feedback for the vehicle heading. Consequently, it has been suggested VCUUV is suitable for autonomous missions.

The VCUUV demonstrated that it attained the maximum speed at 1 Hz beat frequency of 1.2 m/s for straight swimming experiments (Anderson & Chhabra, 2002). It was noted that the higher beat frequency than 1 Hz cannot be tested due to the actuator saturation. With reference to body length, it was found that and VCUUV able to achieved 0.61 BL/s whereas *Robotuna* was 0.65 BL/s (Anderson & Chhabra, 2002; Anderson & Kerrebrock, 2002; Mandujano, 2002). Furthermore, it also been stated that the difference in the kinematics between the VCUUV tail motion and *RoboTuna* may contributed to the discrepancy in speed. Meanwhile, the VCUUV showed that it can provide better manoeuvrability performance with maximum turning rates of 75 °/s compared to approximately 3-5 °/s. for conventional UUVs (Kang, et al., 2000; Anderson & Kerrebrock, 2002).

2.4.5 Essex Robotic Fish

A number of robotic fish were designed by the Human Centred Robotics team at Essex between 2003 and 2007. The most well-known is the G9 robotic fish which was unveiled to public at the London Aquarium in 2005 (Liu & Hu, 2010). These robotic fish are designed to swim like a real fish and realize autonomous navigation. Moreover, there are modelled based on the carangiform fish movement such cod and carp (Hu, 2006; Liu & Hu, 2010) where Sfakiotakis, et al. (1999) noted that the body undulation confined to the last third of the body length.

The G9 (the 9th Generation) robotic fish is 0.52 meter length and Hu (2006) described the hardware configuration of the robotic fish consists such as Gumstix, microcontroller, various embedded sensors, three servo motor and two DC motors. These servo motors are link together in the tail to act as three joints; one DC motor is fixed in the head to change the centre of gravity (COG) of the fish, while another DC motor is used to control a micro-pump (Liu & Hu, 2010). Furthermore, Hu (2006) indicates that the robotic fish is able to bend its body to a large angle (90°/0.20sec) due to high specification of servo motor and soft tail structure. This proves beneficial for manoeuvring.

Hu, et al. (2006) reported several type of swimming pattern has been tested such as cruise straight, cruise in turn, sharp turn and ascent-decent in order to realize the carangiform swimming motion. It has demonstrated good swimming performances in forward and manoeuvring swimming (Liu, et al., 2005). Moreover, it also has shown its ability in managing an unexpected obstacles and swim freely up and down (Hu, et al., 2006)

2.4.6 PF and UPF Series

A series of robotic fish with different purposes have been developed by National Maritime Research Institute (NMRI) in Japan; PF-200, PF-300, PF-550, PF-600, PF-700 and UPF-2001. A two joint link robotic denoted PF-300 was built to investigate turning performance (Hirata, et al., 2000). It is designed based on sea bream fish shape with body length of 0.34 m. The two joints are driven using servo motors located in body and tail peduncle. According to Hirata, et al. (2000), it demonstrated that it able to perform various turning modes by swinging the tail fin and the maximum speed it can achieve is 0.6 BL/s (0.204 m/s) for straight swimming.

The PF-600, with body length about 0.60 m, has been designed to study propulsion performance (Hirata, 2000). It has three joints with a unique link mechanism which provide a way to control the motion of tail peduncle and tail fin independently and optionally. Two types of tail fins are used in the experiment; pike and tuna type. According to Hirata (2000), pike type tail fin configurations tend to have a higher swimming speed than tuna type tail fins at lower frequencies. In contrast, the swimming speed for tuna type tail fin is higher than pike type tail fin at higher frequencies. Therefore it shows that the tuna type tail fin is suitable for high frequencies with the maximum speed of 0.7 BL/s (0.42 m/s).

The PF-700 design is shaped like a mackerel pike which aimed for high speed swimming (Hirata, 2001). It has a long slim cylindrical shape with body length of 0.70 m. It has two joints where the first joint is driven by servo motor for turning purposes. Another joint is driven by DC motor for propulsion purpose where it capable to produce up to 10 Hz tail beat frequencies. As a result, it is able to achieve a maximum swimming speed of 1 BL/s (0.70 m/s). Next the three links robotic fish known as UPF-2001 is designed for high-performance and multi-purpose used. It has length of 1 m and it has revealed that it capable to obtain swim speed of 1 BL/s (1 m/s) at 10 Hz tail beat frequency (Hirata & Kawai, 2001).

Two types of robotic fish have been built to study the manoeuvring of robotic fish in vertical axis. Firstly, PF-200 was adopted with movement of weight mechanism in order to has capability of up down motion. The structure of PF-200 contains two servo motors and a weight located in the head. A servomotor is used for the tail fin and another is used to shift the weight location in order to affect the inclination of the robot fish. Hence, it is able it to manoeuvre in vertical axis (Hirata & Aoki, 2003). Another up-down mechanism has been introduced and implemented on the PF-550. It involves mounting the entire tail mechanism on a rotating shaft. Hirata & Sakurai (2003) suggested that this configuration allows the interchangeable orientation of propulsion system; instead of propel sideways it also has the capability to propel up and down motion that could be useful for vertical axis motion.

2.4.7 *RoboSalmon V2*

A free swimming biomimetic underwater vehicle known as *RoboSalmon* (see Figure 2.7) has been developed at the University of Glasgow which uses a tendon drive based propulsion system. It is 0.85 m long and as the name suggests, it was designed based on the anatomy of Atlantic salmon (Watts & McGookin, 2008, 2013). The *RoboSalmon* tail section is comprised of ten revolute joints with a caudal fin attached to the end. The tendon drive propulsion system relies on the reciprocating motion of tendon cables that attached to the servo motor arm. The tail bending motion is produced when the servo motor arm rotates and pulls on one of the tendons causing the revolute joints to turn (Watts & McGookin, 2008). It can be considered as a simple approach since only one actuator is involved to approximate the real fish swimming motion (Watts & McGookin, 2013).

Several experiments have been conducted by varying parameters such as tail beat amplitude and frequency. It has been recorded that the vehicle maximum forward swimming speed is 0.2 m/s which achieved at a tail beat frequency of 0.6 Hz and amplitude of 0.15 m (Watts & McGookin, 2013). Watts (2009) concluded that biomimetic propulsion system to be more efficiency than propeller system especially at low speed. Furthermore, it also demonstrates that it has superior manoeuvring performance than propeller system where its turning radius significantly reduced (Watts, 2009).

Figure image has been removed due to Copyright restrictions

Figure 2.7: *RoboSalmon* vehicle with tendon drive propulsion system (Watts, 2009)

2.4.8 UWFUV

The University of Washington Fin-actuated Underwater Robot (UWFUV), a fully autonomous, fish like swimming robot has been designed by University of Washington. It mimics carangiform locomotion with 2 DOF tail structure is shown in Figure 2.8. It has total length of 0.54 m with two sealed compartment on the body of the robot. The forward body compartment contains the microcontroller board, sensors, communication devices and pectoral fin servo motors while the aft compartment contains servo motors to drive the tail part (Morgansen, et al., 2007; Triplett, 2008).

Figure image has been removed due to Copyright restrictions

Figure 2.8: The University Washington fin-actuated underwater vehicle (Morgansen, et al., 2007)

The UWFUV is aimed for geometric control methods and coordinated control of multiple vehicle systems studies (Morgansen, et al., 2007; Triplett, 2008). It can reach maximum swimming speed of 0.60 m/s and it also has been demonstrated the coordination swimming of three vehicles where it used low frequency sonar pulses to communicate with each other in underwater (Triplett, 2008).

2.4.9 SPC Series

The Robotics Institute of Beihang University has developed the SPC series of biorobotic autonomous underwater vehicle for real world exploration (Liang, et al., 2011). The SPC-II and SPC-III are among this series where both are designed with two joints caudal fin thruster. These joints are driven by RE40 servomotors and the maximum tail beat frequency can be produce up to 2.5 Hz. The SPC-II is designed streamline shape and FRP (Fiberglass-Reinforced Plastics) material with length of 1.21 m (Liang, et al., 2009). It is capable of performing several basic tasks i.e. forward, turning left, turning right, up and down manoeuvre. The maximum speed it can obtain is l.4 m/s at a 2.5Hz tail beat frequency. It also shows that it can turn with 1 body length turning radius and producing maximum yaw rates at 70 °/s (Wang, et al., 2005). Moreover, the SPC-II performs vertical manoeuvres by changing the pectoral fin's incidence angle where the maximum depth it can achieve is 5 m (Liang, et al., 2005; Liang, et al., 2009). In 2004, the SPC-II has been applied in real situation where it is used to assist an underwater archaeological experiment at the shipwreck site at Dongshan Island in Fujian Province (Wang, et al., 2005; Liang, et al., 2009).

The SPC-III has similar torpedo body shape as a conventional UUV. However, a caudal fin thruster that driven by two servo motors has been implemented at the rear side of the vehicle instead of propeller (Liang, et al., 2011). Its length is 1.75 m and Liang, et al. (2011) show that SPC-III produce a higher propulsion efficiency than other previous SPC series, outcome of the further improvement of mechanical structure and motion control algorithm in SPC-II. The SPC-III has maximum speed of 1.36 m/s when operated at 2.5 Hz tail beat frequency and its turning radius is equal to one body length. Moreover, the comparison between caudal fin and propeller propulsion performance also has been conducted by directly replacing the caudal fin thruster on SPC-III with a screw propeller. It was found that the caudal fin thruster consumed less power than screw propeller when tail beat frequency is operated higher than 1 Hz. It also demonstrates better manoeuvrability than screw propeller since the latter only able to produce the turning radius of 2.5 body length. The SPC-III was deployed at Taihu Lake on November 2007, to sample water quality and blue-green algae concentration. The mission proves to be successful since SPC-III able to perform probe cruise about 49 km and data collection in highly polluted and challenging environments (Liang, et al., 2011).

2.4.10 Pearl Arowana

Ho Chi Minh City University of Technical Education developed four links carangiform robotic fish taken shape of Pearl Arowana (Nguyen, et al., 2011). It is 0.33 m long and is comprised of three joints where the undulatory motion is controlled by the connected servo motor. The propulsive wave is generated when the servo motors is executed in sequence where the side to side amplitude of the undulation is increasing from anterior part towards the caudal fin. For forward swimming, the maximum speed is approximately 0.15 m/s at 3 Hz tail beat frequency and it able to perform turning circle manoeuvre with the turning radius is 0.83 of its body length. Furthermore, the robotic fish also able to perform ascent-decent manoeuvre by installing pump where it is used to regulate the amount of water inside the vehicle body.

2.4.11 NAF-II and NEF-II

Nanyang Technological University (NTU) team developed two series of BCF swimmer; NAF (Oscillating Caudal Fin Propulsor) and NEF (Undulatory BCF Propulsor) series (Low, 2011). The former is modelled after the Asian Arowana that belongs to the carangiform locomotion. The latest prototype of this series is known as NAF-II which is an improvement of NAF-I (Low, et al., 2010). It is 0.66 m long with a three link tail as shown in Figure 2.9. It is a two DOF vehicle with one DOF driven by motor and another depends on spring mechanism. It has demonstrated that it has maximum swimming speed of 0.33 m/s which approximate to 0.5 BL/s and capable to perform basic manoeuvring where up and down motion can be executed by altering the position of counter-weight (Low, et al., 2010 ; Low, 2011).

Figure image has been removed due to Copyright restrictions

Figure 2.9: Three link tail mechanism of a NAF-II prototype (Low, et al., 2009)

Another series of BCF swimmer is known as NEF consist of six-link mechanism shown in Figure 2.10. The total length is 0.82 m and driven by five units of servo motor. The purpose of having higher numbers in DOF is to enhance its capability in performing a flexible locomotion such an eel. Moreover, Low (2011) stated that this arrangement is useful as it also allow to perform several other types of BCF swimming modes which range from pure oscillatory motion in ostraciiform swimmers to pure undulatory motion in anguilliform by manipulating the number of links in this prototype. It has maximum swimming speed of 0.15 m/s which is approximately 0.18 BL/s.

Figure image has been removed due to Copyright restrictions

Figure 2.10: NEF-II with 5 DOF structure (Low, 2011)

2.5 Summary

This chapter reviewed the conventional underwater vehicle technology that is usually based on a propeller driven system. Followed by the discussion on various AUVs designs that currently been used in commercial purpose that relevant to this research study. The hull is designed to minimize the drag and to maximize the vehicle speed where the torpedo shaped is the most popular choice. AUV has been found very effective on uncluttered environment for such surveying mission but it lacks of manoeuvrability. This manoeuvrability issue has grown researcher interest to do design modifications in order to improve its manoeuvrability that includes adding multiple thrusters around the hull. However, this configuration does not exactly solve this issue thus an alternative propulsion system is needed where researchers turn their attention to nature. Inspired by the efficiency and versatile ranges of fish swimming abilities, the current underwater vehicle is designed to adapt the biomimetic propulsion system that replicates the motion of the fish.

Several existence research studies in academic and commercial field concerning biomimetic underwater vehicle are listed. Few of these biomimetic underwater vehicles capable to realize both BCF and MPF locomotion where commonly one type of locomotion is preferred due to reduce the design complexity and time constraint. This includes the attempt to fabricate underwater vehicles using traditional actuators such as multiple motors, joints and links or by using smart material in order to replicate the fish like movement. In addition, the modelling techniques, structure mechanism, swimming mode along with the important finding for each biomimetic underwater vehicle has been summarized. It has been pointed out that the existence research focused on the hydrodynamics mechanism of fishlike swimming, fabricating the skin material, component selection, mechanism and structure design of the models. These serve as a valuable contribution on the ideas and guidelines to the development of the *RoboSalmon* prototype vehicle.

3

RoboSalmon Design

3.1 Introduction

The efficiencies associated with fish swimming capabilities has inspired researchers to find an alternative methods of propulsion for marine vehicles based on natural processes. Several advantages have been identified which involve higher efficiency, manoeuvrability and noiseless propulsion systems (Sfakiotakis, et al., 1999; Morgansen, et al., 2007; Yu, et al., 2007). These improvements can significantly benefit several application especially in marine and military field as some operations that have been considered for this technology are underwater operation, military reconnaissance, leakage detection (Liu & Hu, 2003; Yu, et al., 2007).

This chapter discusses the process involve in designing and developing one such biomimetic or biologically inspired underwater vehicle known as *RoboSalmon*. This biomimetic underwater vehicle has a propulsion system based on fish tail undulation similar to motion of a North Atlantic salmon. The purpose of building this prototype is to validate the simulation responses obtained from the mathematical modelling (see Chapter 4). The prototype is known as *RoboSalmon V3.0* as it is modelled referring on an adult Atlantic Salmon and the initial mechanical design of *RoboSalmon V3.0* is based on the prototypes developed by Watts (2009) which are *RoboSalmon V1.0* and *RoboSalmon V2.0*. Even though all of these *RoboSalmon* are based on biomimetic propulsion system, there is significant difference in the concept of generating the thrust. The former prototypes used a tendon drive system in which a single servomotor is used to control the lateral movement of the tail (Watts, et al., 2007). Watts (2009) found that this method of propulsion provides simplicity and low cost for prototype design. However it does not accurately replicate the biological tail undulation due to limitation in the mechanical design. Meanwhile in *RoboSalmon V3.0*, the realization of undulation motion is achieved by having multiple actuated joints (Mazlan & McGookin, 2012). Accurate replication of real fish undulation motion becomes possible with this technique though this increases the cost and complexity of the design.

At this stage in the discussion it is worth considering the basic structure and functions of the different genera of real fish. Generally, the swimming modes of fish can be divided into two main categories which are Body and/or Caudal Fin (BCF) locomotion and the Median and/or Pectoral Fin (MPF) locomotion (Blake, 2004; Barton, 2007). Sfakiotakis, et al. (1999) point out that fish under BCF locomotion generate thrust by bending their bodies into backward-moving propulsive waves that extend to the caudal fin. Most fish exhibit this type of locomotion which enables the achievement of maximum acceleration rates, maximum swimming flexibility and high sprint speeds (Jobling, 1995). Meanwhile, MPF locomotion is usually associated with low speed, manoeuvring and stabilisation activities (Webb, 1984; Videler, 1993; Sfakiotakis, et al., 1999). Therefore, BCF locomotion is the focus in this research and can be categorized into several types that are anguiliform, subcarangiform, carangiform and thunniform.

Figure image has been removed due to Copyright restrictions

Figure 3.1: BCF swimming movements (a) anguilliform (b) subcarangiform (c) carangiform (d) thunniform mode (Hoar & Randall, 1978)

Anguilliform swimmers such as eel and lamprey are flexible in which the entire body length involves in large amplitude undulations for propulsion (Sfakiotakis, et al., 1999; Moyle & Cech Jr, 2004). However, it is consider as inefficient swimming due to the increase in drag and vortex forces caused by the entire body undulation motion (Kenaley, 2009). Subcarangiform locomotion is basically similar to anguilliform but it only uses approximately two thirds to one half of its body in producing the propulsive wave that responsible for forward motion. The subcarangiform locomotion can be categorized in between anguilliform and carangiform in terms of speed, manoeuvrability and efficiency as shown in Figure 3.1 (Barton, 2007; Fiazza, et al., 2010). This genus of fish is considered to have equal manoeuvring and speed capabilities. Several subcarangiform swimmers includes trout, salmon, cod, goldfish and bass (Barton, 2007; Kenaley, 2009).

Sfakiotakis, et al. (1999) found that carangiform swimming mode are generally faster than anguilliform or subcarangiform swimmers. In the carangiform mode, the anterior of the swimmer body is not very flexible and slightly bent during swimming with most undulation motion only occurs at the last third of the body length that can be found in jack and mackerel (Moyle & Cech Jr, 2004; Barton, 2007). Sfakiotakis, et al. (1999) also found the drawback of this locomotion, the effects include in decreasing turning and acceleration abilities and increasing tendency of recoil motion due to the rigidity of the anterior bodies and the lateral forces that only occurs at the posterior of the body. Finally, the thunniform mode is the most efficient locomotion mode of BCF and it is adopted by some large scale fish, such as shark and tuna (Moyle & Cech Jr, 2004). It is known that the swimmers in this mode have a highly streamlined fusiform body shape that minimizes pressure drag (Donley, et al., 2004) and large lunate caudal fin attached to the body by a narrow caudal peduncle. This tail configuration helps to generate greater thrust for propulsion and maintained for a longer time without causing much yawing movement to the body and head (Sfakiotakis, et al., 1999; Moyle & Cech Jr, 2004; Barton, 2007).

An Atlantic salmon (Salmo Salar) can be classified as subcarangiform locomotion which usually associated with a good balance between speed and manoeuvrability. This is the main reason that the vehicle investigated in this research is based on this genus of fish. The average size of Atlantic salmon is between 40 to 130 cm where the maximum size it can reach is 150 cm (Whitehead, et al., 1989). This chapter outlines the work on the designing and development of *RoboSalmon*. The design of the mechanical, electrical and software systems are discussed throughout this chapter. The chapter is divided into hardware design and electrical interfacing where both discuss each part based on body and tail sections. The hardware design describes the vehicle design process which is based on the anatomy and physiology of this type of real fish. Then the electrical interfacing is described in terms of the device selection and control system involved in determining the vehicle performance.

3.2 Hardware Design

The design of the *RoboSalmon* vehicle inspired by subcarangiform locomotion and its construction is based on the Watts (2009) prototypes which are *RoboSalmon V1.0* and *RoboSalmon V2.0*. The aim is to design a biomimetic vehicle that can perform several tasks in order to determine its manoeuvrability and propulsion performance. This version of the vehicle is known as *RoboSalmon V3.0* and its construction is based on the relative dimension of an adult Atlantic salmon and is 0.90 m in length and weighs 4.30 kg. The vehicle is divided into two sections: the body section and the tail section, as shown in Figure 3.2. The body section will contains the sensors, controller, data logging systems and power management. Then the tail section will comprised of eight revolute joints which act as a propulsion system.

(a)

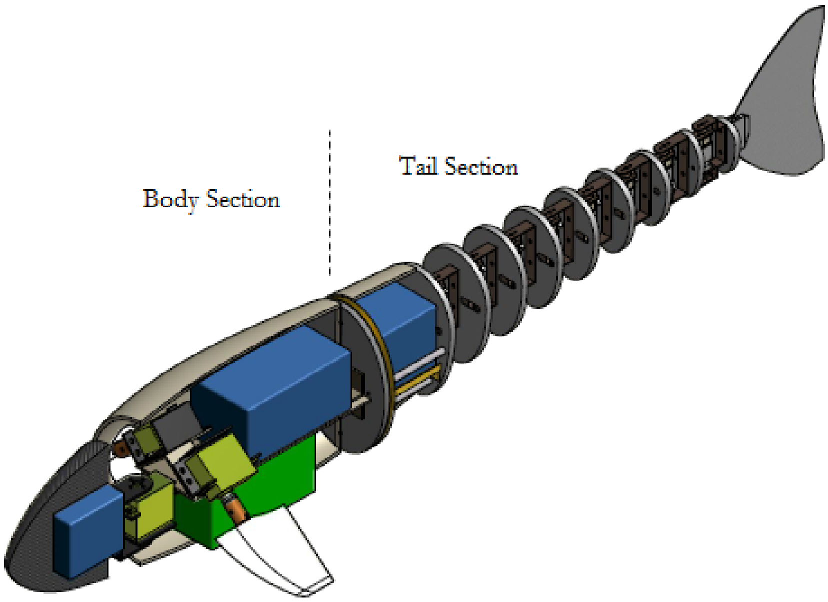

(b)

Figure 3.2: *RoboSalmon V3.0* (a) actual (b) digital prototype

3.2.1 Tail Section

The tail section acts as the main propulsion system for the fish. This section can be divided into three subsection; tail mechanism, caudal fin and tail skin.

3.2.1.1 Tail Mechanism

Naturally the structure of the tail needs to be flexible in order to perform the required undulation motion. To achieve this flexibility the tail design employed in this study is made up of eight sets of actuated joints connected together by aluminium links (see Figure 3.3). In addition, oval cross-sections made from Polyvinyl Chloride (PVC) are attached in between links in order to provide an external shape of the tail. Each joint is actuated with a geared dc motor and instrumented with a deflection sensor. This allows the deflection of each joint to be individually controlled throughout the swimming process.

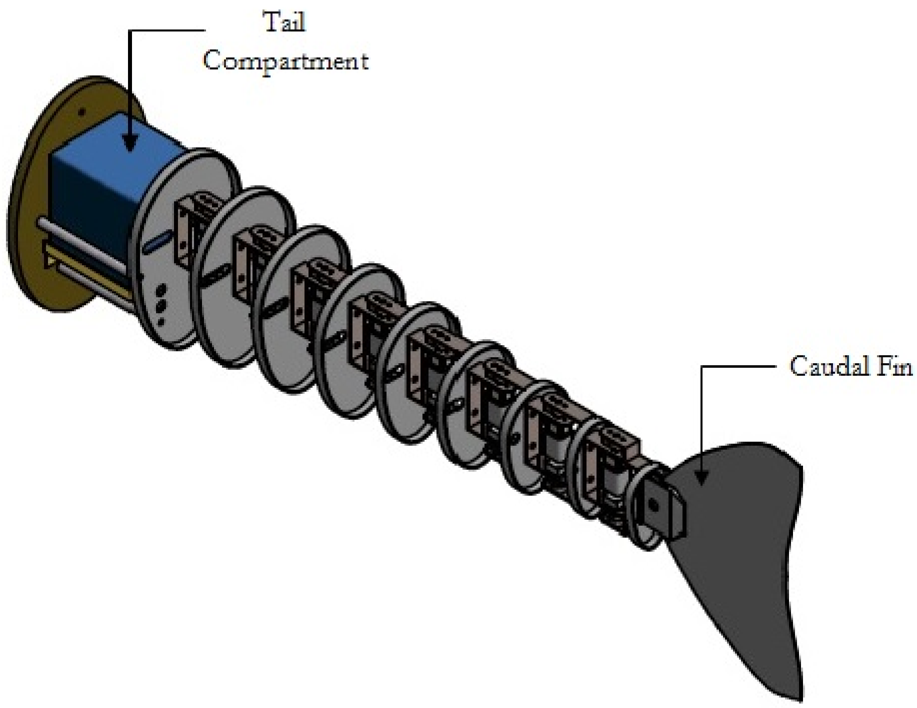

Figure 3.3: Tail section

3.2.1.2 Caudal Fin

A caudal fin will be attached at the rear end of the vehicle and it is known that the Atlantic Salmon types of caudal fin is *homocercal* which taken truncated shape (Barton, 2007; Webster, 2012). Several shapes of caudal fin have been tested in Yamamoto, et al. (1995) study, it is found that fish fin shape caudal fin produces better thrust force than the other shapes considered. Another important condition of the caudal fin is the elasticity in thrust generation where both rigid and flexible foils are being investigated (Yamamoto, et al., 1995; Lauder, et al., 2007). Even though both capable in producing thrust, the flexible foil is preferable as it produce greater efficiency compared to the rigid foil (Yamamoto, et al., 1995) and its availability in most aquatic propulsion systems (Lauder, et al., 2007). In this study, a flexible plastic caudal fin shown in Figure 3.4(b) is design closely to a real fish based on consideration of the fin shape and flexibility.

Figure image has been removed due to Copyright restrictions

(a)

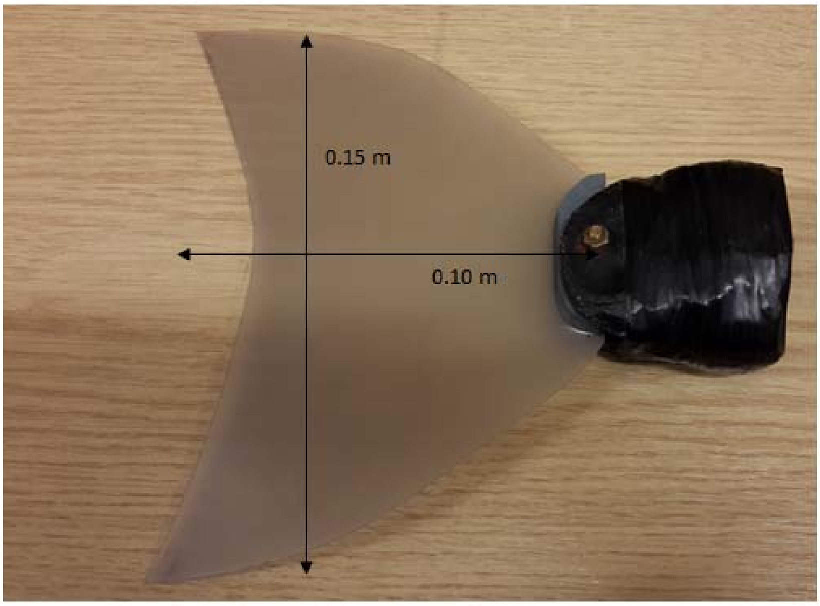

(b)

Figure 3.4: (a) Atlantic salmon (Salmo salar) (Finnish Game and Fisheries Research Institute, 2008) (b) Caudal Fin used on prototype tail propulsion system

3.2.1.3 Tail Skin

Naturally electronic components must be housed within a watertight area. Several solutions have been deduced and investigated where installing individual enclosure for each link appears to be one of the solutions to prevent water from damaging the actuator (Hu, et al., 2006; Low, 2011). However it is difficult to find a waterproof enclosure that fits to the design specification and is inexpensive. Thus in order to avoid complexity, a waterproof skin has been applied to cover fully the entire tail section. Moreover, the skin also needs to be flexible to minimise the restriction of the tail movement.

The method employed in Watts (2009) study as follows where the skin is fabricated by apply coats of liquid latex onto a thin nylon membrane. This produces a flexible and waterproof solution but after period of time, fissure can be seen on the skin which affects its elasticity. Therefore, two types of skins fabricated from silicone and latex rubber (see Figure 3.5) were investigated in this study. Even though these materials are flexible and waterproof, a latex rubber skin is preferred since the silicone rubber does not provide the same level of elasticity that the latex rubber skin provides.

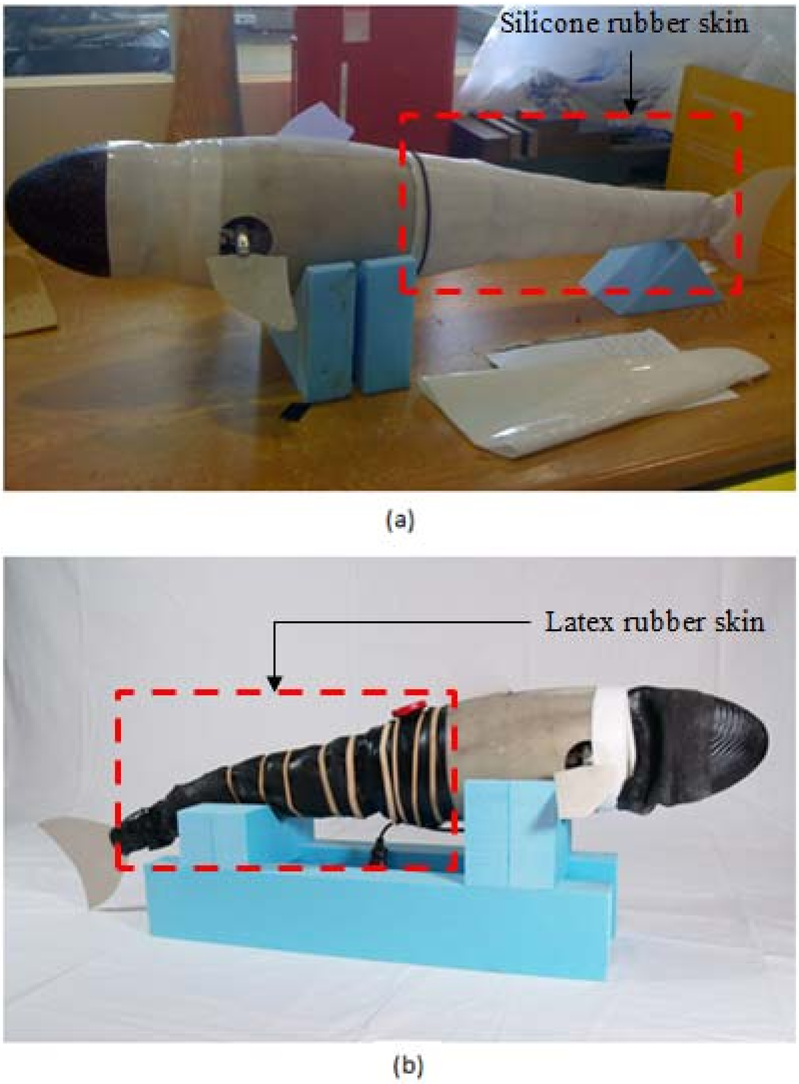

Figure 3.5: *RoboSalmon* with (a) Silicone rubber skin (b) Latex rubber skin

3.2.2 Body Section

The body of the vehicle has been designed with a wet hull where during operation underwater this section becomes flooded. This is necessary in order to compensate for the buoyancy generated by the air contained within the enclosures. Naturally this is an unwanted side effect of waterproofing the enclosures so that the electronic systems remain dry and ensure that water does not cause damage to the circuitry. The outer casing and appearance of the vehicle hull is constructed using fibreglass. The dimensions and form of this hull resembles a fish-like body as shown in Figure 3.6. This material is chosen because it is lightweight, stronger and inexpensive. It also gives freedom to design as it is easily formed using moulding processes.

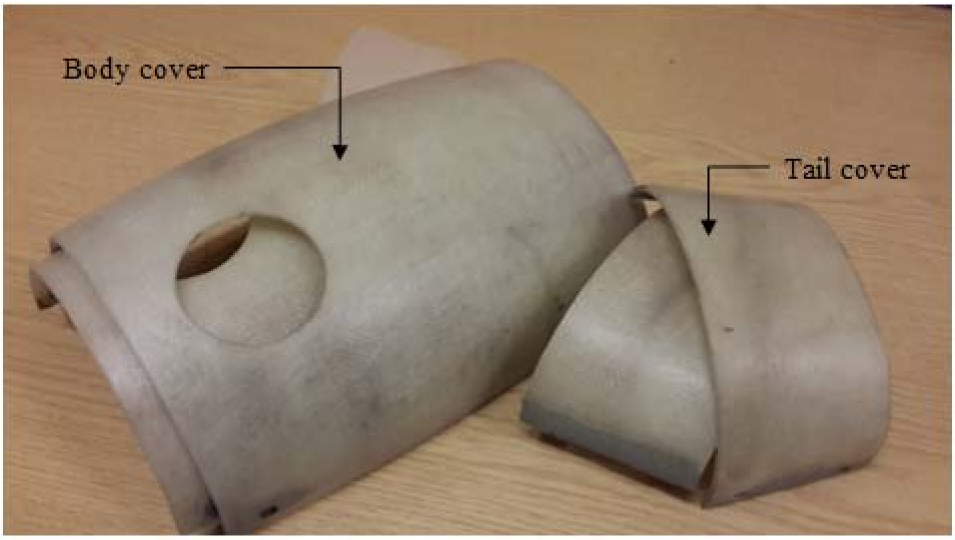

Figure 3.6: Fiberglass body and tail cover

In addition to the main propulsion actuators found in the tail, this vehicle has other actuators that are located in the body section of the vehicle. These actuators consist of three servo motors which one of them is used to drive the head. The head structure is made using styrofoam and coated with carbon fibre for better appearance. Using this materials help to reduce the load for the head servo while met the buoyancy requirement. Other two servo driven pectoral fins are located on either side of the body with ABS plastic pectoral fin (see Figure 3.7) attached at its end. The deflection of each of the pectoral fins can be controlled synchronously or independently. The pectoral fins act as bow planes to control the depth (Triplett, 2008) and also assisting on the roll stability of the vehicle.

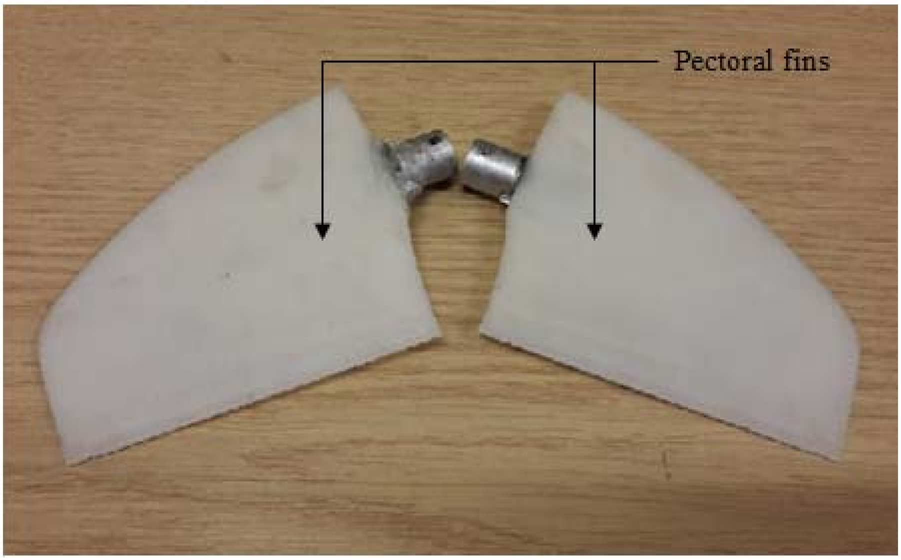

Figure 3.7: Pectoral fins

Also contained within the body section is the sensors, data acquisition systems and power management systems that are used to collect data and perform controlled tasks. The challenge in designing this section has been to locate all of the required devices within the limited space provided by the body. This has been achieved by housing the electronic systems within three watertight enclosures (see Figure 3.8) and waterproofing the servo motors. The enclosures have been labelled as the *upper body enclosure*, *lower body enclosure* and the *head enclosure* as references for further discussion. The enclosures and motors are secured to a 180 mm x 65 mm aluminium frame, which has been designed as the base for this section.

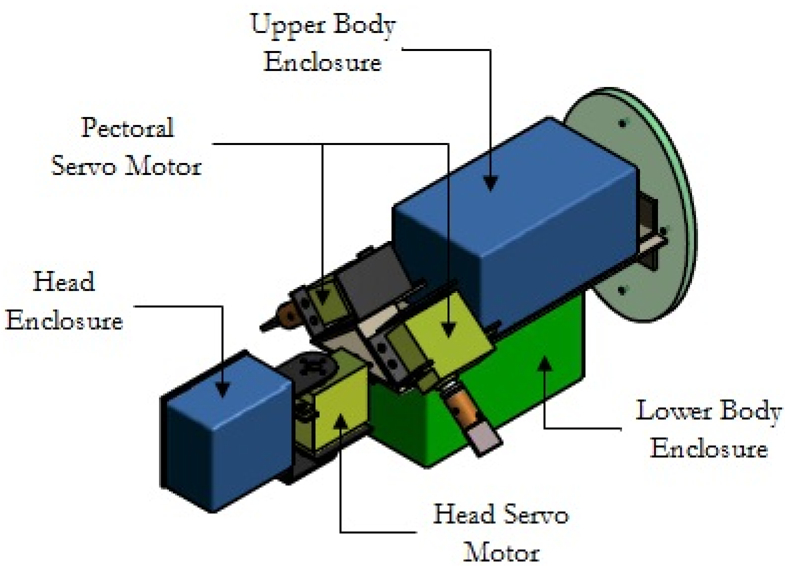

Figure 3.8: Body section

A suitable Ingress Protection (IP) rating enclosure has been selected for this application. The rating is a standardisation system used for connectors and enclosures to define the levels of sealing effectiveness of electrical enclosures against intrusion from foreign bodies and moisture. An aluminium enclosure which rated at IP68 is chosen in which it protected against complete and continuous submersion in water up to 5 metres for 1 hour (DELTRON Enclosures, n.d.). The shortcoming of using this enclosure is regarding its cost and limited size availability.

3.3 Electrical Systems

The block diagram of electrical systems and the communication protocols utilised are shown in Figure 3.9. It can be seen that three nodes denoted by dsPIC30F4013, PIC18F2480 and PIC18F25K80 are linking together using Control Area Network (CAN) interface where it allows all to share information. Each node represents a control system that is responsible for collecting data, managing data transfer and performing tasks.

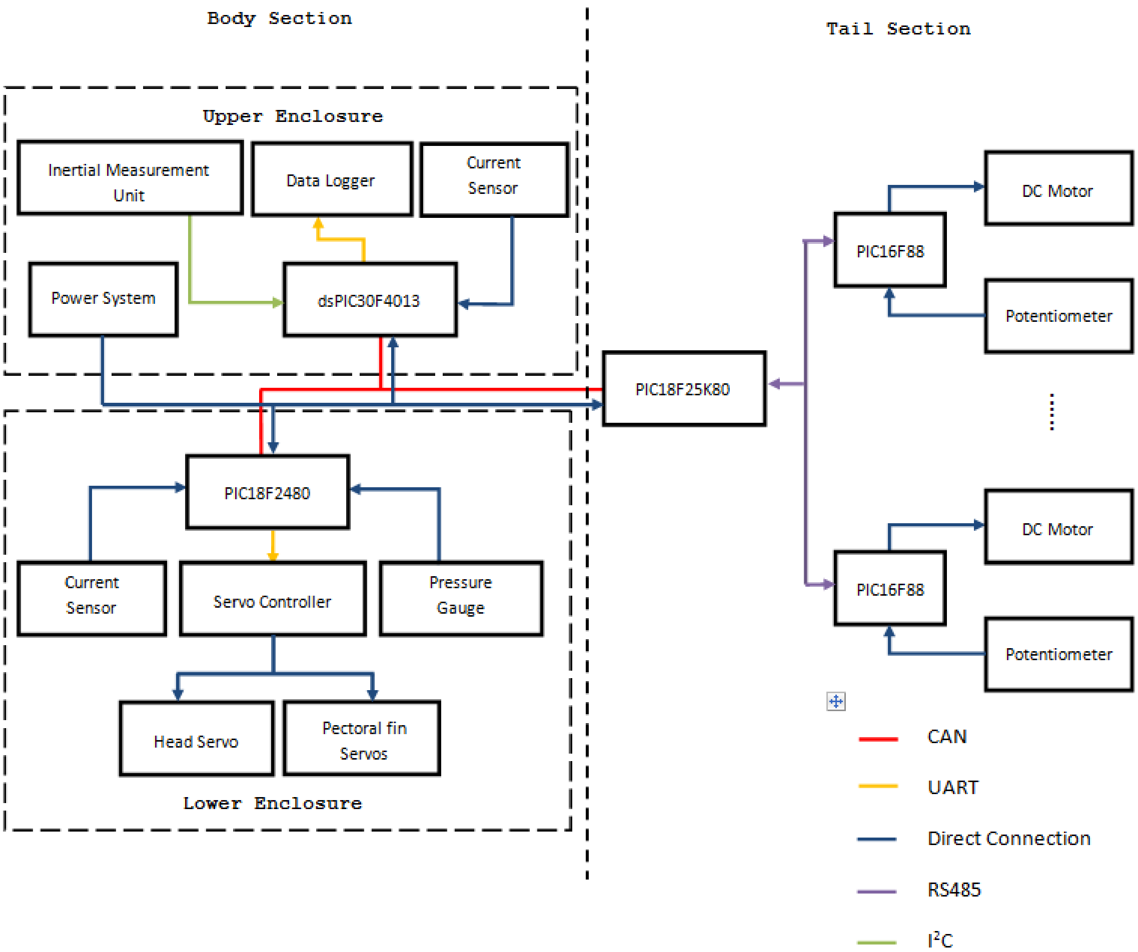

Figure 3.9: Electrical system schematic diagram

3.3.1 Electronic Systems in the Body Section

As discussed in Section 3.2.2, the body section contains 3 watertight enclosures which are intended to be used for housing the main electronic systems for the vehicle. However, only the upper and lower enclosures have been utilised in this study. The intended purpose of head enclosure is to house communication circuitry so that the robot has the ability to receive external commands from human operators. This provides the user with a selection of several pre-stored programmes to access and execute. Only the upper and lower enclosures are discussed in this section. Both the upper and lower enclosures have the same physical dimensions (i.e. 114.3 mm x 64.5 mm x 55.9 mm). The boxes used are rated at IP68 and have self-adhesive hard neoprene rubber seals. This combination provides water immersion protection up to 5 m depths (DELTRON Enclosures, n.d.). For further protection, all circuit boards are coated with AQUA STOP, a protective layer in order to prevent the electrical components damage from the damp or water ingress (Future Developments, 2002). The schematic designs of electric circuit and the layout of printed circuit boards (PCBs) shown in Appendix A, drawn using tools from Cadence; OrCAD Capture and OrCAD PCB Editor. These tools are easy to use and prove useful in transition from circuit design to circuit board (Davies, 2011).

3.3.1.1 Upper Enclosure

The upper enclosure will consist of the circuit board shown in Figure 3.10. This circuit board has the dsPIC30F microcontroller, current sensor, data logger and inertial measurement unit embedded within it.

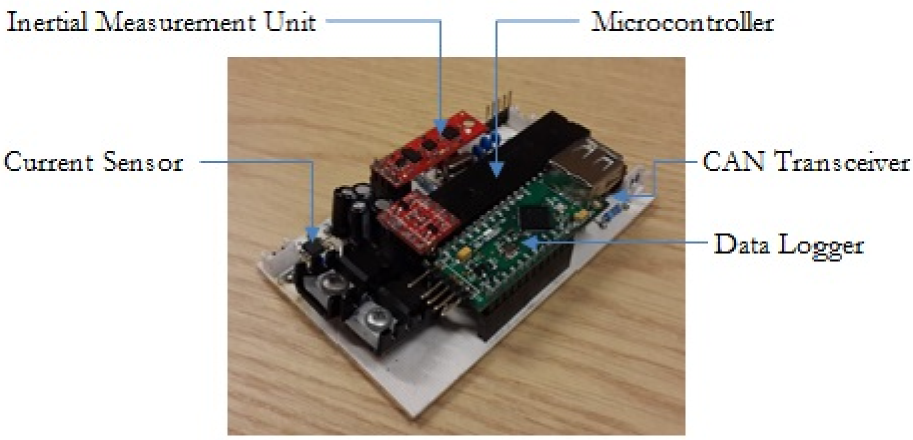

(a)

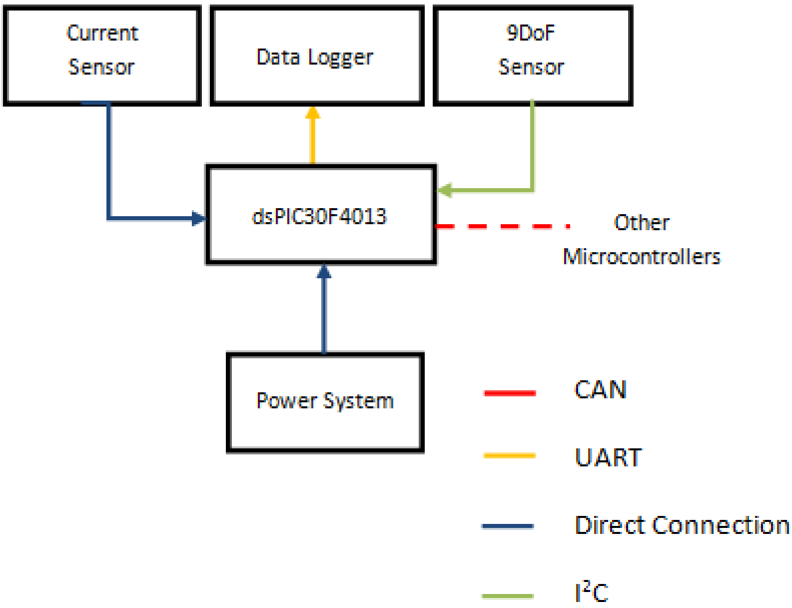

(b)

Figure 3.10: Upper enclosure (a) circuit board (b) block diagram

The function of each component is discussed in details below:

dsPIC30F Microcontroller

Peripheral Interface Controller (PIC) microcontrollers, developed by Microchip Technology, are used throughout this research. PIC microcontrollers are widely used in the field of robotics due to their low cost, wide availability and ease of programming. A dsPIC30F4013 has been chosen as the main microcontroller that acts as the brain of the vehicle. The dsPIC30F4013 is a high-performance 16-bit microcontroller unit (MCU) architecture that offer the greater processing power compares to 16F and 18F microcontroller which is suitable for smart sensing applications (Microchip Technology Inc., 2010). The key cause of this selection is because it equips with the varieties of communication modules; Serial Peripheral Interfaces (SPI), Inter-Integrated Circuit (I^2C), Universal Asynchronous Receiver / Transmitter (UART) and Controller Area Networks (CAN). These modules prove useful in this study for communications between the different integrated circuits and data acquisition from the sensor systems.

Current Sensor

One of the research objectives is to analyse the vehicle power consumption during operation. This is achieved by using an Allegro ACS712 current sensor where it provides an economical and precise way of sensing AC and DC currents based on the Hall-effect. The device is powered by 5V supply voltage and is easy to be implemented with the addition of filter capacitors in order to improve the signal to noise ratio. This device able to provide current measurement up to ±5A with sensitivity of 185 mV/A (Allegro MicroSystems, n.d.). An analogue voltage output signal varies linearly with sensed current is measured by analogue to digital converter (ADC) channel of microcontroller when it pass through the sensor.

Data logger

Ibrahim (2008) stated that data logging is a process of recording sensor measurements over period of time for post analysis. The approach taken in this study is to store all measured data on board the vehicle. One concerns using of this approach is the data storage capacity while it is also noted the difficulty in determining if any malfunction occurred before the vehicle been recovered. Since each experiment runs over a short period of time (average less than 5 minutes), thus data storage capacity is not an issue and the probability of faults occurring can be minimized by proper calibration and limiting number of runs on each session.

USB flash drives are commonly used as data storage as they offer simple, inexpensive and virtually unlimited data storage (Otten, 2008; Dart, 2009). Though Dart (2009) also argued that this type of microcontrollers lack the interfaces, resources and performance. The dsPIC30F4013 microcontroller capable to handle all data measurement but it does not have USB embedded host capability which can be solved by interfacing it with a V2DIP1-32 module via either UART, SPI or parallel FIFO (Future Technology Devices International Limited (FTDI), 2010). In this study the dsPIC30F4013 microcontroller uses the UART to communicate to the VNC2 chip embedded on V2DIP1-32 module. The UART can support baud rates from 300 baud to 3M baud with the default are set at 9600 baud. The chip equips with firmware where it lists of serial commands can be utilized by the microcontroller to create files and write data to the files in a flash drive.

Inertial Measurement Unit

The linear and angular motions of the vehicle have been investigated in this study where sensors such as accelerometers and gyroscopes are widely used for this purpose. The accelerometer is used to measure accelerations and display these either in units of meters per second squared (m/s^2), or G-force (g), which is approximately 9.81 m/s^2. Gyroscopes can be used to measure angular velocity of vehicle about the three axes: x, y and z. The angular velocity usually represented in units of rotations per minute (RPM) or degrees per second (°/s).

Both sensor types are used together in an Inertial Measurement Unit (IMU) to provide better measurements of the vehicle's orientation, position and velocities. After considering the size, sensor interfacing and cost of generally available IMUs, the 9DOF Sensor stick produced by SparkFun is selected for use in this study. It is powered by 3.3V and embedded with ADXL345 accelerometer, the HMC5883L magnetometer, and the ITG-3200 gyro on approximately 0.035 x 0.01 m^2 board (Sparkfun Electronics, n.d.). It uses I^2C interface to communicate to the microcontroller. Even though, it is term 9DOF it only measures 6 DOF due to redundancy in axis measurement. Nonetheless it helps to improve the quality of the final measurement. General descriptions of the sensors used are provided in Table 3.1 below:

Table 3.1: Sensor specification parameters

	Device	**Full-Scale Range**	**Interface**	**Axes**
Accelerometer	ADXL345	±2, 4, 8, 16g	SPI and I^2C	3
Gyroscope	ITG-3200	±2000°/s	I^2C	3
Magnetometer	HMC5883L	±8 Gauss Fields	I^2C	3

The ADXL345 is a 3-axis accelerometer and suitable for mobile device applications (Analog Devices, 2013). The measurement range has been set up at ±2g because the lower range will provide better resolution for a slow moving vehicle. ITG-3200 is a triple-axis angular rate gyroscope in which provides the orientation of the vehicle in motion with the sensitivity of 14.375 LSBs per °/sec and range of ±2000°/sec (InvenSense, 2010). Several example of its application are motion-enabled game controllers, motion-based portable gaming and health and sports monitoring. Lastly, HMC5883L is a compass with 1° to 2° heading accuracy. It is widely used in mobile phones and navigation device where in this research it is use to determine the heading of the vehicle.

Power system

Naturally an on board power system is needed for any untethered vehicle. Commonly the process of specifying the power requirements relies on the size and utilisation of the vehicle. Størkersen and Hasvold (2004) summarized several factors need to be considered when selecting a power source for an AUV. These factors include the cost, energy density, maintenance requirements and safety. Hasvold, et al. (2006) discovered that for low performance end such testing and experimentation purposes, the AUV power system commonly relied on the conventional Lead based and Nickel based rechargeable technologies. The introduction of Lithium polymer, a commercialised Lithium based battery technology capable of providing greater performance than nickel and lead based systems (Hasvold, et al., 2006). However, it applications is limited to a higher performance end due to the operating cost and battery safety (Størkersen & Hasvold, 2004; Hasvold, et al., 2006).

Therefore, a NiMH type of battery is selected for this vehicle because it provides a simple, inexpensive, safe and appropriate energy density to power the vehicle systems (Navarro-Serment, et al., 1999; Kemp, et al., 2005). Navarro-Serment, et al.(1999) also stated that the NiMH has no memory effect which allow it to be charged at any time without affecting the battery life. The vehicle is powered using a rechargeable NiMH 12V 2600 mAh batteries pack since the battery pack voltage must be chosen equal or a little higher than the devices required. Moreover, it is capable to provide an approximate lifetime of 2 hours of continuous operation.

3.3.1.2 Lower Enclosure

The lower enclosure shown in Figure 3.11 contains circuit board powered from the battery in upper enclosure. The 12V supplied is regulated to 5V in order to be used by devices mounted on this board which include PIC18 microcontroller, current and pressure sensor and servo controller.

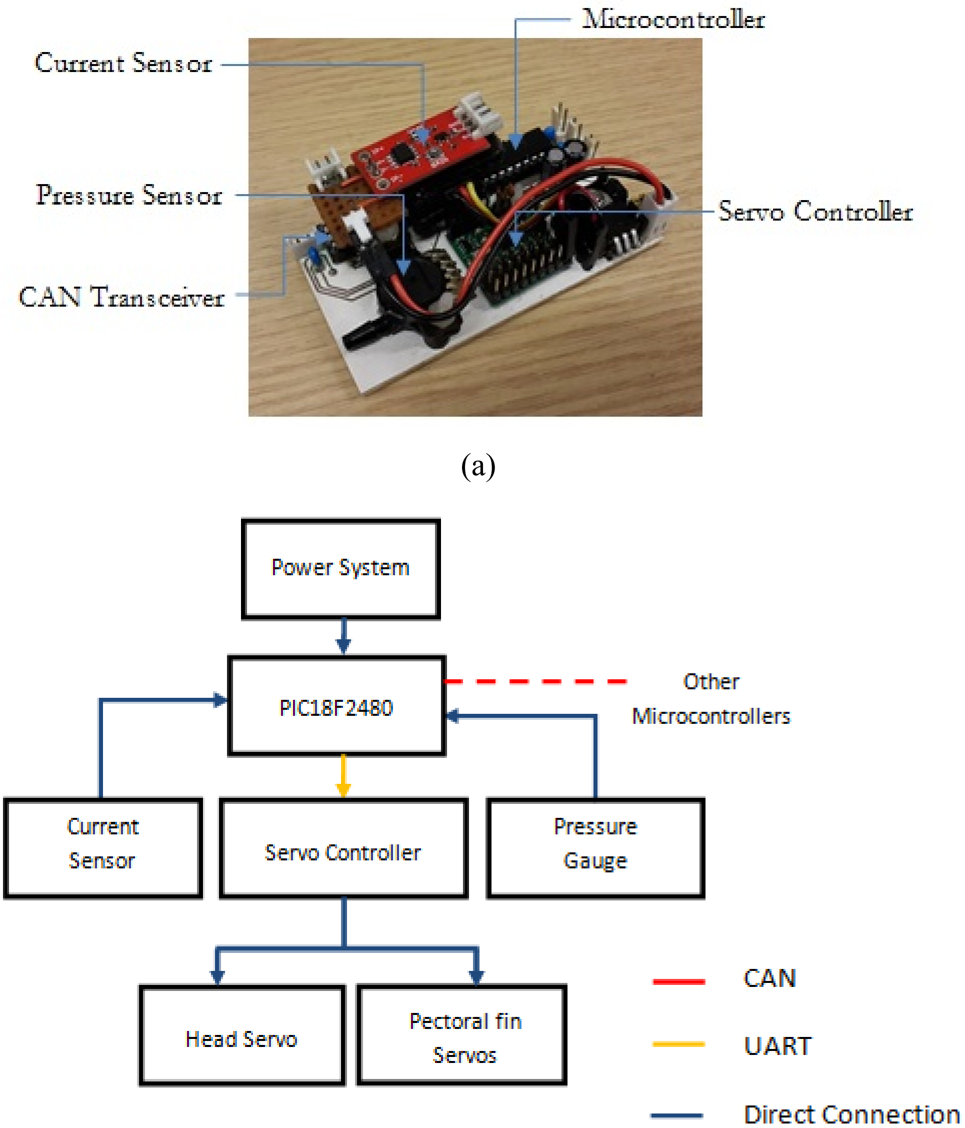

(a)

(b)

Figure 3.11: Lower enclosure (a) circuit board (b) block diagram

The function of each component is discussed in details below:

PIC18 microcontroller

The microcontroller chosen for this enclosure is PIC18F2480 where it equips with ADC channel and CAN modules. These modules provide the communication tools needed for data measurement and data transferred between microcontrollers. This microcontroller is used to read the current and pressure values and providing desired angle command to the servo controller. The latter operation is executed when receiving command via CAN bus from the main microcontroller. The commands can be varies (i.e. straight, turning left or right) where the PIC18F2480 will determine the appropriate angle to pass thru serial communication.

Servo controller

The head and pectoral fins angles are controlled using micro serial servo controller designed by Pololu (2005). It offers a solution to control multiples servo motor with each servo speed and range can be controlled independently (Pololu, 2005). This proves useful as it allows the head and pectoral fins to be executed at different angle when it received the serial command from PIC18F2480 microcontroller.

Pressure sensor

MPX4250 is a low cost pressure sensor and it has demonstrated it capability to monitor the depth of the underwater vehicle in Mohd Aras, et al. (2012) and Kuhn, et al. (2014). It typical supply voltage is 5.1 V and is connected directly to microcontroller ADC channel where its output signal is proportional to the applied pressure. Then the vehicle depth is determined based on changes in the pressure. Even though in this research, none of the experiments was conducted for vehicle vertical movement but the depth measurements were collected and stored in the data logger.

3.3.2 Electronic Systems in the Tail Section

As mentioned in Section 3.2.1, the tail section provides the main propulsive force for the vehicle. The undulation motion of the tail is generated by a set of 8 actuated joints, which require precise control in order to create smooth tail movements. The selected design is to have multiple low cost microcontrollers to solve the programming complexity and limitation on a single microcontroller approach. The PIC16F88 is chosen for this configuration because it has analogue to digital converter (ADC) and pulse-width modulation (PWM) modules. These modules are used to read the potentiometer values and providing variable speed control for motors.

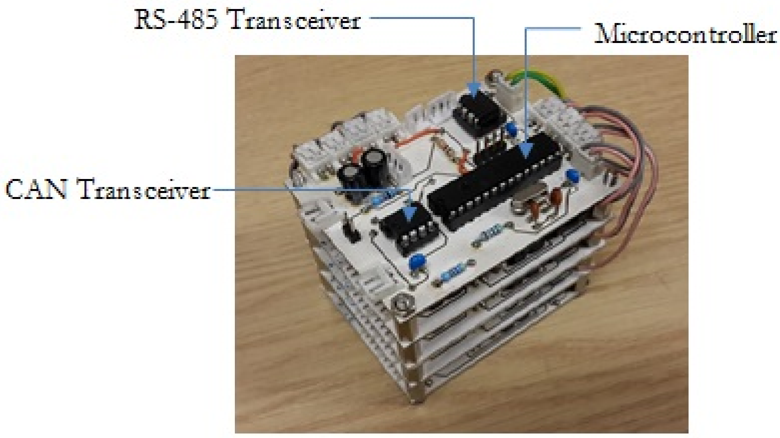

(a)

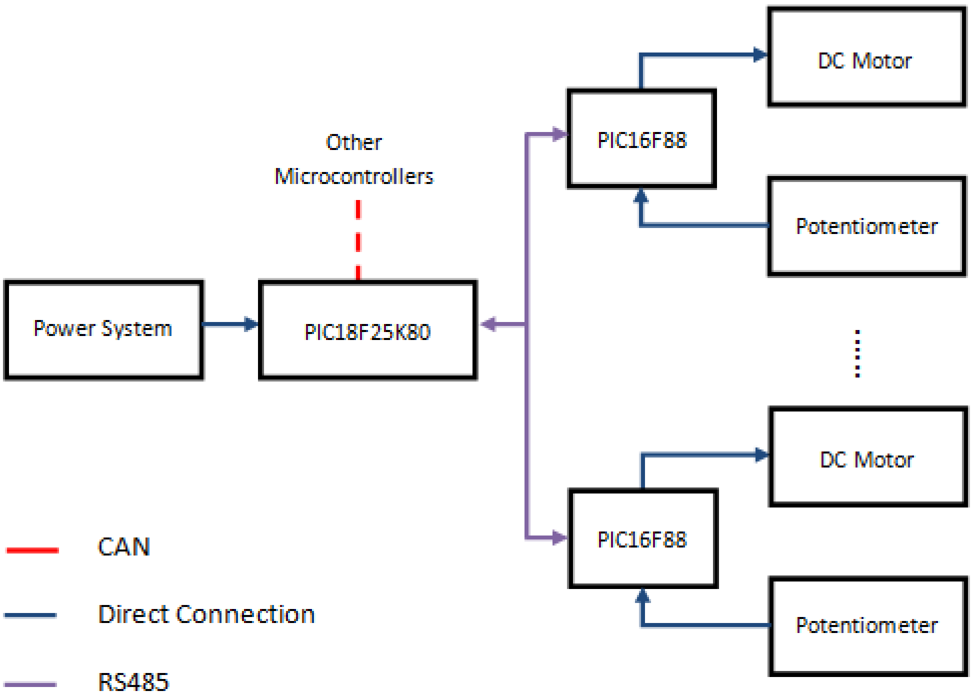

(b)

Figure 3.12: Tail motor drive (a) circuit board (b) block diagram

The tail design circuit board consists of a single master, PIC18F25K80 connected to 8 slave units, PIC16F88 through RS485 serial interface. RS485 is a serial communication method and widely used as communication interface in data acquisition and control applications where multiple nodes communicate with each other. Initially, the chosen master microcontroller is PIC18F2480 but as the experiment progressed, the tail programme demands a bigger memory. Therefore the microcontroller is replaced by PIC18F25K80 which is a direct substitution but provides a greater memory. Also, the circuit has been divided into 5 layers as shown in Figure 3.12 in order to accommodate the limited space in the end of the tail section. The electronic components are distributed as described in Table 3.2.

Table 3.2: Electronic components distribution in tail section

Number of Layer	Device	Interface
1	PIC18F25K80, CAN and RS485 transceiver	CAN, RS485
2	2 x PIC16F88, 2 x RS485 transceiver, SN754410	RS485
3	2 x PIC16F88, 2 x RS485 transceiver, SN754410	RS485
4	2 x PIC16F88, 2 x RS485 transceiver, SN754410	RS485
5	2 x PIC16F88, 2 x RS485 transceiver, SN754410	RS485

The master microcontroller is connected to the microcontrollers in upper and lower enclosure via CAN bus. The CAN bus is responsible to carries the control command between enclosures. The tail section process begins when the master microcontroller received commands from the main microcontroller in the upper enclosure. These commands comprise of tail frequency and vehicle heading angle in which it used to calculate the required tail deflection angle. It then passes the information to an appropriate slave to perform the operations. Each slave is assigned to control a DC motor and potentiometer where the DC motor is used to rotates the link to the desired angle with the potentiometer act as feedback control for the angle position.

The motors are required to be driven clockwise or counter clockwise at a given speed. This can be done by varying the on/off digital signal known as Pulse Width Modulation (PWM) (Tipsuwan & Mo-Yuen, 1999) which can be generated in software or hardware supplied by the microcontroller. The PIC16F88 has a built-in hardware called Capture/Compare/PWM (CCP) module which is used to generate a PWM signal (Microchip Technology Inc., 2009). This signal is transmits to the H-bridge integrated circuit, Texas Instruments SN754410 chip. It allows the speed and direction of a DC motor to be controlled by only one PWM output and two digital outputs from microcontroller. It can drive up to 1 A of current, and operate between 4.5V and 36V and capable two drive two motor at the same time (Texas Instruments, 1995).

3.4 Summary

This chapter covers the components selection and construction of a biomimetic underwater vehicle prototype known as *RoboSalmon*. This is the third version of *RoboSalmon* developed in Glasgow University where the previous two version were developed and tested in Watts (2009) study. Firstly, the basic structure and functions of the different genera of real has been considered. Then, the vehicle hardware design is discussed in detail in the next section where it is based on the physiology of an adult Atlantic salmon. It consists of a multiple jointed fully actuated tail that is used to replicate the undulation tail gait of a real fish. Followed by the description of component selection and electronics system configuration that chosen for the vehicle. This configuration comprise the motion control of multiple actuator motors, the motion detection by sensors, power system and data collection.

4

Mathematical Modelling

4.1 Introduction

In recent years the growth of powerful inexpensive computers and affordable software has increased the utilisation of simulation models in solving problems and aiding in decision-making in a variety of industries (Sargent, 2010). This approach is usually used when conducting experiments on a real system that would be impossible or impractical. This is because the simulation model is able to provide a solution with sufficient accuracy which is inexpensive, flexible and less time consuming (Robinson, 1997; Cau, et al., 2005; Watts, 2009). Using simulation as part of the design process allows the complexity of the entire system to be reduced through the replacement or redesign of key components. Naturally the importance of mathematical manipulation has to be taken into consideration as to the equations used affect the results and ultimate design achieved (Bhandari, et al., 2012). Mathematical modelling is useful in determining the outcome of a system under specific operating conditions and can be used to achieve many objectives set by the user. However, the accuracy of the model depends largely on both the amount of knowledge available about a system and how well the modelling is done.

This chapter discusses the mathematical modelling of a biomimetic underwater vehicle with the propulsion system based on fish-like undulation motion. Watts & McGookin (2008) investigated the development of a mathematical model for a biomimetic underwater vehicle using conventional marine vessel techniques. Several modifications need to be made to the representations of the hydrodynamics, biology and morphology of this type of fish-like vehicle in order to mimic closely a real fish (Watts, 2009). Also, there are significant differences in the way conventional underwater vehicles and fish produce forward movement; the former by using a propeller and the latter by using undulation. Thus the realization of undulation movement is inspired and modelled based on a robotic manipulator arm (Niku, 2001, 2011). The mathematical model presented in this chapter is developed in a similar manner. The main difference is that each tail joint is actuated in the vehicle considered in this study (see Figure 4.1). This provides a flexible and versatile swimming tail propulsor.

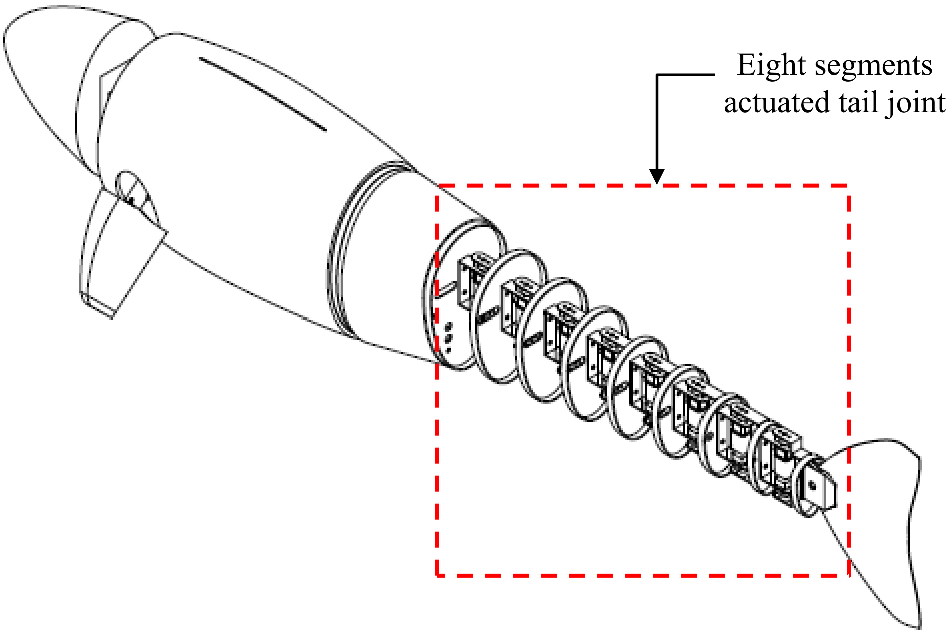

Figure 4.1: Multiple individually actuated tail joint (red box)

The development of the mathematical model and the subsequent multi-rate simulation are described according to the following structure. This chapter starts with a brief introduction to the approach employed for developing the vehicle model. This includes the state space modelling and corresponding multi-rate simulation structure. This is followed by information about dynamic variables and the reference frames in determining the position and orientation of the vehicle. Then the mathematical model is discussed in terms of its three main constituent parts, which are vehicle kinematics, vehicle dynamics and the tail propulsion system. The relationship of the body fixed reference frame to Earth fixed reference frame is described in the vehicle kinematics section. The vehicle dynamics section describes the vehicle motions with respect to the body fixed frame. The last of the modelling aspects is concerned with the tail propulsion system. This associated section describes the modelling process used to represent undulating movement of the tail during swimming. Finally, the techniques that involved in the model validation are been described.

4.2 Multi-rate Simulation

The computer simulation used in this study is based on the vehicle mathematical model that will be discussed latter in this chapter. The development and utilisation of such a simulation is becoming common practice when conducting physical experiments on a real system are impossible due to fragility of the system or impractical due to limiting constraints e.g. time, budget (Maria, 1997; Watts, 2009). It has been demonstrated that it can become a useful tool to predict the performance of vehicle if such constraints are removed.

The elements of the mathematical model (i.e. kinematics, dynamics and thrust generation) are constructed into state space form so that they are easier to be implemented within a multi-rate simulation structure. Chapra & Canale (2003) found that MATLAB (Matrix Laboratory) is a software system that works in an interactive environment that can be used for numerical computation, visualization and programming. It consists a wide range of functions which prove useful in developing algorithms and analysing data (Gockenbach, 1999). Arnold (2007) and Pearce et al. (2009) stated simulation of a dynamic system usually consists of fast and slow subsystems where it need to deal with various time constants.

The fast and slow subsystems are identifiable to the time constant where some device may respond quicker than others. Thus, multi-rate methods that implement different time constants in different subsystems could be an efficient way to solve the problem (Arnold, 2007). A multi-rate simulation partition the simulation into segments that allows it to be sampled or updated at different rates (Pearce, et al., 2009; Leyendecker & Ober-Blöbaum, 2013). The slow dynamic segment of the system is sampled with a large time constants while the fast dynamic segment is integrated with a small time constants to ensure numerical error bound and stability (Oberschelp & Vocking, 2004; Pekarek, et al., 2004). This method also speeds up the overall run time by reducing the computational effort and prove useful method when dealing with many repeated simulation runs (Oberschelp & Vocking, 2004; Bednar & Crosbie, 2007).

The multi-rate simulation structure is illustrated in Figure 4.2 where the motor time sample h_m was chosen to be 0.001s while the vehicle model and guidance model are only updated when condition 1 and 2 are met respectively. The vehicle dynamic and kinematic is sampled at h_v equal to 0.005s with time sample while h_g is 0.5s chosen for the vehicle guidance system. These values have been chosen to simplify the mathematical algorithms as well to accommodate number of step in one tail beat cycle. Moreover, by using these values (i.e. minor time steps) improve the accuracy of the results.

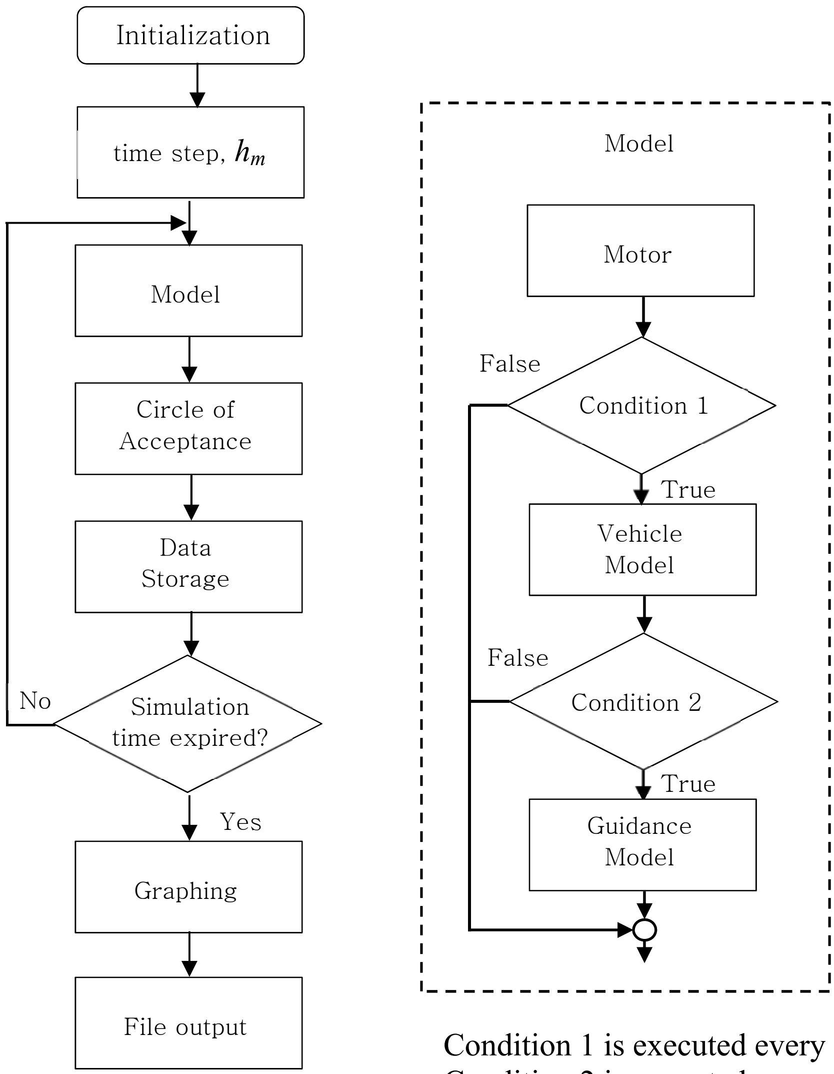

Condition 1 is executed every h_v time step
Condition 2 is executed every h_g time step

Figure 4.2: Multi-rate simulation structure

4.3 State Space Modelling

The state space representation is a convenient way to describe a system dynamic in a computer simulation, it consist of *n* first order differential equations (Murray-Smith, 1995; Rowell, 2002). It is because it has the capabilities to solve time invariant with multiple inputs and outputs (MIMO) systems. The time derivative of each state variable is expressed in terms of the state variables $x_1(t) \ldots x_n(t)$ and the system inputs $u_1(t) \ldots u_r(t)$ for a system of order *n*, and with *r* inputs while the coefficients a_{ij} and b_{ij} are constants.

$$\frac{d}{dt}\begin{bmatrix} x_1 \\ x_1 \\ \vdots \\ x_n \end{bmatrix} = \begin{bmatrix} a_{11} & a_{12} & \cdots & a_{1n} \\ a_{21} & a_{22} & \cdots & a_{2n} \\ \vdots & \vdots & & \vdots \\ a_{n1} & a_{n2} & \cdots & a_{nn} \end{bmatrix}\begin{bmatrix} x_1 \\ x_1 \\ \vdots \\ x_n \end{bmatrix} + \begin{bmatrix} b_{11} & \cdots & b_{1r} \\ b_{21} & \cdots & b_{2r} \\ \vdots & & \vdots \\ b_{n1} & \cdots & b_{nr} \end{bmatrix}\begin{bmatrix} u_1 \\ \vdots \\ u_r \end{bmatrix} \tag{4.1}$$

The matrix form of the state space model above is summarized into vector form as in Equation (4.2).

$$\dot{\boldsymbol{x}} = \boldsymbol{Ax} + \boldsymbol{Bu} \tag{4.2}$$

Where $\boldsymbol{x}$ is the state vector is a column vector of length n, $\boldsymbol{u}$ is input vector is a column vector of length r and the coefficient matrices of $\boldsymbol{A}$ ($n \times n$ square matrix of a_{ij}) and $\boldsymbol{B}$ ($n \times r$ matrix of b_{ij}) based on the system structure and elements. In addition, the output equation can be written in the form:

$$\boldsymbol{y} = \boldsymbol{Cx} + \boldsymbol{Du} \tag{4.3}$$

Where $\boldsymbol{y}$ is a column vector of the output variables and constant coefficient matrices of $\boldsymbol{C}$ ($m \times n$ matrix of c_{ij}) and $\boldsymbol{D}$ ($m \times r$ matrix of d_{ij}) represent weight of the state variables and the system inputs with m is the total of system variables that defined as outputs. Murray-Smith (1995) discussed that the solution of the differential equation can be obtained by introducing the numerical integration. This technique will give an approximation of true values of x where the error in values approximation can be reduced by choosing an appropriate sampling rate.

4.4 Reference Frames

A marine vehicle experience motion in 6 degrees of freedom (DOFs) which are the set of independent displacements and rotations. It is usually used to determine the position and orientation of the vehicle. The motion in the horizontal plane is referred to as surge (steady propulsion motion), sway (sideways motion) and yaw (rotation about the vertical axis which describes the heading of the vehicle). The remaining three DOFs are roll (rotation about longitudinal axis), pitch (rotation about transverse axis) and heave (vertical motion) (Fossen, 1994, 2011).

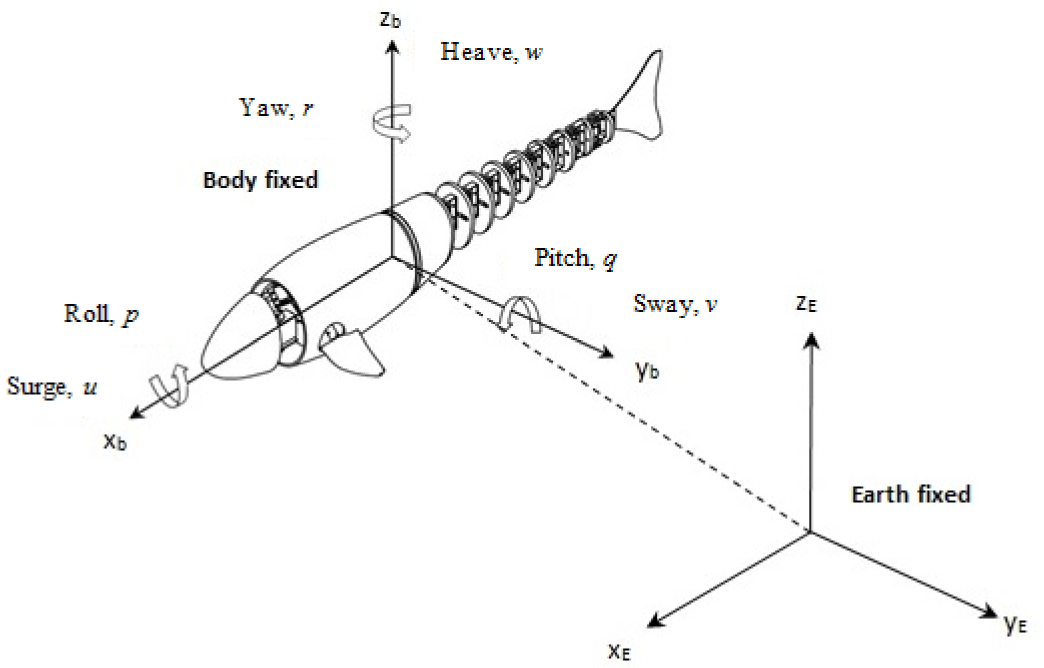

Figure 4.3: Body fixed and Earth fixed reference frames

It has become common practice to define two coordinate frames as in Figure 4.3 when analysing the motion of marine vehicle known as body-fixed reference frame and Earth fixed reference frame. The body fixed reference frame is a moving coordinate frame that is fixed to the vehicle. Fossen (1994, 2011) stated that a low speed marine vehicle is not affected by the motion of the Earth thus the acceleration of a point on the surface of the Earth can be neglected. Therefore, the Earth-fixed reference can be set to be inertial. The position and orientation of the vehicle are describes relative to the inertial reference frame while the linear and angular velocities of the vehicle should be expressed in the body reference frame.

Table 4.1: Notation used for marine vehicles (Fossen, 1994)

DOF		Forces and moments	Linear and angular velocity	Positions and Euler angles
1	Motions in x direction (surge)	X	u	x
2	Motions in y direction (sway)	Y	v	y
3	Motions in z direction (heave)	Z	w	z
4	rotation in x axis (roll)	K	p	φ
5	rotation in y axis (pitch)	M	q	θ
6	rotation in z axis (yaw)	N	r	ψ

Based on Table 4.1, the general motion of a marine vehicle in 6 DOF can be described by the following vectors in Equations (4.4). Where η is the position and orientation vector in the Earth fixed frame, v denotes the linear and angular velocity vector with coordinates in body fixed frame and τ describe the forces and moments acting on the vehicle in the body fixed frame.

$$
\begin{aligned}
\eta &= \left[\eta_1^T, \eta_2^T\right]^T; \quad \eta_1 = \left[x, y, z\right]^T; \quad \eta_2 = \left[\phi, \theta, \psi\right]^T \\
v &= \left[v_1^T, v_2^T\right]^T; \quad v_1 = \left[u, v, w\right]^T; \quad v_2 = \left[p, q, r\right]^T \\
\tau &= \left[\tau_1^T, \tau_2^T\right]^T; \quad \tau_1 = \left[X, Y, Z\right]^T; \quad \tau_2 = \left[K, M, N\right]^T
\end{aligned}
\tag{4.4}
$$

4.5 Vehicle Kinematic

According to Fossen (1994, 2011), Euler angles are a common method used in marine guidance and control systems to determine geometrical relationship of the motion vehicle relative to earth-fixed reference frame. Euler angles are a combination of three rotations in different axes which need to be carried out in sequence. The linear and angular velocities transformations are dealt separately where v_1 and v_2 are the linear and angular velocities in the body-fixed frame; $\dot{\eta}_1$ and $\dot{\eta}_2$ are the linear and angular velocities in the Earth-fixed frame.

$$
\begin{aligned}
\dot{\boldsymbol{\eta}}_1 &= \boldsymbol{J}_1(\boldsymbol{\eta}_2)\boldsymbol{v}_1 \\
\dot{\boldsymbol{\eta}}_2 &= \boldsymbol{J}_2(\boldsymbol{\eta}_2)\boldsymbol{v}_2
\end{aligned}
\tag{4.5}
$$

Here J_1 and J_2 represent the Euler transformation matrices; J_1 for the linear velocities and J_2 for the angular velocities transformation (Fossen, 2011).

$$
\begin{aligned}
\boldsymbol{J}_1(\boldsymbol{\eta}_2) &= \begin{bmatrix} c\psi c\theta & -s\psi c\phi + c\psi s\theta s\phi & s\psi s\phi + c\psi c\phi s\theta \\ s\psi c\theta & c\psi c\phi + s\phi s\theta s\psi & -c\psi s\phi + s\theta s\psi c\phi \\ -s\theta & c\theta s\phi & c\theta c\phi \end{bmatrix} \\
\boldsymbol{J}_2(\boldsymbol{\eta}_2) &= \begin{bmatrix} 1 & s\phi t\theta & c\phi t\theta \\ 0 & c\phi & -s\phi \\ 0 & s\phi / c\theta & c\phi / c\theta \end{bmatrix}
\end{aligned}
\tag{4.6}
$$

The 6 DOF kinematic equations can be expressed in vector form as

$$\dot{\boldsymbol{\eta}} = \boldsymbol{J}(\boldsymbol{\eta})\boldsymbol{\nu}$$
$$\Updownarrow$$
$$\begin{bmatrix} \dot{\boldsymbol{\eta}}_1 \\ \dot{\boldsymbol{\eta}}_2 \end{bmatrix} = \begin{bmatrix} \boldsymbol{J}_1(\boldsymbol{\eta}_2) & \boldsymbol{0}_{3x3} \\ \boldsymbol{0}_{3x3} & \boldsymbol{J}_2(\boldsymbol{\eta}_2) \end{bmatrix} \begin{bmatrix} \boldsymbol{\nu}_1 \\ \boldsymbol{\nu}_2 \end{bmatrix} \tag{4.7}$$

4.6 Vehicle Dynamics

The dynamics of the main hull of the biomimetic vehicle has been modelled using the same techniques that apply to conventional marine vehicles (Watts, et al., 2007). The development of a 6 degree of freedom (DOF) model proves useful for predicting the performance of the marine vehicle and design control systems for navigation and guidance. In this context the model is validated against the response of the physical system so that it accurately represents the actual dynamics of the system. (Murray-Smith, 1995; Fossen, 2011). The equations of motion associated with the 6 DOF dynamics of a free moving vehicle can be represented by the following equation (Fossen 1994, 2011):

$$\boldsymbol{M}\dot{\boldsymbol{v}} + \boldsymbol{C}(\boldsymbol{v})\boldsymbol{v} + \boldsymbol{D}(\boldsymbol{v})\boldsymbol{v} + \boldsymbol{g}(\boldsymbol{\eta}) = \boldsymbol{\tau} \tag{4.8}$$

Here $\boldsymbol{M}$ is the mass and inertia matrix (including added mass), $\boldsymbol{C(v)}$ is the matrix of Coriolis and centripetal terms (including added mass), $\boldsymbol{D(v)}$ is the damping matrix, $\boldsymbol{g(\eta)}$ is the vector of gravitational forces and moments, $\boldsymbol{\tau}$ is vector of control inputs, $\boldsymbol{\eta}$ is the position and orientation vector and $\boldsymbol{v}$ denotes the linear and angular velocity vector (see Section 4.5).

4.6.1 Rigid Body Dynamics

It has been discussed that the vehicle is designed based on a real fish in Chapter 3 where the vehicle will consist of two parts which are rigid hull and a flexible tail. The vehicle is assumed to be a rigid body for modelling purposes and it is noted that the assumption of the flexible tail as a rigid body is difficult to justify. However, owing to the small amount of mass in the flexible tail compared to the mass in the rigid hull. It is reasonable to approximate the flexible tail as a rigid body.

Fossen (1994) states the importance of Newton-Euler formulation contribution towards rigid body dynamic equation. This formulation is based on Newton's Second Law of

Motion, which describes dynamic systems in terms of linear, p_c and angular momentum, h_c.

$$\begin{aligned} \dot{p}_c &\triangleq f_c; \quad p_c \triangleq m v_c \\ \dot{h}_c &\triangleq m_c; \quad h_c \triangleq I_c \omega \end{aligned} \tag{4.9}$$

Here f_c and mc are forces and moments referred to the body's centre of gravity, ω is the angular velocity vector, m is the mass of the body and I_c is the Inertia about the body's centre of gravity (Fossen, 1994). The Equations (4.9) also known as Euler's First and Second Axioms (Fossen, 2011) are used to derive the rigid body dynamic equation. General 6 DOF rigid body equations of motion are taken form in Equation (4.10) with the first three equations representing translational motion and other three representing rotational motion.

$$\begin{aligned}
m\left[\dot{u} - vr + wq - x_g\left(q^2 + r^2\right) + y_g\left(pq - \dot{r}\right) + z_g\left(pr + \dot{q}\right)\right] &= X \\
m\left[\dot{v} - wp + ur - y_g\left(r^2 + p^2\right) + z_g\left(qr - \dot{p}\right) + x_g\left(qp + \dot{r}\right)\right] &= Y \\
m\left[\dot{w} - uq + vp - z_g\left(p^2 + q^2\right) + x_g\left(rp - \dot{q}\right) + y_g\left(rq + \dot{p}\right)\right] &= Z \\
I_x\dot{p} + \left(I_z - I_y\right)qr - \left(\dot{r} + pq\right)I_{xz} + \left(r^2 - q^2\right)I_{yz} + \left(pr - \dot{q}\right)I_{xy} + m\left[y_g\left(\dot{w} - uq + vp\right) - z_g\left(\dot{v} - wp + ur\right)\right] &= K \\
I_y\dot{q} + \left(I_x - I_z\right)rp - \left(\dot{p} + qr\right)I_{xy} + \left(p^2 - r^2\right)I_{zx} + \left(qp - \dot{r}\right)I_{yz} + m\left[z_g\left(\dot{u} - vr + wq\right) - x_g\left(\dot{w} - uq + vp\right)\right] &= M \\
I_z\dot{r} + \left(I_y - I_x\right)pq - \left(\dot{q} + rp\right)I_{yz} + \left(q^2 - p^2\right)I_{xy} + \left(rq - \dot{p}\right)I_{zx} + m\left[x_g\left(\dot{v} - wp + ur\right) - y_g\left(\dot{u} - vr + wq\right)\right] &= N
\end{aligned} \tag{4.10}$$

Here, notation of m is mass, $[X,Y,Z,K,M,N]$ are the external forces and moments, $[u,v,w,p,q,r]$ are the linear and angular velocity vector with coordinates in body fixed frame, $[I_x, I_y, I_z]$ are the moment of inertia with respect to x_b, y_b and z_b axes, and $[I_{xy}, I_{xz}, I_{yz}]$ are the product of inertia. These rigid body equations also can be expressed in compact vector form as:

$$\boldsymbol{M_{RB}}\dot{\boldsymbol{v}} + \boldsymbol{C_{RB}}\left(\boldsymbol{v}\right)\boldsymbol{v} = \boldsymbol{\tau_{RB}} \tag{4.11}$$

Here $\upsilon = [u,v,w,p,q,r]^T$ is the body linear and angular velocity vector and $\tau_{RB} = [X,Y,Z,K,M,N]^T$ is a generalized vector of external forces and moments.

4.6.2 Mass and Inertia Matrix

The mass and inertia matrix, ***M*** in Equation (4.8) consists of rigid body mass, $\boldsymbol{M_{RB}}$ and added mass, M_A.

$$\boldsymbol{M} = \boldsymbol{M_{RB}} + \boldsymbol{M_A} \tag{4.12}$$

The $\boldsymbol{M_{RB}}$ term can be written as

$$M_{RB} = \begin{bmatrix} mI_{3x3} & -mS(\mathrm{r}_g^b) \\ mS(\mathrm{r}_g^b) & I_b \end{bmatrix} = \begin{bmatrix} m & 0 & 0 & 0 & mz_g & -my_g \\ 0 & m & 0 & -mz_g & 0 & mx_g \\ 0 & 0 & m & my_g & -mx_g & 0 \\ 0 & -mz_g & my_g & I_x & -I_{xy} & -I_{xz} \\ mz_g & 0 & -mx_g & -I_{yx} & I_y & -I_{yz} \\ -my_g & mx_g & 0 & -I_{zx} & -I_{zy} & I_z \end{bmatrix} \tag{4.13}$$

Fossen (1994, 2011) found that the general 6 DOF rigid body equation of motion in Equation (4.10) can be simplified by choosing the origin of the body fixed coordinate system coincides with the centre of gravity which $r_g^b = [0,0,0]^T$ and $I_b = I_g$ which result to

$$M_{RB} = \begin{bmatrix} mI_{3x3} & 0_{3x3} \\ 0_{3x3} & I_g \end{bmatrix} = \begin{bmatrix} m & 0 & 0 & 0 & 0 & 0 \\ 0 & m & 0 & 0 & 0 & 0 \\ 0 & 0 & m & 0 & 0 & 0 \\ 0 & 0 & 0 & I_x & 0 & 0 \\ 0 & 0 & 0 & 0 & I_y & 0 \\ 0 & 0 & 0 & 0 & 0 & I_z \end{bmatrix} \tag{4.14}$$

4.6.3 Coriolis and Centripetal Matrix

The Coriolis and Centripetal Matrix, ***C(v)***, consists of rigid body, $\boldsymbol{C_{RB}(v)}$ and added mass terms, $\boldsymbol{C_A(v)}$ (Fossen, 2011). The $\boldsymbol{C_{RB}(v)}$ matrix is shown in Equation (4.15) with $r_g^b = [0,0,0]^T$ as the origin of the body fixed reference frame is positioned at the centre of gravity (Fossen, 1994).

$$C_{RB} = \begin{bmatrix} 0 & 0 & 0 & 0 & mw & -mv \\ 0 & 0 & 0 & -mw & 0 & mu \\ 0 & 0 & 0 & mv & -mv & 0 \\ 0 & mw & -mv & 0 & I_z r & -I_y q \\ -mw & 0 & mu & -I_z r & 0 & I_x p \\ mv & -mv & 0 & I_y q & -I_x p & 0 \end{bmatrix} \tag{4.15}$$

Simplified 6 DOF Rigid Body Equations of Motion

Applying the condition in Equations (4.14) and (4.15) simplified the rigid body equation in Equation (4.10) into the following representation

$$\begin{aligned} m(\dot{u} - vr + wq) &= X \\ m(\dot{v} - wp + ur) &= Y \\ m(\dot{w} - uq + vp) &= Z \\ I_x \dot{p} + (I_z - I_y) qr &= K \\ I_y \dot{q} + (I_x - I_z) rp &= M \\ I_z \dot{r} + (I_y - I_x) pq &= N \end{aligned} \tag{4.16}$$

4.6.4 Hydrodynamic Forces and Moments

The forces and moment acting on the vehicle can be sum of added mass due to inertia of surrounding fluid, hydrodynamic damping, restoring forces and propulsion forces. Assume that the external forces and moments $\boldsymbol{\tau_{RB}}$ can be expressed as:

$$\boldsymbol{\tau_{RB}} = \underbrace{-\boldsymbol{M_A}\dot{\boldsymbol{v}} - \boldsymbol{C_A}(\boldsymbol{v})\boldsymbol{v}}_{\text{added mass}} \underbrace{-\boldsymbol{D}(\boldsymbol{v})\boldsymbol{v}}_{\text{damping}} - \underbrace{\boldsymbol{g}(\boldsymbol{\eta})}_{\text{restoring forces}} + \underbrace{\boldsymbol{\tau}}_{\text{control input}} \tag{4.17}$$

Hence the vehicle equation of motion can be written as in Equation (4.8) where

$$\boldsymbol{M} = \boldsymbol{M_{RB}} + \boldsymbol{M_A}; \qquad \boldsymbol{C}(\boldsymbol{v}) = \boldsymbol{C_{RB}}(\boldsymbol{v}) + \boldsymbol{C_A}(\boldsymbol{v})$$

4.6.5 Added Mass Terms

According to Yuh (2000), additional effects such as force and moment acting on moving object need to be considered when dealing in underwater environment. This is because some amount of surrounding fluid must move corresponding to the moving object in fluid.

These additional effects are known as added (virtual) mass consists of added moments of inertia and cross coupling terms such as force coefficients due to linear and angular accelerations (Yuh, 2000). The general inertia matrix of added mass, $\boldsymbol{M_A}$ is expressed as shown

$$M_A = \begin{bmatrix} X_{\dot{u}} & X_{\dot{v}} & X_{\dot{w}} & X_{\dot{p}} & X_{\dot{q}} & X_{\dot{r}} \\ Y_{\dot{u}} & Y_{\dot{v}} & Y_{\dot{w}} & Y_{\dot{p}} & Y_{\dot{q}} & Y_{\dot{r}} \\ Z_{\dot{u}} & Z_{\dot{v}} & Z_{\dot{w}} & Z_{\dot{p}} & Z_{\dot{q}} & Z_{\dot{r}} \\ K_{\dot{u}} & K_{\dot{v}} & K_{\dot{w}} & K_{\dot{p}} & K_{\dot{q}} & K_{\dot{r}} \\ M_{\dot{u}} & M_{\dot{v}} & M_{\dot{w}} & M_{\dot{p}} & M_{\dot{q}} & M_{\dot{r}} \\ N_{\dot{u}} & N_{\dot{v}} & N_{\dot{w}} & N_{\dot{p}} & N_{\dot{q}} & N_{\dot{r}} \end{bmatrix} \tag{4.18}$$

Assumptions can be made in order to simplify the model as Fossen (1994, 2011) suggested. First assumption is the underwater vehicle moves at low speed, nonlinear and coupled. Second assumption is since it has shape of prolate ellipsoid (see Figure 4.4) thus it has several planes of symmetry so the off-diagonal elements in added mass matrix $\boldsymbol{M_A}$ can be removed. Hence, the simplified expressions are shown below.

$$M_A = -\mathrm{diag}\left\{X_{\dot{u}}, Y_{\dot{v}}, Z_{\dot{w}}, K_{\dot{p}}, M_{\dot{q}}, N_{\dot{r}}\right\} \tag{4.19}$$

These assumptions also lead to the added mass terms for the Coriolis and centripetal matrix, $\boldsymbol{C_A}$ being simplified as shown in Equation (4.20).

$$C_A(\nu) = \begin{bmatrix} 0 & 0 & 0 & 0 & -Z_{\dot{w}}w & Y_{\dot{v}}v \\ 0 & 0 & 0 & Z_{\dot{w}}w & 0 & -X_{\dot{u}}u \\ 0 & 0 & 0 & -Y_{\dot{v}}v & X_{\dot{u}}u & 0 \\ 0 & -Z_{\dot{w}}w & Y_{\dot{v}}v & 0 & -N_{\dot{r}}r & M_{\dot{q}}q \\ Z_{\dot{w}}w & 0 & -X_{\dot{u}}u & N_{\dot{r}}r & 0 & -K_{\dot{p}}p \\ -Y_{\dot{v}}v & X_{\dot{u}}u & 0 & -M_{\dot{q}}q & K_{\dot{p}}p & 0 \end{bmatrix} \tag{4.20}$$

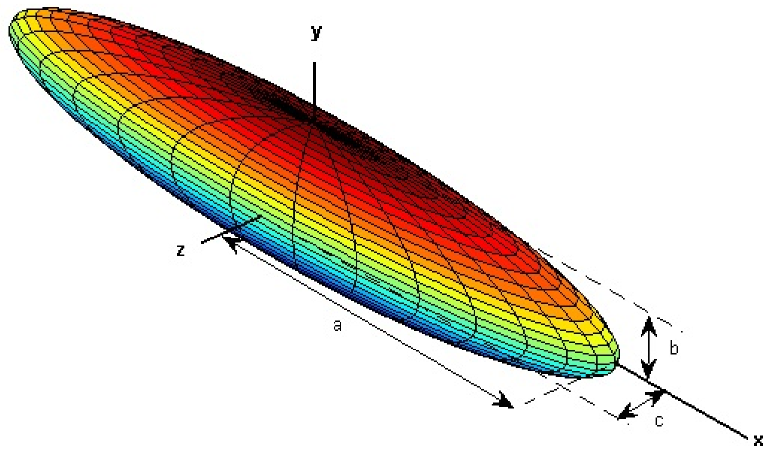

(a)

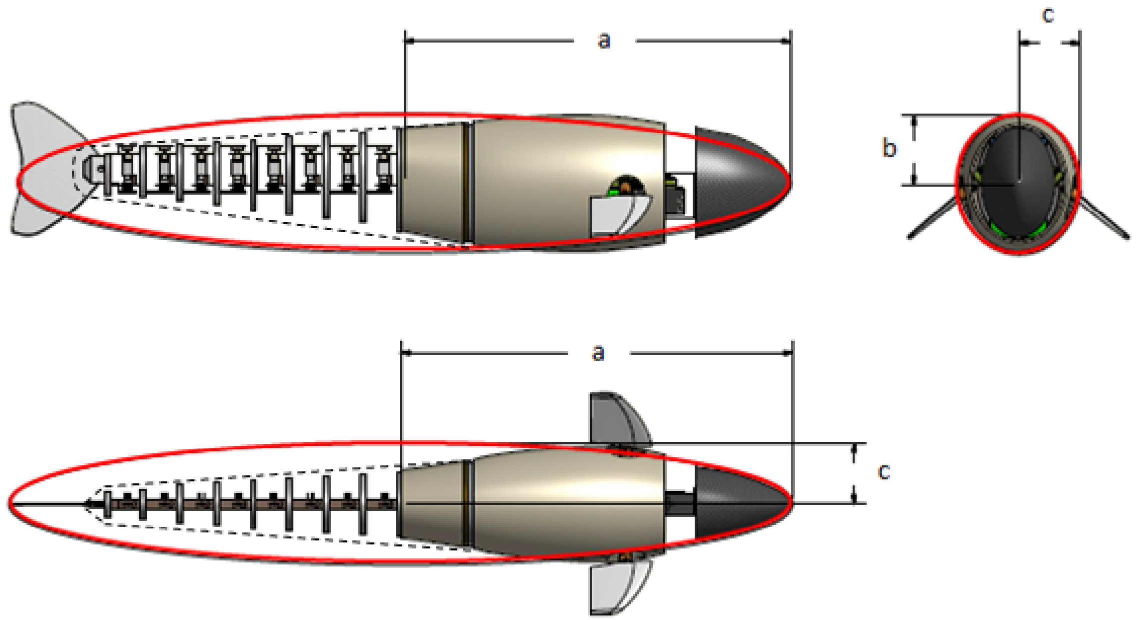

(b)

Figure 4.4: (a) Prolate Ellipsoid model with semi-axes a,b and c (b) Projection of Prolate Ellipsoid shape (red) to vehicle model

Fossen (1994) stated the added mass coefficients can assumed to be constant for an underwater vehicle as it does not effect by wave circular frequency. A prolate ellipsoid with the origin at the centre of the ellipsoid shown in Figure 4.4(a) is selected as the representation of the vehicle. In addition, Figure 4.4(b) shows how closely the vehicle model taken shape of this prolate ellipsoid. Thus it is reasonable to assume in mathematical modelling that the vehicle has a prolate ellipsoid shape. The formula for diagonal added mass derivatives for this shape are listed in Equation (4.21) with the cross-coupling terms are neglected due to body symmetry about three planes (Imlay, 1961; Fossen, 1994).

$$
\begin{aligned}
X_{\dot{u}} &= -\frac{\alpha_0}{2-\alpha_0} m \\
Y_{\dot{v}} = Z_{\dot{w}} &= -\frac{\beta_0}{2-\beta_0} m \\
K_{\dot{p}} &= 0 \\
N_{\dot{r}} = M_{\dot{q}} &= -\frac{1}{5} \frac{\left(b^2-a^2\right)^2 \left(\alpha_0-\beta_0\right)}{2\left(b^2-a^2\right)+\left(b^2+a^2\right)\left(\beta_0-\alpha_0\right)} m \\
e &= 1-\left(\frac{b}{a}\right)^2 \\
\alpha_0 &= \frac{2\left(1-e^2\right)}{e^3}\left(\frac{1}{2}\ln\frac{1+e}{1-e}-e\right) \\
\beta_0 &= \frac{1}{e^2}-\frac{1-e^2}{2e^3}\ln\frac{1+e}{1-e}
\end{aligned}
\tag{4.21}
$$

Here m is defined as the mass of the vehicle, eccentricity, e and α_0 and β_0 are variables associated with e.

4.6.6 Hydrodynamic Damping

According to Fossen (1994), hydrodynamic damping for ocean vehicles is mainly caused by radiation-induced potential damping due to forced body oscillations, skin friction, wave drift damping and damping due to vortex shedding. However, for a submerged vehicle, two significant hydrodynamic damping forces are considered which are skin friction and vortex shedding (Bende, et al., 2012). The hydrodynamic damping is difficult to be modelled without experimentation but it is a common approach to trade off the accuracy of the model by making several assumptions in order to simplify it (Silva, et al., 2007; Silva & Sousa, 2008). As mentioned earlier, the body of vehicle taken shape of prolate ellipsoid thus for streamlined body without the fins, the hydrodynamic damping can be model as:

$$D_{RB} = -\frac{1}{2}\rho C_D\left(Rn\right)A\left|u\right|u \tag{4.22}$$

Where ρ is water density, C_D is drag coefficient based on representative area, A is frontal area and u is the velocity (Videler, 1993; Iosilevskii & Weihs, 2008). The drag coefficient depends on the shape of the bodies which a simple ellipsoid body can be approximated as (Hoerner, 1965):

$$C_D = 0.44\left(\frac{d}{l}\right) + 4C_f\left(\frac{l}{d}\right) + 4C_f\left(\frac{d}{l}\right)^{\frac{1}{2}} \tag{4.23}$$

Here C_f is the friction drag coefficient with d/l is thickness ratio. Blake (1983) argued that contribution due of turning, fins and added mass will produce an actual higher values in Equation (4.22). Therefore the drag contributes by pectoral fins and caudal fin need to be taken into consideration with the shape of the fins is assumed to be wedge. The pectoral fins have the capability to rotate within certain angles while swimming which result the drag values to vary corresponding to the angle of deflection. However, for simulation purpose, the pectoral fins are set to be parallel with the body all time. Since the reference area of pectoral fins will be too small in x direction Thus, it can be assumed that the pectoral fins mainly effected by drag in the z direction and roll movement.

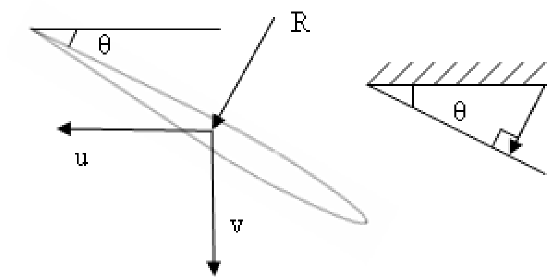

Figure 4.5: Drag calculation for caudal fin

The drag forces generated by the undulation movement are modelled by setting the caudal fin area as reference. The drag calculation of the caudal fin will depend on the angle between the end of the caudal fin and the axis shown in Figure 4.5. It is assumed that the drag values for the caudal fin will be varied along the undulation movement with the value tend to be higher when it goes perpendicular to the body. The trigonometry relationships in Equation (4.24) illustrate that the drag force of caudal fin can be resolved into *x* and *y* components.

$$\begin{aligned} R &= \sqrt{u^2 + v^2} \\ D_{Caudal} &= -\frac{1}{2}\rho C_D\left(Rn\right)A\left|R\right|R \\ D_x &= D_{Caudal}\cos\left(90-\theta\right) \\ D_y &= D_{Caudal}\sin\left(90-\theta\right) \end{aligned} \tag{4.24}$$

Here R is the resultant velocity, θ is angle between the tip of caudal fin and x-axis, D_x and D_y are the drag values in x and y direction respectively.

4.6.7 Restoring Forces and Moments

An underwater vehicle is affected by gravitational and buoyancy forces known as *restoring forces* in hydrostatic terminology (Fossen, 2011). The gravitational force, f_G acts through the centre of gravity of the vehicle and buoyancy force, f_B act through the centre of buoyancy. The position of these two forces is crucial in determining vehicle stability. Fossen (1994) stated the stability can be referred to as the tendency to return to an equilibrium state of motion after the removal of external factor without any corrective action (i.e. rudder). The greater the distance between the centre of buoyancy and the centre of gravity will produce more stable vehicle but less manoeuvrable. However, if they are positioned at the same spot, the vehicle is expected to be highly maneuverable and unstable in which demand constantly active control (i.e. pilot or computer). The general form of restoring force and moment is expressed in Equation (4.25) (Fossen, 1994, 2011).

$$g(\eta)=\begin{bmatrix} (W-B)\sin\theta \\ -(W-B)\cos\theta\sin\phi \\ -(W-B)\cos\theta\cos\phi \\ -(y_gW-y_bB)\cos\theta\cos\phi+(z_gW-z_bB)\cos\theta\sin\phi \\ (z_gW-z_bB)\sin\theta+(x_gW-x_bB)\cos\theta\cos\phi \\ -(x_gW-x_bB)\cos\theta\sin\phi-(y_gW-y_bB)\sin\theta \end{bmatrix} \tag{4.25}$$

As mentioned previously, the aim is to model the vehicle so that it closely mimics a real fish. Lauder & Madden (2006) have shown that for a real fish, the centre of buoyancy is situated below the centre of gravity, which make fish statically unstable. Even small changes in the relative positions of these centres can affect the net rolling moment and thus cause increased instability. Standen & Lauder (2005) study indicate that fish dynamic stability relies on the size and presence of multiple fins that positioned around the fish body. These fin act as multiple control surfaces used to maintain the fish posture and locomotion (Standen & Lauder, 2005; Lauder & Madden, 2006).

This dynamic instability is controlled by the fish in order to provide advantages in manoeuvring capabilities, especially when they require fast dynamic response changes

(Videler, 1993; Weihs, 1993; Lauder & Madden, 2006). However, most underwater vehicles are designed with the centre of gravity situated directly below the centre of buoyancy in order to make it statically stable (Lautrup, 2011). When a vehicle manoeuvres, it subject to a slight displacement (i.e. roll motion) from its upright position. By positioning the centre of gravity below the centre of buoyancy, it creates restoring moments where it tends to restore it back to its original position after removal of the external forces (Kreith, 1999; Young, et al., 2007). This is considered as a passive approach since it is self-correcting the roll motion (von Alt, et al., 1994; McGookin, 1997).

In addition most current AUVs are design to be slightly positively buoyant and relying on prior trim adjustments to the control surfaces or thrusters (Griffiths, 1999; Steenson, 2011). The purpose of positive buoyancy design is to make it easier for recovery if there is a system failure (Palmer, et al., 2009 ; Eng You, et al., 2010; Steenson, 2011). However, Fossen (2011) mentions that designing a vehicle to exhibit a buoyancy force much greater than its weight must be undertaken with caution. A positively buoyant vehicle requires greater controllability and continued downward thrust for it to fully submerge. This requires continued use of the on board resources (i.e. power) to operate under the water surface. Therefore it is wise to prioritize the design between the positive buoyancy and controllability depending on the operational requirements of the vehicle.

In order to simplify the modelling process for the vehicle considered in this study, a neutrally buoyant operation condition is assumed (Leonard, 1997; Pettersen & Egeland, 1999). Neutral buoyancy is when the weight of the body, W, is equal to the buoyancy force, B, but it is not necessarily with coincident centres of gravity and buoyancy. It is also assumed that the position of centre of buoyancy is higher than centre of gravity in order to minimize controllability demand in stabilizing the vehicle. Therefore, with $W = B$ and the distance between the centre of gravity and the centre located vertically on the z axis, that is $x_b = x_g$ and $y_g = y_b$. The matrix can be simplified as shown in Equation (4.26) below:

$$g(\eta) = \begin{bmatrix} 0 \\ 0 \\ 0 \\ \left(z_g W - z_b B\right)\cos\theta\sin\phi \\ \left(z_g W - z_b B\right)\sin\theta \\ 0 \end{bmatrix} \tag{4.26}$$

4.7 Tail Propulsion System

The tail propulsion system is modelled based on fish-like undulation motion is discussed in this section. The undulation part that responsible to generate thrust was inspired by a manipulator arm design where its outcome is treated as an input control that feeds into a vehicle dynamic model.

4.7.1 Tail Kinematics

The swimming pattern, or *gait*, of real fish has been studied by numerous biologists (Gray, 1968; Blake, 1983; Sfakiotakis, et al., 1999). Lighthill (1960) suggested that the undulatory motion is assumed to take the form of a traveling wave along the length of the tail. The origin of the wave is said to occur at the joining point between fish body and tail with the parameter of traveling wave changes depending on the desired fish swimming motion. The swimming of fish could be viewed as making the fish body approximate the following traveling wave:

$$y_{body}\left(x,t\right)=\left(c_1x+c_2x^2\right)\sin\left(kx+\omega t\right) \tag{4.27}$$

Here y_{body} is the lateral displacement of a tail unit from the centre axis (m), x is displacement along the tail, k is the body wave number, c_1 is the linear wave amplitude envelope, c_2 is the quadratic wave amplitude envelope, ω is angular frequency and t is time. Moreover, the Equation (4.27) can be rewritten into the following discrete form (Liu & Hu, 2004; Yu, et al., 2010)

$$y_{body}\left(x,i\right)=\left(c_1x+c_2x^2\right)\sin\left(kx\pm\frac{2\pi}{M}i\right) \quad \left(i=0,1,\ldots,M-1\right) \tag{4.28}$$

Where i denotes the i^{th} variable of the sequences $y_{body}(x,i)$ ($i = 0, 1, . . ., M - 1$) in one oscillation period, M is the resolution of the discrete traveling wave. The kinematics of the fish tail can be determined by varying the parameters c_1, c_2, k and ω. These values are not standard and can be diversified for range of swimming motions where Liu & Hu (2010) and Yu, Tan, & Zhang (2010) studies have listed several parameter values for anguilliform and carangiform swimmer. In this study, the c_1 and c_2 values are chosen to closely mimicking the realistic subcarangiform swimmer.

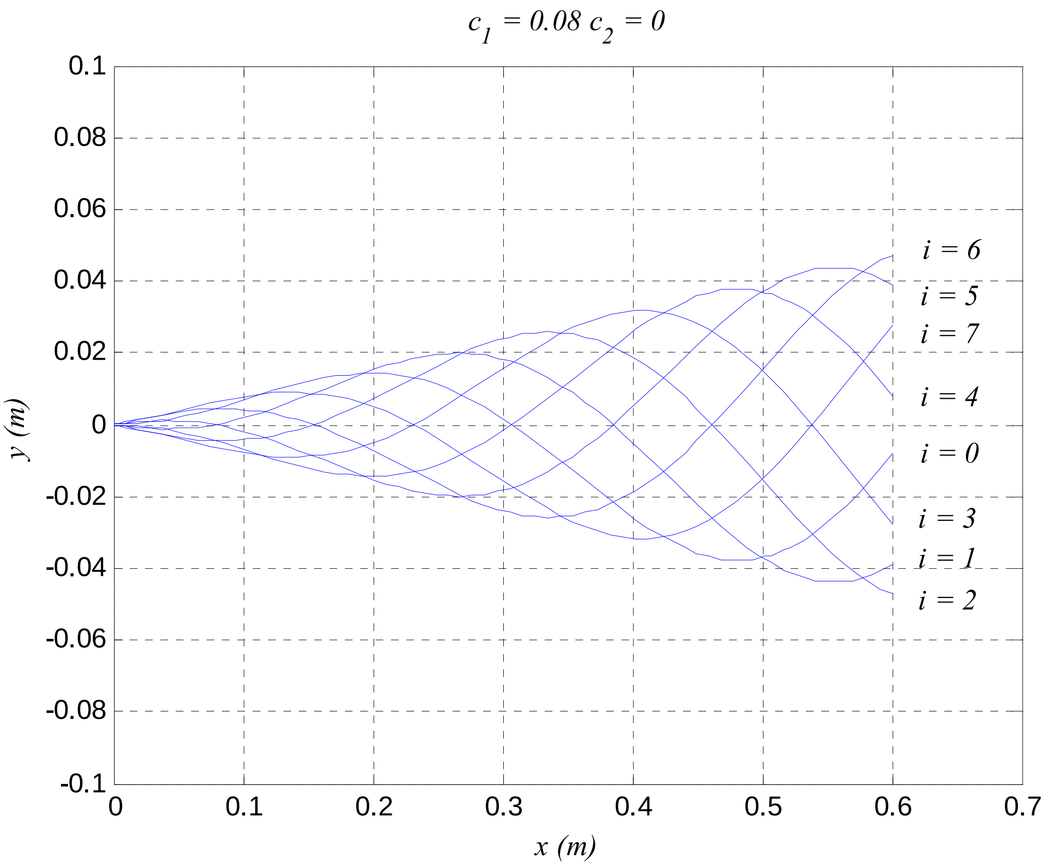

Figure 4.6: Fish kinematics using travelling wave equation

Figure 4.6 illustrates the fish kinematics that generated by using travelling wave equation with parameter values of c_1 = 0.08, c_2 = 0, k = 10.2 and M = 8. It indicates one complete cycle of undulation motion $(i = 0, 1, \cdots 7)$ where each of the lateral displacement will represents a step.

In Atlantic salmon studies, on average the salmon have 57 - 60 vertebrae (Stead & Laird, 2002; Witten, et al., 2005). According to Liu & Hu (2010), these vertebrae could be viewed as mini joints in order to approximate the wave of motion occurred during swimming. However, the vehicle has limited numbers of joints (i.e. 8 joints) which make it difficult to generate a smooth wave. Even though it is known that by increasing the numbers of links leads to better manoeuvrability and redundancy (Yu, et al., 2007). The number of links usually limited to a relatively small value between 2 to 10 links. This is due to the increased complexity associated with having more links making the implementation and control of the tail impractical (Yu, et al., 2005a).

4.7.2 Denavit Hartenberg Representation

The basic idea is to drive the multiple joints within the tail section to reproducing the same tail motion as a real fish. Niku (2001, 2011) found that the Denavit-Hartenberg representation is a simple way of representing the kinematics of robotic links and joints that can be used for any robot configuration regardless of its sequence and complexity. This method is ideally suited to derivation of the kinematics of the multi-jointed tail used in this project. It allows the kinematic tail parameters to be determined and the transformation matrices for each joint to be calculated. The vehicle is designed with 8 revolute (rotational) joints, each driven by a separate DC motor. The combined motion of these actuated joints provides the undulating motion needed to propel the vehicle. In order to control this tail motion, the position of the joints at specific points in the swimming gait must be determined using kinematics. Hence, the Denavit-Hartenberg representation is employed with each joint being assigned a 2-axis reference frame as shown in Figure 4.7.

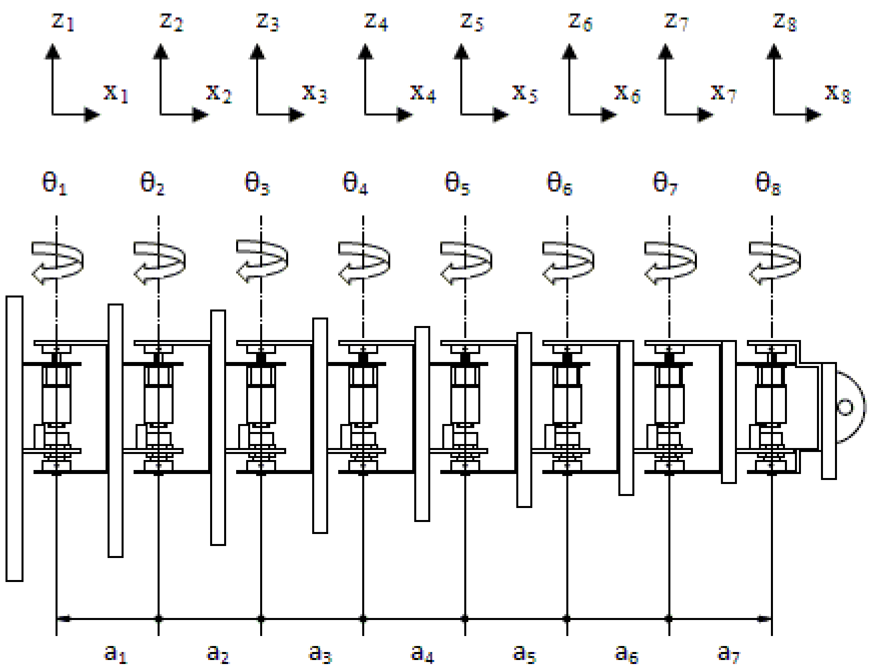

Figure 4.7: Multi-joint tail configuration

The reference frame are defined from the first joint that attached to the body to the final joint attach to the caudal fin. The transformation matrix in Equation (4.29) represents the four link parameter to describe the robot kinematic (Waldron & Schmiedeler, 2008).

$$ {}^{i-1}_{i}T = R_x\left(\alpha_{i-1}\right) D_x\left(a_{i-1}\right) R_z\left(\theta_i\right) D_z\left(d_i\right) $$

$$ {}^{i-1}_{i}T = \begin{bmatrix} c\theta_i & -s\theta_i & 0 & a_{i-1} \\ s\theta_i c\alpha_{i-1} & c\theta_i c\alpha_{i-1} & -s\alpha_{i-1} & -s\alpha_{i-1} d_i \\ s\theta_i s\alpha_{i-1} & c\theta_i s\alpha_{i-1} & c\alpha_{i-1} & c\alpha_{i-1} d_i \\ 0 & 0 & 0 & 1 \end{bmatrix} \tag{4.29} $$

These parameters a_{i-1}, α_{i-1}, d_i and θ_i are the link length, link twist, link offset and joint angle, respectively. The matrix is use to coordinate transformation from one frame $\{i\}$ relative to frame $\{i-1\}$.In this equation R_x and R_z are rotational transformations, D_x and D_z are translational transformations, and $c\theta_i$ is $cos(\theta_i)$ and $s\theta_i$ is $sin(\theta_i)$.

Table 4.2: *RoboSalmon* tail parameter table

i	$\boldsymbol{\theta_i}$	$\boldsymbol{d_i}$	$\boldsymbol{a_{i-1}}$	$\boldsymbol{\alpha_{i-1}}$
1	θ_1	0	0.054	0
2	θ_2	0	0.054	0
3	θ_3	0	0.054	0
4	θ_4	0	0.054	0
5	θ_5	0	0.054	0
6	θ_6	0	0.054	0
7	θ_7	0	0.054	0
8	θ_8	0	0.054	0
9	0	0	0.185	0

The transformations between two successive joints can be written by simply substituting the parameter in Table 4.2 and shown as follow:

$$
{}^0_1T = \begin{bmatrix} c\theta_1 & -s\theta_1 & 0 & a_0 \\ s\theta_1 & c\theta_1 & 0 & 0 \\ 0 & 0 & 1 & 0 \\ 0 & 0 & 0 & 1 \end{bmatrix} \quad
{}^1_2T = \begin{bmatrix} c\theta_2 & -s\theta_2 & 0 & a_1 \\ s\theta_2 & c\theta_2 & 0 & 0 \\ 0 & 0 & 1 & 0 \\ 0 & 0 & 0 & 1 \end{bmatrix} \quad
{}^2_3T = \begin{bmatrix} c\theta_3 & -s\theta_3 & 0 & a_2 \\ s\theta_3 & c\theta_3 & 0 & 0 \\ 0 & 0 & 1 & 0 \\ 0 & 0 & 0 & 1 \end{bmatrix}
$$

$$
{}^3_4T = \begin{bmatrix} c\theta_4 & -s\theta_4 & 0 & a_3 \\ s\theta_4 & c\theta_4 & 0 & 0 \\ 0 & 0 & 1 & 0 \\ 0 & 0 & 0 & 1 \end{bmatrix} \quad
{}^4_5T = \begin{bmatrix} c\theta_5 & -s\theta_5 & 0 & a_4 \\ s\theta_5 & c\theta_5 & 0 & 0 \\ 0 & 0 & 1 & 0 \\ 0 & 0 & 0 & 1 \end{bmatrix} \quad
{}^5_6T = \begin{bmatrix} c\theta_6 & -s\theta_6 & 0 & a_5 \\ s\theta_6 & c\theta_6 & 0 & 0 \\ 0 & 0 & 1 & 0 \\ 0 & 0 & 0 & 1 \end{bmatrix} \qquad (4.30)
$$

$$
{}^6_7T = \begin{bmatrix} c\theta_7 & -s\theta_7 & 0 & a_6 \\ s\theta_7 & c\theta_7 & 0 & 0 \\ 0 & 0 & 1 & 0 \\ 0 & 0 & 0 & 1 \end{bmatrix} \quad
{}^7_8T = \begin{bmatrix} c\theta_8 & -s\theta_8 & 0 & a_7 \\ s\theta_8 & c\theta_8 & 0 & 0 \\ 0 & 0 & 1 & 0 \\ 0 & 0 & 0 & 1 \end{bmatrix} \quad
{}^8_9T = \begin{bmatrix} 1 & 0 & 0 & a_8 \\ 0 & 1 & 0 & 0 \\ 0 & 0 & 1 & 0 \\ 0 & 0 & 0 & 1 \end{bmatrix}
$$

The position and orientation of caudal fin relative to the vehicle's body is determined by using the total transformation matrix describing the forward kinematics of the tail. This is achieved by multiplying all transformation matrices for all eight tail joints, as shown in Equation (4.31).

$$
{}^0_9T = {}^0_1T\,{}^1_2T \cdots {}^8_9T \qquad (4.31)
$$

In this case frame $\{0\}$ indicates the first frame attached to the hull of the vehicle and frame $\{8\}$ is the caudal fin. As a result, it allows the position and orientation of caudal fin relative to its body to be determined. The transformation matrices for each frame with respect to the body fame are listed in Equation (4.32).

$$
\begin{aligned}
&1^{st}\ frame : {}^0_1T \\
&2^{nd}\ frame : {}^0_1T\,{}^1_2T \\
&3^{rd}\ frame : {}^0_1T\,{}^1_2T\,{}^2_3T \\
&4^{th}\ frame : {}^0_1T\,{}^1_2T\,{}^2_3T\,{}^3_4T \\
&5^{th}\ frame : {}^0_1T\,{}^1_2T\,{}^2_3T\,{}^3_4T\,{}^4_5T \\
&6^{th}\ frame : {}^0_1T\,{}^1_2T\,{}^2_3T\,{}^3_4T\,{}^4_5T\,{}^5_6T \\
&7^{th}\ frame : {}^0_1T\,{}^1_2T\,{}^2_3T\,{}^3_4T\,{}^4_5T\,{}^5_6T\,{}^6_7T \\
&8^{th}\ frame : {}^0_1T\,{}^1_2T\,{}^2_3T\,{}^3_4T\,{}^4_5T\,{}^5_6T\,{}^6_7T\,{}^7_8T \\
&9^{th}\ frame : {}^0_1T\,{}^1_2T\,{}^2_3T\,{}^3_4T\,{}^4_5T\,{}^5_6T\,{}^6_7T\,{}^7_8T\,{}^8_9T
\end{aligned} \qquad (4.32)
$$

In this modelling, only two parameter been used which are deflection angle θ and link displacement a. The values for deflection angles, θ are obtained from the plot in Figure

4.6. The tail mechanisms are arranged on top of the plot to approximate the shape of the traveling wave where the relative angle between joints are then been measured. The total transformation between the hull and the caudal fin is shown below:

$$ {}^{0}_{9}T = \begin{bmatrix} r_{11} & r_{12} & r_{13} & P_x \\ r_{21} & r_{22} & r_{23} & P_y \\ r_{31} & r_{32} & r_{33} & P_z \\ 0 & 0 & 0 & 1 \end{bmatrix} \tag{4.33} $$

Where

$$ \mathrm{r}_{11} = \cos\left(\theta_1+\theta_2+\theta_3+\theta_4+\theta_5+\theta_6+\theta_7+\theta_8\right) $$

$$ r_{21} = \sin\left(\theta_1+\theta_2+\theta_3+\theta_4+\theta_5+\theta_6+\theta_7+\theta_8\right) $$

$$ r_{31} = 0 $$

$$ r_{12} = -\sin\left(\theta_1+\theta_2+\theta_3+\theta_4+\theta_5+\theta_6+\theta_7+\theta_8\right) $$

$$ r_{22} = \cos\left(\theta_1+\theta_2+\theta_3+\theta_4+\theta_5+\theta_6+\theta_7+\theta_8\right) $$

$$ r_{32} = 0 $$

$$ r_{13} = 0 $$

$$ r_{23} = 0 $$

$$ r_{33} = 1 $$

$$ \begin{aligned} P_x = {} & a_8\cos\left(\theta_1+\theta_2+\theta_3+\theta_4+\theta_5+\theta_6+\theta_7+\theta_8\right)+a_7\cos\left(\theta_1+\theta_2+\theta_3+\theta_4+\theta_5+\theta_6+\theta_7\right) \\ & +a_6\cos\left(\theta_1+\theta_2+\theta_3+\theta_4+\theta_5+\theta_6\right)+a_5\cos\left(\theta_1+\theta_2+\theta_3+\theta_4+\theta_5\right) \\ & +a_4\cos\left(\theta_1+\theta_2+\theta_3+\theta_4\right)+a_3\cos\left(\theta_1+\theta_2+\theta_3\right)+a_2\cos\left(\theta_1+\theta_2\right)+a_1c\theta_1+a_0 \end{aligned} $$

$$ \begin{aligned} P_y = {} & a_8\sin\left(\theta_1+\theta_2+\theta_3+\theta_4+\theta_5+\theta_6+\theta_7+\theta_8\right)+a_7\sin\left(\theta_1+\theta_2+\theta_3+\theta_4+\theta_5+\theta_6+\theta_7\right) \\ & +a_6\sin\left(\theta_1+\theta_2+\theta_3+\theta_4+\theta_5+\theta_6\right)+a_5\sin\left(\theta_1+\theta_2+\theta_3+\theta_4+\theta_5\right) \\ & +a_4\sin\left(\theta_1+\theta_2+\theta_3+\theta_4\right)+a_3\sin\left(\theta_1+\theta_2+\theta_3\right)+a_2\sin\left(\theta_1+\theta_2\right)+a_1s\theta_1 \end{aligned} $$

$$ P_z = 0 $$

Using the transformation matrices in Equation (4.32), the x and y coordinates of each link can be obtained. The representation of the fish kinematics using the *RoboSalmon* tail assembly is shown in Figure 4.8. This method also allows the measurement of lateral displacement of each link from the centreline that might affect the vehicle roll motion.

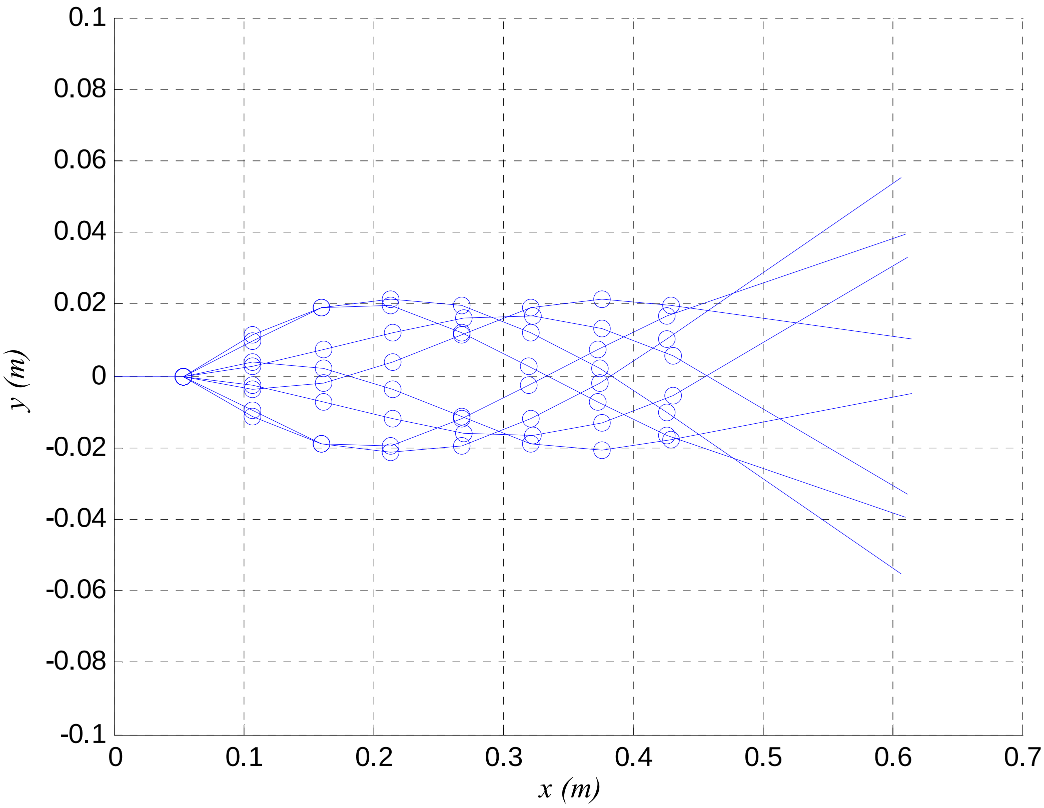

Figure 4.8: Fish kinematics using *RoboSalmon* tail assembly with circle indicate joints

4.7.3 DC Motor Model

As mentioned previously, the eight joints that constitute the tail system are driven by individual DC motors. Each DC motor is designed to move its associate tail segment to a desired angular position so that the combined motion of the tail mimics the biological undulation exhibited by real fish. Bolton (2008) found that a DC motor is a common actuator used in positional or speed control systems. Several advantages of a DC motor are it has better control, good for high precision robots, reliable and low maintenance (Niku, 2001). Moreover it is polarity sensitive, where the motor directions depend on input voltage. A Micro Spur DC Gearmotor is chosen as actuator to produce the undulating movement. It is manufacture by with the gear ratio of 298:1 and high torque (Precision Microdrives, n.d.). Moreover it has specification of 12 mm in diameter and weight of 9.6 g which is fit the requirement for the tail part.

The torque T_m produced by a DC motor is given by where K_t is armature constant and I is armature current. The armature circuit has resistance R and inductance L, and the motion generate a back emf, $V_e = K_e\dot{\theta}$. The rotor of the dc motor has inertia J and in system international (SI) units, K_t is equal to K_e. Thus the following Equations (4.34) and (4.35) are obtained by using a combination Newton's laws and Kirchhoff's law.

$$J\ddot{\theta} + B\dot{\theta} = KI \tag{4.34}$$

$$L\frac{dI}{dt} + RI = V - K\dot{\theta} \tag{4.35}$$

The differential equations derived from equation above can be written in the state space form, the angular position, angular velocity and electric current are expressed as the state variable and the voltage as an input and the output is chosen to be the angular position. The equations in state-space form can be represented as following:

$$\dot{x}_n(t) = Ax_n(t) + Bu_n(t)$$
$$y_n(t) = Cx_n(t)$$

$$\dot{x}_n(t) = \begin{bmatrix} \dot{x}_{1n}(t) \\ \dot{x}_{2n}(t) \\ \dot{x}_{3n}(t) \end{bmatrix} \quad x_n(t) = \begin{bmatrix} x_{1n}(t) \\ x_{2n}(t) \\ x_{3n}(t) \end{bmatrix} \quad u_n(t) = V$$

$$A = \begin{bmatrix} -\frac{R}{L} & 0 & -\frac{K}{L} \\ 0 & 0 & 1 \\ \frac{K}{J_n} & 0 & -\frac{B}{J_n} \end{bmatrix} \quad B = \begin{bmatrix} \frac{1}{L} \\ 0 \\ 0 \end{bmatrix} \quad C = \begin{bmatrix} 0 & 1 & 0 \end{bmatrix} \tag{4.36}$$

Where

$$x_{1n} = I; \quad x_{2n} = \theta; \quad x_{3n} = \dot{\theta}$$
$$n = 1,2,3\ldots8$$

The state space models for all motors are shown in matrices form in Equation (4.37) where each motor has 3 states that bring to a total of 24 motor states variable (i.e. 8 DC motors). It can be seen these motors have a different constant values. This is due to the changing in total moment of inertia value which is the addition of DC motor and load (i.e. link). The load values are associates with the position of motor in the tail configuration. The motor attached to the hull will has the highest load value whereas the motor at the other end will has the lowest value.

$$
\begin{aligned}
\dot{x}_1 &= \begin{bmatrix} -16 & 0 & -0.9 \\ 0 & 0 & 1 \\ 673.63 & 0 & -149.70 \end{bmatrix} x_1 + \begin{bmatrix} 2 \\ 0 \\ 0 \end{bmatrix} u & \dot{x}_5 &= \begin{bmatrix} -16 & 0 & -0.9 \\ 0 & 0 & 1 \\ 1347.30 & 0 & -299.39 \end{bmatrix} x_5 + \begin{bmatrix} 2 \\ 0 \\ 0 \end{bmatrix} u \\
\dot{x}_2 &= \begin{bmatrix} -16 & 0 & -0.9 \\ 0 & 0 & 1 \\ 769.86 & 0 & -171.08 \end{bmatrix} x_2 + \begin{bmatrix} 2 \\ 0 \\ 0 \end{bmatrix} u & \dot{x}_6 &= \begin{bmatrix} -16 & 0 & -0.9 \\ 0 & 0 & 1 \\ 1796.30 & 0 & -399.19 \end{bmatrix} x_6 + \begin{bmatrix} 2 \\ 0 \\ 0 \end{bmatrix} u \\
\dot{x}_3 &= \begin{bmatrix} -16 & 0 & -0.9 \\ 0 & 0 & 1 \\ 898.17 & 0 & -199.59 \end{bmatrix} x_3 + \begin{bmatrix} 2 \\ 0 \\ 0 \end{bmatrix} u & \dot{x}_7 &= \begin{bmatrix} -16 & 0 & -0.9 \\ 0 & 0 & 1 \\ 2694.50 & 0 & -598.78 \end{bmatrix} x_7 + \begin{bmatrix} 2 \\ 0 \\ 0 \end{bmatrix} u \\
\dot{x}_4 &= \begin{bmatrix} -16 & 0 & -0.9 \\ 0 & 0 & 1 \\ 1077.80 & 0 & -239.51 \end{bmatrix} x_4 + \begin{bmatrix} 2 \\ 0 \\ 0 \end{bmatrix} u & \dot{x}_8 &= \begin{bmatrix} -16 & 0 & -0.9 \\ 0 & 0 & 1 \\ 5389.00 & 0 & -1197.60 \end{bmatrix} x_8 + \begin{bmatrix} 2 \\ 0 \\ 0 \end{bmatrix} u
\end{aligned}
\tag{4.37}
$$

4.7.4 Gear Ratio

A DC motor can rotate at high speed up to thousands of revolutions per minute. In order to avoid the tail parts to move rapidly, the gearing system has been utilised where this configuration increases the DC motor torque while decrease its speed (Niku, 2001, 2011).

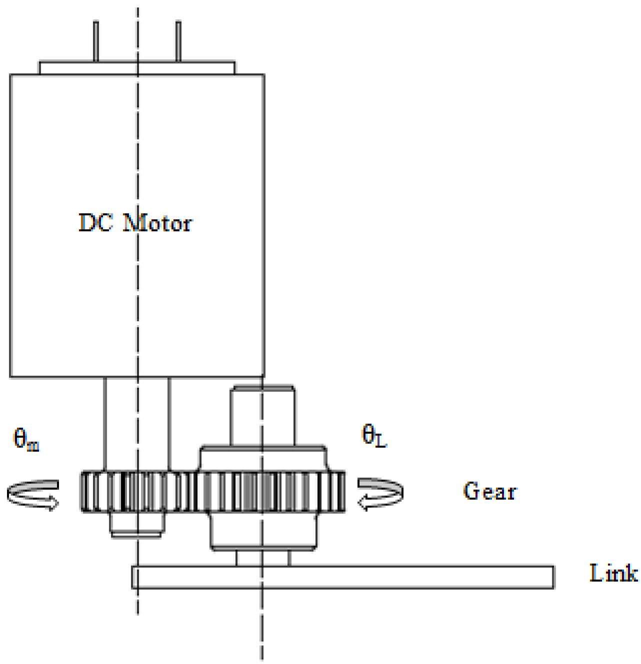

Figure 4.9: Schematic model of revolute joint. θ_m is the angular position of the motor (rad) and θ_L is the load position of the motor

However, the gear train introduced between the motor and load shown in Figure 4.9 will result difference between the angle moved by the load, θ_L and the angle moved by the motor, θ_m. Precision Microdrives (n.d.) indicates that the DC Gearmotor used in this study has gear ratio of 298:1 i.e. the driver gear must rotates 298 revolutions to turn the driven gear 1 revolution.

4.7.5 DC Motor Position Control

A control system is needed to control the angular position of the DC motor. The aim is to rotate the DC motor until it achieved the desired angular position so that the cumulative effort will take form of undulation movement. Figure 4.10 shows motor block diagram which constructed from Equations (4.34) and (4.35) with a PID controller and rotary potentiometer are added to the system. According to Bolton (2008), a rotary potentiometer can be treated as a potential divider, it has rotation as an input and potential difference as an output. In simulation modelling, the potentiometer will act as a feedback that provides the actual angular position of each joint. A proportional integral derivative (PID) controller is designed for the system and its transfer function is:

$$u(s) = K_p \Delta\theta(s) + K_d s \Delta\theta(s) + \frac{K_i}{s} \Delta\theta(s) \tag{4.38}$$

Where

$$\Delta\theta = \theta_d - \theta_a$$

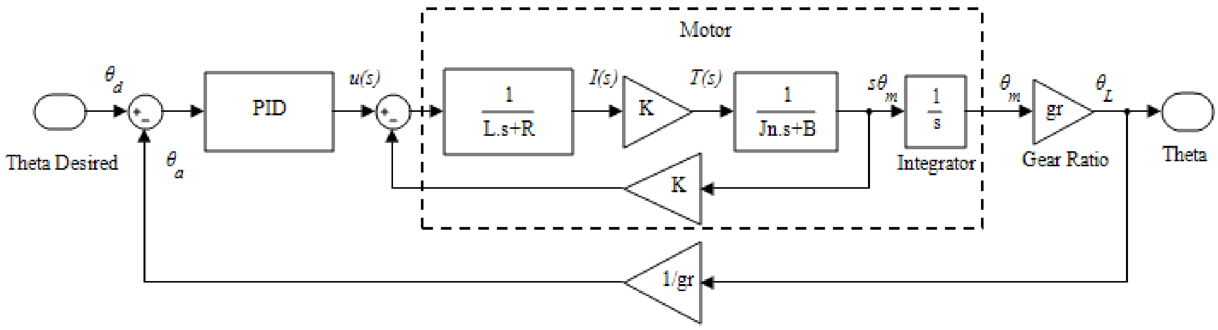

Figure 4.10: Motor block diagram with PID controller

The gain values of the K_p, K_i and K_d are theoretically can be determine to compensate the plant in order to achieve the desired performance of the system, in terms of setting time, steady state error and overshoot (Martono, 2006). The PID controller is designed to meet several requirements based on the information in the DC motor datasheet (Precision Microdrives, n.d.).

Actuators are subject to physical limitation which contributes to the control design. The control signal produced by the controller must not exceed the maximum limit for the given values. Therefore, in this study, the limitation of input voltage that can be supplied to the motor is set to be between plus and minus 12 V and the maximum current is 0.788 A (Precision Microdrives, n.d.). If the limit has been exceeded for a reasonable period of time undesirable control behaviour may be obtained. This process is known as actuator saturation and it can be prevent by applying a saturation block at the output of PID controller as shown in Figure 4.11.

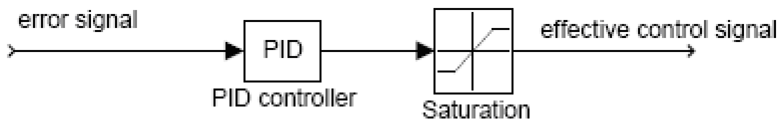

Figure 4.11: PID controller with saturation block.

It is known that the integral term is introduced so that it can eliminate the steady state error. However the use of integral action which in the PID controller combined with actuator saturation can produce some undesirable effects. Bohn & Atherton (1995) explained that the large error may contribute to the undesirable effect and it is known as integrator windup. Several numbers of strategies have been used in order to reduce the effects of integrator windup which are clamp integrator output, stop integration on saturation and back-calculation (Bohn & Atherton, 1995; Åström, 2002; Sazawa, et al., 2010). An anti-windup scheme has to be implement in the simulation as to limit the voltage provide to the motor, 12 V. The windup effect occurs in all control systems where an integrator is used in the controller. The problem is obviously that the controller continues to integrate though the manipulated variable has already reached its bound. As the controller output further grows unnecessarily, this is called the windup effect. An anti-windup scheme is implemented to counteract the integration of the controller when such a case arises will be explained later.

4.7.6 Thrust Generation

One of the challenges in this modelling process is to estimates the thrust produce by the undulation movement. The biologist and mathematician have been fascinated with the fish locomotion for a long time in which led them to develop formulation and techniques in order to investigate the process. Even though with the recent growth in computing power that generally contributes to the improvement for thrust estimation presented in Schultz and Webb (2002) and it appears that there have not been unique existing solutions in determining the thrust produced by the undulation movement.

It is known that propulsive forces are generated as fish moves its body and fins relative to water by displacing the water. Sfakiotakis, et al. (1999) found that a body and/or caudal fin (BCF) such as subcarangiform and carangiform locomotion generate thrust by bending their bodies into a backward moving propulsive wave that extends to its caudal fin in which Videler (1993) noted that the caudal fin will has the largest lateral amplitude and highest lateral velocity. Thus under this condition, the elongated body theory that developed by Lighthill (1960; 1970) is chosen in which it is commonly used to estimate the propulsive forces for these type of locomotion (Sfakiotakis, et al., 1999; Schultz & Webb, 2002; Webb, et al., 2012). This is because it assumes that the thrust generation only occurs at the trailing edge of the tail (Videler, 1993; Tytell & Lauder, 2004).

Videler (1993) and Ellerby (2010) studies describe Lighthill's theory as a mathematical modelling of momentum transfer between fish and water based on the tail kinematics. The caudal fin motion consists of combination of heave and pitch where Triantafyllou, et al. (2000) noted that heave and pitch are the lateral and angular motion of the caudal fin respectively. It appeared that these axes differ from the defined vehicle body fixed and Earth fixed reference frames in Figure 4.3. The difference is caused by initial theory that is based on the tail flukes of cetacean mammals such as whales and dolphins nonetheless the same theory can also be applied for vertical orientation caudal fin (Chopra, 1976).

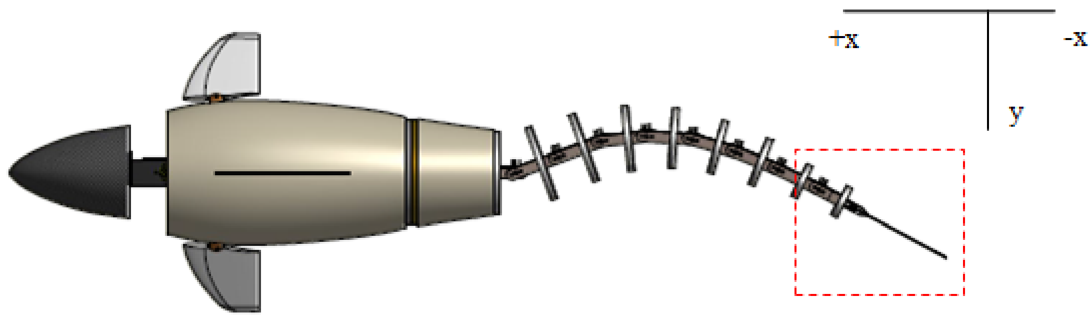

(a)

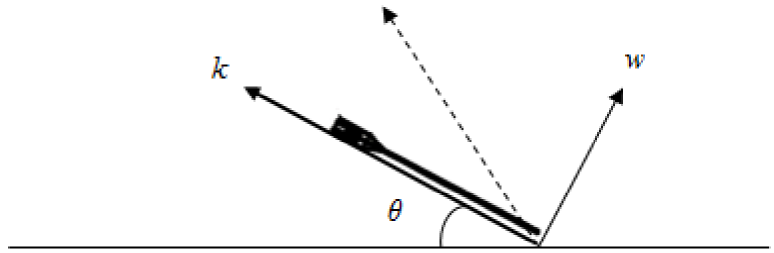

(b)

Figure 4.12: (a) Top view of the outline of a *RoboSalmon* swimming motion in time (b) The red box in Figure 4.12(a) is redrawn on a larger scale with the broken arrow indicates the instantaneous velocity vector of the caudal fin tip has been resolved into components *k* and *w*

A small axes modification has been made and shown in Figure 4.12. The component k is the parallel velocity to the caudal fin (ms^{-1}) and w is the velocity perpendicular to it (ms^{-1}) where it consists of angular motion, θ (angle between caudal fin tip and x-axis) and rate of change in x direction (forward motion) and y direction (lateral motion) with respect to time.

$$\begin{aligned} k &= \frac{dy}{dt}\sin\theta + \frac{dx}{dt}\cos\theta \\ w &= \frac{dy}{dt}\cos\theta - \frac{dx}{dt}\sin\theta \end{aligned} \tag{4.39}$$

Then, the average thrust force is calculated using Equation (4.40) :

$$T = \left(mwk\sin\theta + \frac{1}{2}mw^2\cos\theta \right)_{tail} \tag{4.40}$$

Where T is the thrust force (N), m is the virtual mass of water per unit length (kgm^{-1}). Manoeuvring procedure involved by altering the vehicle tail centreline. Since the thrust calculation the position of the undulation centreline is being altered, the thrust calculation for the vehicle need to be modified using Equation (4.41). The thrust forces acts in sway and yaw component are considered. X_T and Y_T are considered as the thrust generate will be divided into two components while manoeuvring and N_T is Y_T multiply by centre of gravity.

$$\begin{aligned} X_T &= T\cos\left(tail\ deflection\ angle\right) \\ Y_T &= T\sin\left(tail\ deflection\ angle\right) \\ N_T &= Y_T\,(centre\ of\ \ gravity) \end{aligned} \tag{4.41}$$

4.8 *RoboSalmon* State Space Equations

The 6 DOF dynamics of the *RoboSalmon* vehicle in Equation (4.42) is obtained with the combination of Equations in (4.11) and (4.17).

$$\boldsymbol{M_{RB}}\dot{\boldsymbol{v}} + \boldsymbol{C_{RB}}\left(\boldsymbol{v}\right)\boldsymbol{v} = -\boldsymbol{M_A}\dot{\boldsymbol{v}} - \boldsymbol{C_A}\left(\boldsymbol{v}\right)\boldsymbol{v} - \boldsymbol{D}\left(\boldsymbol{v}\right)\boldsymbol{v} - \boldsymbol{g}\left(\boldsymbol{\eta}\right) + \boldsymbol{\tau} \tag{4.42}$$

This also can be represented in the matrix form as followed:

$$\begin{bmatrix} m & 0 & 0 & 0 & 0 & 0 \\ 0 & m & 0 & 0 & 0 & 0 \\ 0 & 0 & m & 0 & 0 & 0 \\ 0 & 0 & 0 & I_x & 0 & 0 \\ 0 & 0 & 0 & 0 & I_y & 0 \\ 0 & 0 & 0 & 0 & 0 & I_z \end{bmatrix} \begin{bmatrix} \dot{u} \\ \dot{v} \\ \dot{w} \\ \dot{p} \\ \dot{q} \\ \dot{r} \end{bmatrix} + \cdots$$

$$\cdots + \begin{bmatrix} 0 & 0 & 0 & 0 & mw & -mv \\ 0 & 0 & 0 & -mw & 0 & mu \\ 0 & 0 & 0 & mv & -mv & 0 \\ 0 & mw & -mv & 0 & I_z r & -I_y q \\ -mw & 0 & mu & -I_z r & 0 & I_x p \\ mv & -mv & 0 & I_y q & -I_x p & 0 \end{bmatrix} \begin{bmatrix} u \\ v \\ w \\ p \\ q \\ r \end{bmatrix} = \begin{bmatrix} X \\ Y \\ Z \\ K \\ M \\ N \end{bmatrix} \tag{4.43}$$

Where

$$X = X_A + X_D + X_G + X_T; \quad Y = Y_A + Y_D + Y_G + Y_T; \quad Z = Z_A + Z_D + Z_G + Z_T$$

$$K = K_A + K_D + K_G + K_T; \quad M = M_A + M_D + M_G + M_T; \quad N = N_A + N_D + N_G + N_T$$

The X, Y, Z, K, M, and N is a vector of external forces and moments that consist added mass, damping, gravitational/buoyancy forces and moments and thrust term. Then, the equation is rearranged into state space form as shown below:

$$\dot{\boldsymbol{v}} = \boldsymbol{M}^{-1}\left(\boldsymbol{\tau} - \boldsymbol{C}(\boldsymbol{v})\boldsymbol{v} + \boldsymbol{D}(\boldsymbol{v})\boldsymbol{v} + \boldsymbol{g}(\boldsymbol{\eta})\right)$$

$$\boldsymbol{M} = \boldsymbol{M}_{RB} + \boldsymbol{M}_{A}; \qquad \boldsymbol{C}(\boldsymbol{v}) = \boldsymbol{C}_{RB}(\boldsymbol{v}) + \boldsymbol{C}_{A}(\boldsymbol{v}) \tag{4.44}$$

The details of the state equations for each of the 6 degrees of freedom and related constants are given in Appendix C.

4.9 Model Validation

The mathematical model is designed to provide information regarding the system performance. In order to produce a credible model it is an important part of any modelling procedure to undergo *model validation* (Balci, 1994; Law, 2009). According to Balci (1994), model validation is a process to ensure that the model is sufficiently accurate with respect to its purpose. This is achieved by ensuring that the simulated output from the model is a reasonably accurate match to the response of the real system under similar operating conditions. The model confidence level is based on the accuracy of the model where the sufficient accurate term is used since none of the model exist is 100% accurate and the accuracy only can be determine with reference to the purpose of the model where the validity is assumed to be different for each purpose (Robinson, 1997; Sargent, 2010). Therefore the purpose and intended use of the model plays an important role and needs to be determined before the validation process.

Several validation techniques been discussed and categorized in Balci (1994) studies where these techniques allow an accuracy measurement to be conducted on the model and physical system. Two types of validation methods are been chosen which are a qualitative measurement, analogue matching (Gray, 1992) and a quantitative measurement, integral least squares (ILS) (Murray-Smith, 1995). Several research conducted by Gray (1992), Worrall (2008) and Watts (2009) have successfully implemented these methods to validate their mathematical model of engineering systems. The validation methods are discussed in details below where it results is shown in Appendix D.

4.9.1 Analogue Matching

Analogue matching also known as visual inspection (Gray, 1992), can be categorize as an informal technique where Balci (1994) noted that it relies heavily on human reasoning and subjectively without mathematical formality. Gray, et al. (1998) found that it provides the simplest validation technique where the plot of the time response of the model is compared to the physical system. This technique also allows the parameters in the model to be altered in order to produce best fit to represent the physical system. An example of the analogue matching technique is shown in Figure 4.13 for a forward swimming experimental program. It is configured with the tail beat amplitude of 0.05 m and frequency set at 0.5 Hz.

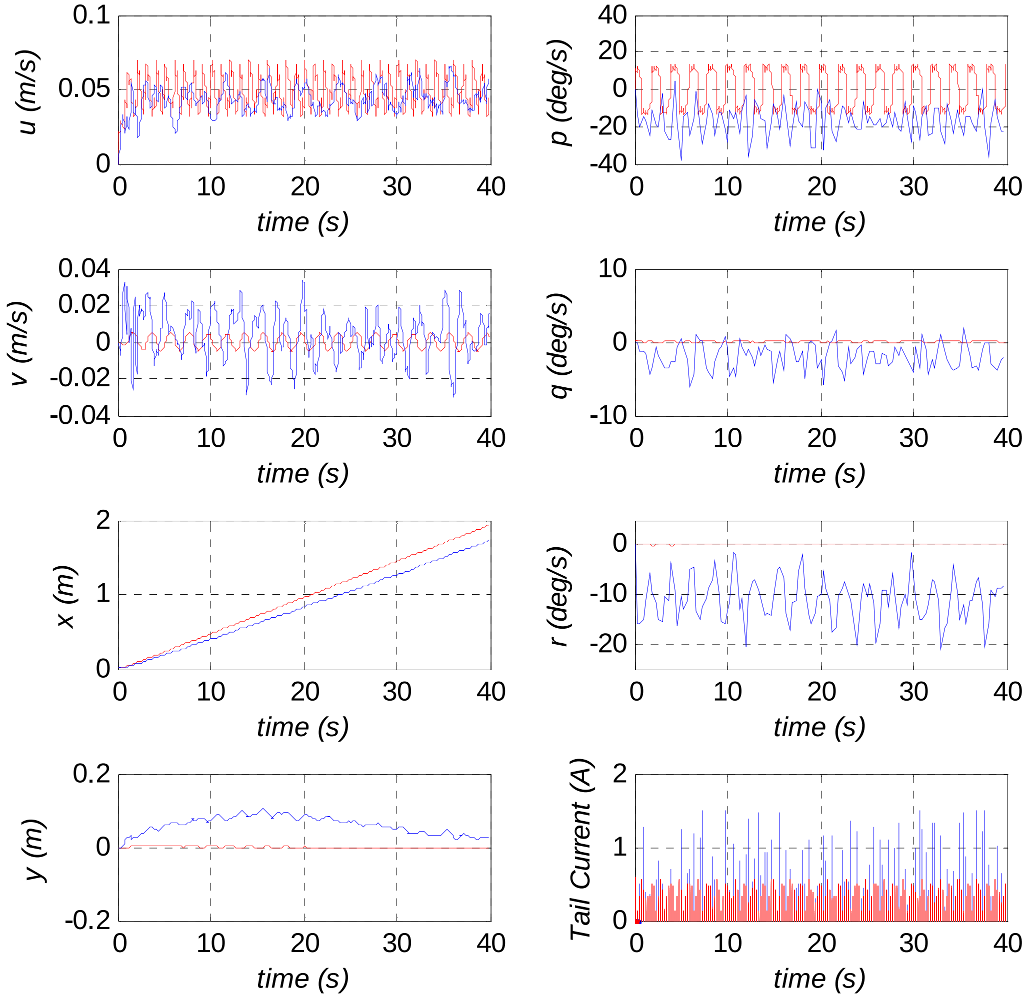

Figure 4.13: The analogue matching validation technique for *RoboSalmon* forward swimming. The blue trace is the experimental data and red trace for simulation data

It can be observed that the surge velocity of the model simulation data appears reasonably match to an experimental data when applied under similar operating conditions. It can be noticed that several of the graphs do not match especially for pitch and yaw angular velocities. Even though these data are less critical for the validation process, it can be seen that the model simulation data have the same shape of plot with the experimental data but on different scale of amplitude as shown in Figure 4.14.

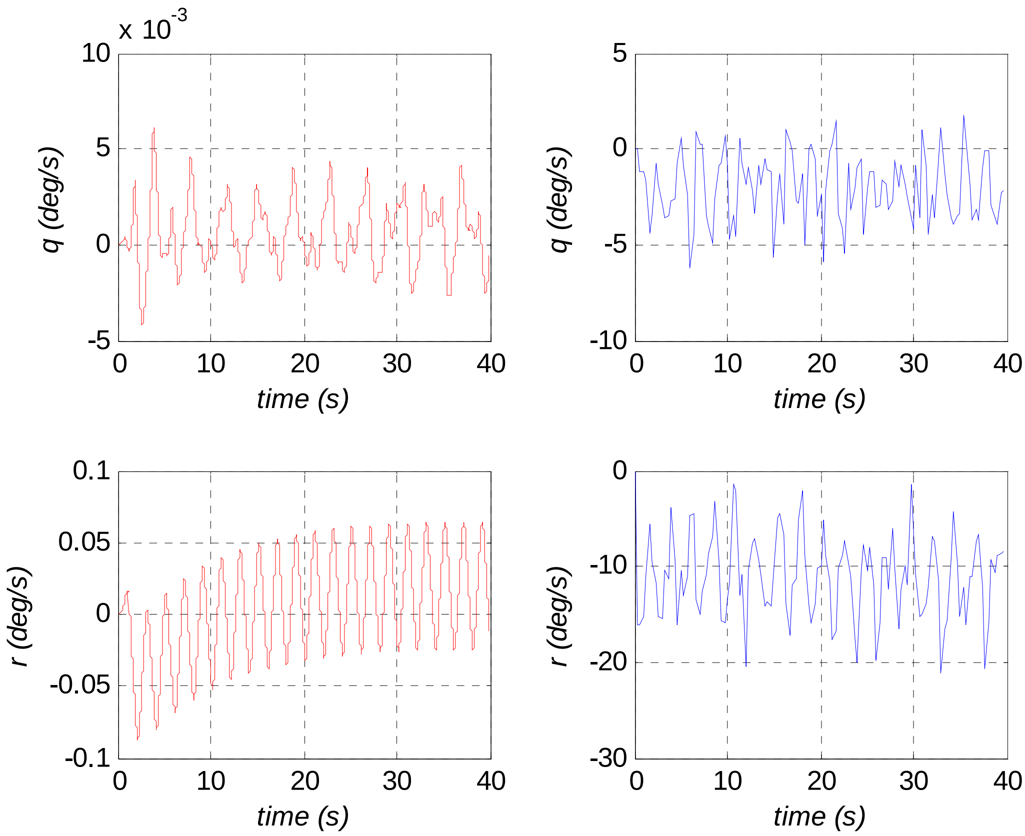

Figure 4.14: The pitch and yaw angular velocities graph in Figure 4.13 is redrawn with the blue trace is the experimental data and red trace for simulation data.

Moreover, it can be reasoned the difference in x and y position graphs where the vehicle does not travel in straightforward path. This is because the vehicle is affected by the amplitude shifting (i.e. recoil motion) that can be seen in roll and yaw angular velocities graphs. For these reasons, the model is said to be a good representation of *RoboSalmon* vehicle. In addition, the validation results from the Analogue Matching technique used are shown for a selection of *RoboSalmon* experimental in Appendix D.

4.9.2 The Integral Least Squares

The integral least squares (ILS) (Murray-Smith, 1995) method provides a quantitative measurement of the model accuracy. This model validation technique required all data to be collected from the physical system. Then it compares the model output data with the physical output data under the same input parameters. The validation technique is implemented by using Equation (4.45) where the error is the difference between the model response and the physical response.

$$Q_m = \sum (error)^2 \tag{4.45}$$

The accuracy of the model is determined by measuring the Q_m value where the smaller value will provide the higher model accuracy. The validation results for a Selection of *RoboSalmon* experimental using the ILS technique is presented along with the Analogue Matching results in Appendix D.

4.10 Summary

This chapter has described the development of a multi-variable mathematical model to investigate the dynamics and electro-mechanics of *RoboSalmon* vehicle. The state space together with the multi-rate technique that has been used for the model simulation is discussed. The references frames and sets of variables used within the model have been defined. These variables are used to determine the position and orientation of the vehicle. The vehicle is modelled based on the conventional underwater vehicle techniques with several modifications made to incorporate the thrust production from the tail undulation part. The vehicle body is assumed to be rigid with a multi-jointed robotic manipulator arm is implemented within the tail part to replicate the undulatory motion of a real fish tail. The tail kinematic, the rigid body dynamics and associated hydrodynamics of the vehicle are evaluated using the model. Finally, the techniques used for the model validation were discussed along with an example result. These techniques provide both qualitative and quantitative measurement to compare the vehicle performance between the model and physical system.

5

Forward Swimming

5.1 Introduction

Sfakiotakis, et al. (1999) stated that the temporal features of fish swimming can be divided into two groups; *periodic* and *transient* movement. The periodic or steady swimming is defined as a cyclic repetition of the propulsive movements. It is commonly used for long distance swimming with small changes in velocity owing to slight variations in thrust within propulsion cycles (Weihs & Webb, 1983 as cited in Webb, 1988). Transient or unsteady swimming on other hand, involves rapid changes in swimming state. Examples of this are the fast start (where the fish goes from stationary to fast swimming velocity in a short period of time), escape manoeuvre (changes direction and velocity) and turns (manoeuvres to change direction). These movements only last for a brief period of time and typically are used for catching prey or avoiding a predator (Domenici & Blake, 1997; Blake, 2004).

More research has been conducted into periodic movement compared to the transient movement. This is because experiments on steady swimming are easier to measure and analyse (Hoar & Randall, 1978) than unsteady swimming. It appears that the transient movement experiment is difficult to set up, repeat, and verify the effectiveness of the proposed method (Sfakiotakis, et al., 1999). Although both periodic and transient movements are considered in this thesis, the periodic movement is the main focus of this chapter where the forward swimming performance is presented and discussed. The performance of the vehicle is investigated by varying a number of characteristics such as tail beat amplitude and tail beat frequencies.

5.2 Data Collection

The processes involved in observation, collecting and analyse data are crucial in determining the performance of the vehicle. The vehicle physical data are collected using two types of approaches in order to determine the position and orientation of the vehicle. These approaches are by utilizing the inertial measurement unit (IMU) data and images from the camera. This section discussed in details the experiment setup, image and sensor data post processing involved in the study.

5.2.1 Laboratory Equipment

A pool of dimensions 4.14 m x 2.16 m x 0.79 m was constructed for the experimentation with white PVC frame is constructed on top of the pool as shown in Figure 5.1. Numbers of white ceramic tiles (0.33 m x 0.25 m) are placed at the bottom of pool. The purpose is to provide a background grid (reference) for the camera. The camera is mounted on a frame 1.5 m above the pool allows video of the swimming environment to be recorded

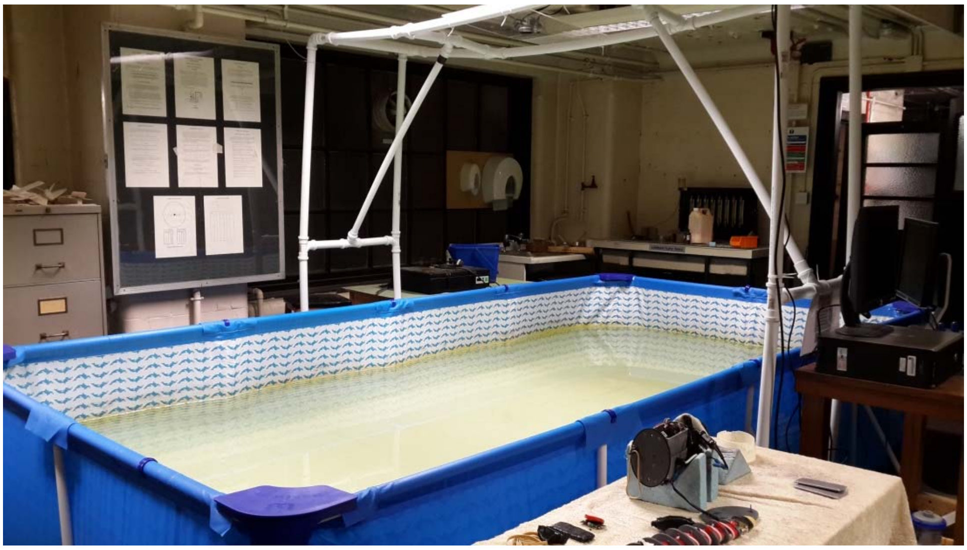

Figure 5.1: Experimental setup

The camera is operated using a remote control and throughout each run, the image recorded by the camera is display on the PC monitor via HDMI cable. This allows smooth start and stop recording process that indicates by the *RoboSalmon* visibility in the camera view. A computer also includes in the setup where it is used to program *RoboSalmon* and post processing data analysis.

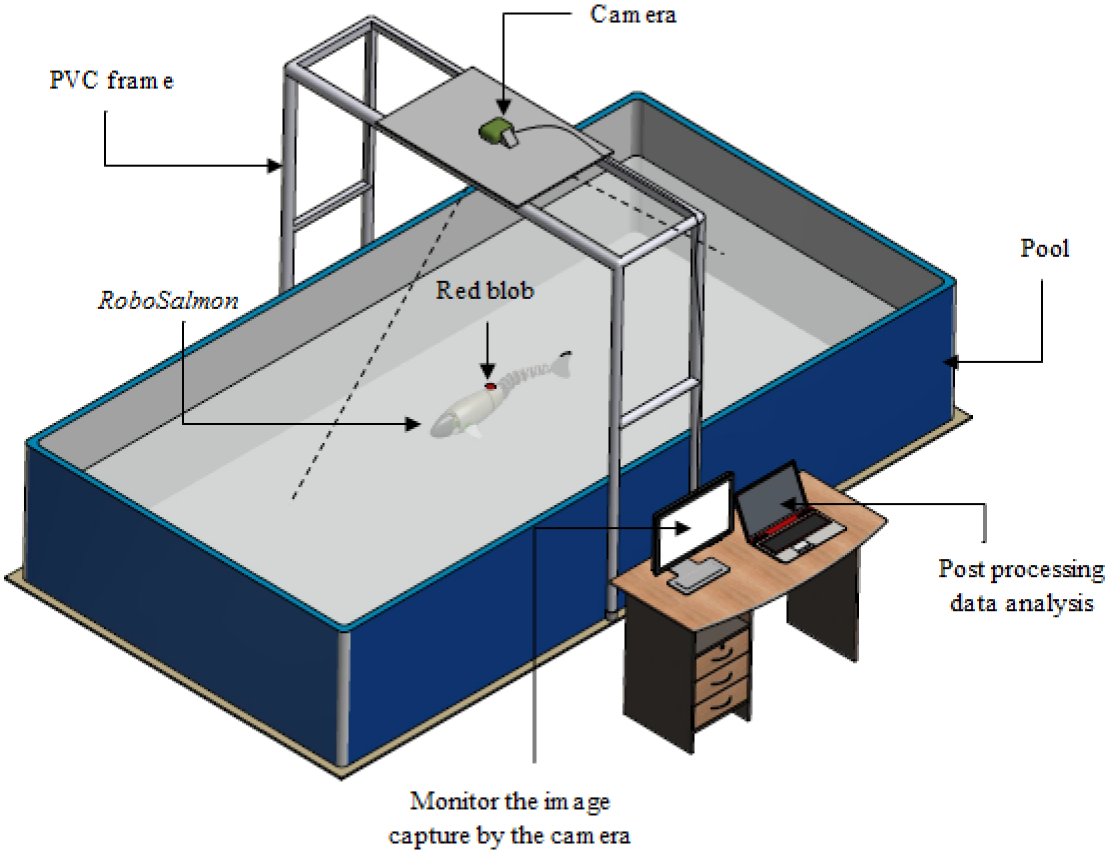

Figure 5.2: Schematic image of laboratory equipment

5.2.2 Experimental Procedure

The main experimental procedure employed in this study is illustrated in Figure 5.3. The first step is to position the *RoboSalmon* on the left side of the pool. The camera is set on video mode and start to capture the video. The *RoboSalmon* vehicle is switched on and starts executing the program. This program is installed into the microcontroller where several characteristics (i.e. tail beat amplitude/frequency, tail deflection angle) can be varied throughout the experimentations.

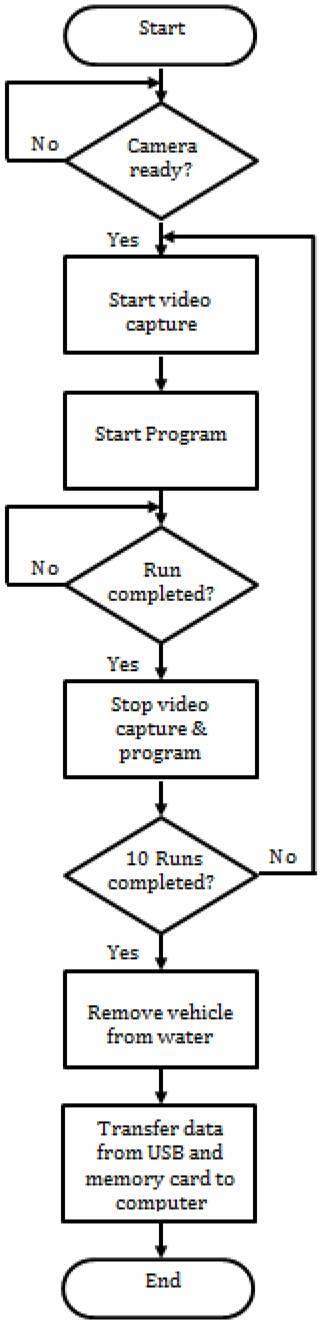

Figure 5.3: Flowchart of experimental procedure

On average the vehicle took about 40 second run time. Once the run was completed (i.e. moving left to right), the vehicle and camera operation were stopped. The vehicle data are saved into USB drive while the video image is saved on the memory card. This procedure is repeated at least ten times. By repeating the experimental data, it allows mean, standard deviation, and standard error to be calculated where it used to estimate the measurement confidence level. After all runs been completed, the vehicle is removed from the pool. The USB drive and memory card are retrieved and transferred to the computer to be analysed.

5.2.3 Image Processing

The camera positioned on top of the frame capture the vehicle motion in *x* and *y* directions. Through image processing techniques it is possible to determine the relative position of the vehicle from individual images extracted from the camera videos. By performing a transformation from pixel coordinates to world coordinates the position and orientation of the vehicle within the pool can be determined (Araujo, et al., 2009).

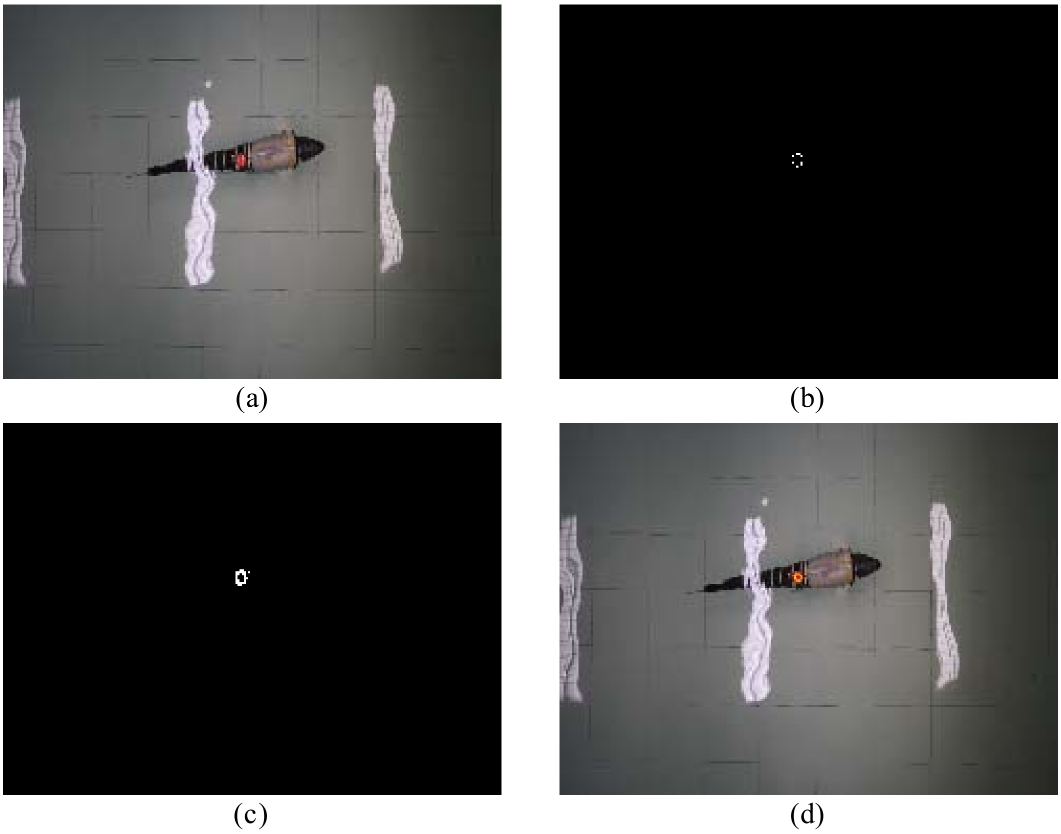

Figure 5.4: Image processing steps (a) image captured by the camera (b) conversion to binary image with the object (white) and background (black) (c) Image undergo morphological operations (d) the centre of the red blob is indicate by (+) yellow

The video file is split into individual frames for analysis purpose. Figure 5.4 shows an example of the individual frame. According to Attaway (2013), colour image represented by grid or matrices of pixels. Each pixel has a particular colour which described by the amount of red, green and blue. In this study, the analysis process involved detecting the centre of the red blob on the *RoboSalmon* vehicle. This is done by checking each pixel in the red, green and blue (RGB) image whether it within the range of desired colour (red) components and filter out all of the others.

The RGB image is converts into binary image through this process where if it detects within the range, the pixel is set to white otherwise it is set to black (see Figure 5.4(b)) (The Mathworks Inc., 2014). It can be seen only a small number of pixels are within the range values at this state. Even though the range can be modified, Watts (2009) noted that it is not a good practice since it will lead to numerous erroneous detection points across the frame. Morphological operations such as of opening, dilation and closing function have been implemented on the binary image. It allows smoothing object contours that will give better processing result (Gonzalez, et al., 2004) as shown in Figure 5.4(c) where it can noticed that the size of the blob is enlarged. Then, the white pixels corresponding to the red blob are determined using a *bwlabel* function. Ideally, there should be either one object detected in the frame or none if the red blob out of frame. The centre of the white pixels is measured and indicates by yellow plus a symbol in Figure 5.4(d). This process has been repeated for all frames and it can be suggests that it allows the vehicle positional (x and y coordinates) data with respect to time to be determined. However, this position need to be scaled accordingly using Equation (5.1) from pixel to metre before further analysis (Watts, 2009). The *x_scaledfactor* and *y_scaledfactor* are determined by camera pixel resolution of 1440 x 1080 (width x height) in conjunction to reference tile at the bottom of the pool.

$$
\begin{aligned}
x_{pos\_scaled} &= x_{pos}\left(x\_scaledfactor\right) \\
y_{pos\_scaled} &= y_{pos}\left(\mathrm{y}\_scaledfactor\right)
\end{aligned}
\tag{5.1}
$$

The video file has frame rate of 25 frames per second which produce 25 sets of positional data in seconds. This positional data from subsequent images can be used to determine instantaneous velocity information, which can be compared with the corresponding IMU data. This method helps to reduce errors in collecting data by the on-board IMU while providing an solution to determine the positions and velocities of the vehicle in the Earth-fixed reference frame (Watts, 2009; Fossen, 2011).

5.2.4 Sensor Data Post Processing

The on-board sensors such as the IMU allows the vehicle angular velocities (i.e. roll, pitch and yaw) with respect to the body fixed reference frames to be measured and stored using the USB data logger. In addition, the current and pressure sensor allow the vehicle power consumption and depth to be determined. The stored data are retrieved by the computer using the USB port for analysis. A set of data collection from a sample run of the

RoboSalmon vehicle forward swimming is shown in Figure 5.5. It shows the data collected by the on-board sensors that has been transferred from raw values to the meaningful readings such as deg/s and Amp.

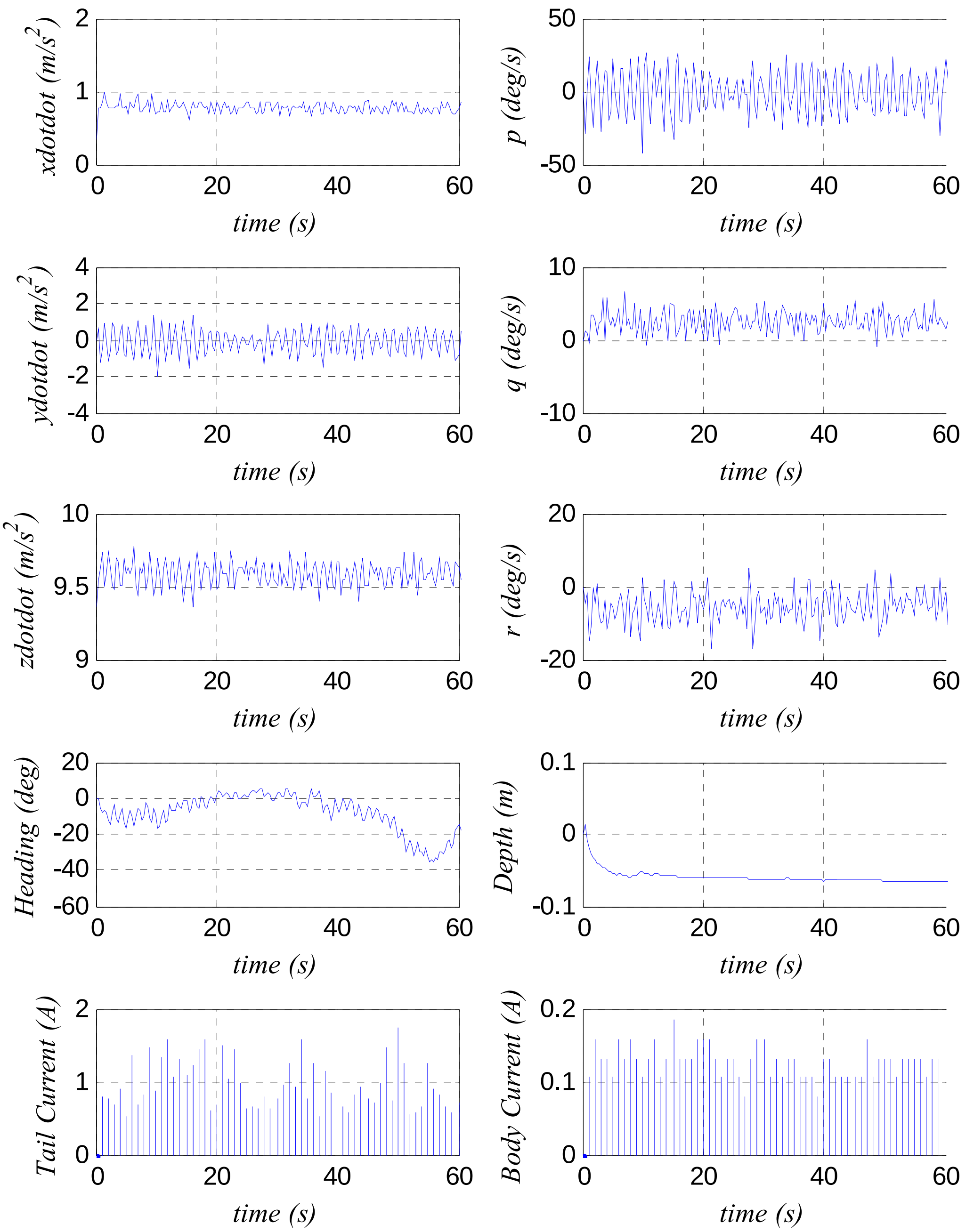

Figure 5.5: Selection of on-board sensors post processing

It been mentioned earlier that the processing image provide the positions and velocities of the vehicle in the earth fixed reference frame. In order to compare these data towards the on-board sensor, the velocities of the vehicle need to be translate to body fixed reference frame. The linear velocity transformation is dealt using Equation (5.2) where ν_1 is the linear velocity in the body-fixed frame; $\dot{\eta}_1$ and η_2 are the linear velocity and angular position in the Earth-fixed frame.

$$\nu_1 = \left(J_1(\eta_2)\right)^{-1} \dot{\eta}_1 \tag{5.2}$$

Here $\nu_1 = [u, v, w]^T$, $\eta_2 = [\phi, \theta, \psi]^T$, $\dot{\eta}_1 = [\dot{x}, \dot{y}, \dot{z}]^T$ and J_1 represent the Euler transformation matrices for the linear velocities (Fossen, 1994, 2011). Watts (2009) stated that J_1 requires the Earth-fixed angular position which can be measured using Predictor-Corrector method (Matko, et al., 1992). It is used to predict the Earth-fixed angular position by using body-fixed angular velocity ν_2 that obtained from the on-board IMU and Earth-fixed angular positions initial conditions $[0, 0, 0]$. Moreover, $\dot{\eta}_1$ values can be measured by differentiation the x and y position from the image processing. An example of the vehicle linear Earth-fixed position and body-fixed velocities are display in Figure 5.6.

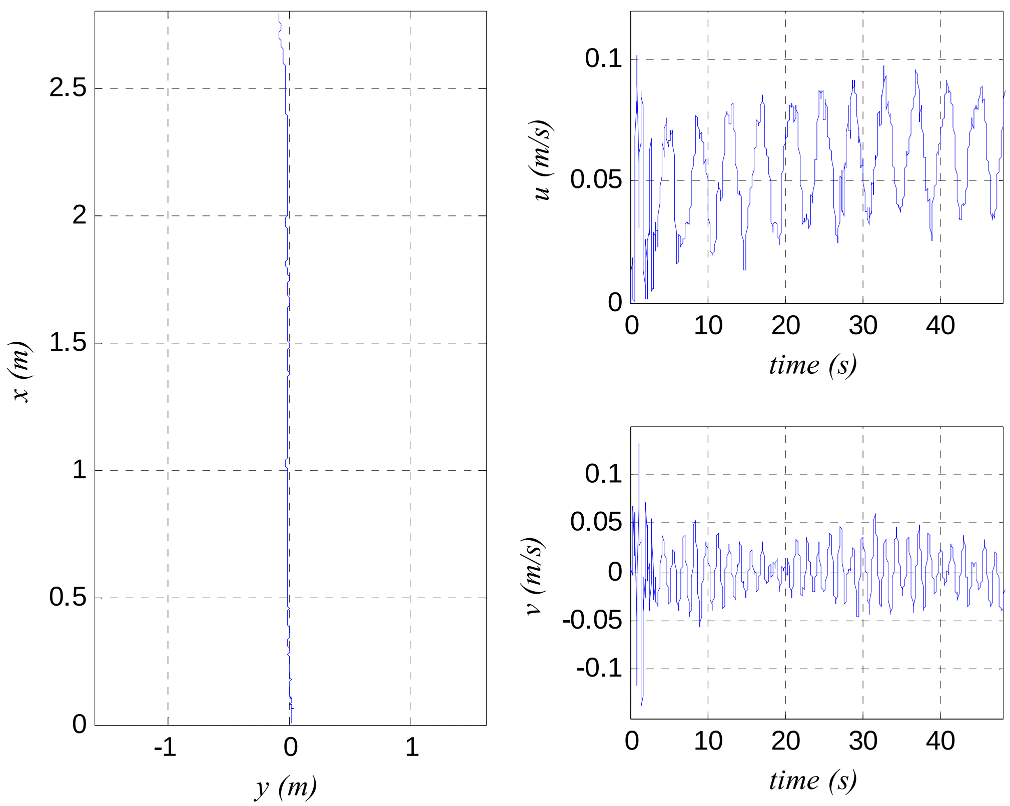

Figure 5.6: Image post processing

5.3 Forward Swimming

Bainbridge (1957) listed several factors that affect the fish swimming velocity which are the form of the body, size, surface texture and the tail beat frequency and amplitude. This is supported by the evidence found in other biomimetic vehicle research studies (Kumph, 2000; Liu & Hu, 2010; Nguyen, et al., 2011). In this study, the relationship between the measured vehicle velocity and the tail beat amplitude and frequency is considered for the forward swimming experiments. A total of 24 types of experiment have been conducted where these experiments are designed to consider every combination of the selected amplitude and tail frequency values.

According to Videler (1993), an average fish undulates with the maximum amplitude that is approximately 10% of its body length. However, Liu & Hu (2010) argue that for biomimetic vehicle, bigger amplitude for the undulation is required to counter the effect of the head swing during swimming. The desired tail beat amplitude is chosen based on this condition where the minimum and maximum amplitude are 0.05 m and 0.20 m respectively. The effect of frequency on the vehicle velocity is investigated by varying the frequency between 0.5 Hz to 3 Hz in increments of 0.5 Hz. This range of frequencies is chosen in order to have variety of frequencies to be tested while simplify the time command send to the tail microcontroller that used to coordinate the undulation motion. During the forward swimming experiment, the vehicle is positioned on the left side of the pool. It moves from stationary towards the right side as shown in Figure 5.7 where the vehicle path is indicated by the red dot.

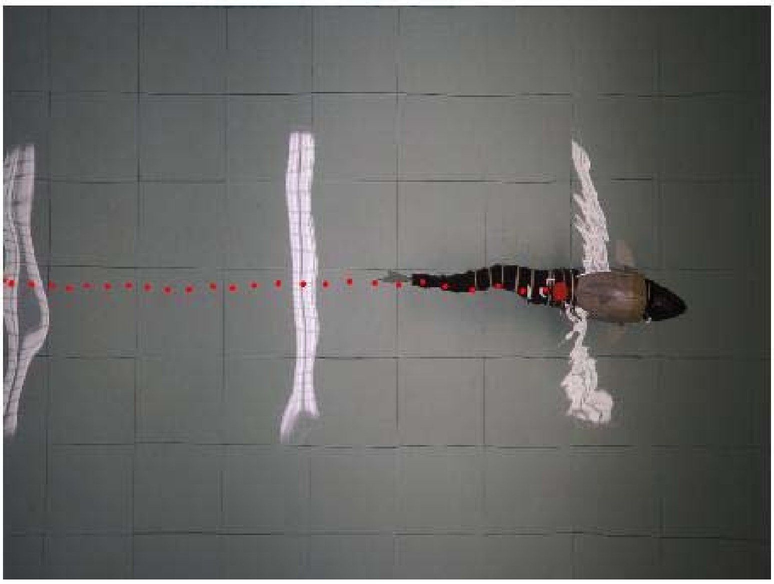

Figure 5.7: Vehicle path for forward swimming

The camera image then provides the vehicle's x-y positional data where the surge and sway velocities are calculated by using numerical differentiation illustrated in Figure 5.8. These procedure been repeated multiple time for each configuration in order to determine the average and the standard error of surge velocity.

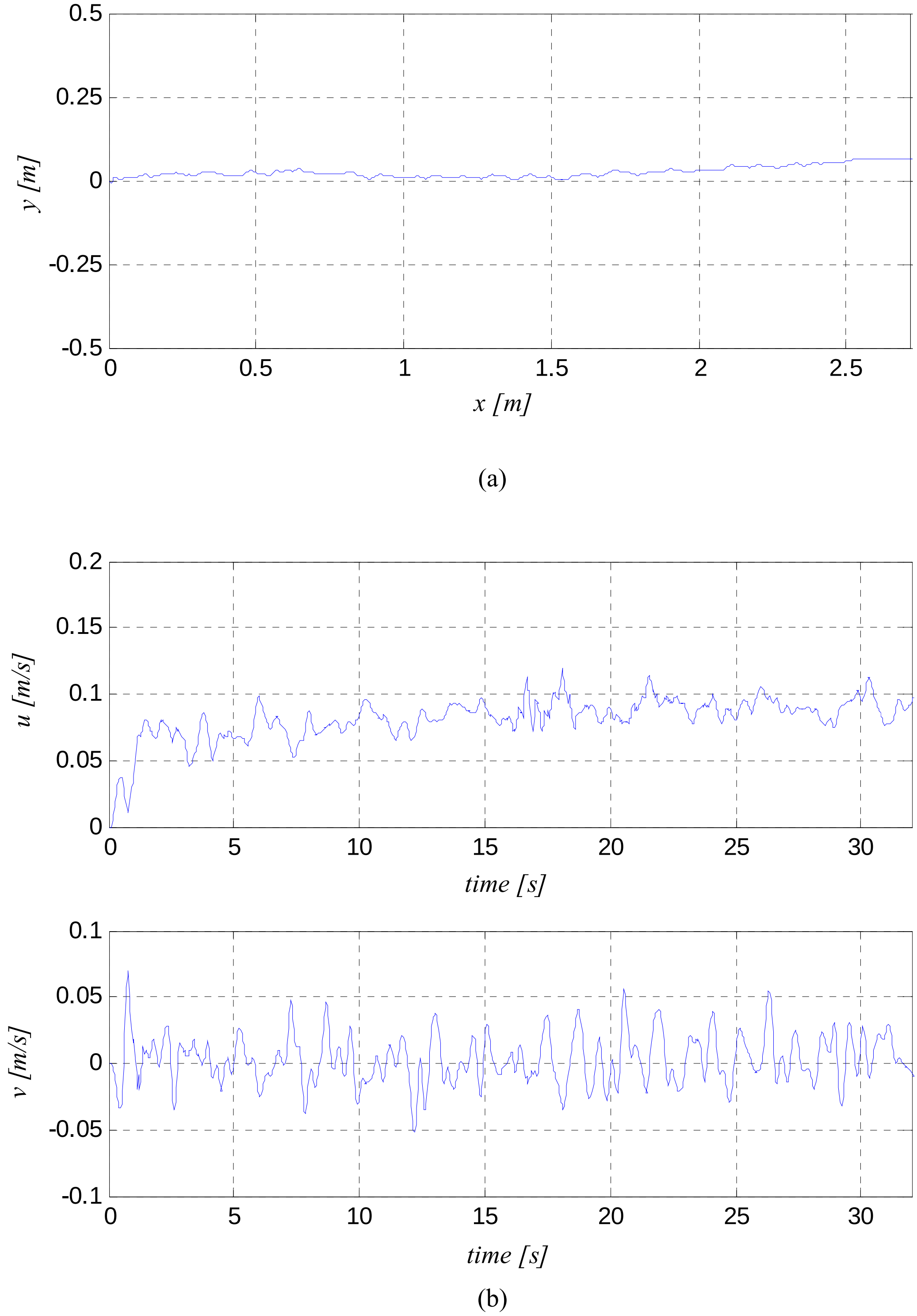

Figure 5.8: Data obtained from image processing (a) vehicle's x-y position (b) surge and sway

Figure 5.9 shows the data collected by the on board sensor suite which includes the linear acceleration, angular velocities, current and depth of the vehicle. The *xdotdot*, *ydotdot* and *zdotdot* are referred to acceleration in x, y and z direction respectively collected from the ADXL345 accelerometer sensor. These values can be used to obtain the vehicle velocity and position by undergo double/single trapezoidal integration method. These velocity and position values then can be compared to the values extract from camera image. Next, the ITG-3200 gyroscope sensor provides angular velocities data for p (roll), q (pitch) and r (yaw) motion. Moreover, further integration of these values will give information regarding the vehicle orientation in body fixed reference frames.

The heading angle is obtained from HMC5883L magnetometer sensor. This data is only used constantly during the navigation experimentation. It capable to provide progression of vehicle heading relative to its initial heading which is useful for navigation. None of the experiment designed for up/down motion nevertheless the MPX4250 pressure sensor can provide the vehicle depth measurement for future use. Finally, the body and tail current is measured using ACS712 current sensor. This value is used to determine the vehicle power consumption. All of this collected information proves useful as it provides the position and orientation of the vehicle in addition to the power consumption. Moreover, it also worth to mention the time difference in data collected between the video camera and on board sensors. This discrepancy is contributed by the limitation in field of view of the video camera since it not able to cover full length of the swimming pool.

The average surge velocity values for each frequency/amplitude combination are summarized in Table 5.1. It can be observed that the vehicle velocity tends to increase as both the amplitude and frequency increase. However, a number of combinations do not meet the expected response due to the deflection limitations of the tail actuators. The actuator saturation occurs when larger amplitudes or higher frequencies are commanded. The amplitude/frequency values that cause the actuators to saturate are highlighted in Table 5.1 in grey. As expected this actuator saturation causes the vehicle to travel at a lower surge velocity than is expected for those amplitude and frequency values. Although the desired amplitude does not been achieved which is not the case for the frequencies results the vehicle velocity to maintain at a reasonable surge velocities due to the high frequency undulations.

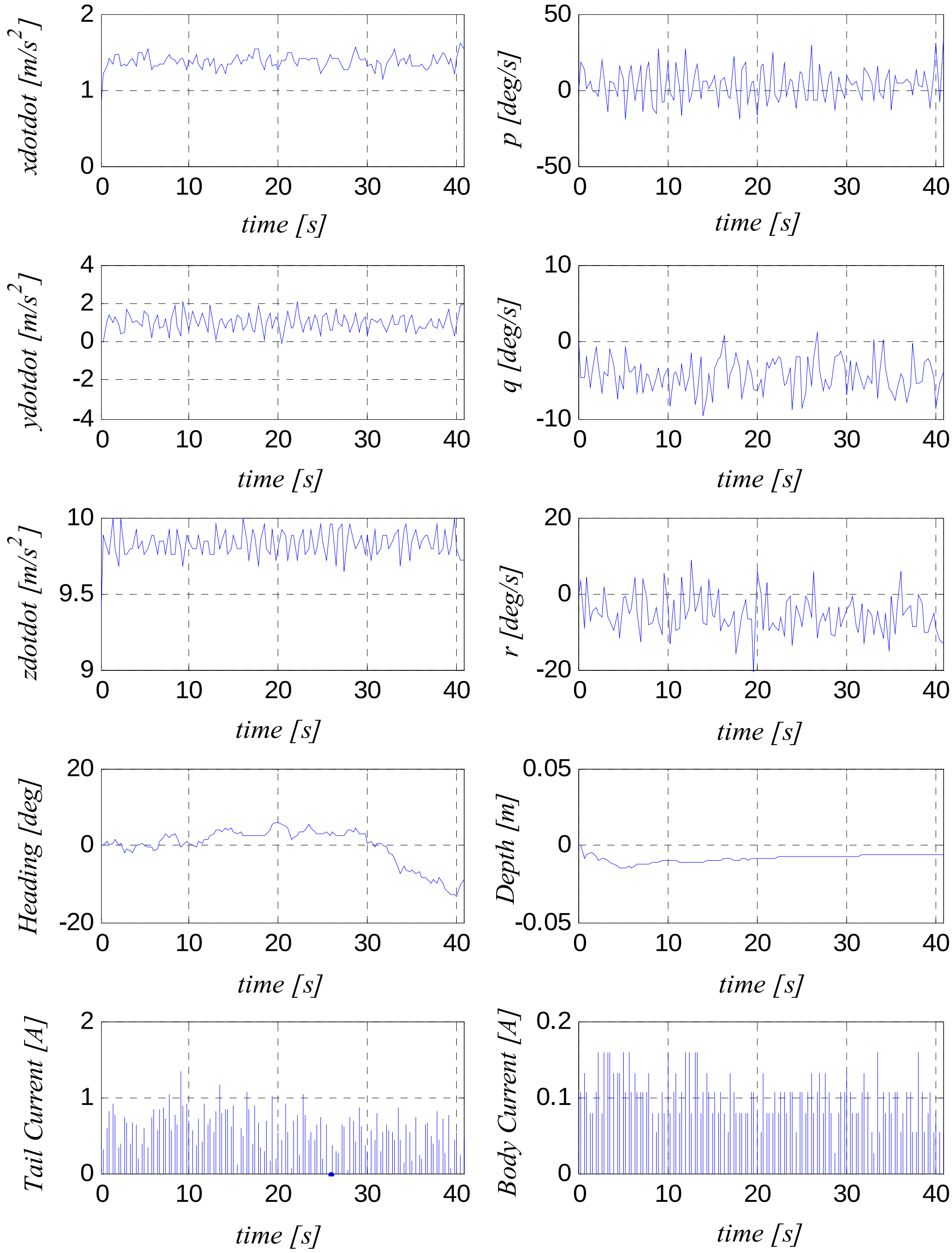

Figure 5.9: Data obtained from sensors on-board the vehicle

Table 5.1: Surge velocity relates to tail beat amplitude and frequency

		Amplitude (m)			
		0.05	**0.10**	**0.15**	**0.20**
Frequency (Hz)	**0.5**	0.055 ms^{-1}	0.061 ms^{-1}	0.079 ms^{-1}	0.086 ms^{-1}
	1.0	0.078 ms^{-1}	0.088 ms^{-1}	0.143 ms^{-1}	0.095 ms^{-1}
	1.5	0.090 ms^{-1}	0.075 ms^{-1}	0.085 ms^{-1}	0.086 ms^{-1}
	2.0	0.092 ms^{-1}	0.067 ms^{-1}	0.084 ms^{-1}	0.073 ms^{-1}
	2.5	0.065 ms^{-1}	0.069 ms^{-1}	0.107 ms^{-1}	0.089 ms^{-1}
	3.0	0.074 ms^{-1}	0.082 ms^{-1}	0.122 ms^{-1}	0.095 ms^{-1}

Actuator saturation

All frequency/amplitude combinations for forward swimming are plotted in Figure 5.10 where it can clearly shows the influence of the actuator saturation towards vehicle surge velocity. Without saturation, it can be observed that with constant tail beat amplitude configuration, the vehicle surge velocity is linearly increasing with tail beat frequency. While when saturation occurred, the surge velocity starts to decrease. The frequency effect on surge velocity can be examined mostly for the smallest amplitude (0.05 m) where the saturation only occurred after the frequency is above 2 Hz.

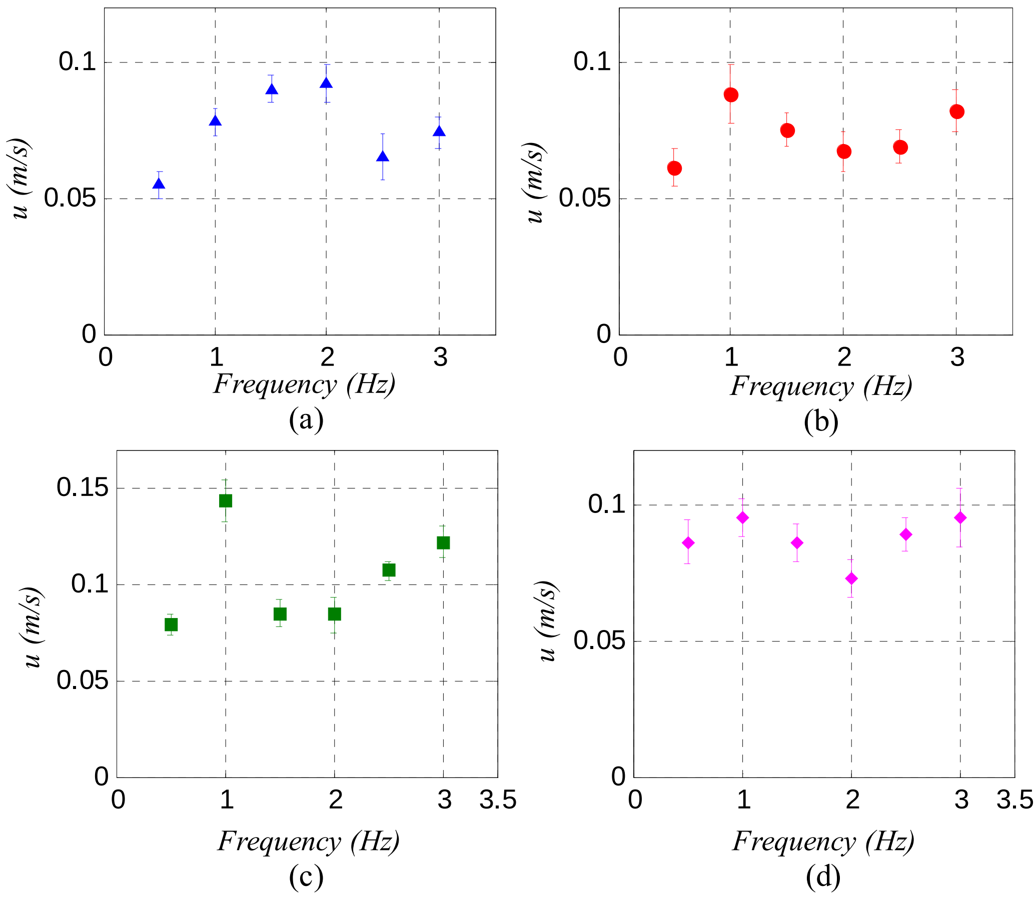

Figure 5.10: Relationship between surge velocity and frequency for all forward swimming experiments corresponding to the tail beat amplitude of (a) 0.05 m (b) 0.10 m (c) 0.15 m and (d) 0.20 m

Meanwhile the tail configuration of 0.10 m and 0.15 m amplitude can operate up to 1 Hz before the saturation occurs. Even though there is slightly increased surge velocity for 0.20 m tail beat amplitude at 1 Hz. However, through observation it has been noticed that the desired tail amplitude only achieved when operates at the lowest frequency. After actuator saturation occurred, the vehicle surge velocity drop as consequences not able to achieve the desired tail beat amplitude. Still, the vehicle able to travel at a reasonable velocity caused by the increased in tail beat frequency for all tail beat amplitude configuration.

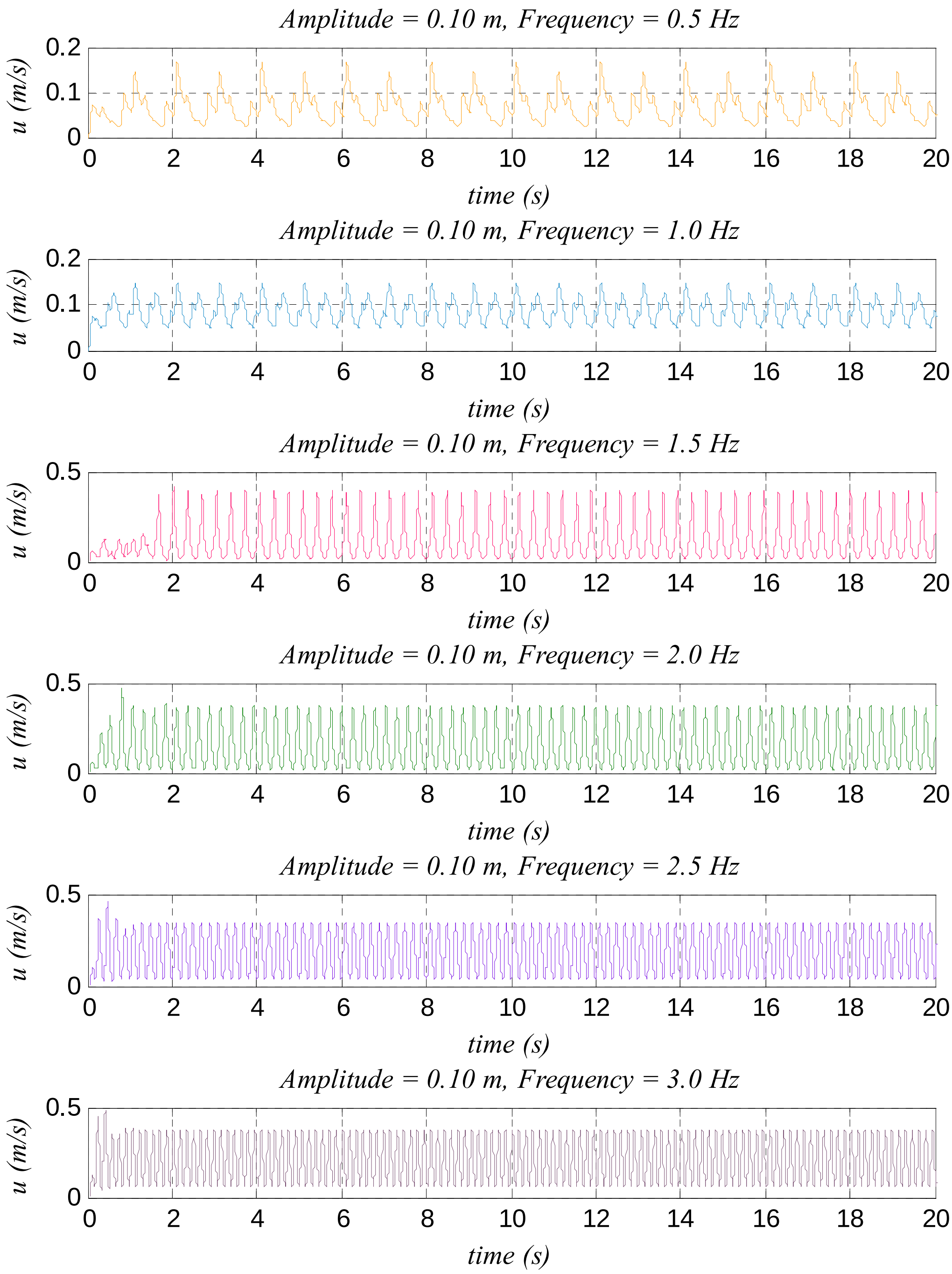

Figure 5.11: Estimation of vehicle surge velocities for 0.10 m tail beat amplitude with tail beat frequencies of 0.5 Hz, 1 Hz, 1.5 Hz, 2 Hz, 2.5 Hz and 3 Hz

Since the vehicle encounters actuator saturation during experimentation which limits its performance and further physical trials to be carried out. However, the estimation of forward swimming can be obtained by performing computer simulation. The simulation study able to show the vehicle performance related to the tail beat amplitude and frequency when no actuator saturation occurs. An example of the simulated vehicle surge velocity performance relates to the tail beat frequency is illustrated in Figure 5.11 with the tail beat amplitude respect to 10% of the body length of vehicle configuration is been selected. This is because Videler (1993) found it is common for a real fish to have a tail amplitude of this value at an optimal speed. The simulated surge velocity results are set to range between 0.5 Hz to 3 Hz. It is known that not all of these values able to materialize during experiment due to actuator limitation. It can be seen from the figure that the surge velocity tends to have a bigger ripple amplitude closely together when a higher tail beat frequency is been applied. As expected, it contributes to a higher average speed of the vehicle which listed in Table 5.2.

Table 5.2: Average vehicle surge velocity respect to different tail beat frequency

Tail Beat		**Average Surge Velocity (m/s)**	
Amplitude (m)	**Frequency (Hz)**	**Experiment**	**Simulation**
0.10	0.5	0.061	0.067
0.10	1.0	0.088	0.086
0.10	1.5	0.075	0.117
0.10	2.0	0.067	0.149
0.10	2.5	0.069	0.184
0.10	3.0	0.082	0.211

Actuator saturation

The computer simulations shows the surge velocity values are reasonably close the values measured during experimentation. Moreover, it can be deduced the positive trend of tail beat frequency relates to the vehicle surge velocity if the motor saturation does not occurred. The surge velocity increases when the tail beat is increases. Next, the vehicle surge velocity relates to tail beat amplitude is been investigated where four configurations of tail beat amplitudes (0.05 m, 0.10 m, 0.15 m and 0.20 m) with 1 Hz tail beat frequency have been investigated.

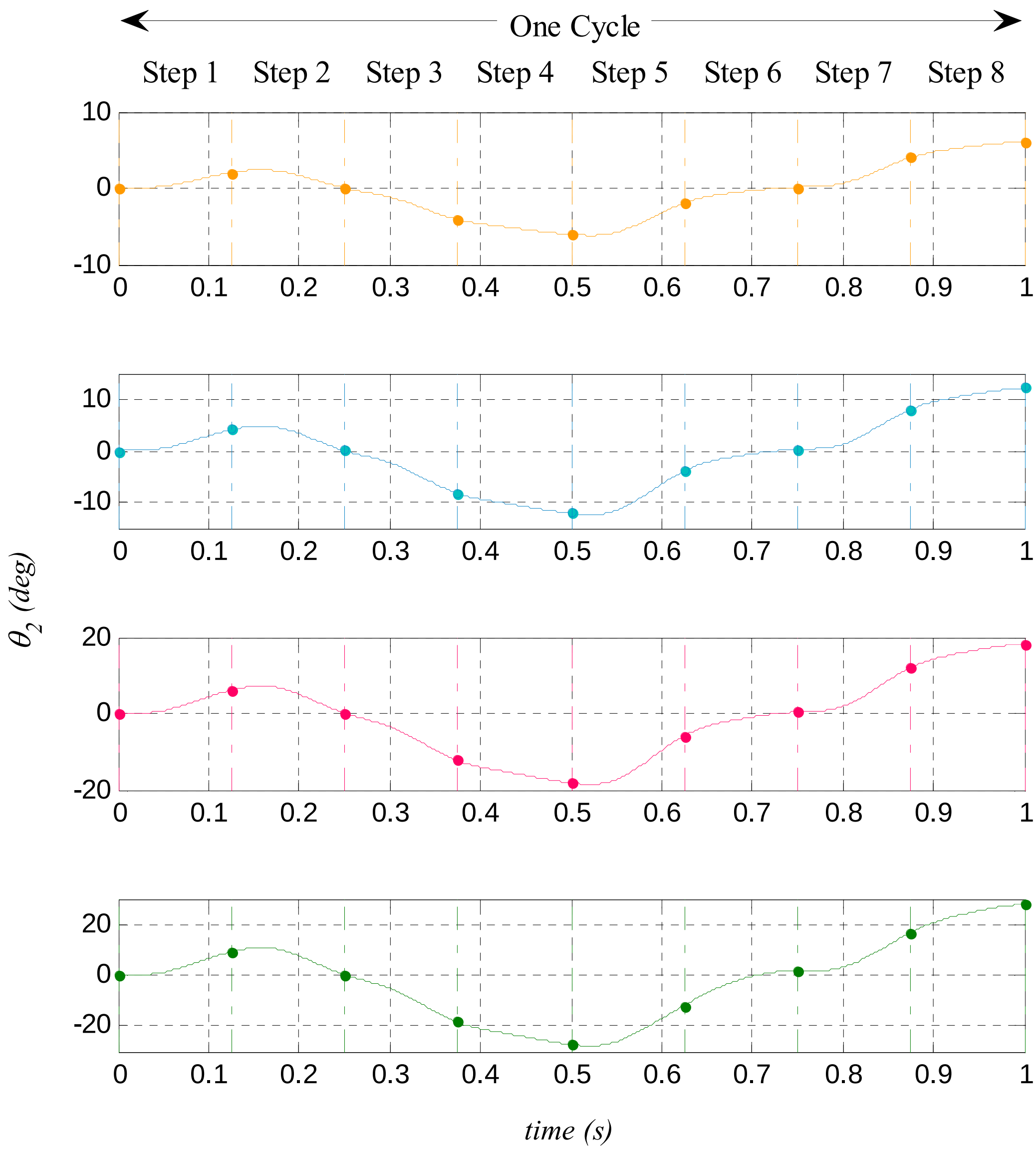

Figure 5.12: Actuator angular position respond based on various tail beat amplitudes when operates at 1 Hz tail beat frequency. The circles indicate the final angular position on each step with the tail beat amplitude of 0.05 m (yellow), 0.10 m (blue), 0.15 m (red) and 0.20 m (green)

One of the motors (*Motor2*) that is responsible in generating undulation motion is been analysed when operate on various tail beat amplitude but at a constant tail frequency (1 Hz). A cycle of undulation motion for each motor/link will consist of eight steps. The motors are requires to driven the link to the desired angular position within specified time which the time is depend on the tail beat frequency. In this case (1 Hz tail beat frequency):

$$\text{One cycle time, } t_m = \frac{1}{f} = 1\ s \tag{5.3}$$

Thus, the time, t_s for each step is

$$t_s = \frac{t_m}{8\ steps} = 0.125\ s\,/\,step \tag{5.4}$$

Therefore the motor needs to move from one angular position to another desired angular position within 0.125 s each time. The desired angular positions for *Motor2* are listed in Table 5.3 and it can be observed that all tail beat amplitude configurations have the same shape but different in magnitude shown in Figure 5.12. Moreover, the result of simulated angular positions in Table 5.4 show that the motor able to reach the desired position within required time when operates at tail beat frequency of 1 Hz and for all tail beat amplitude.

Table 5.3: Desired motor angular position for one cycle

		Time (s)							
		0.125	**0.25**	**0.375**	**0.5**	**0.625**	**0.750**	**0.875**	**1**
Tail beat amplitude (m)	**0.05**	2 º	0º	-4º	-6 º	-2º	0º	4º	6º
	0.10	4º	0º	-8º	-12º	-4º	0º	8º	12º
	0.15	6º	0º	-12º	-18º	-6º	0º	12º	18º
	0.20	9º	0 º	-18º	-27º	-9º	0º	18º	27º

Table 5.4: Simulated motor angular position for one cycle

		Time (s)							
		0.125	**0.25**	**0.375**	**0.5**	**0.625**	**0.750**	**0.875**	**1**
Tail beat amplitude (m)	**0.05**	2.029º	0.027 º	-4.102º	-6.043º	-1.966º	0.127º	3.99º	6.10º
	0.10	4.058º	0.054 º	-8.203º	-12.09º	-3.933º	0.254º	7.98º	12.20º
	0.15	6.087º	0.082 º	-12.30º	-18.13º	-5.899º	0.381º	11.97º	18.30º
	0.20	9.131º	0.123 º	-18.46º	-27.19º	-11.05º	1.758º	16.69º	27.89º

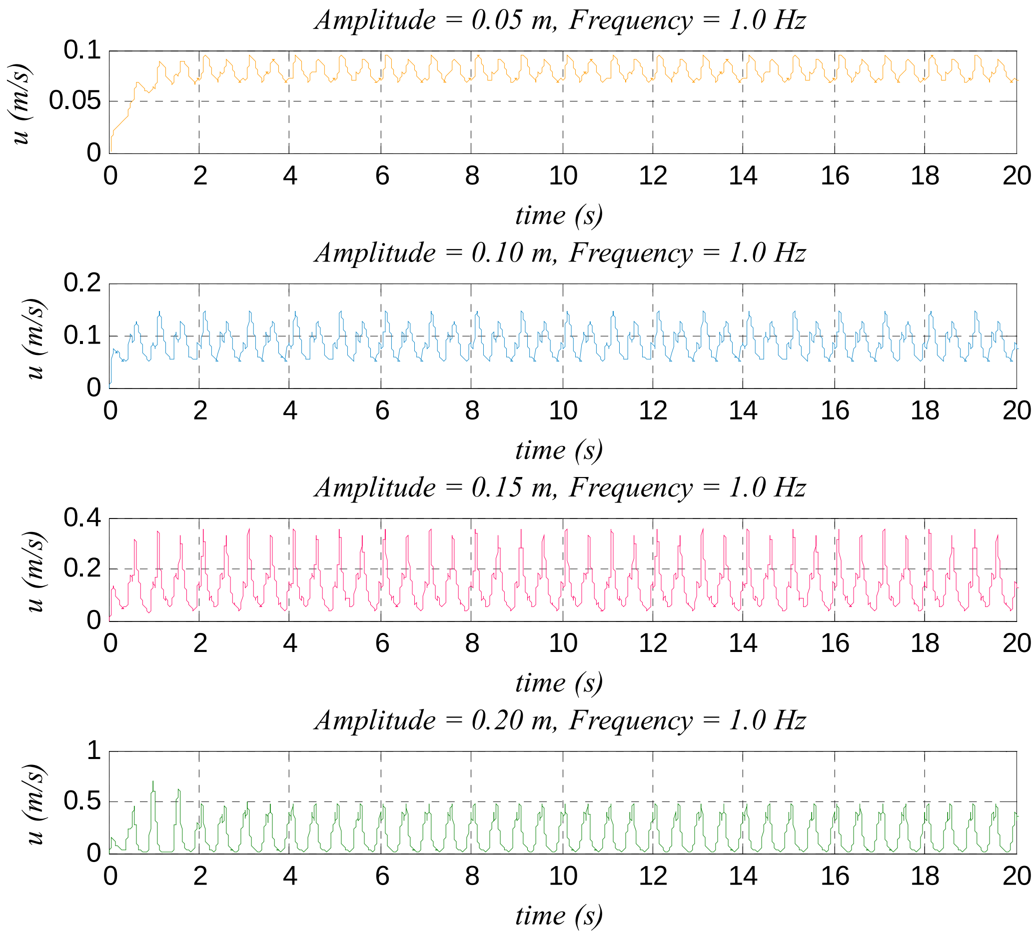

Figure 5.13: Simulated vehicle surge velocities for 1 Hz tail beat frequency with tail beat amplitude of 0.05 m, 0.10 m, 0.15 m and 0.20 m

Table 5.5: Average vehicle surge velocity respect to different tail beat amplitude

Tail Beat		Average Surge Velocity (m/s)	
Amplitude (m)	**Frequency (Hz)**	**Experiment**	**Simulation**
0.05	1.0	0.078	0.079
0.10	1.0	0.088	0.086
0.15	1.0	0.143	0.134
0.20	1.0	0.095	0.166

Actuator saturation

Furthermore, it can be observed the surge velocity increases in response to the increase in tail beat amplitude shown in Figure 5.13 with the average velocity results are summarized in Table 5.5. The simulated values agree well to experimentation values and increases linearly to the tail beat amplitude.

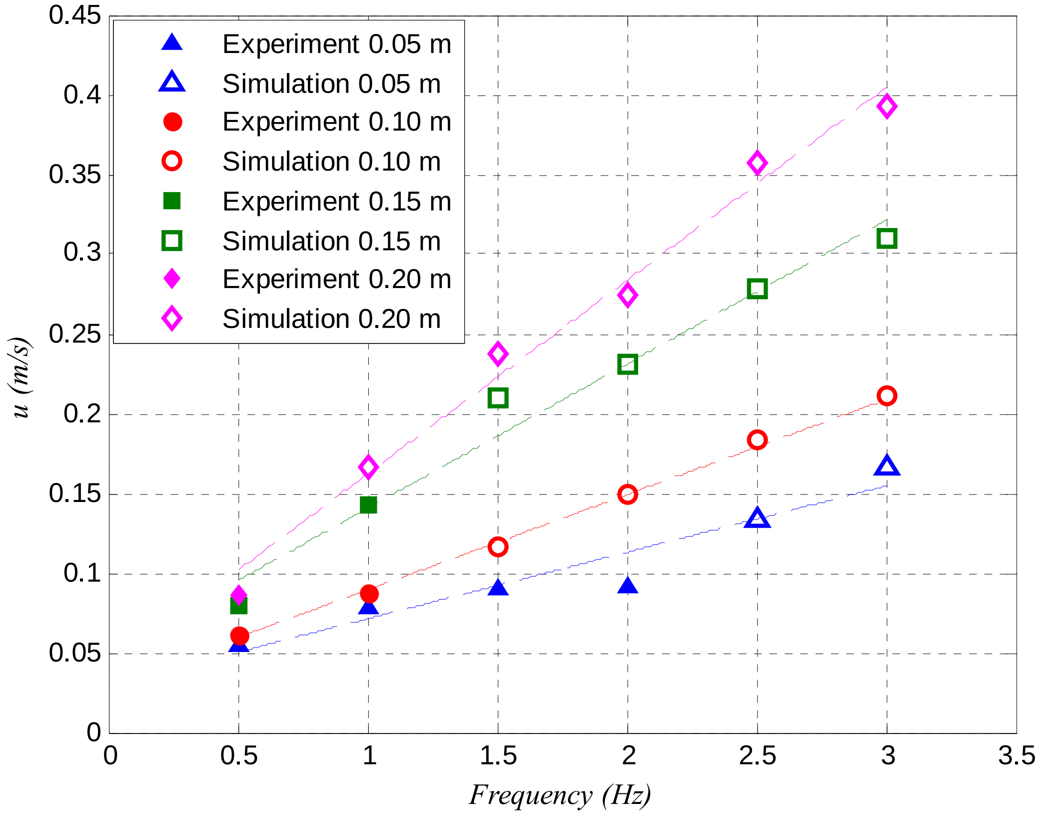

Figure 5.14: Surge velocity relates to tail beat amplitude and frequency. The saturated values are replaced with the simulation values

Figure 5.14 shows the forward swimming result for all combination of frequency/amplitude is redrawn with addition of the expected surge velocity result if the actuator saturation did not occur. These prediction lines are drawn based on the trend observed during experimentation supported by the model simulation results. It shows the linear increases of vehicle surge velocity relates to tail beat frequency. In addition, it also shows the effect of increase in tail beat amplitude also helps increase in the vehicle surge velocity.

Next, a 3D image in Figure 5.15 has been plotted for all forward swimming experiments to illustrate the overall configuration relationship to the tail beat amplitude and frequency if the actuator does saturated and not saturated. Based on the result, the linear relationship can clearly be seen with the maximum surge velocity can be obtained when it is configured at the highest tail beat amplitude and frequency.

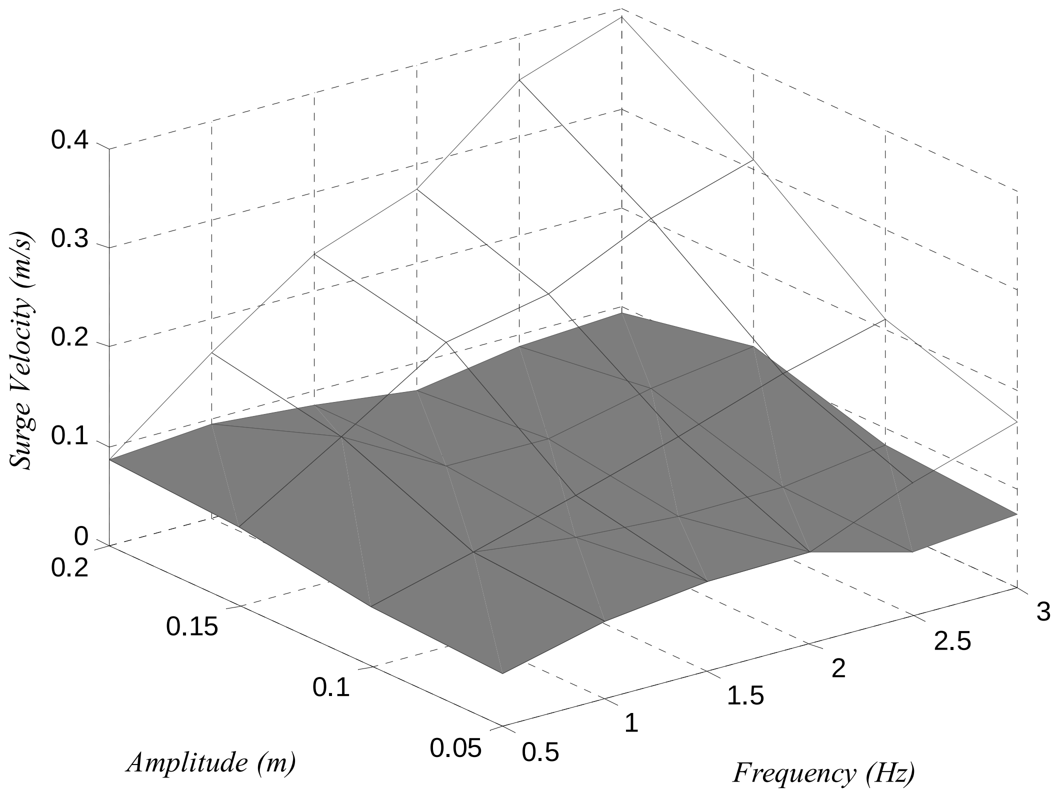

Figure 5.15: 3D Plot relationship between surge velocity, tail beat amplitude and tail beat frequency. (a) experimental values (grey) (b) saturated values in experimental values are replaced with simulation values (mesh plot)

5.3.1 Strouhal Number

The swimming performance of the vehicle can be evaluated by using the Strouhal number which quantifies the wakes behind the flow of flapping foils (Triantafyllou & Triantafyllou, 1995). It relates how fast the vortices are being generated and the space between them. The value of the Strouhal number is found to vary in the range from 0.25 < St < 0.35 for optimal swimming propulsion efficiency (Triantafyllou, et al., 1993; Triantafyllou & Triantafyllou, 1995). Existing data has revealed that number of fish and cetaceans (i.e. trout, shark, dolphin) species have Strouhal Numbers lie within this predicted range (Triantafyllou, et al., 1993; Rohr & Fish, 2004; Eloy, 2012). Whereas, Techet (2008) noted that higher thrust values can be achieved at higher values of Strouhal number but with less efficiency. The Strouhal number can be defined as the product of the tail beat frequency, f and peak-to-peak tail amplitude, A, divided by the speed of the fish, U.

$$St = \frac{fA}{U} \tag{5.5}$$

Watts (2009) argues that it is important to compare the biomimetic to biological systems in term of swimming performance. This is true since the vehicle is inspired and modelled according to the specification of a real fish thus it is reasonably to compare its performance to the biological system. As mentioned previously, only tail beat amplitude and frequency are varied during the forward velocity experiments. Most of existing research of Atlantic salmon has focused on the sustained swimming speed which it operates optimally (Bainbridge, 1957; Tang & Wardle, 1992) thus the Strouhal number is within the range of efficient swimming (0.25 to 0.35) (Videler, 1993 as cited in Eloy, 2012). Also, it is common to assume that fish have a tail beat amplitude of 10% of its body length during steady swimming (Videler, 1993) which make it possible to calculate the tail beat frequency. For example, Bainbridge (1957) found that Atlantic salmon with body length of 0.85 m able to achieved sustainable speed of 5.8 BL/s (4.95 m/s) while the Tang & Wardle (1992) study listed two different body length of Atlantic salmon; one has length of 0.45 m with speed of 1.93 BL/s (0.867 m/s) and another fish is 0.15 m in length with achievable speed of 2.43 BL/s (0.368 m/s). Thus, the frequency range can be measured by using equations below:

$$f_{lower} = \frac{(0.25)(U)}{A}; \quad f_{upper} = \frac{(0.35)(U)}{A} \tag{5.6}$$

Where $A = 2 \text{ x } (10\% \text{ of bodylength})$ and U is the swimming speed. However, even the lowest tail beat frequency is measured at 2.41 Hz which is higher than the achievable tail beat frequency that can be produced by the vehicle. Owing to limited availability of research data on fish swimming, an estimation of the swimming speed that occur within the operating vehicle frequency has to be made with an assumption that the real salmon maintains in the range of optimal efficiency for lower tail beat frequencies. The range estimation of swimming speed of real salmon and vehicle data is shown in Figure 5.16. The vehicle data chosen for the comparison is with tail beat amplitude of 0.10 m which agrees with the tail beat amplitude condition of a real fish. Naturally, it can be observed that the forward speed of the vehicle is much lower than the estimated minimum range of real salmon.

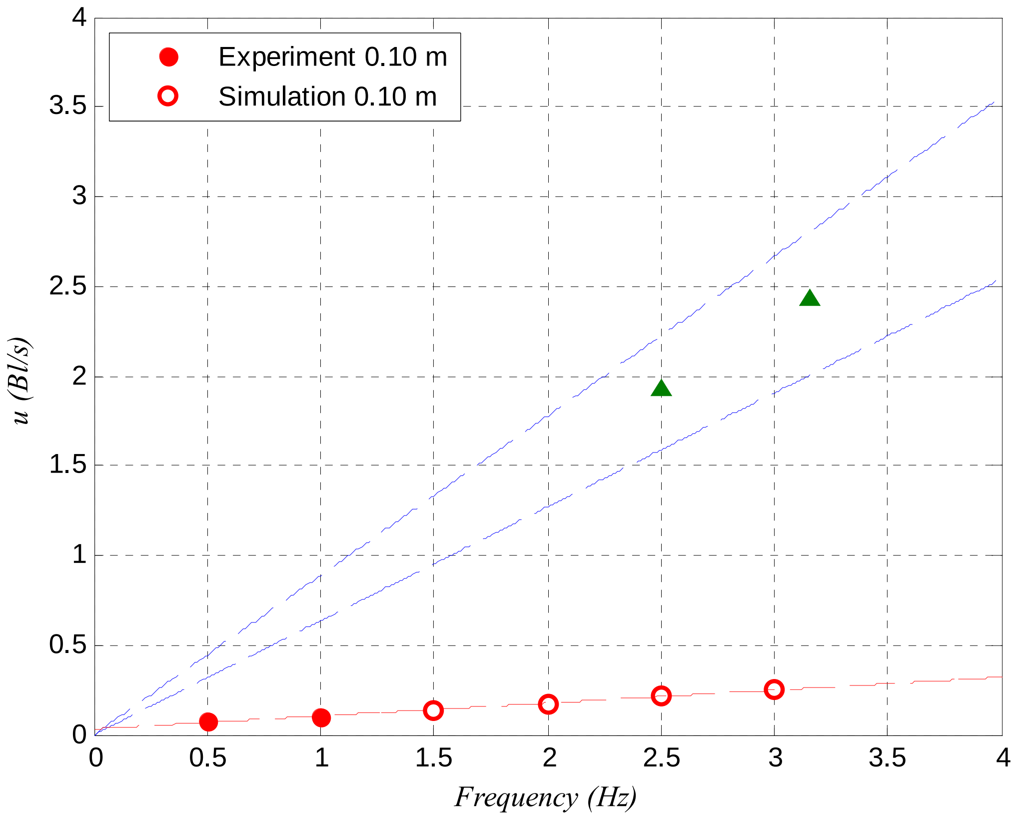

Figure 5.16: Comparison of swimming speed relates to frequency. Estimated range of optimal speed of Atlantic Salmon (blue dashed lines), Atlantic Salmon (Tang & Wardle, 1992) (green points), *RoboSalmon* (red points) with extrapolated data (red dashed lines)

This result is expected since in this case the replication of the real fish tail undulation motion is by using multiple gear DC motors. It can be claimed that the motors being underspecified that caused them to saturate. Moreover, this method tends to has a low efficiency because of the amount of energy consumes for continuously accelerates and braking of the rotor, gearbox and transmission components in which this energy loss is dissipated as heat (Apalkov, et al., 2012). The motor gearing also has tendency to restrict the tail movement. Furthermore, Shatara (2011) claims that this method also poses some other issues such as risk of mechanical breakdown and noisy operation. Therefore, it is possible that due to these factors, the actuated tail of the vehicle does not perfectly mimicking the undulation motion which then affects the thrust generation. In order to compare the overall vehicle performance to the biological system, the Strouhal number is calculated and shown in Figure 5.17(a). It can be observed that the Strouhal number linearly increased as the tail beat frequency set increased and values range between 0.91 and 12.63.

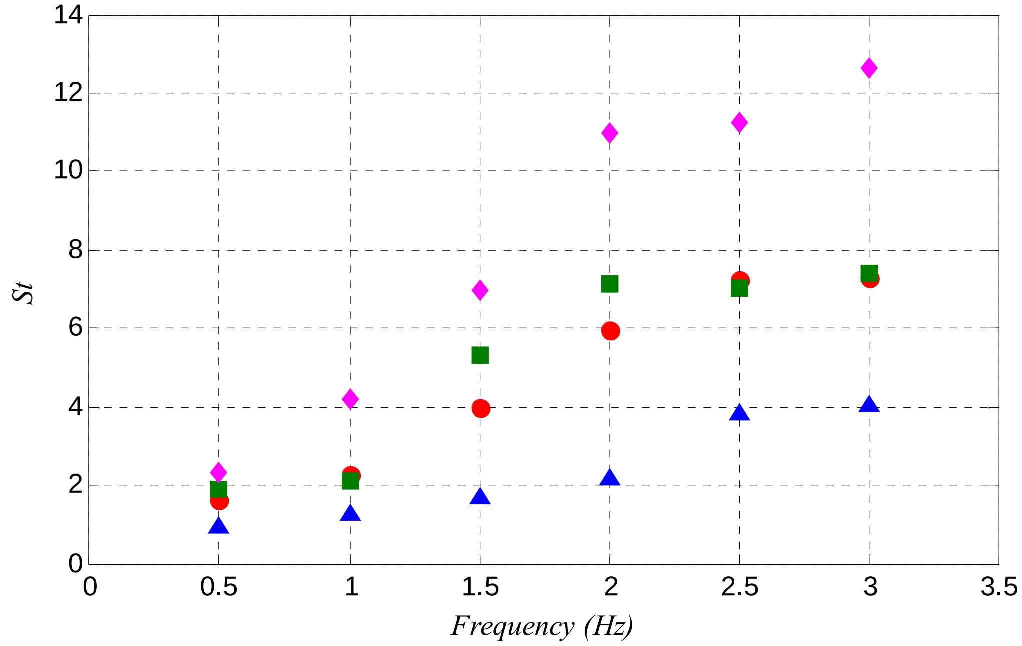

(a)

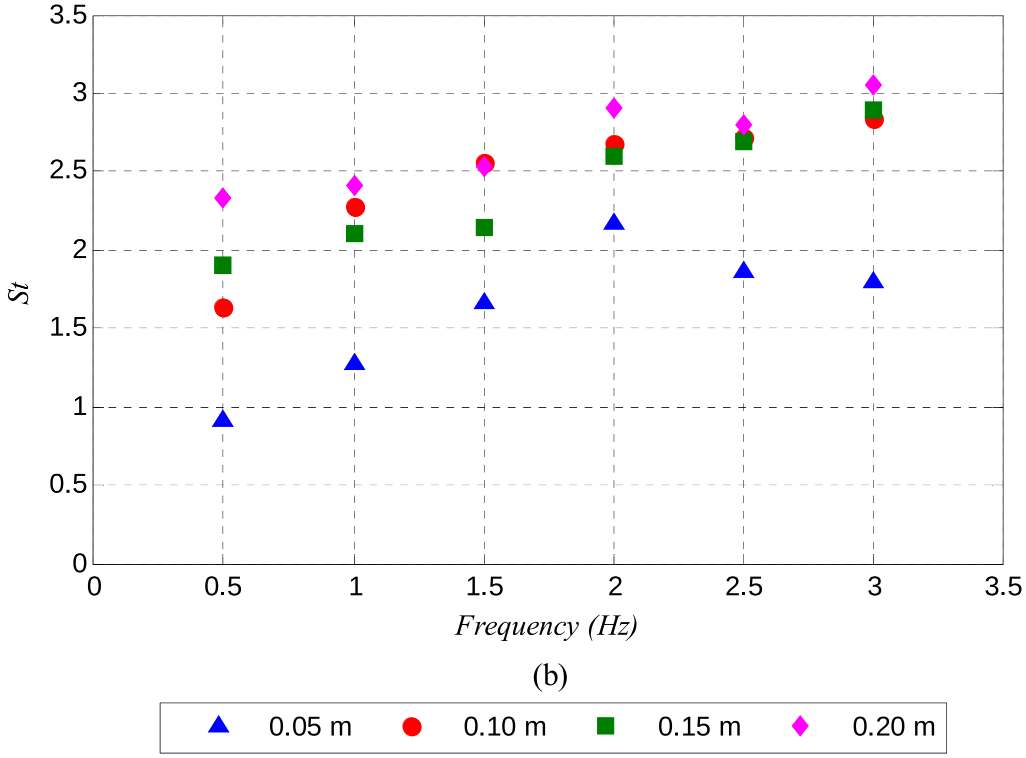

(b)

Figure 5.17: Strouhal number vs. frequency for the *RoboSalmon* (a) experimental (non-saturated and saturated) (b) non-saturated and simulated values

Figure 5.17(b) shows the difference in Strouhal number if the saturation does not occurred. The Strouhal number is calculated by replacing the actuator saturation surge velocities with the simulated values (see Figure 5.15). It can be seen Strouhal number range is significantly reduced to between 0.91 and 3.05 which is affected by the improved in the

RoboSalmon surge velocity. Moreover, a trend of Strouhal number relates to the tail beat amplitude/frequency has been noticed. A smaller tail beat amplitude with a lower tail beat frequency tend to has lower Strouhal number but as the tail beat frequency is increasing, the configurations with larger tail beat amplitude that produce higher surge velocity will then have smaller Strouhal number. Thus, it can be deduced that for a vehicle with larger tail beat amplitude need to be efficient, it will require a higher tail beat frequency configuration.

Even though, tail beat frequency and amplitude affect greatly on the vehicle surge velocity in turn reduced the Strouhal number but none of these values lies within the range of the efficient swimming. Thus, it shows that the *RoboSalmon* performance is not as efficient compared to a real fish relatively due to the low swimming speed. Therefore, it can be suggest that the specification of the motors needs to be improved to match the efficiency and speeds of real fish.

According to Lauder & Tytell (2005), it has been found that certain fish may have their Strouhal Number greater than the optimal range at low swimming speed. It is suggested either these fish swim inefficiently or the Strouhal Number does not adequately capture the complexities of fish swimming efficiency at this condition. Videler & Weihs (1982) claim that at low speed fish usually implement two types of swimming behaviour which are bursts-and-coast and steady swimming. Burst-and-coast swimming behaviour in fish consists of cyclic bursts of swimming movements followed by a coast phase in which the body is kept motionless and straight (Videler, 1993). Also, Weihs (as cited in Videler, 1993) points out fish tends to use burst-and-coast swimming instead of steady swimming as it helps saving half of its energy.

5.3.2 Power

The efficient swimming of the fish-like vehicle is discussed in this section. It involves the two stage approach adopted by Watts (2009), the first stage involves a common approach used to measure power consumption for battery powered vehicle i.e. the electrical power consumption is calculated by using the values obtained from the current sensor which discussed in detail in Chapter 3. The second stage involves the measurement of vehicle useful swimming power output.

5.3.2.1 Electrical Power

The plot of current and voltage measurement for a typical run of 0.05 m tail beat amplitude and 1 Hz frequency are shown in Figure 5.18 with the tail power consumption is calculated using Equation (5.7) by multiplying the current, I and voltage, V.

$$P_{\text{Electrical}} = IV \tag{5.7}$$

It can be observed from the graph below that the power consumed is not constant since it is affected by the different current demand by each motor throughout the tail undulation motion.

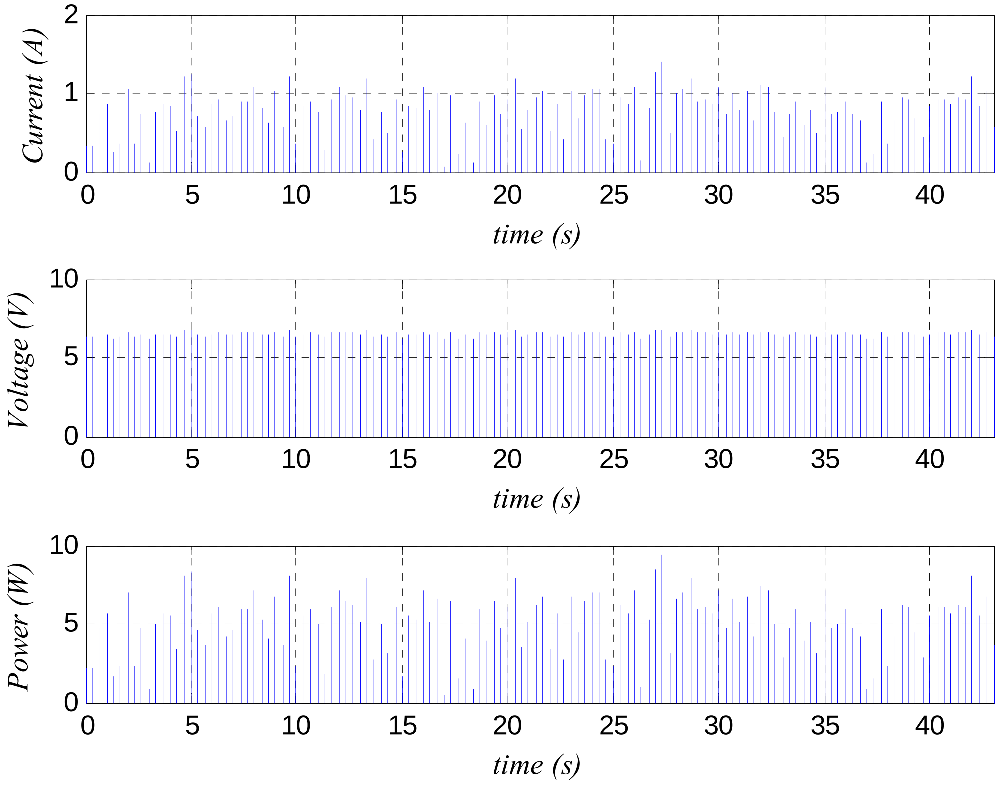

Figure 5.18: The *RoboSalmon* tail current (top), voltage (middle) and power consumption (bottom)

The average electrical power consumption for each configuration of non-saturated actuator is measured and plotted in Figure 5.19. It is clear from the graph that the average power consumption increases gradually with the surge velocity. Even at the lowest surge velocity the average power consumption is 3.96 W. This high level of power consumption is a direct result of the high amount of current supplied to the multiple actuator used to imitating the fish tail undulation.

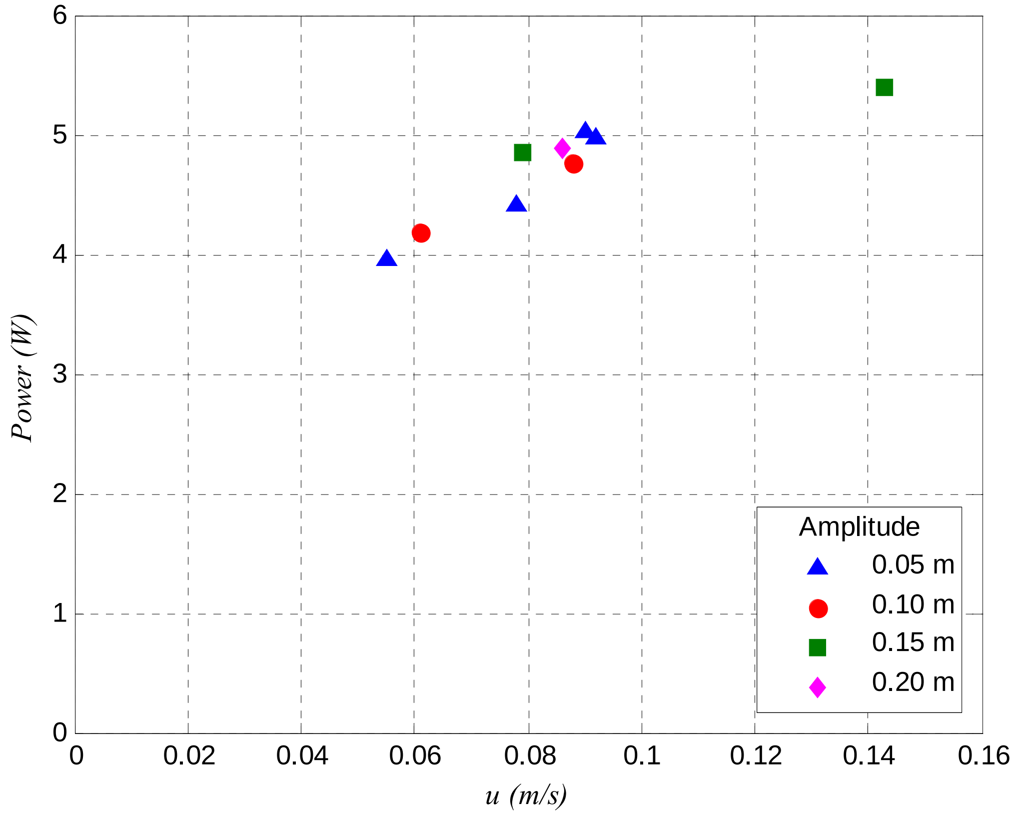

Figure 5.19: Electrical power consumption

5.3.2.2 Mechanical Power

This subsection discussed the approach used to calculate the *RoboSalmon* useful swimming power output and compares it to a real fish. This power measurement emphasis on the mechanical part of the real fish (i.e. muscle) and *RoboSalmon* (i.e. tail kinematics).

Real fish Power Output

The mechanical power of a real fish swimming output is generated by muscle (Rome, et al., 1993) and by having BCF locomotion, the thrust is known to be produce by bending it bodies backward moving propulsive wave that extends to its caudal fin (Sfakiotakis, et al., 1999). Hoar & Randall (1978) stated that the muscle system can be categorized into two functional groups known as red and white based on their colour. Red muscle is a slow, with low contractile power and used within sustained swimming speed (Jayne & Lauder,

1994) whereas the white muscle is faster and more powerful which usually used for high speed swimming. Moreover, the white muscle is also used for rapid movement such as escape response and burst swimming where the power demand from the musculature is the greatest which eventually leads to rapid fatigue (Hoar & Randall, 1970).

The power output estimation is calculated with only red muscle being considered as long as the real fish swims within sustained swimming. Tang & Wardle (1992) reported that it can be measured by applying the amount of 5 - 8 Wkg^{-1} for the maximum red muscle power output capacity in addition to the assumption that all red muscle is being used which forms 3 - 4% of the body mass. It is estimated that its value lies between 0.86 - 1.38 W for salmon that has similar dimensions to the vehicle. This value indicated the estimation of fish power output at its maximum sustained swimming speed. Watts (2009) argues that a better comparison is needed since the vehicle swims at a lower speed. One way to achieve this is outlined in Tang & Wardle (1992) which shows that the real fish power output value increases as the cube of the swimming speed (see Figure 5.20). Therefore, estimation of real fish power output values can be made for the lower speed.

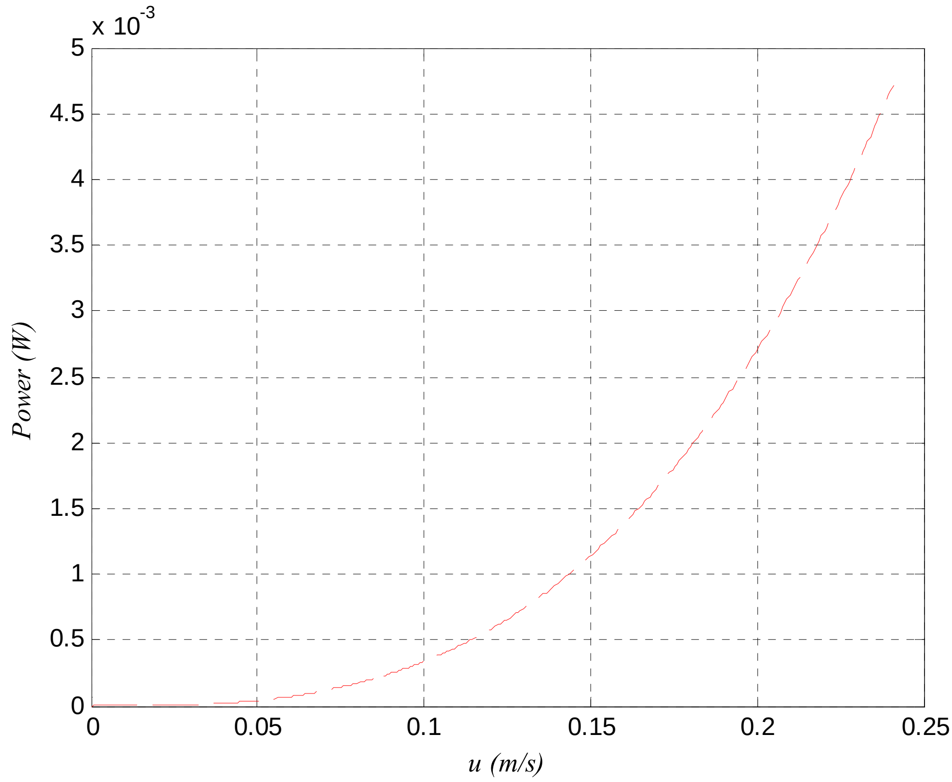

Figure 5.20: Estimation of real fish swimming power relates to the swimming speed

RoboSalmon Power Output

The large amplitude elongated body theory (Lighthill, 1971) is a popular method that combines kinematic parameters with hydrodynamic models for thrust estimation (Schultz & Webb, 2002). The method has been applied in Tang & Wardle (1992) where the image of real fish is analysed to obtain the kinematic parameter of the *RoboSalmon* caudal fin motion. The useful swimming power output is then calculated by multiplying thrust, T and surge velocity, u.

$$P_{\text{Swimming Output}} = Tu \tag{5.8}$$

Thus the same approach is applied in this case to the non-saturated actuator which illustrated in Figure 5.21 where the relationship between power output and surge velocity is appear to be linear.

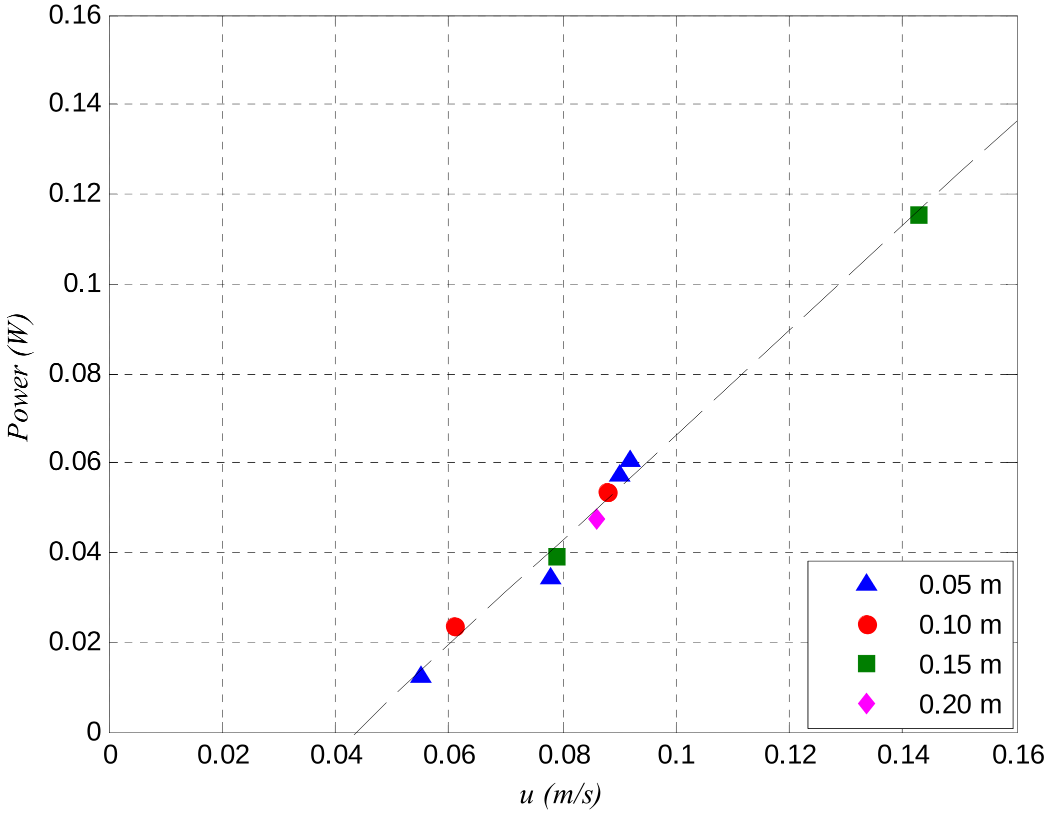

Figure 5.21: *RoboSalmon* swimming power output

The comparison of power output of a real fish and *RoboSalmon* can be made based on Figure 5.20 and Figure 5.21. It can be seen large discrepancy between them and this is expected since the vehicle suffers inefficiency in generating thrust namely caused by underspecified motors and mechanism power losses.

5.3.2.3 Propulsive Efficiency

The propulsive efficiency is expressed as Froude efficiency, η and it is used to measure the rate at which mechanical power is transformed into thrust. Tytell (2010) stated that it provides a useful way of comparing the swimming performance of different fishes and underwater vehicles. Therefore, in this research it is used to measure vehicle swimming efficiency which defined as:

$$\eta = \frac{P_{\text{Out}}}{P_{In}} = \frac{P_{\text{Swimming Output}}}{P_{\text{Electrical}}} = \frac{Tu}{P} \tag{5.9}$$

Here u is the mean forward velocity of the fish, T is the time averaged thrust produced, and P is the time averaged power required (Sfakiotakis, et al., 1999).

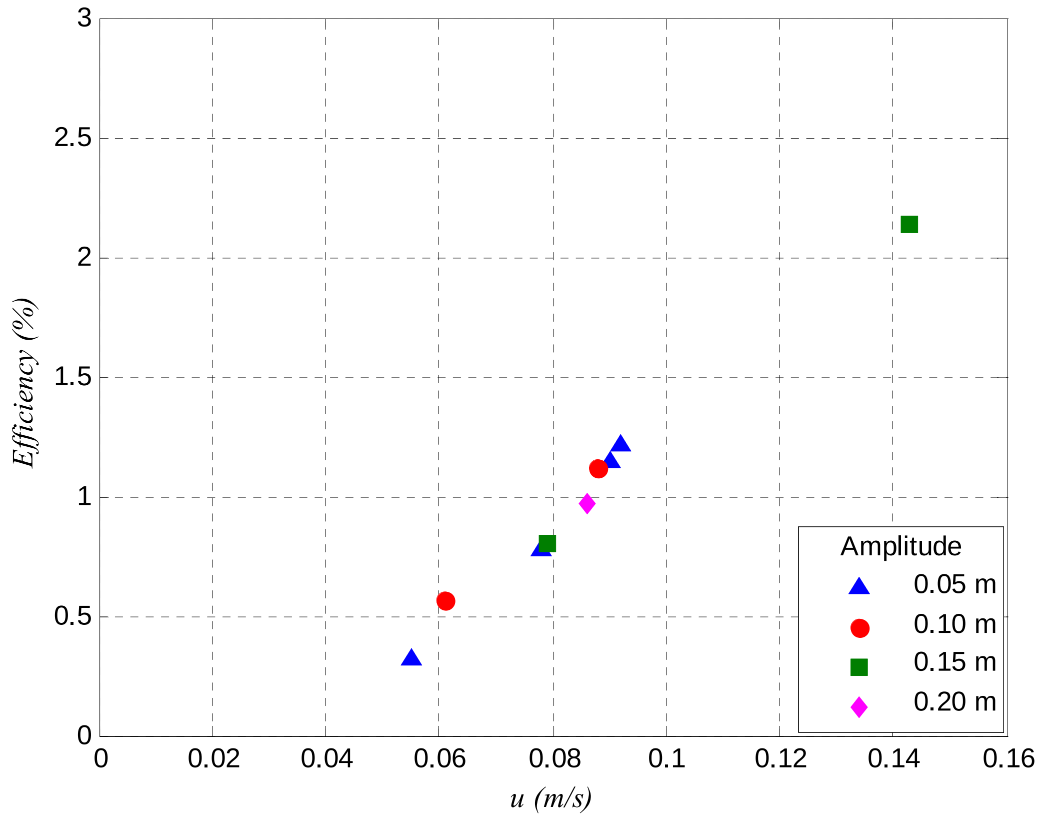

Figure 5.22: *RoboSalmon* propulsion efficiency

It is shown in Figure 5.22 that the propulsion efficiency increases linearly with the vehicle swimming speed. It also can be observed that the efficiency is improving when a larger tail beat amplitude or higher tail beat frequency has been applied. Thus, it suggests that a higher percentage of total power is converted into the useful swimming power at higher and larger tail beat frequency and amplitude respectively. The maximum propulsion efficiency value is measured at 2.14%. Even though, the vehicle has low efficiency but it still has better efficiency than the propeller based system in Watts (2009) study. The propeller based system is estimated to have approximately 0.8% efficiency for surge velocity condition less than 0.2 ms^{-1} (Watts, 2009).

Several factors can be related to the low propulsion efficiency where the most significant is due to the high power consumed by the multiple actuators in performing the undulation motion. Moreover, power losses due to mechanical and friction also can be considered since dealing with a complex mechanism in the tail part. These losses are contributed by the moving parts such as gear and link mechanism. In addition, it can be suggested that the *RoboSalmon* vehicle has low efficiency owing to underspecified actuator that has been mentioned earlier.

5.3.3 Recoil Motion

Swimming using the BCF propulsion system increases the tendency for the body to recoil. This recoil movement occurs at the anterior of the body due to the lateral force concentrated at the posterior (Sfakiotakis, et al., 1999). The recoil motion experienced by the vehicle can be seen in

Figure 5.8(a) where the vehicle trajectory appeared not in the straight path. These recoil motion in roll, pitch and yaw that effect the *RoboSalmon* vehicle are been discussed in detail in this section.

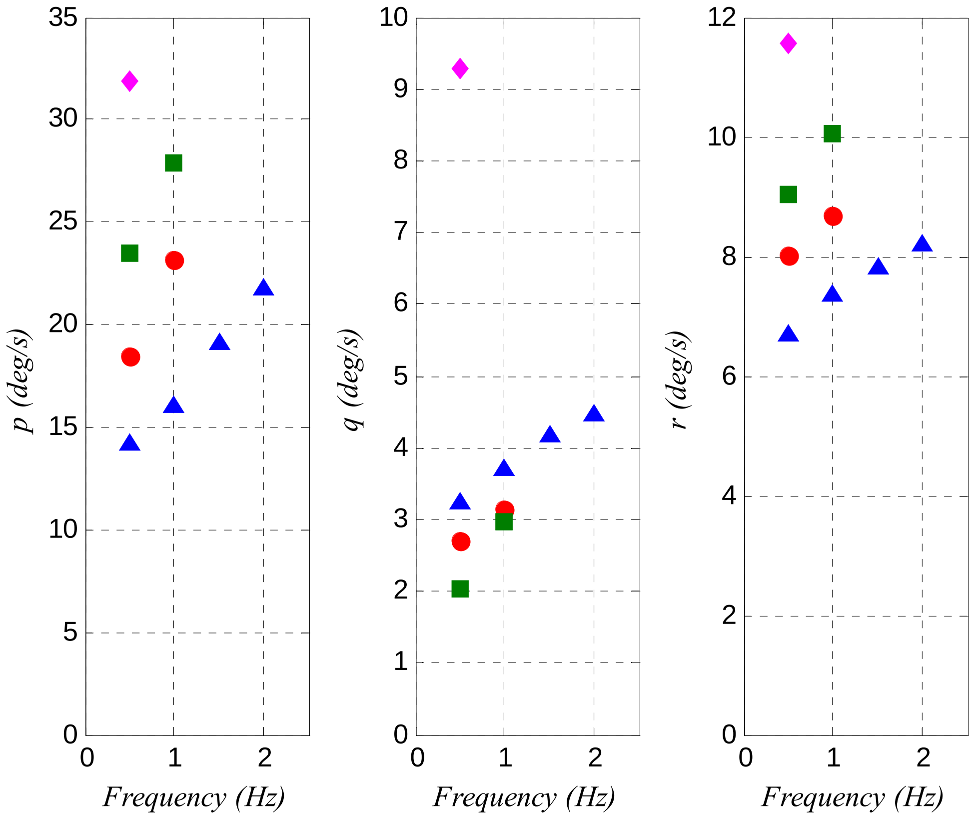

Figure 5.23: Quantitative comparison of magnitude in roll, pitch and yaw angular velocities. The tail beat amplitudes are indicated by the blue points (0.05 m), red points (0.10 m), green points (0.15 m) and magenta point (0.20 m)

Figure 5.23 show the quantitative comparison of magnitude in vehicle recoil motion in roll, pitch and yaw for non-saturated actuator. As expected significant changes in the orientation of the vehicle can be seen especially in roll and yaw plane. As seen, the vehicle roll and yaw angular velocity is increased linearly with the tail beat frequency and amplitude. The vehicle proves to have a higher roll and yaw values when the rates of undulation motion keep on increasing. It also can be highlighted that the sharp rise in roll angular velocity when larger tail beat amplitude is demanded. It also worth noted that the vehicle roll angular velocity is greatly reduced when compares with the rolling motion of the tendon drive propulsion system study (Watts, 2009; Watts & McGookin, 2013).

The similar result can be seen for the vehicle pitch angular velocity but for a smaller scale compared to the roll and yaw rates which it values are increasing linearly with the frequency. However, the vehicle acts oppositely when larger tail beat amplitude is demanded. The pitch angular velocity is decreasing steadily for all tail beat amplitude except for the largest amplitude (0.20 m).

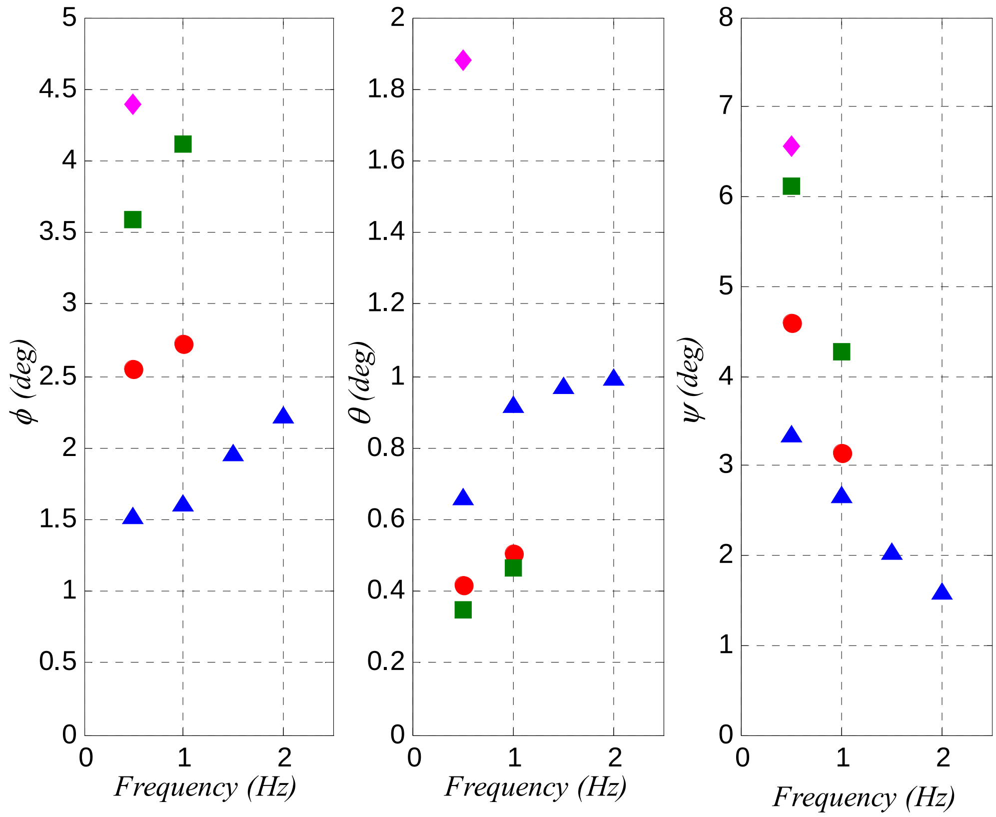

Figure 5.24: Quantitative comparisons of magnitude in roll, pitch and yaw angular position. The tail beat amplitudes are indicated by the blue points (0.05 m), red points (0.10 m), green points (0.15 m) and magenta point (0.20 m)

The angular position illustrated in Figure 5.24 is obtained by integrating the gyroscope velocity data. It can be seen that the roll angular position increases linearly with tail beat amplitude and frequency. Therefore, it can be deduced that the magnitude of roll angular position mainly is affected by the changes in tail beat amplitude. During the experiment trials for this study, it was apparent that the changes in roll angular deflection for the smallest tail beat amplitude are difficult to detect and considered to be negligibly small. However, the vehicle exhibits larger roll deflections when larger amplitudes are demanded. The lateral displacement caused by the undulation motion will interrupt the vehicle stability during swimming. Thus, when bigger lateral displacement is performed will affect the vehicle to roll to one side of the body.

The changes in magnitude of pitch angular deflection is small except when the tail beat amplitude and frequency configuration is set at 0.20 m and 0.5 Hz respectively. This is due to the combined influence of the caudal fin being positioned farthest from the body and slower rates of undulation motion. In this scenario it is observed that the whole vehicle body tilts to one side and slightly upwards during the undulation cycle.

The quantitative values for yaw angular velocity are difficult to be determined. The vehicle is expected to move in straight line in the forward swimming experiment. However, the uneven lateral force causes by the recoil motion affect the vehicle final position where the positions are varied in each run and configuration. The relationship between the yaw angular position and tail beat amplitude/frequency has been observed where the amplitude in yaw angle starts to decrease when the smaller tail beat amplitude and higher frequency is been applied. Based on the result obtained, it can be deduced that the vehicle subjected to small quantity of recoil motion with the roll and yaw as the major contributor. It also worth noted that an uneven mass distribution of components in the vehicle may also added to the recoil movement. The resulting recoil motion causes the vehicle swimming trajectory to move away from the expected straight path and generates a yawing motion.

5.4 Actuated Head

Several methods for minimizing the recoil motion are mentioned in Watts & McGookin (2013). One of the methods that have been tested in this research involves the utilisation of an actuated head during forward swimming to counteract the recoil of the tail.

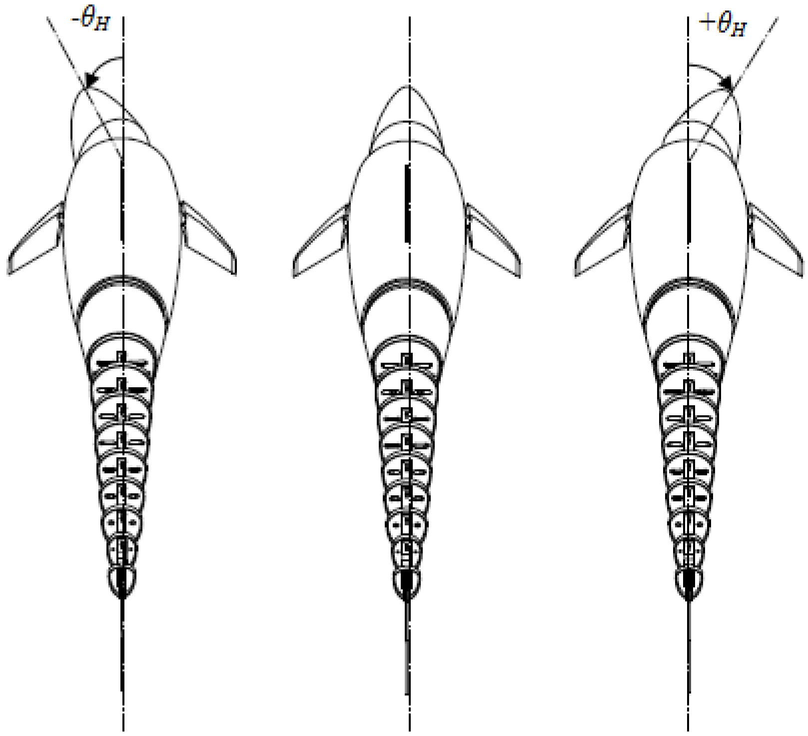

Figure 5.25: Actuated head configuration -18º (left), 0º (centre) and +18º (right)

The experiment has been carried out for the tail beat amplitude and frequency is configured at 0.15 m and 1 Hz respectively with a servo motor is used to control the head movement. The actuated head is configured as shown in Figure 5.25 with the head movement is set to continuously oscillate in sinusoidal fashion with an angular deflections, θ_H at ±18 degrees. A number of different head angles have been tested and the smallest head deflection angle, θ_H is determined to be at ±18 degrees. The continuous head movement will increase the vehicle overall power consumption. For that reason, applying less than 18 degree head deflection angle is unnecessary since it does not have an effect on the vehicle motion.

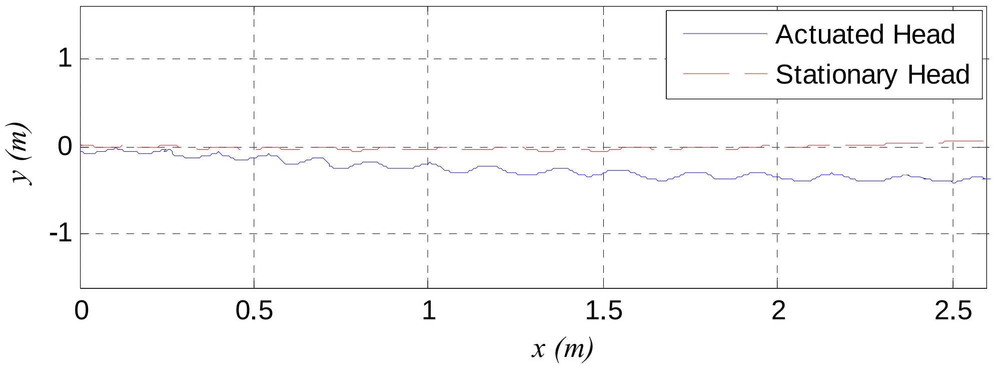

Figure 5.26: XY Trajectory with and without actuated head deflection

Figure 5.26 shows a comparison between the vehicle's trajectory with and without the influence of the actuated head. It can be seen that the actuated head trajectory is not as smooth as the trajectory of vehicle with the head held stationary. This illustrates that the vehicle with an actuator head tends to exhibit larger oscillations throughout the forward swimming cycle. The vehicle's linear and angular velocities in addition to power consumption are recorded in Table 5.6.

Table 5.6: Velocities comparison between actuated and stationary head

	Velocity			Overall Power Consumption (W)
	Surge (m/s)	Roll (deg/s)	Yaw (deg/s)	
Actuated Head	0.086	52.74	11.82	14.1881
Stationary Head	0.116	27.06	9.87	10.8085

These results indicate that the motion of the vehicle with actuated head produces larger recoil motions, which in turn contribute to a decrease in the magnitude of the vehicle's surge velocity. Large amount of energy is wasted by continuous moving head, pushing the water to sides as it moving forward. It generates unnecessary extra roll and yaw angular velocities which affected the vehicle performance. Moreover, it also suggested the vehicle drag is subject to be increased as it needs to encounter extra frontal area causes by the continuous moving head during the forward swimming.

Another reason of the vehicle with actuated head configuration poor performance is caused by the ineffective thrust generation. It is known that the forward thrust depends on the effective lateral movement of caudal fin. Since the vehicle is affected by high roll motion when the actuated head it utilised, the lateral movement of vehicle caudal fin and the thrust generation are both critically reduced. Thus, it can be conclude that the actuated head approach not able to minimize or cancel out the unwanted (recoil) motion but worsen the vehicle performance. Therefore, this approach has not been tested further for other forward swimming.

5.5 Summary

This chapter described the *RoboSalmon* experimentation and simulation outcomes for the forward motion. It involved the analysis of varying several tail beat parameters; amplitude and frequency. It was found that vehicle surge velocity depends on these tail beat parameters where it increases as the tail beat parameter are set to increase. It has been showed that the vehicle's surge velocity is increase affected by the increase in tail beat frequency and keeping the amplitude constant. A similar observation also has been made when varying the tail beat amplitude while maintaining a constant frequency. Moreover, it has been observed that the actuator saturation occurred during experimentation which significantly limits the useful result obtained by varying *RoboSalmon* tail beat parameters. The highest vehicle surge velocity obtained is 0.143 ms^{-1} when the tail beat frequency and amplitude are set at 1 Hz and 0.15 m respectively. Furthermore, the tail beat parameters that not supported during experimentation due to actuator saturation has been tested thru computer simulation. The results obtained supported the observation made for *RoboSalmon* in experimentation where the surge velocity increases based on the increase in tail beat amplitude and frequency.

These surge velocities have been compared to the real salmon and it shows that the ranges of *RoboSalmon* surge velocities are much lower than the estimated values for real salmon. The *RoboSalmon* Strouhal number also has been calculated and the values are not within the range quoted for an efficient swimming of a real fish. Although, it is claimed that real fish tends to use burst-and-coast swimming instead of steady swimming at low velocity. Still, the measured result shows that the *RoboSalmon* performance is not as efficient compared to a real fish relatively due to the mechanical limitations imposed by the tail actuators. It has been suggested that an improvement in the operational specification of the motors used to actuate the tail sections would provide an increase range of achievable velocities. Based on the current design tail beat parameters, it can be suggested the required motor speed specification should be at least 160 rpm.

The *RoboSalmon* propulsion efficiency is found increased linearly with the surge velocity with the maximum efficiency measured at 2.14%. It is found that this low efficiency values is caused by the recoil motion experienced by the vehicle. Even though it has low efficiency, the trend obtained suggests that the *RoboSalmon* propulsion efficiency will improve when higher and larger tail beat frequency and amplitude are applied. Next, the utilisation of an actuated head during forward swimming has been tested in order to counteract the recoil motion. However, the continuous head motion creates even a larger recoil motion, which in turn contributed significantly to the decrease in the magnitude of the *RoboSalmon* surge velocity.

6

Manoeuvring Swimming

6.1 Introduction

Turning is one of the important manoeuvres employed by biological fish for tracking prey and, avoiding obstacles and predators. There has been increased interest in studies regarding manoeuvring capabilities of fishlike propulsion systems (Hirata, et al., 2000; Liu & Hu, 2005; Rossi, et al., 2011b; Wang, et al., 2011). This is because the researchers inspired by the high manoeuvring ability of several kinds of fish such as eel, salmon and tuna (Melsaac & Ostrowski, 1999; Hirata, 2000; Yu, et al., 2008). The implementation of biological propulsion systems on vehicles has been shown to improve their manoeuvring and turning capability at low speed conditions which has been lacking in conventional underwater vehicles (Bandyopadhyay, 2004, 2005; Watts, 2009; Watts & McGookin, 2013). Anderson & Chhabra (2002) stated that the poor manoeuvring performance of conventional underwater vehicle designs because they require several body lengths turning radius at low speeds. Whereas fish are able to achieve faster degrees of turning with a radius considerably less than their own body length.

As discussed in the previous chapter, the trajectory of the vehicle is profoundly influenced by the recoil motion, particularly in the case of forward swimming. However, Weihs (2002) highlighted the lack of stability, especially in yaw motion, for body caudal fin propulsion systems which contributes significantly to vehicle manoeuvrability. In this chapter, some of the typical manoeuvring tests are performed on the vehicle in order to determine its stability and turning performance. Faltinsen (2006) and Fossen (2011) stated it is common that the manoeuvring performance characteristics of a marine vehicle is assessed using tests documented by the International Maritime Organization (IMO) and the International Towing Tank Conference (ITTC). These tests include turning circle manoeuvres, zigzag manoeuvres, pull out and stopping trials. Although the manoeuvrability tests considered in this chapter are usually applied for marine vehicles longer than 100 m (American Bureau of Shipping, 2006; Faltinsen, 2006), a similar approach can be utilised to determine the stability and manoeuvrability of the vehicle discussed in this research.

Based on the study conducted by Liu & Hu (2010), the manoeuvring pattern can be classified as either cruise in turning and sharp turning. Since the biomimetic vehicle considered here must maintain forward propulsion through periodic swimming then the cruise in turning swim pattern is utilised in this study. In this case the manoeuvring experimentation involves varying the similar parameters used for forward swimming (e.g. tail beat frequency and amplitude) except with the addition of tail deflection angle to generate the desired turning motion.

6.2 Tail Manoeuvring System

This section presents the method used for controlling the vehicle heading motion which involves varying three parameters; tail beat frequency f, tail beat amplitude A, and tail deflection angle, δ_T. The vehicle heading can be modified by altering the centreline of the tail undulation for a period of time (see Figure 6.1). The limitations on actuators and diameter links are taken into consideration in determining the angle and shape of undulation movement. In the turning mode the centreline of the tail movement is designed to be curved rather than a straight line as in forward swimming. This angle is referred to as the tail deflection angle, δ_T. As mentioned in Chapter 3, the tail mechanism consists of eight connected revolute joints. The tail deflection angle is divides among these joints using Equation (6.1). Here *x_motor* is number of motor and n is the maximum deflection angle for each joint.

$$\sum_{x\_motor=1}^{8} \left(x\_motor\right) n = \delta_T \tag{6.1}$$

Figure 6.1 shows the changes in tail centreline, it can be seen that it depends on the magnitude of the deflection angle for each of the tail joint. In addition to the yawing motion created by tail centreline, the turning manoeuvre can further be improved by deflecting the head angle toward the direction of turning (Weihs, 2002). This simple approach is easily applied on the physical vehicle in the experimental studies. Moreover, it also helps reduce the complexity in calculating the thrust as the tail gait remains unchanged.

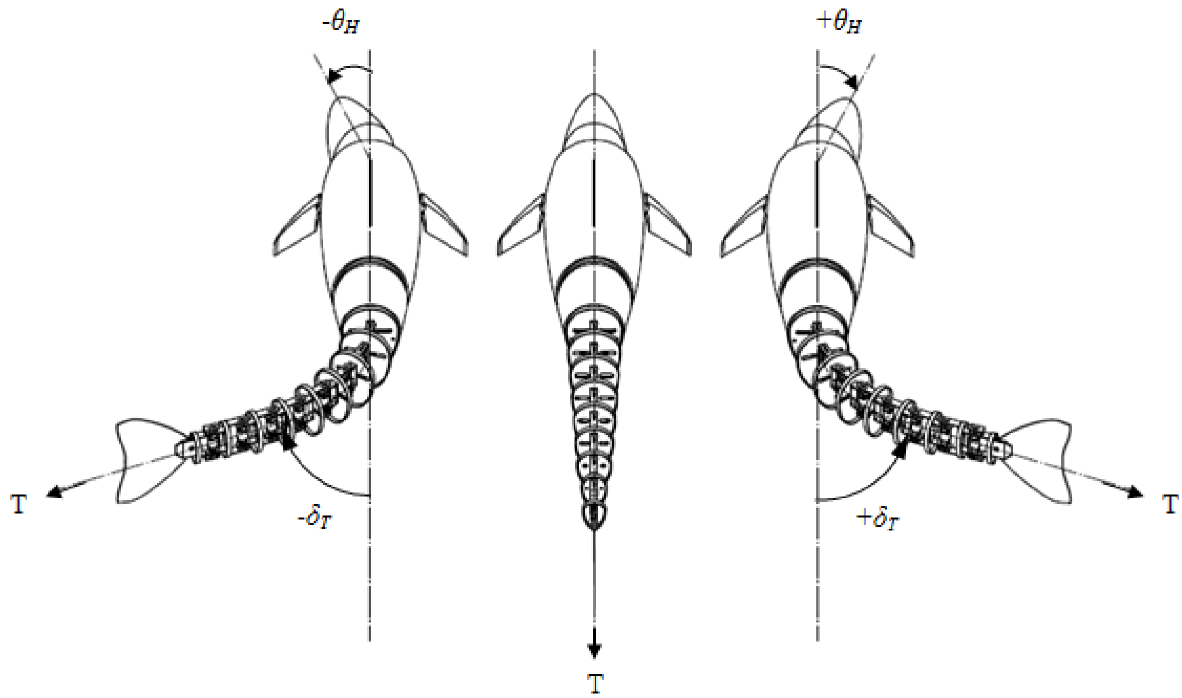

(a) (b) (c)

Figure 6.1: Tail deflection angle (a) left (b) centre (c) right

6.3 Cruise in Turning

The vehicle course changing ability is investigated through the turning circle manoeuvre test (Fossen, 1994; Faltinsen, 2006; Fossen, 2011). Throughout the manoeuvre the vehicle turns at a constant forward speed and turning rate. With conventional vehicles (e.g. ships) this approach is by setting the rudder to a predefined angle and holding it constant until circular path is obtained. Predominantly this test is used to provide standard measures of manoeuvrability such as tactical diameter, advance and transfer (see Figure 6.2) (Fossen, 2011). Moreover, it also provides information regarding the vehicle turning radius. In the context of this test, the tactical diameter is the lateral distance it takes for the vehicle to complete a 180˚ change of heading, the advance is the forward distance it takes for a 90˚ change of heading and the transfer is lateral distance it takes for a 90˚ change of heading (American Bureau of Shipping, 2006).

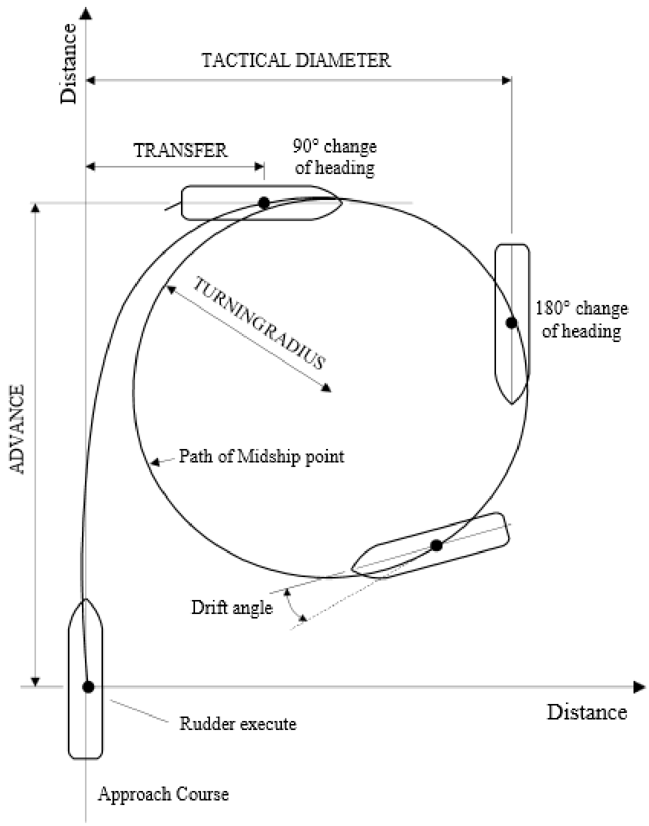

Figure 6.2: Turning circle test (American Bureau of Shipping, 2006)

Cruise in turning is a common biological swimming pattern applied to the fishlike propulsion systems. This swimming pattern can be described as being similar to the forward swimming gait except with the tail centreline is deflected in the desired direction of turning. According to Yu, et al. (2005b), the tail centreline is designed to be deflected to one side of its body so that it acts in a similar way to a rudder while the head is deflected in the direction of turning. Implementation of this swimming pattern also provides user configuration flexibility which leads to various speeds and turning radii (Hu, et al., 2006; Xu, et al., 2012).

The experiment is designed to investigate the vehicle swimming behaviour while turning by varying three parameters; tail beat amplitude, tail beat frequency and tail deflection angle. Based on observation and knowledge on actuator saturation occurred for forward swimming, two sets of tail beat amplitude (0.10 m and 0.15 m) and frequency (0.5 Hz and 1 Hz) have been chosen. There will be 4 configurations of tail beat amplitude and frequency where each configuration has been varies with the tail deflection angle, $\delta_T = \{10°, 20°, 30°, 40°, 50°\}$

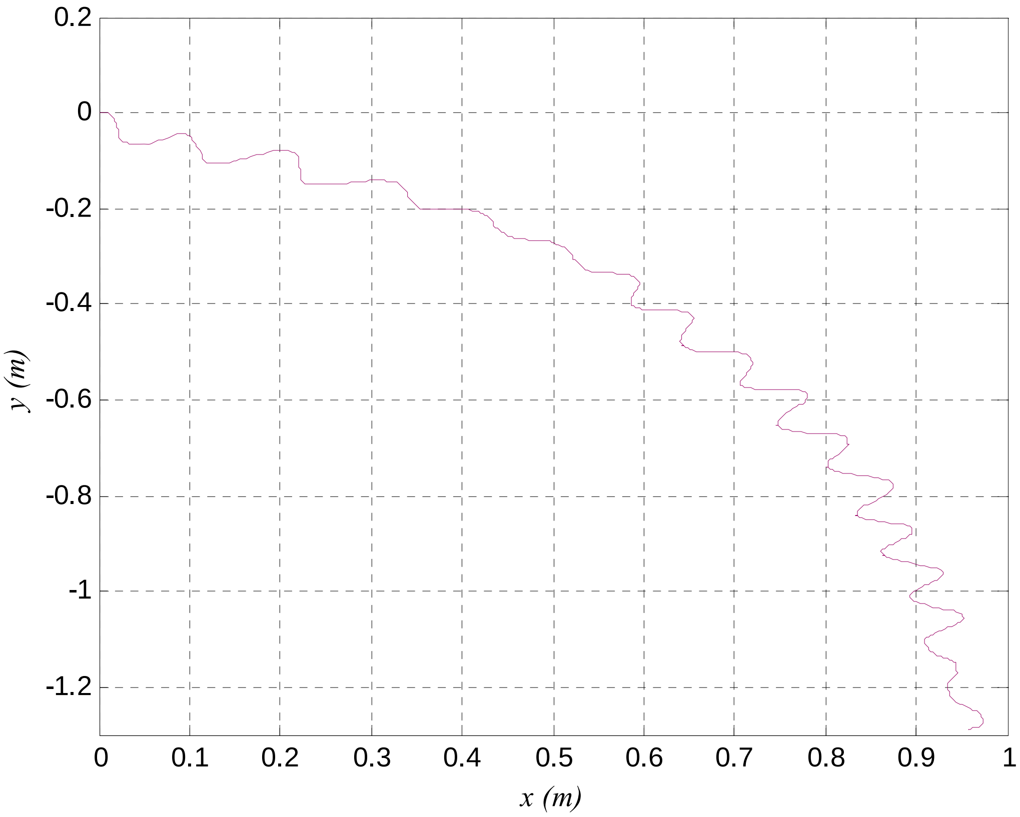

Figure 6.3: *RoboSalmon* path trajectory for configuration of 0.10 m tail beat amplitude, 1 Hz tail beat frequency and -50° tail deflection angle

The vehicle manoeuvring capability is been investigated with the turning radius, R_T as one of the characteristics that is examined for cruise in turning. It defined as the size of the smallest circular turn radius that the vehicle able to achieve (Menciassi, et al., 2011). Various turning radius and speed can be analysed for this manoeuvre motion. This is because, it performs a steady constant turn and the turning radius, R_T reflects this motion. As expected, even at the -50° tail deflection angle, the vehicle is not able to turn in full circle as it turning radius is bigger than the pool width as seen in Figure 6.3. However, given an arc with known width, W, and height, H, the vehicle turning radius can be measured using Equation (6.2) below.

$$R_T = \frac{H}{2} + \frac{W^2}{8H} \tag{6.2}$$

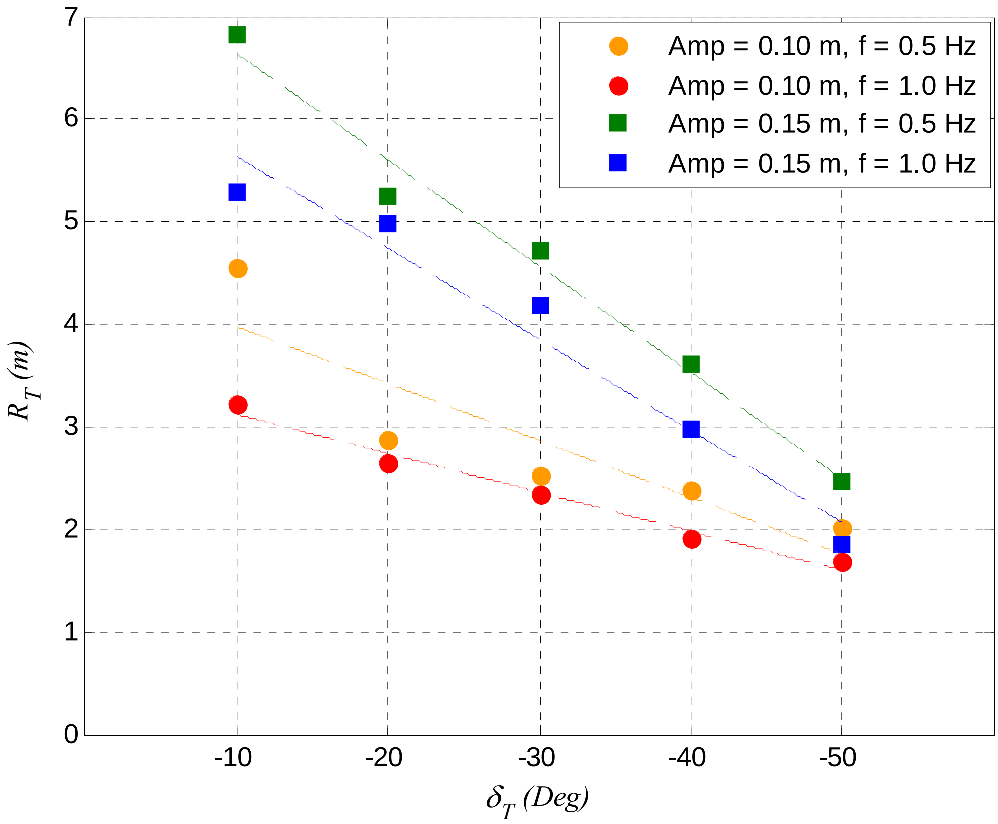

Figure 6.4: Experimental values of vehicle turning radius for cruise in turning

The turning radii for all experiments are measured and plotted in Figure 6.4. It shows that the vehicle turning radius can be influenced by several factors e.g. tail beat amplitude, tail beat frequency and tail deflection angle. The turning radius acts inversely to the tail deflection angle and tail beat frequency. As the tail deflection angle increases, the turning rate will be increase and causes the vehicle turning circle to decrease. The same trend can be said with the increased in tail beat frequency. This is because the higher tail beat frequency increases the vehicle speed as well creates a greater turning motion. On the contrary, bigger turning radius has been produced when larger tail beat amplitude been applied.

Figure 6.5 shows the turning radius obtained from the simulations model is well in agreement with the experimental values for tail beat configuration of 0.10 m and 1 Hz.. Similar relationship has been observed where the turning radius is reduces with the increases of tail deflection angle. Thus, it can be said that the simulation model can be used to estimate the vehicle turning radius for untested tail deflection during experimentation. This proves to be useful, as it essentially reduces the experimentation time.

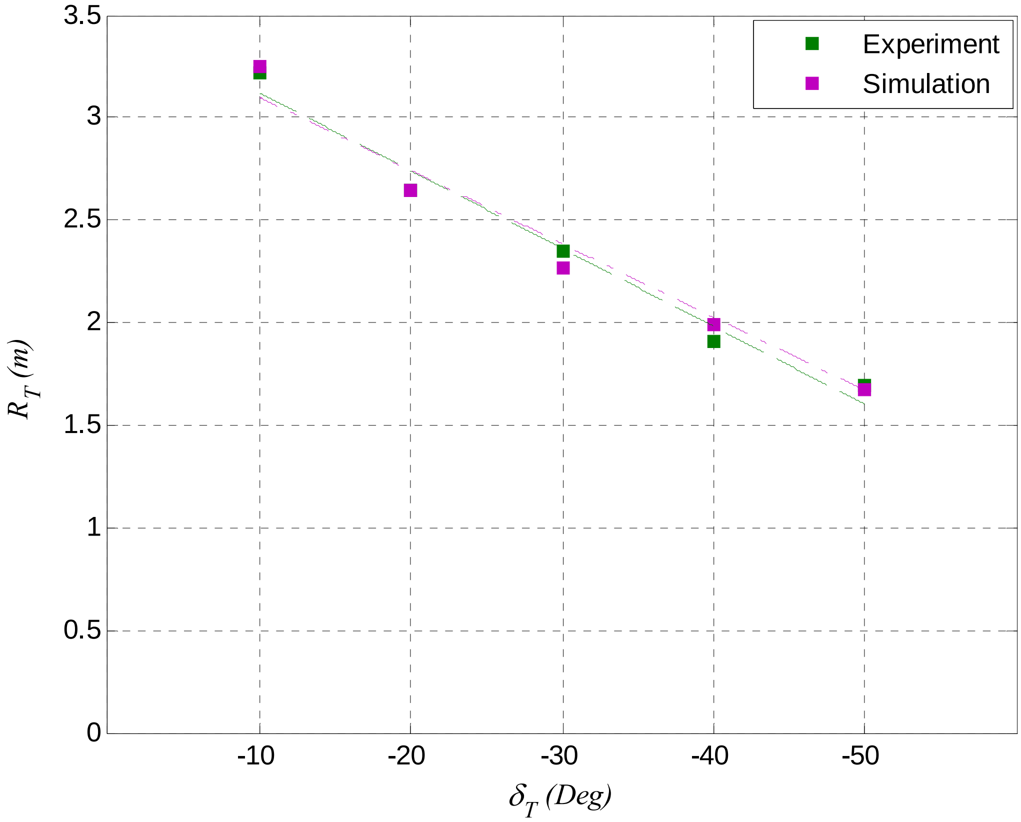

Figure 6.5: Comparison between experiment and simulation data of vehicle turning radius for cruise in turning for tail beat frequency of 1 Hz and 0.10 m

Also, it is noticed that the vehicle surge velocity decreases during the turning manoeuvres as shown in Figure 6.6. This is because propulsion thrust purely on the surge velocity for forward swimming. However, when the tail centreline being altered, some of the thrust propulsion is used to generate the turning motion and becomes sway velocity.

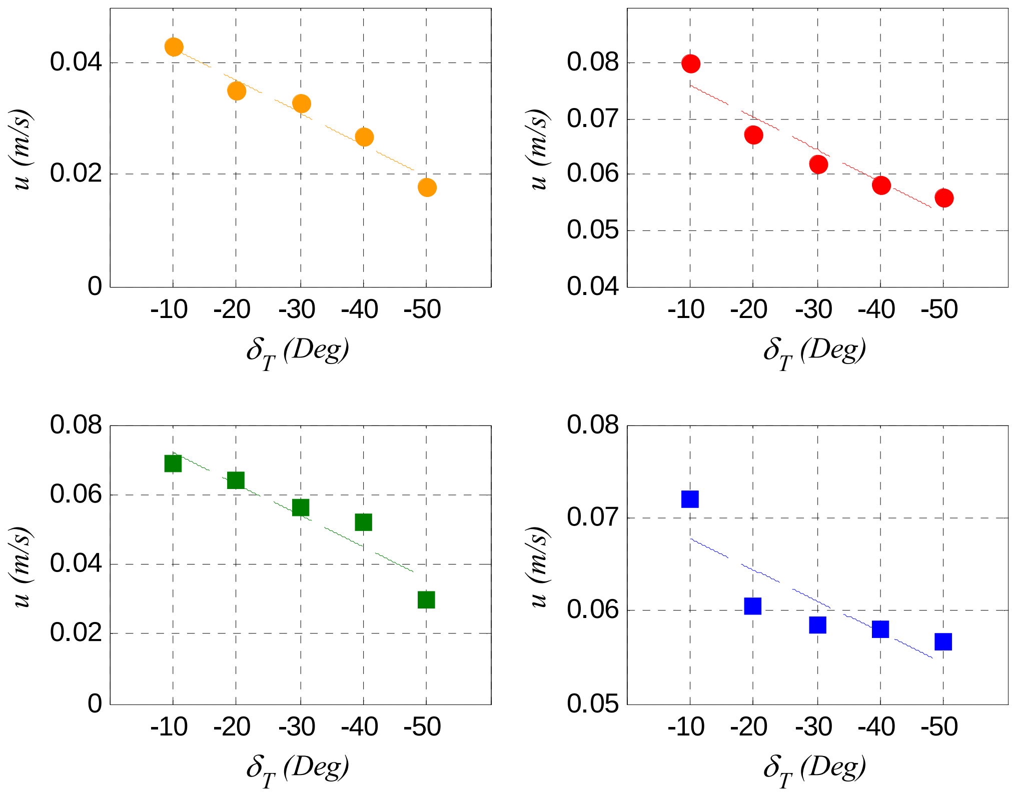

Figure 6.6: Experimental values of surge velocity vs tail deflection angle with tail beat amplitude and frequency of (a) 0.10 m, 0.5 Hz (b) 0.10 m. 1.0 Hz (c) 0.15 m, 0.5 Hz (d) 0.15 m, 1.0 Hz

Figure 6.7(a) shows the average roll rates measured during the experiments and it can be seen that the average roll rate increases with tail deflection angle. This behaviour is to be expects since the fish will tend to bank or list to one side as it performs the constant turning manoeuvre. The average yaw rate of the vehicle for different tail deflection angle is presented in Figure 6.7(b). It can be observed that alterations in the centreline generate the turning moment of the vehicle which in turn changes its yaw rate. It is clearly illustrated that the yaw rate increases proportionally to the tail deflection angle.

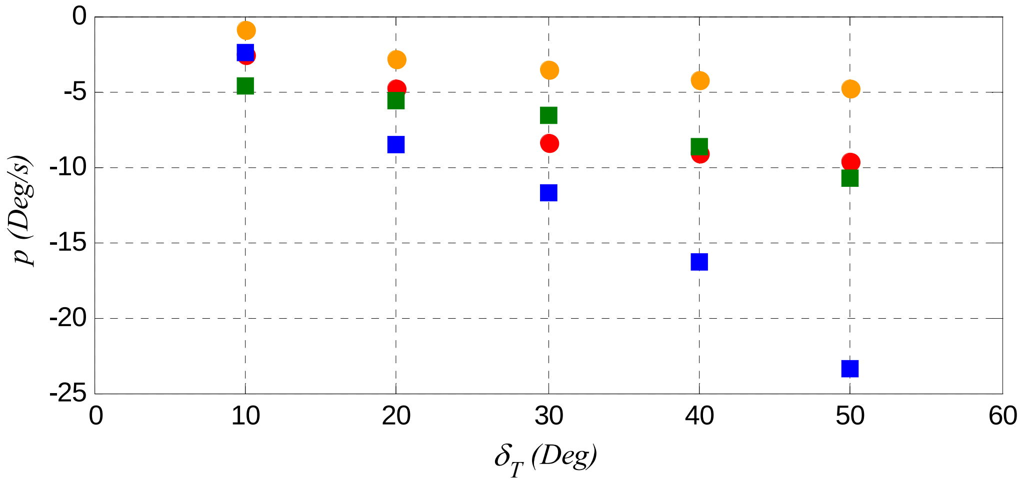

(a)

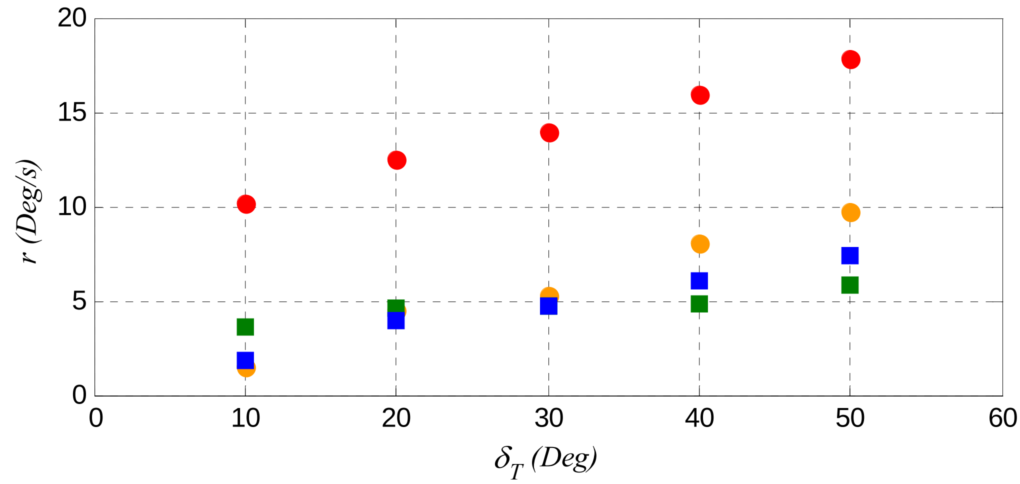

(b)

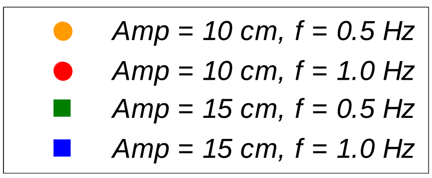

Figure 6.7: (a) Roll and (b) yaw rate for turning manoeuvre

It can be observed from these figures that the vehicle manoeuvrability is enhanced when the yaw rates is increased. These results show that the smallest turning radius is achieved when the vehicle operates at tail beat amplitude of 0.10 m, a tail beat frequency of 1 Hz and a tail deflection angle of -50°. On the other hand, the vehicle with configuration of larger tail beat amplitude tends to have high roll rate. The vehicle will experience greater moment under this configuration due to the position of caudal fin farthest from the body. As consequence, it disrupts the lateral movement which then cause inefficient thrust generation and reduce the turning motion.

Similar experiment configurations are implemented to investigate the vehicle turning behaviour when the tail deflection angle is sets on the opposite side of the body. However, due to the experiment time consuming, only one set of tail beat amplitude and frequency is chosen for this task. The tail beat amplitude and frequency of 0.10 m and 1 Hz but opposite direction of tail deflection angle are chosen based on the previous result.

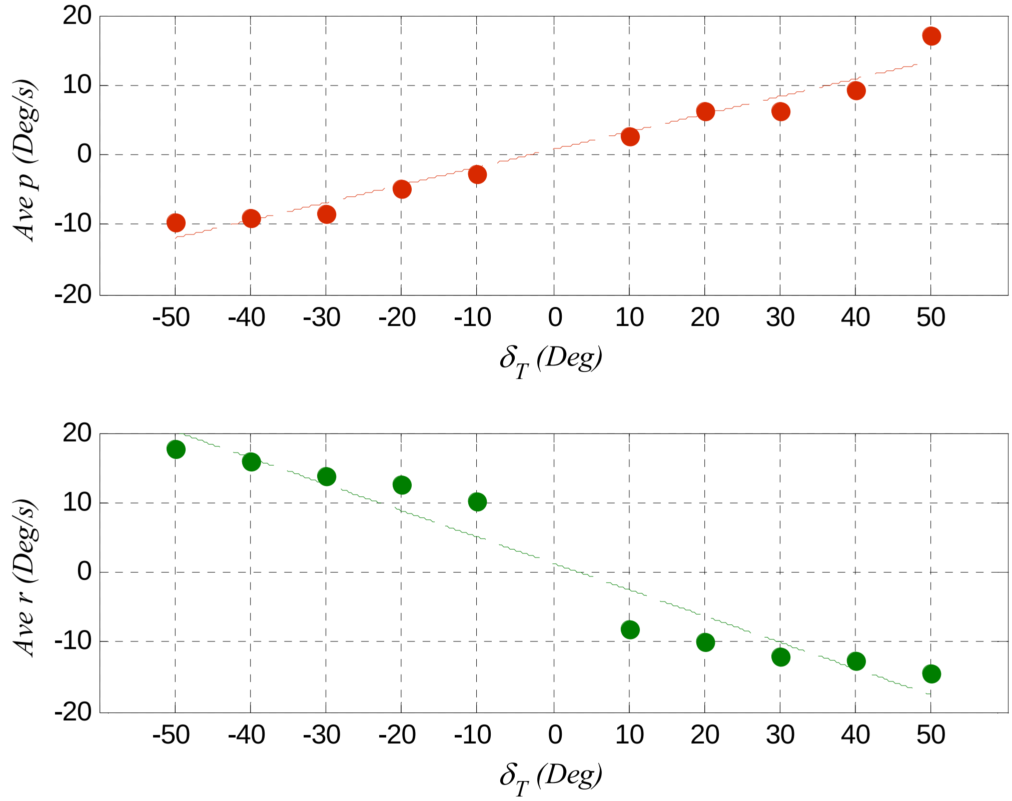

Figure 6.8: Average roll and yaw rates relate to tail deflection angle

The average roll and yaw rates obtained from 0.10 m tail beat amplitude and 1 Hz tail beat frequency with various tail deflection angles are displayed in Figure 6.8. It can be observed that average roll and yaw rates magnitude increases corresponding to the increases in the deflection angle. It also can be noticed that the vehicle is not correctly trimmed to produce zero total yaw moment at 0º tail deflection angle. This difference leads to an unequal vehicle path trajectory when operated at the same condition but opposite tail deflection angle.

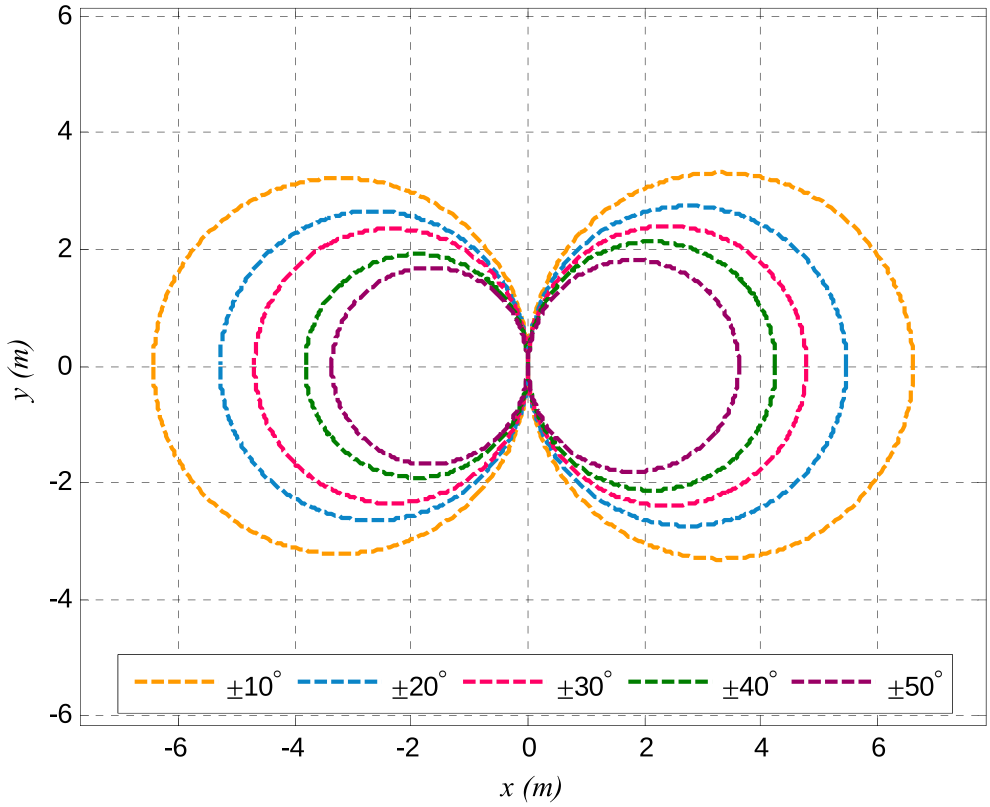

Figure 6.9: Experimental measured values of vehicle turning radius, R_T for both direction of tail deflection angle, δ_T

The vehicle turning radius for both direction of tail deflection angle is measured and presented in Figure 6.9. These results demonstrate that as the angular velocity increases with tail deflection angle, the vehicle turning radius decreases as expected. The results also highlight that the vehicle turning performance is not symmetrical which the right tail deflection angles tend to produce larger radii. This is caused by the difference yaw motion that has been highlighted in Figure 6.8. Furthermore, it also can be observed the large difference in path trajectory between 10º and 20º tail deflection angle. This might cause by the 10º tail deflection angle is too small for *RoboSalmon* to be responsive in addition to the incorrect trim. The overall asymmetrical trajectory can be contributed by several factors mainly on tail mechanism system that may lead to unequal lateral movement production during swimming. Another factor is relates to the components installation that may tip to vehicle slightly imbalance in roll and yaw plane.

Earlier it has been mentioned that the vehicle is not able to perform a complete circle manoeuvre even operate at 50º tail deflection angle due to the limited size of the pool. Thus, turning at higher tail deflection angle (>50º) is next been carried out. This can be considered as a more aggressive turning motion compared to the previous analysis of turning radius. For the biomimetic underwater vehicle considered, the turning circle test the tail deflection angle is used to initiate the turning motion in a similar way to the rudder.

Figure 6.10 shows the vehicle performing turning circle with configuration of 0.10 m tail beat amplitude, 1 Hz tail beat frequency and with 90º tail deflection angle. This tail beat configuration has been chosen because it has the optimal yaw rates that have been shown previously in Figure 6.7(b) and 90º is the maximum value allowed for tail deflection angle. The image below shows the vehicle motion in performing turning circle and it is clearly seen that the tail bending to the right corresponding to the altered tail centreline.

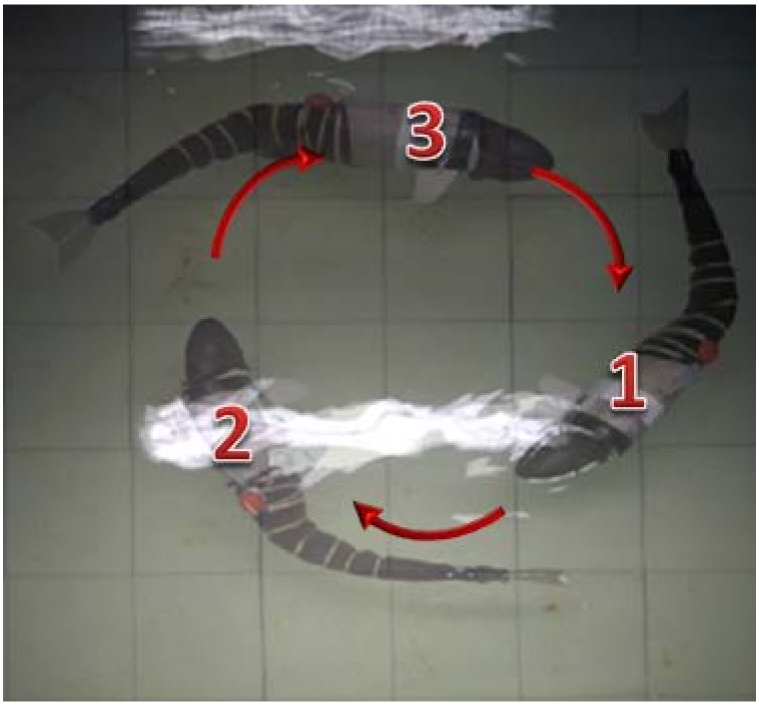

Figure 6.10: Turning circle for a 90º tail deflection angle where (1) start, (2) middle and (3) final position.

Image processing is used to extract the data from the overhead camera images in order to plot the vehicle path trajectory as shown in Figure 6.11. From this trajectory data the vehicle's manoeuvring characteristics can be obtained (see Table 6.1). This data illustrates that at low speed the approximate vehicle turning radius of 0.58 m is achieved which is just over half of its body length. A conventional underwater vehicle has an average turn radius of 3 -15 times of the body length (Beem & Triantafyllou, 2012). Thus, this proves that vehicles with fish like propulsion systems tend to exhibit better manoeuvring capability than conventional underwater vehicles (Watts, 2009).

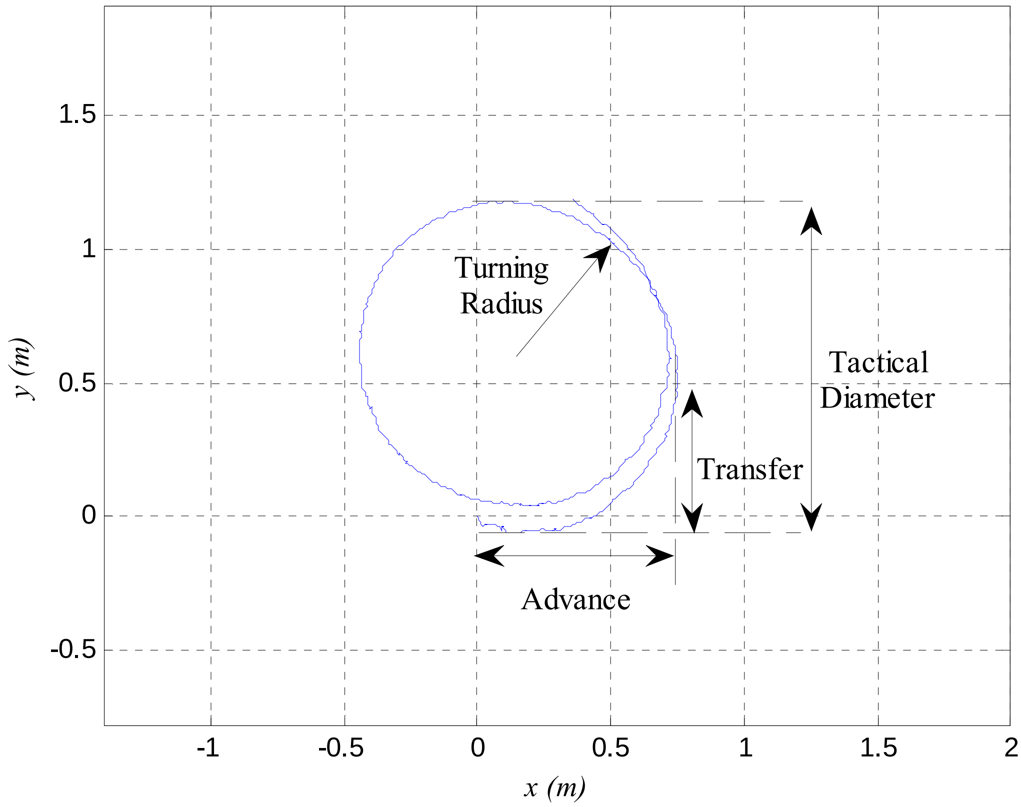

Figure 6.11: Turning circle parameters for the vehicle with tail deflection angle of 90° (experiment)

Table 6.1: Turning circle characteristic

Steady turning radius:	0.58 m
Transfer at 90 degrees heading:	0.42 m
Advance at 90 degrees heading:	0.74 m
Tactical diameter at 180 degrees heading:	1.22 m

The resultant vehicle speed, U, in the horizontal plane is measured using Equation (6.3):

$$U = \sqrt{u^2 + v^2} \tag{6.3}$$

Here U is formed from the root of the sum of the squares of the surge velocity, u, and sway velocity, v. Figure 6.12 shows the turning rate and resultant horizontal velocity for the turn. These plots show that a steady turning rate and resultant velocity are obtained during turning circle manoeuvre. As expected, when the tail deflection angle is executed the yaw rate start to undulate on one side of the body and the vehicle reaches a steady resultant velocity after a short initial transient. The vehicle average turning rate is 3.84 deg/s and the maximum turning rate is recorded at 16 deg/s.

The vehicle has an average turning speed of 0.045 m/s which less than measured for forward swimming under same tail beat configuration i.e. 0.088 m/s. It is expected that the vehicle speed decreases when performing turning circle as similar relationship has been deduced for other tail deflection angle (see Figure 6.6). The vehicle speed is reduces almost half of its forward speed due to the tail centreline is been altered practically perpendicular to the vehicle body. Thus most of the thrust produce is used for turning motion.

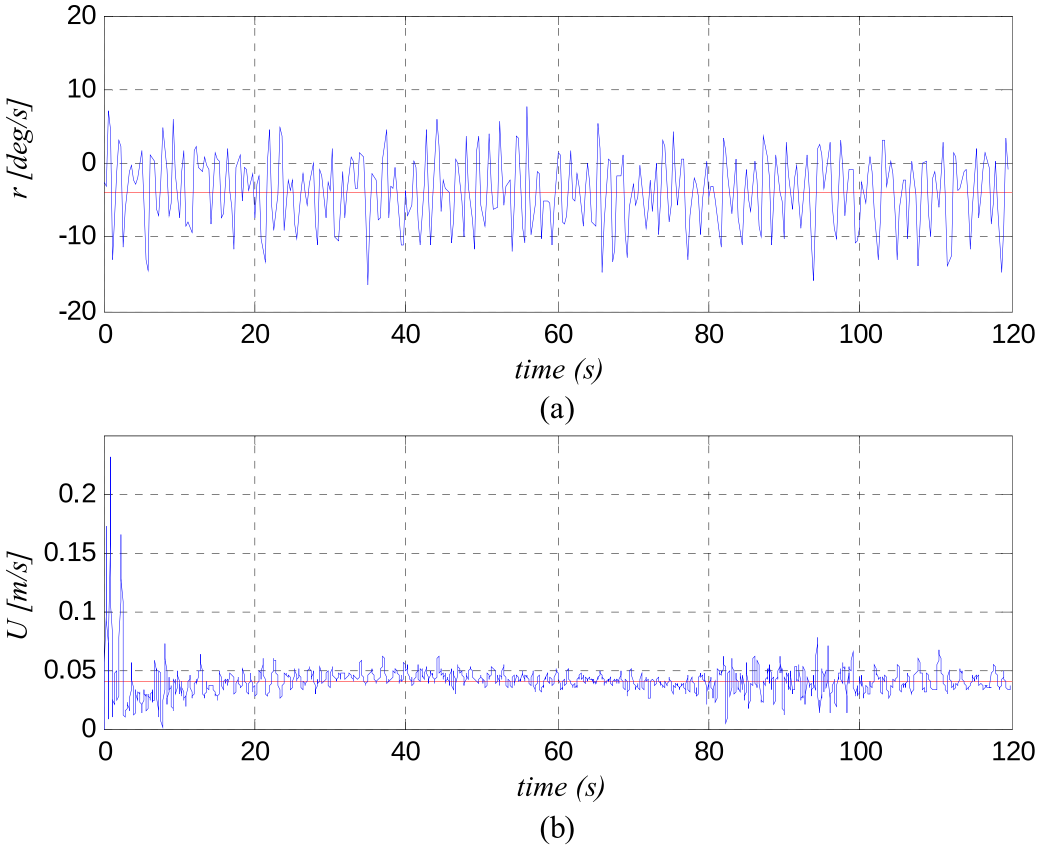

Figure 6.12: The tail deflection angle configuration of 90°. (a) Yaw rate (blue) and average yaw rate (red) (b) vehicle speed (blue) and average speed (red)

A similar tail condition has been applied to the simulation model shown in Figure 6.13 where the turning radius is measured at 0.622 m. In addition the vehicle has speed of 0.0635 m/s and average turning rate of 4.53 deg/s. These values is reasonably close to the experimental value which show further proved that the simulation model can provide a good estimation on the vehicle performance physically.

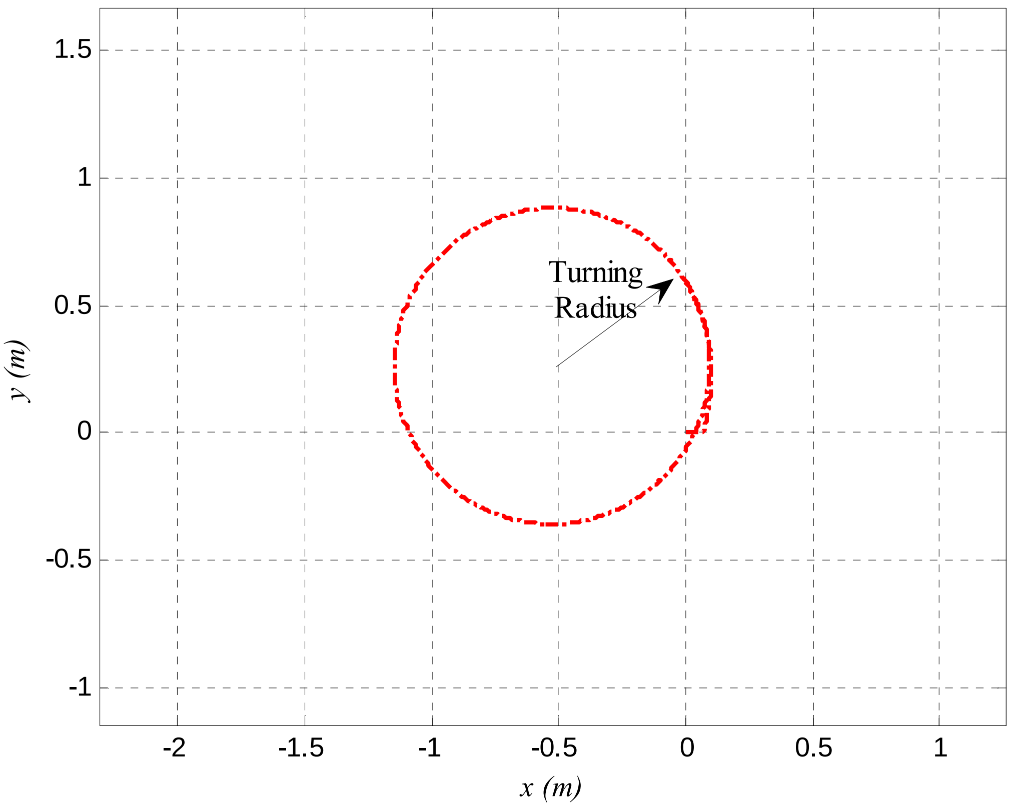

Figure 6.13: Simulation result of turning circle parameters for the vehicle with tail deflection angle of 90°

Thus, by having reasonable accurate simulation model, the vehicle turning circle manoeuvres for higher tail deflection angles (i.e. ±60˚, ±70˚, ±80˚ and ±90˚) can be measured. The simulated vehicle turning circle manoeuvres for all tail deflection angles are shown in Figure 6.14 where both turning direction will generate a symmetrical path trajectory. It can be clearly see the effect of increases in tail deflection will result smaller radius.

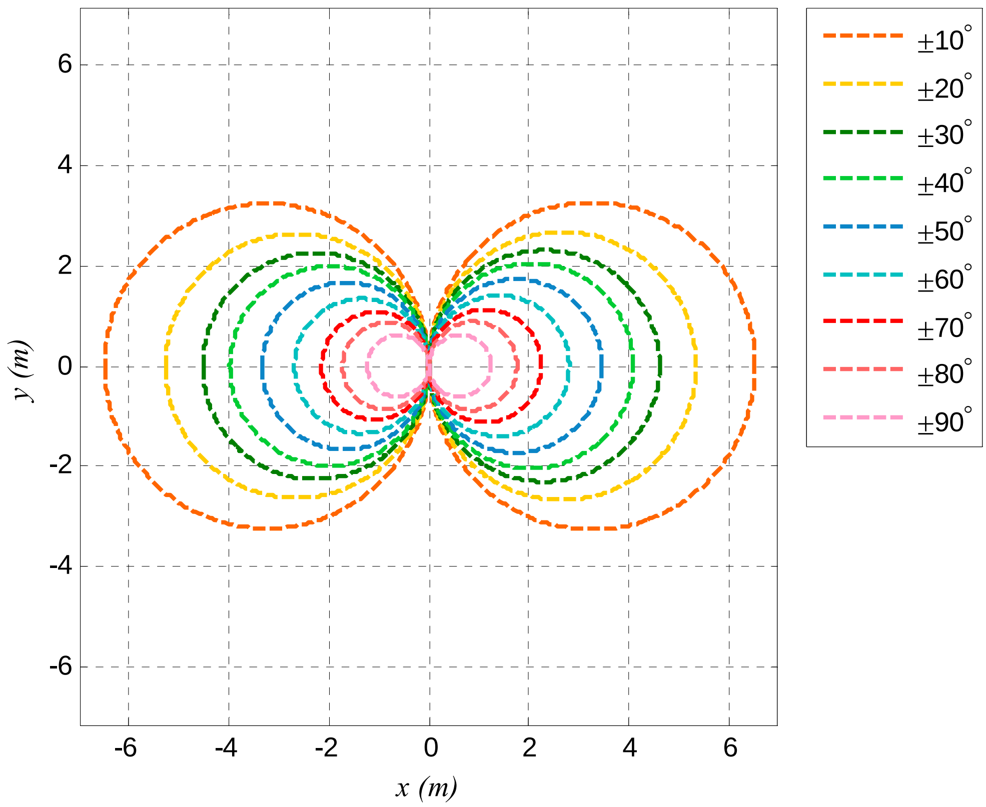

Figure 6.14: Simulated values of vehicle turning circle with ±10º, ±20º, ±30º, ±40º, ±50º, ±60º, ±70º, ±80º and ±90º tail deflection angles

6.4 Zig-zag Manoeuvre

The zig-zag manoeuvre is another standard marine vehicle manoeuvre test implemented on this vehicle (American Bureau of Shipping, 2006; Faltinsen, 2006; Fossen, 2011). The zig-zag manoeuvre can be defined as the change in heading as response to the amount of rudder applied. Generally, the zig-zag manoeuvre is carried out for 10º/10º or 20º/20º by turning the rudder alternatively by 10º or 20º to either side (Journée & Pinkster, 2002; Fossen, 2011). In this study, the zig-zag manoeuvre has been implemented on the simulation model but not been tested during experimentation due to hardware fragility (i.e. motor failure), limited space and time constraint. The tail deflection angle is set to be 20º from an initially straight course and the heading is maintained until the vehicle heading reached the desired heading in the opposite direction. Triantafyllou & Hover (2003) claims that several important characteristics of the yaw response can be examined using this type of manoeuvre. These characteristics include the response time, yaw overshoot and the time for one complete cycle.

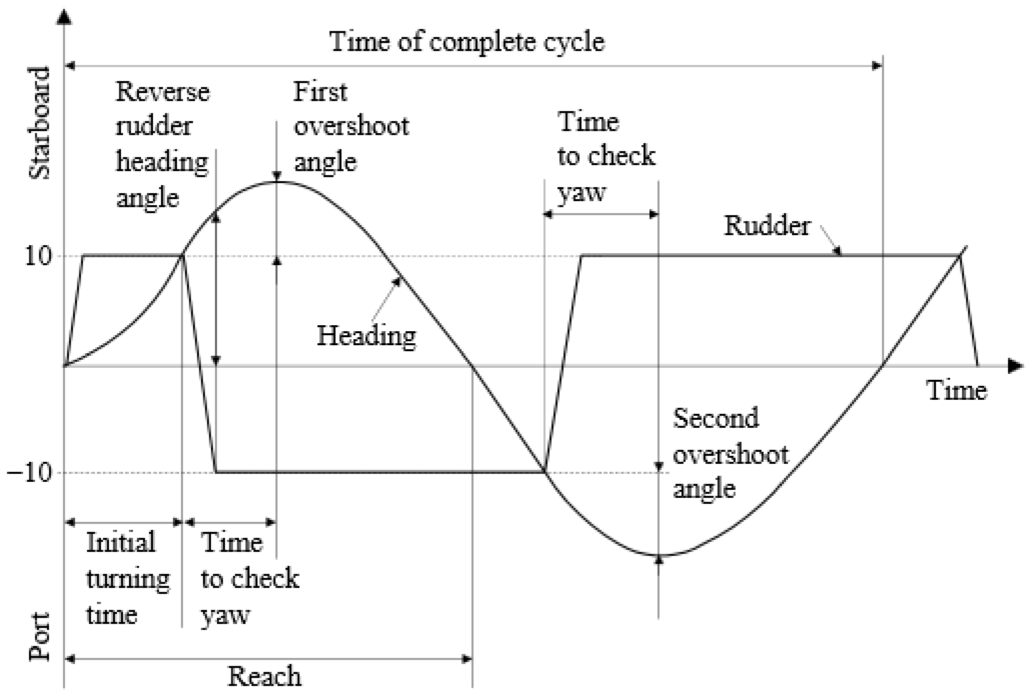

Figure 6.15: Characteristic of zig-zag manoeuvre (American Bureau of Shipping, 2006)

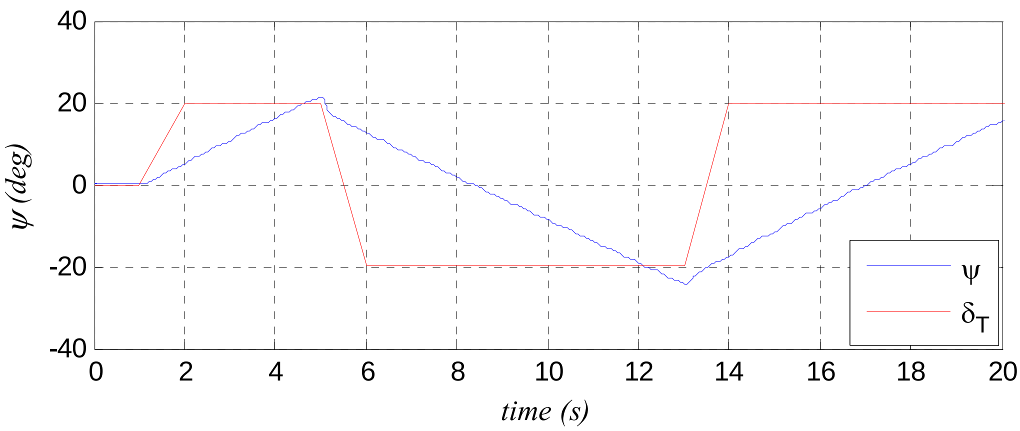

Figure 6.16: Simulated the vehicle performance in 20º/20º zig-zag manoeuvre. The vehicle heading is indicates by blue line and tail deflection angle is indicates by red line

Figure 6.16 illustrates the simulated trajectory of the vehicle for the ±20º zig-zag manoeuvre for tail beat amplitude and frequency of 0.10 m and 1 Hz respectively. The time for one complete cycle of zig-zag manoeuvre is measured at approximately 17 seconds. It also can be seen the small yaw overshoot angle as the vehicle heading angle exceeds ±20º while the tail centreline has turned another way. The first and second overshoot angle values are 1.44º and 4.32º. Moreover, the response time indicates the vehicle takes shorter time to change its heading from the time tail centre being execute. Thus based on these characteristic, it can be suggested that the vehicle exhibits high manoeuvrability.

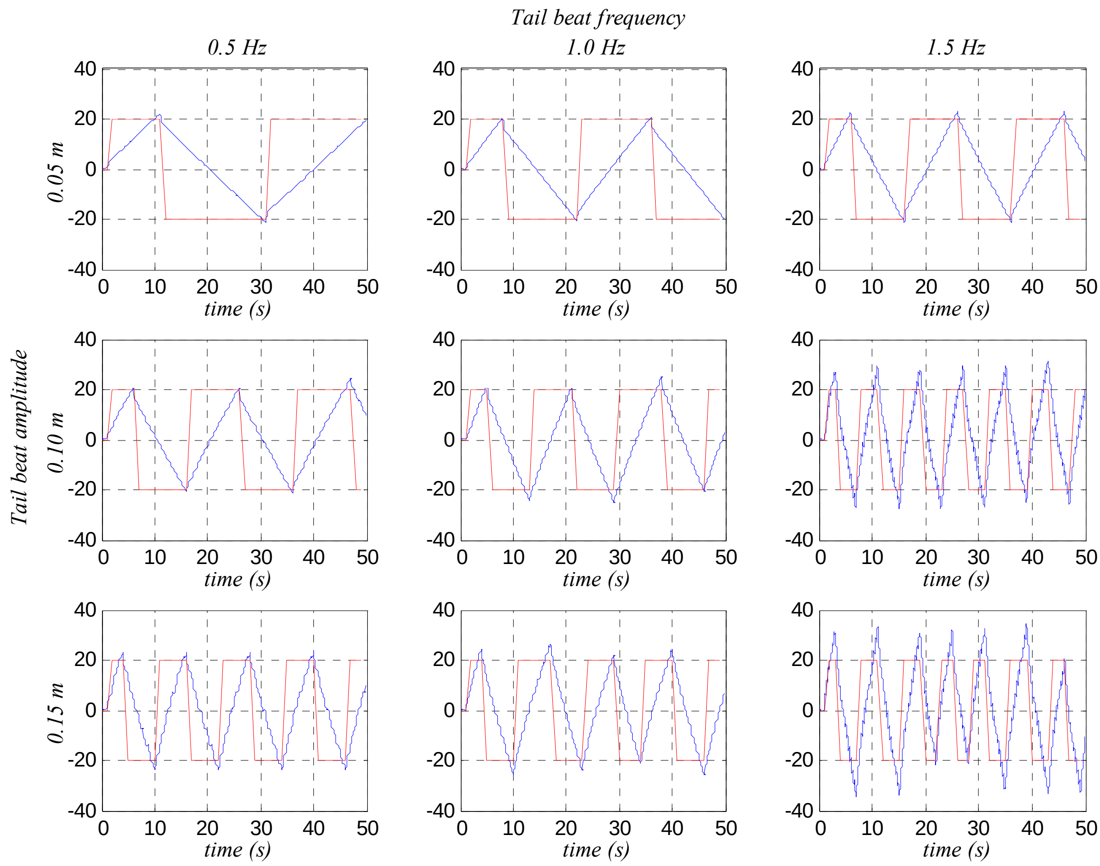

Figure 6.17: The vehicle zigzag manoeuvre for various tail beat configurations

Furthermore, the zig-zag manoeuvre has been tested for various tail configurations shown in Figure 6.17. It can be summarized that the vehicle with lower tail configuration takes longer time to perform this type of manoeuvre. As the tail beat amplitudes and frequencies are set to increase, the vehicle speed is increases result shorter time to complete one cycle manoeuvre. The vehicle demonstrated high manoeuvring capability when operated at higher tail beat amplitude and frequency. However, this quick changing heading ability tends to overshoot the desired heading. This suggests that high tail beat amplitude and frequency (e.g. 0.15 m and 1.5 Hz) not suitable to manoeuvre at tight space.

6.5 Power Consumption

The vehicle power consumption is next been investigated in determining the manoeuvring performance. Table 6.2 presents the average *Robosalmon* tail power consumption for tail beat configuration (Amp = 0.10 m, f = 1 Hz) for various tail deflection angles. It can be noticed there a slight change in the power consumed when the tail centreline has been altered. This suggests an increase value in power reflect to the increase in tail deflection angle. Moreover, the power values consumed by these deflection angles mirrored when operating at opposite direction.

Table 6.2: Experimental values of power consumption for various tail deflection angles for tail beat amplitude of 0.10 m and 1 Hz tail beat frequency

Tail beat		Tail deflection angle (deg)	Average Power consumption (W)
Amplitude (m)	Frequency (Hz)		
0.10	1	-50	5.42
0.10	1	-40	5.35
0.10	1	-30	5.10
0.10	1	-20	5.03
0.10	1	-10	4.89
0.10	1	0	4.76
0.10	1	10	4.78
0.10	1	20	4.87
0.10	1	30	5.06
0.10	1	40	5.30
0.10	1	50	5.44
0.10	1	90	5.75

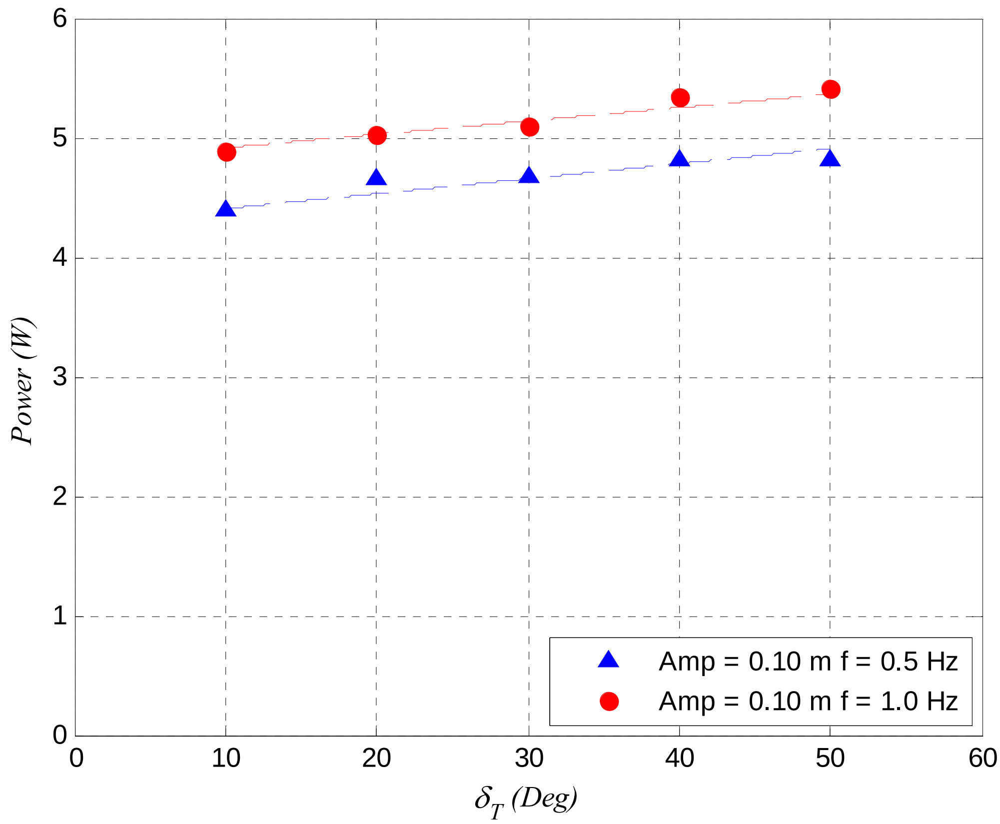

Figure 6.18: Comparison of vehicle power consumption for various tail deflection angles with 0.10 m tail beat amplitude and two tails beat frequencies (0.5 Hz and 1 Hz)

The next step is to compare the power consumed by the vehicle operated when at constant tail beat amplitude but changing tail beat frequency. There is significant difference in the vehicle power consumption can be seen in Figure 6.18 when two different tail beat frequency has been applied. This is reasonable as when operates at high tail beat frequency will draw lot more motor current which contribute to a higher power consumption.

6.6 Summary

This chapter discussed the experimental and simulation *RoboSalmon* manoeuvring results. The cruise in turning manoeuvring pattern has been analysed where the vehicle commanded to turn in circle and zig-zag manoeuvres. The vehicle heading can be can be modified by altering the centreline of the tail undulation for a period of time. It has been shown that the vehicle manoeuvring performances are influenced by three parameters which are tail beat frequency f, tail beat amplitude A, and tail deflection angle, δ_T. Firstly, the experiment is designed where the vehicle tail deflection angle is command to a predefined angle and holding it constant until circular path is obtained. Sets of tail beat configurations have been tested with different values of tail deflection angle. It can be observed that as the tail deflection angle is set to increase, it produces increase in roll and yaw angular velocities that result decrease in the vehicle turning radius. The vehicle turning radius is affected by the tail beat parameter (i.e. tail beat amplitude/frequency) where its turning radius is increases when applied larger tail beat amplitude while its value decreases when applied higher tail beat frequency. It also found that the vehicle surge velocity decreases during the turning manoeuvres since when the tail centreline being altered, some of the thrust propulsion is used to generate the turning motion and becomes sway velocity.

The *RoboSalmon* has been tested experimentally for the largest tail deflection angle that is 90^o with the tail beat amplitude and frequency set to be 0.10 m and 1 Hz respectively. The vehicle demonstrated better manoeuvring capability than the conventional underwater vehicles as it able to attain 0.58 m turning radius. This value is just over half of its body length whereas in general, conventional underwater vehicle tend to has an average turn radius of 3 -15 times of the body length. As expected, its average turning speed was measured at 0.045 m/s which less almost half than the measured value of 0.088 m/s for forward swimming under same tail beat configuration.

The vehicle manoeuvring performance also has been analysed using the computer simulation. The results obtained from the simulation model indicate that it is reasonably accurate to the experimental result. This proves useful where it can be used to estimate the vehicle performance for the tail deflection angle that not been tested experimentally. The vehicle has been simulate to perform turning motion in both direction where it demonstrate symmetrical path trajectory in addition to the effect of increases in tail deflection will produce a smaller turning radius.

Another manoeuvre that has been simulated for the *RoboSalmon* is the zig-zag manoeuvre. In this manoeuvre, the tail deflection angle is set to be 20º from an initially straight course and the heading is maintained until the vehicle heading reached the desired heading in the opposite direction. The result shows high manoeuvrability performance where the vehicle takes shorter time to change its heading from the time tail centre being execute. It also found that at lower tail beat configuration, the vehicle takes longer time to perform one complete cycle. As the vehicle speed increases when operated at larger or higher tail beat amplitudes and frequencies, it results a shorter time to complete the cycle. However, it can be seen that this quick changing heading ability have a tendency to overshoot the desired heading. Finally, the vehicle average power consumption during manoeuvring also has been investigated in this chapter where it was found that the increases in average power consumed by the vehicle is affected by the increase in tail deflection angle.

7

Autonomous Control & Guidance

7.1 Introduction

This chapter outlines the design of vehicle heading controller and guidance system. The heading controller is designed for the system to act as steering system in order to control the tail deflection angle. As been mentioned earlier, it is necessary to control the tail deflection angle in order to enable the vehicle to manoeuvre. A PID heading controller is designed for this purpose. This controller has been implemented and tested on both simulation and experimentation. Also, another type of controller has been design based on the sliding mode methodology is used. However, it is only being tested in simulation environment. Moreover, in order to navigate it is necessary to have a feedback sensor (e.g. compass) that can be used to provide the current vehicle heading. The performances of these controllers are compared and analysed. Finally, the guidance law implemented for the vehicle is been discussed. The autonomy of this vehicle is provided through a line of sight guidance system that is used navigate through a series of waypoints by providing the necessary reference yaw angle for the heading controller to make the vehicle follow.

7.2 Heading Controller

One of the objectives in this research is to design an autonomous underwater vehicle and it is obvious that one of the key requirements is to have a control system to regulate the swimming direction of the vehicle. It has been shown in the previous chapter that the vehicle heading can be controlled by altering the tail centreline. Thus, the process of controlling the vehicle's heading through manipulation of the tail centreline during the course changing manoeuvre is discussed in this section

A heading controller is designed with the intention to steer the vehicle towards a desired heading angle. Generally, this desired heading is compared with the vehicle heading, the difference between these two values is used by controller to compute the tail deflection angle required to compensate for the heading difference. The structure of the heading control system is given in Figure 7.1.

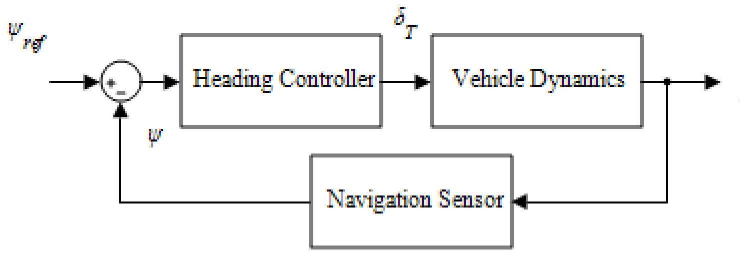

Figure 7.1: Vehicle heading control system

It is known that the dynamics and kinematics of underwater vehicle performing coupled manoeuvre is highly nonlinear (Fossen, 1994, 2011). In order to design the controller system, the vehicle 6 DOF equations of motion need to be linearized. This is because it is easier to be analysed than a nonlinear model. The linearized steering equation of motion can be expressed as in Equation (4.2) where it consists of two states; yaw rate and heading angle.

$$\begin{aligned} \dot{r} &= \frac{N_t + N_d}{I_z - N_{\dot{r}}} \\ \dot{\psi} &= r \end{aligned} \tag{7.1}$$

Subscripts t and d stand for thrust and drag terms. Also, it has been aware the vehicle heading can be controlled by altering the tail deflection angle, $\delta_{T.}$ Thus, δ_T that's belong to the thrust equation (see Equation (7.2)) is treats as an input to the controller.

$$N_t = \left(T \sin\left(\delta_T\right)\right)\left(l_c\right) \tag{7.2}$$

Where T is thrust and l_c is the *RoboSalmon* centre of gravity.

7.3 Reference Heading Model

Before moving to design the heading controller system, it is convenient to discuss a method to generate smooth reference trajectory. In this study, it will referred as the reference heading model and the difference between desired heading and actual heading is referred as tracking error. The tracking error is considered an importance element as large tracking errors caused by a rapid change during course changing manoeuvre could contribute to the actuator saturation. This can be avoided by using the dynamic of desired heading instead of a constant reference heading (Fossen, 1994). According to Fossen (2011), a linear reference model has been implemented in most cases e.g. industrial systems due to avoid complex programming. Moreover, he stated that marine craft commonly used a dynamic of mass damper spring system which is a second order system to generate the smooth trajectory. Therefore, a second order differential reference model in Equation (7.3) is introduced in this study to smooth out the commanded input given to control system in the simulation.

$$\ddot{\psi}_d + 2\zeta\omega_n\dot{\psi}_d + \omega_n^2\psi_d = \omega_n^2\psi_c \tag{7.3}$$

Here ζ is desired damping ratio, ω_n is desired natural frequency and ψ_c is the commanded heading reference angle. The ζ and ω_n values are selected to be 1 and 6.3 rad/s. This produce a critically damped desired heading response with sufficient rise time that agreed to the *RoboSalmon* average turning rate (i.e. 4.53 deg/s) measured during experimentation. The reference model for 90º heading angle is shown in Figure 7.2 and it shows that the reference model response is satisfactory to be used by the heading controller to track a large desired heading. Moreover, the results produced by this model will be a good indication on the vehicle dynamic performance in the actual environment.

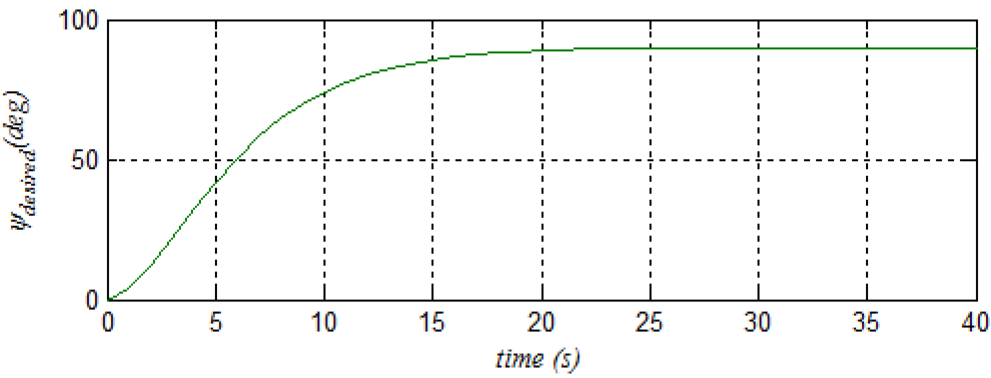

Figure 7.2: Heading reference model for 90º

Figure 7.3 shows the comparison of vehicle response when the vehicle is commanded to steer to 60º heading angle with or without heading reference model conditions. It can be clearly observed the difference between these two conditions as without reference model produce an undesirable response (i.e. sharp rise in tail deflection angle). This is caused by the large tracking error which then results higher demand in tail deflection angle to steer the vehicle towards the desired heading. On the other hand, a smooth vehicle response can be seen when applied with reference model. The tail deflection angle is gradually increases due to the low heading tracking error and the maximum amplitude required by the vehicle to steer is much lower compared to the without reference model condition. Thus, it is useful to use the reference model in order to obtain a smooth trajectory while avoiding actuator saturation.

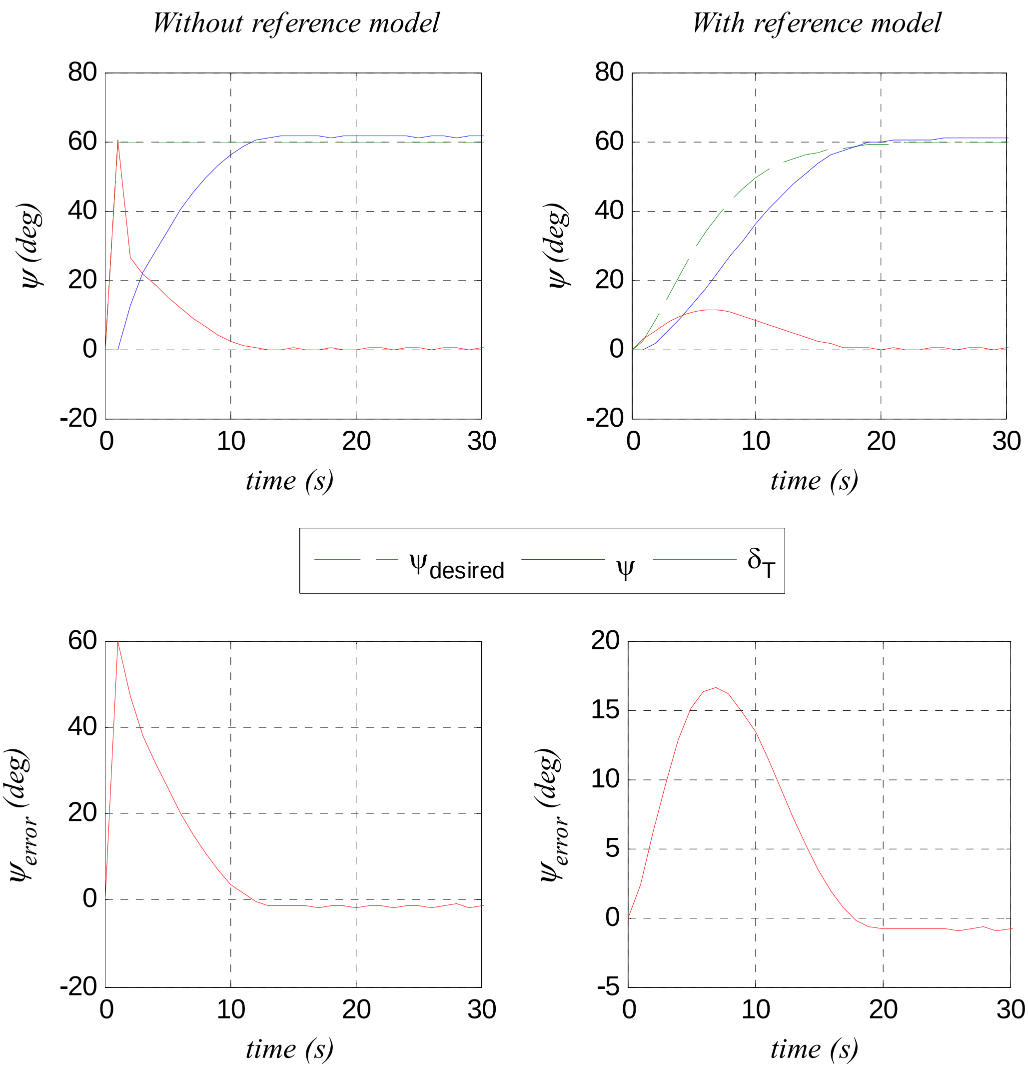

Figure 7.3: Comparison of vehicle control performance when applied with or without filtered command

7.4 PID Heading Controller

A PID methodology is employed in the design of the heading controller. This type of controller has been widely used because it is simple and easy to implement (Killingsworth & Krstic, 2006; Loueipour & Hadian, 2011). Generally, this method consists of three terms which are K_p, K_i and K_d that referred to the gain of the proportional integral and derivative term respectively. These gain values are selected based on the desired response of the system. According to Åström (2002), the process involves in obtaining these values is known as tuning method. A number of methods has been developed for tuning the gains with Ziegler-Nichols being one of the common methods applied (Åström, 2002). However, in this study the PID gains are obtained manually using a trial and error approach where it is the simplest method but also a time-consuming task (Killingsworth & Krstic, 2006). This is an active procedure where the system response depends on the values of K_p, K_i and K_d. Thus, certain guidelines need to be followed when tuning the gains to acquire the desired response for a specific system. The guidelines are summarize by Martono (2006) as follows. Firstly, the K_p, K_i and K_d gains are set to zero then K_p gain is set to increase until the output oscillates. Next, the K_d gain is increases to yield a critically damped response within an appropriate settling time and the steady state error is measures. K_i gain is introduced to eliminate the steady state error and finally fine tune the system to maintain critically damped response. The gain values obtained for proportional, integral and derivative are 0.018, 0.0001 and 0.00001 respectively with the settling time for the system is less than 25 seconds.

7.5 Integrator Windup

The windup phenomenon is caused by the involvement of integral action and actuator saturations (Edwards & Postlethwaite, 1999; Åström, 2002). Bohn & Atherton (1995) mentioned that the integrator windup where it happens when the control signal reaches the actuator limits. If the controller continues to integrate, the integrator value becomes very large without having any effect on the system. Eliminating this integrator error may take a long time. Thus, it results an undesirable performance in the form of large overshoot and high settling time (Bohn & Atherton, 1995; Edwards & Postlethwaite, 1999). There are many different strategies that help to protect against windup. This study considers a back calculation anti-windup scheme that has extra feedback around the integrator as shown in Figure 7.4. The feedback signal e_s is the difference between the saturated and unsaturated control signal when the controller output exceed the actuator limits. Therefore, it has value of zero when there is no saturation occurred. The signal e_s is fed to the input of the integrator through gain $1/T_t$.

Figure image has been removed due to Copyright restrictions

$$K_p = K, \quad K_i = \frac{K}{T_i}, \quad K_d = KT_d$$

Figure 7.4: Back Calculation anti-windup PID controller (Modified from Åström, 2002)

7.5.1 PID heading controller performance

As been mentioned earlier, the PID heading controller performance has been analysed in both simulation and the experimentation environment. The heading experimentation has utilized the same experiment setup used for forward and manoeuvre test. The difference can be seen as this heading tracking is a closed loop system meanwhile the previous experimentations (i.e. forward and manoeuvre) are an open loop system. For simulation test, the feedback operation is measures using the ψ value based on Earth fixed reference frame.

7.5.1.1 PID Experimentation Results

The PID controller has been implemented in the *RoboSalmon* vehicle for the experimentation heading test. The feedback vehicle heading measurement is provided by the magnetic compass (i.e. HMC5883L 3-axis digital compass). It capable to provide 1 to 2 degree compass heading accuracy that is sufficient for this heading test. It is also well aware that the compass needs to position on a flat surface to obtain the correct reading. Since the vehicle is affected by the recoil motions it is expected to create a problem for vehicle heading calculation. However, the error in compass reading can be corrected by measuring the compass tilt angle in which the data is provided by the accelerometer. This calibration method is used to improve the heading accuracy by reducing the compass reading error when the vehicle rolls and pitches.

The vehicle propulsion velocity can be varied by controlling the tail beat amplitude and frequency in a similar way to changing the tail deflection angle turns the vehicle toward the desired direction. However in order to avoid complexity, a constant tail beat amplitude and frequency configuration is been applied to the vehicle for this task and no specific automatic control mechanism it utilised. The desired vehicle heading is set as constant values (e.g. -30º, 30º and -60º) and have been tested with one set of tail beat amplitude and frequency configuration of 0.10 m and 1 Hz respectively. The aim of this experiment is to analyse the vehicle steering system performance where it need to guide the vehicle so that it moves within the acceptable range of desired heading.

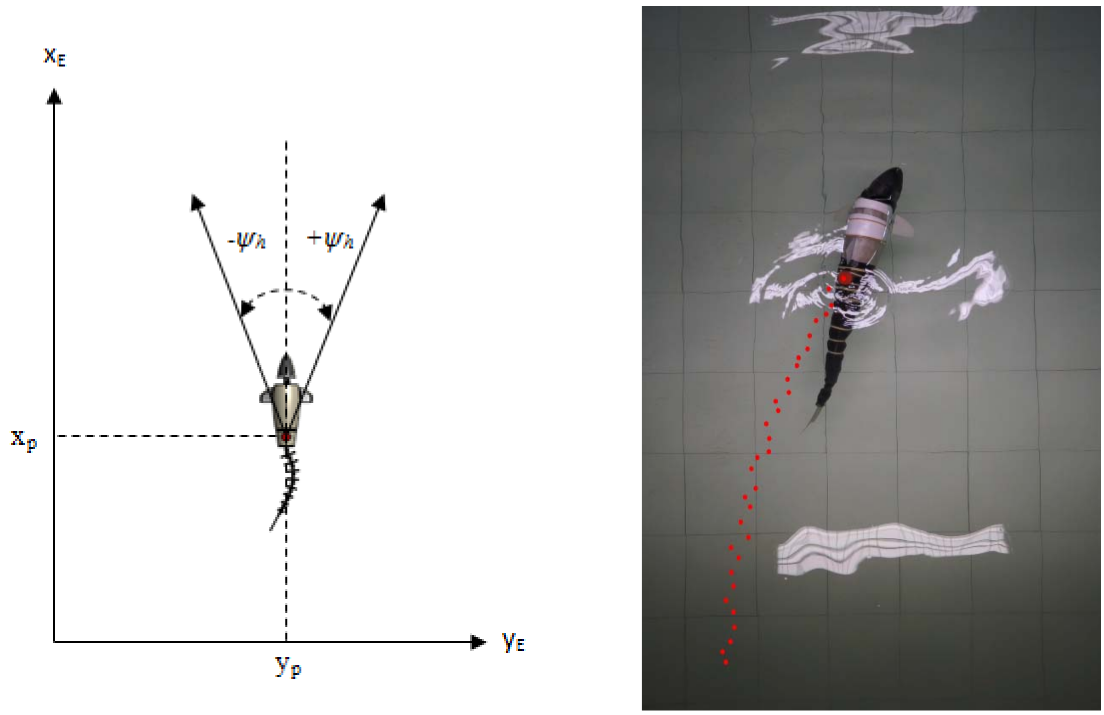

(a) (b)

Figure 7.5: The vehicle (a) heading with respect to earth reference frame (b) path trajectory for 30° heading indicated by the red dots

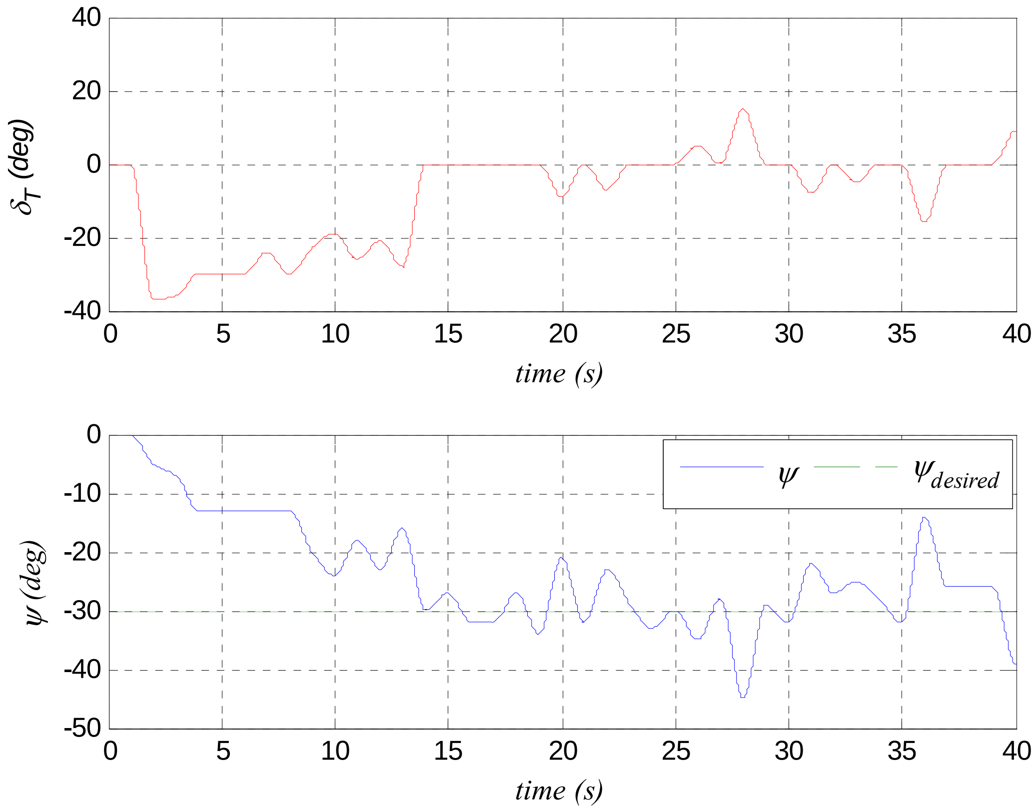

Figure 7.6: The Vehicle performance in terms of heading and tail deflection angle with desired heading of -30º (Experiment)

It can be seen in Figure 7.6 that the vehicle heading is changing results from the alteration of tail deflection angle. Once the vehicle obtained the desired angle, the tail centreline reverts back to the initial position. In the event of disturbance, the desired heading is maintained by altering the tail centreline left and right accordingly. Figure 7.7 shows the vehicle performance when the opposite direction of the desired heading angle is demanded. The vehicle is commanded to acquire 30º heading angle and it can be observed similar shape but the vehicle able to achieve the desired heading quicker with almost half of the maximum tail deflection angle required for -30º heading angle. This is expected as it already been observed previously the asymmetric tuning manoeuvre.

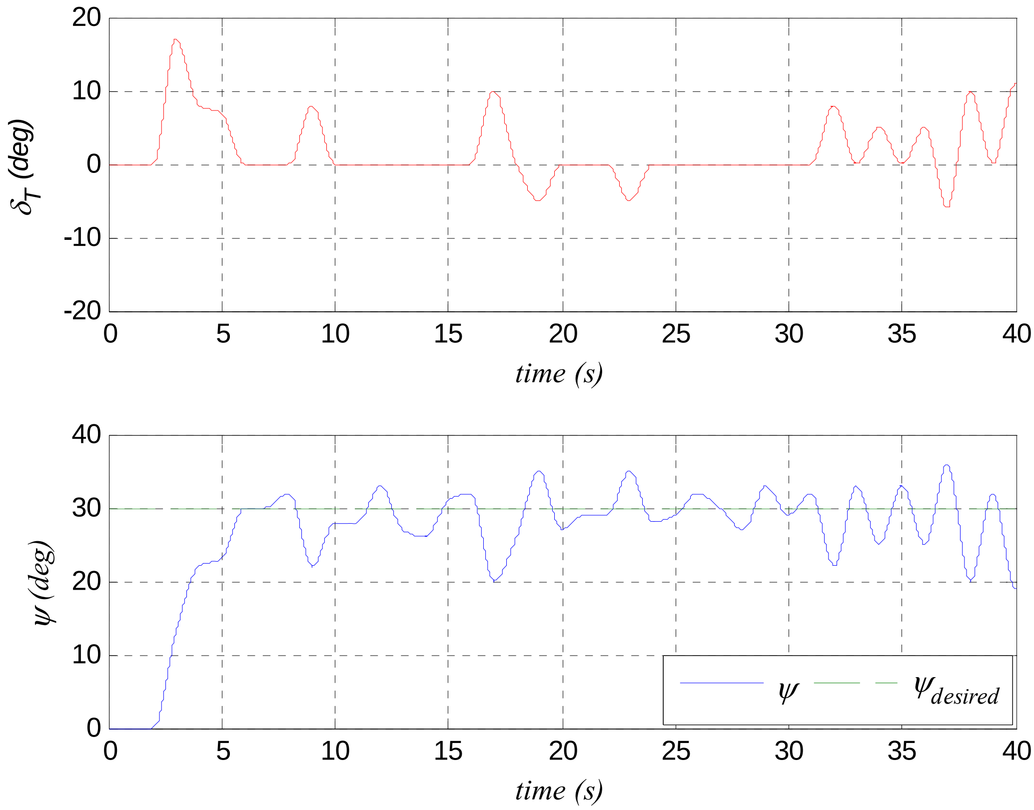

Figure 7.7: The Vehicle performance in terms of heading and tail deflection angle with desired heading of 30º (Experiment)

Furthermore, the heading error both direction heading are plotted in Figure 7.8, it can be seen that the error converge to zero for the heading tracking. It also can be seen the oscillation where the vehicle tried to maintain the desired heading angle. When the heading errors is small (i.e. <= 2º), the tail centreline is set to maintain the previous deflection angle. This is due to the compass error reading and to avoid unnecessary movement that may lead to vehicle instability.

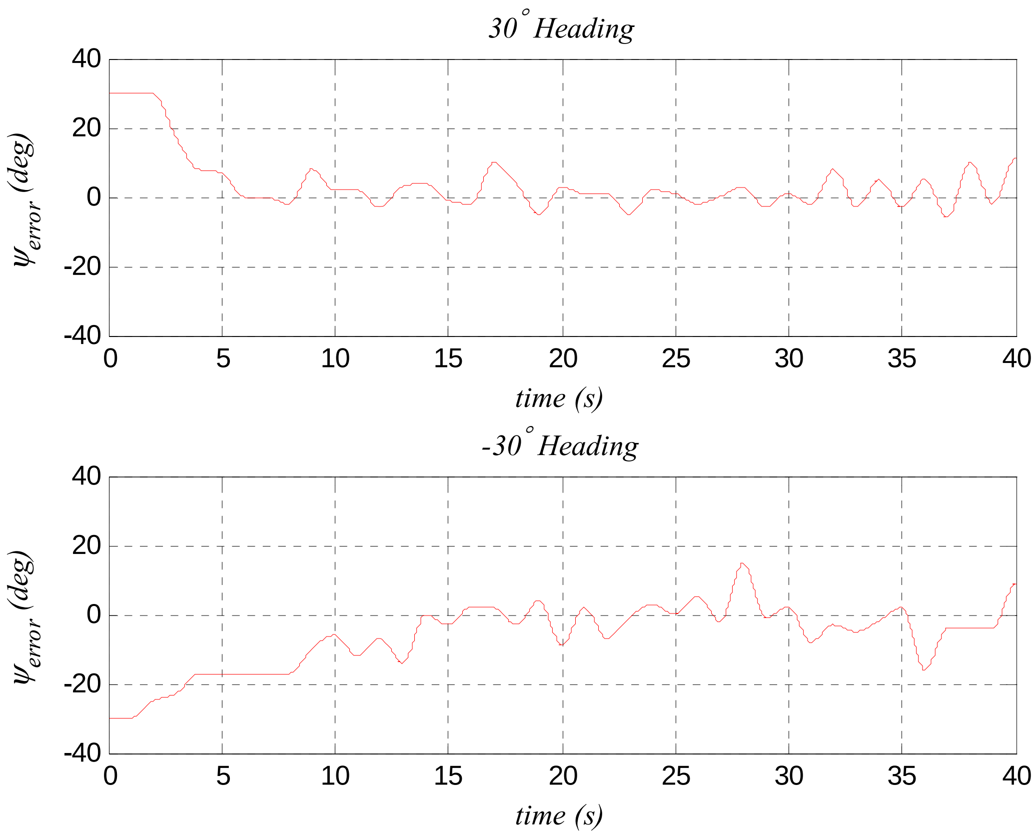

Figure 7.8: Heading errors for 30º and -30º heading angles

Also, the heading test for a higher heading angle is been tested and its performance is shown in Figure 7.9 and Figure 7.10. The vehicle able to achieved the commanded desired heading. It has been illustrated that large tail deflection angle (sharp rise) is executed at beginning and once the vehicle heading within the range of desired heading angle, much smaller tail deflection angle is been used. It gradually approaches the desired heading angle and once obtained or within acceptable range (<=2º), the tail centreline is set to zero. Therefore, the result of the proposed PID controller shows satisfactory performance in the heading tracking. The tail deflection angle is approaching zero as the vehicle moves closer to the target (desired heading). Moreover, it can be observe the steady state cannot be completely be eliminated thus it is necessary to set up an acceptable range of heading error to avoid continuous tail changing for negligible small heading angle. Finally, even though the vehicle demonstrated good performance in heading tracking that may useful for autonomous navigation, further tuning process need to be carried out so that the heading steering system performance can be improved so that the error quickly converge to zero.

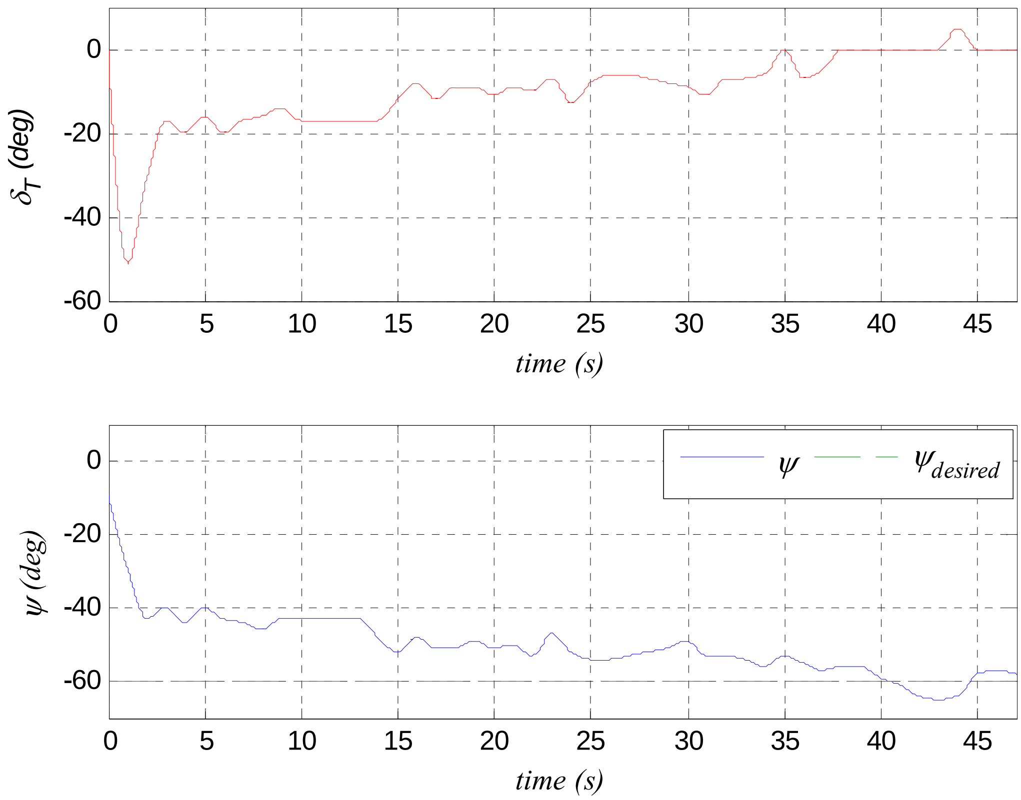

Figure 7.9: The Vehicle performance in terms of heading and tail deflection angle with desired heading of -60º (Experiment)

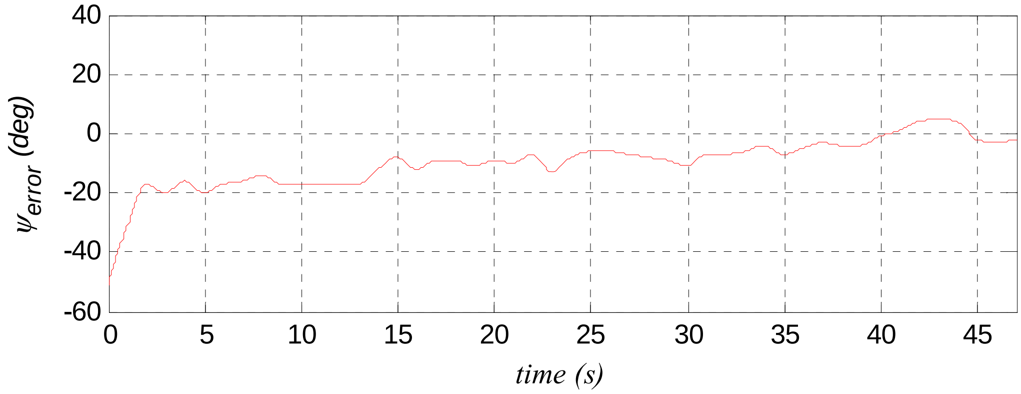

Figure 7.10: Heading errors for -60º heading angles

7.5.1.2 PID Simulation Results

The PID heading control system performance is illustrated in Figure 7.11 where the vehicle is commanded to execute several heading course change. The vehicle is required to steer into 60º, 0º, -60º and 0º heading. It can be seen the satisfactory of vehicle heading controller performance where it able to track heading throughout the course changing. It can be noticed that the low values in tail deflection angle affected by the by the low heading tracking error. The tracking errors converge to zero and the tail centreline revert to its initial position for straight swimming as the desired heading is attained. Moreover, it also demonstrated the symmetrical in controlled manoeuvre when the vehicle is directing from 60º to 0º and -60º to 0º.

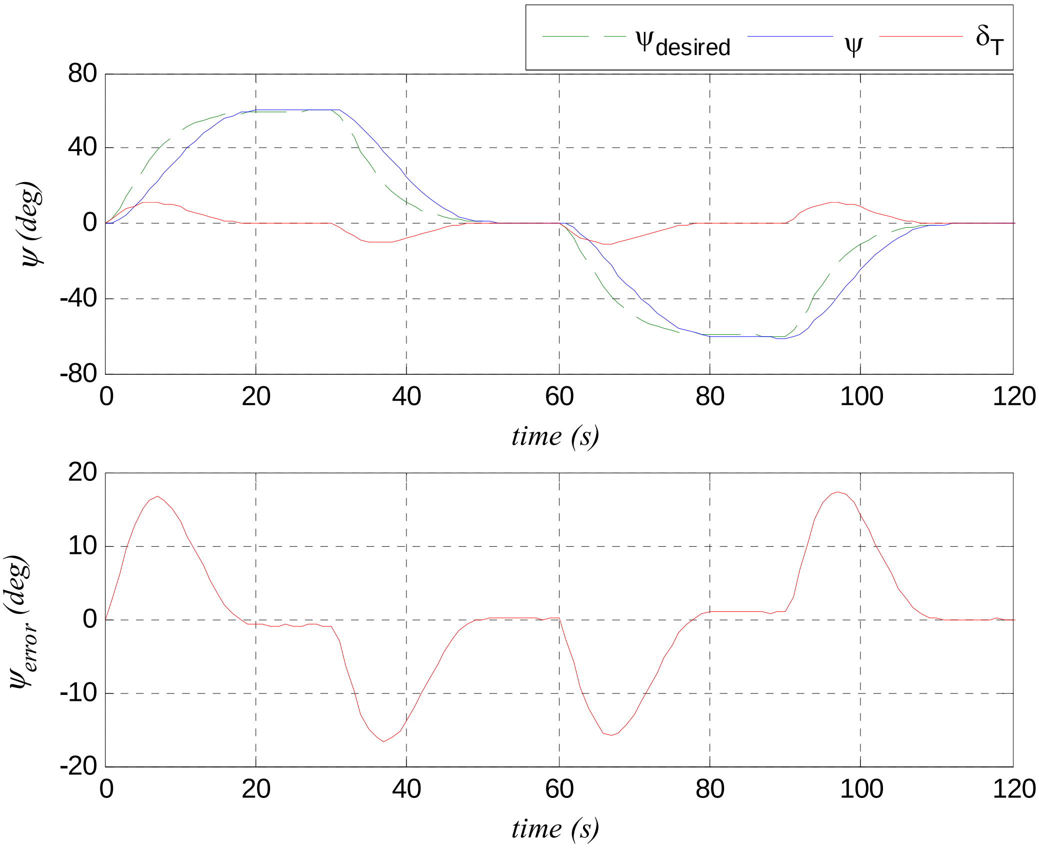

Figure 7.11: Vehicle heading motion based on change in tail centreline for PID controller. The vehicle is commanded to 60º, 0º and 60º headings

Comparing the results of PID heading control performance for -60º heading angle between experiment and simulation, it can be clearly seen the difference in the requirement of the tail centreline need to achieved the desired heading. This is because the second order reference model has been implemented in the simulation environment meanwhile in the actual environment, it acts as a linear reference model which result a large tracking error. As consequence, a sharp rise instead of gradually increases in tail deflection angle is demanded by the system.

7.6 Sliding Mode Heading Controller

The sliding mode (McGookin, et al., 2000b; Fossen, 2011) is designed as an alternative heading control system for the *RoboSalmon*. According to Utkin (2008) and Fossen (2011), the sliding mode can be considered as a robust nonlinear technique that is suitable for a model that is operating under uncertainty conditions. It is found that the sliding mode technique does not required the exact modelling (i.e. complex) since it is insensitive to the unmodelled dynamics and external disturbance (McGookin, et al., 2000b; Utkin, 2008). Healey & Lienard (1993) and McGookin, et al. (2000a) studies highlighted the advantages of this technique to marine craft applications.

In this study, the controller purpose is to control the vehicle heading by providing the required tail deflection angle, δ_T to the *RoboSalmon* model. Generally, the controller is designed to make the state of the system follow some desired state response where the difference (i.e. state error) can be quantified using Equation (7.4)

$$\Delta \boldsymbol{x} = \boldsymbol{x} - \boldsymbol{x_d} \tag{7.4}$$

A single input, multistate (SIMS) (Healey & Lienard, 1993) system is designed for this controller. The proposed sliding mode controller is realized by the decoupled three states which are sway linear velocity, yaw angular velocity and yaw angular position from equation of motion into the following single input state space equation.

$$\dot{x}_h = A_h x_h + b_h \delta_T \tag{7.5}$$

Where x_h is the state vector A_h, is the corresponding system matrix, b_h is the input matrix and δ_T is the tail deflection angle. This linearization of the vehicle equation is obtained through small reference input. The δ_T is the control signal that will be provide to model where in sliding mode control, the δ_T will consists of two components which are the nominal equivalent control, δ_{T_eq} and the switching term δ_{T_sw}.

$$\delta_T = \delta_{T\_eq} + \delta_{T\_sw} \tag{7.6}$$

These two component serve for the different purpose where the equivalent control used to kept system states on the sliding mode meanwhile the switching control is used to drive the system state reaching the sliding surface (Liu & Wang, 2011). The equivalent control (i.e. linear controller) is designed about an equilibrium point for the system where it is chosen as a state feedback gain controller (Healey & Lienard, 1993; McGookin, 1997; Fossen,

2011) as shown in Equation (7.7) with *k* is the feedback gain obtained from pole placement theory.

$$\delta_{T\_eq} = -k_h^T x_h \tag{7.7}$$

It is found that there is limitation on the effective operating condition of the controller, outcome from the designed around a nominal linear plant (McGookin, et al., 2000b; McGookin, et al., 2000a). Thus, a nonlinear switching term derived from a state hyperplane (i.e. sliding surface, σ_h) has been introduced to compensate for variation in the vehicle operating condition (McGookin, 1997). The sliding surface equation can be expressed as follow:

$$\sigma_h\left(\Delta x_h\right) = h_h^T\left(x_h - x_{hd}\right) \tag{7.8}$$

Differentiating with time

$$\dot{\sigma}_h\left(\Delta x_h\right) = h_h^T\left(\dot{x}_h - \dot{x}_{hd}\right) \tag{7.9}$$

Substituting Equations (7.5) ,(7.6) and (7.7) into Equation (7.9)

$$\begin{aligned}
\dot{\sigma}_h\left(\Delta x_h\right) &= h_h^T\left(A_h x_h + b_h\left(\delta_{T_eq} + \delta_{T_sw}\right) - \dot{x}_{hd}\right) \\
&= h_h^T\left(A_h x_h + b_h\left(-k_h^T x_h\right) + b_h \delta_{T_sw} - \dot{x}_{hd}\right) \\
&= h_h^T\left(A_h x_h - b_h k_h^T x_h + b_h \delta_{T_sw} - \dot{x}_{hd}\right) \\
&= h_h^T\left(\left(A_h - b_h k_h^T\right) x_h + b_h \delta_{T_sw} - \dot{x}_{hd}\right) \\
&= h_h^T\left(\left(A_{ch}\right) x_h + b_h \delta_{T_sw} - \dot{x}_{hd}\right)
\end{aligned} \tag{7.10}$$

It is simplified with a closed loop system matrix created by feedback gain, A_{ch}.

$$A_{ch} = A_h - b_h k_h^T \tag{7.11}$$

Rearranging Equation (7.10) with $h_h^T A_{ch} = 0$

$$
\begin{aligned}
\dot{\sigma}_h(\Delta x_h) &= h_h^T\left((A_{ch})x_h + b_h\delta_{T\_sw} - \dot{x}_{hd}\right)\\
\dot{\sigma}_h(\Delta x_h) &= h_h^T A_{ch}x_h + h_h^T b_h\delta_{T\_sw} - h_h^T\dot{x}_{hd}\\
h_h^T b_h\delta_{T\_sw} &= -h_h^T A_{ch}x_h + h_h^T\dot{x}_{hd} + \dot{\sigma}_h(\Delta x_h)\\
\delta_{T\_sw} &= \frac{1}{h_h^T b_h}\left(-\cancel{h_h^T A_{ch}}\,x_h + h_h^T\dot{x}_{hd} + \dot{\sigma}_h(\Delta x_h)\right)\\
\delta_{T\_sw} &= \frac{1}{h_h^T b_h}\left(h_h^T\dot{x}_{hd} + \dot{\sigma}_h(\Delta x_h)\right)
\end{aligned}
\tag{7.12}
$$

Moreover, the term $\dot{\sigma}_h$ (Healey & Lienard, 1993; Fossen, 2011) is given by

$$
\dot{\sigma}_h(\Delta x_h) = -\eta_h\, sgn\left(\sigma_h(\Delta x_h)\right) \tag{7.13}
$$

Therefore, the nonlinear control law be represent as

$$
\delta_{T\_sw} = \frac{1}{h_h^T b_h}\left(h_h^T\dot{x}_{hd} - \eta_h\, sgn\left(\sigma_h(\Delta x_h)\right)\right) \tag{7.14}
$$

The switching gain η_h is used to determine the magnitude of this switching action while the *sgn* (*signum*) function (McGookin, et al., 2000b; Fossen, 2011) provide the switching action where it is used to indicate the direction of the sliding surface to the controller so that Δx_h can be drive to zero.

$$
\sigma_h(\Delta x_h) = \begin{cases} 1 & \text{if } \sigma_h > 0\\ 0 & \text{if } \sigma_h = 0\\ -1 & \text{if } \sigma_h < 0 \end{cases} \tag{7.15}
$$

Healey & Lienard (1993) and Fossen (1994, 2011) found that the *sgn* can lead to chattering where this effect needs to be eliminate for the controller to work properly. However, it is found that it is better to replace the *sgn* by a continuous function *tanh* (the hyperbolic tangent function) (Healey & Lienard, 1993; Akcakaya, et al., 2009; Fossen, 2011) where the switching gain, η_h and boundary layer thickness, ϕ_h is selected to eliminate control chattering (oscillation phenomenon).

$$\delta_{T\_sw} = \frac{1}{h_h^T b_h}\left(h_h^T \dot{x}_{hd} - \eta_h \, tanh\left(\frac{\sigma_h\left(\Delta x_h\right)}{\phi_h} \right) \right) \tag{7.16}$$

The total controller equation becomes

$$\delta_T = -k_h^T x_h + \frac{1}{h_h^T b_h}\left(h_h^T \dot{x}_{hd} - \eta_h \, tanh\left(\frac{\sigma_h\left(\Delta x_h\right)}{\phi_h} \right) \right) \tag{7.17}$$

The proposed sliding mode controller is realized by linearizing the equations system. As been mentioned previously, the linearized equations will consist of three states which are sway linear velocity, yaw angular velocity and yaw angular position. This linearization of the vehicle equations are obtained through small reference input and can be rearranged into single input space form equation as in Equation (7.5).

$$\begin{aligned} \dot{v} &= \frac{Y_t + Y_d + X_{\dot{u}} ur - mur}{m - Y_{\dot{v}}} \\ \dot{r} &= \frac{N_t + N_d - X_{\dot{u}} uv + Y_{\dot{v}} uv}{I_z - N_{\dot{r}}} \\ \dot{\psi} &= r \end{aligned} \tag{7.18}$$

Table 7.1 listed the heading parameters that consist of closed loop poles, switching gain and boundary layer that been chosen to determine the performance of sliding mode heading controller. The poles represent the three states (i.e. v, r, ψ) where two of the poles need to be select while the third one is set zero (McGookin, et al., 2000a; Fossen, 2011). The require feedback gain, k is obtained from pole placement theory. Then, h can be measured as it is the right eigenvector of A_c (see Equation (7.5)) (McGookin, et al., 2000a; Fossen, 2011). For the Matlab computation, referred to Fossen (2011)

Table 7.1: Sliding Mode heading controller parameters

Heading parameters	
Closed loop poles, p_h	[-0.31, -0.32, 0]
Switching gain, η_h	1.8
Boundary layer, ϕ_h	0.2

The heading control law for tail centreline become

$$\delta_T(t) = -0.3238v(t) + 0.0759r(t) + 1.2796\,tanh\left(0.3145\left(\Delta\psi(t)\right)\right) \tag{7.19}$$

It can be observed that the nonlinear switching term will consist only heading error, $\Delta\psi$ while $\Delta v(t)$ and $\Delta r(t)$ are set to zero. This is due to the aim in this study that is to control only the vehicle heading. The linear feedback of $v(t)$ and $r(t)$ terms are included for the purpose to stabilize the sway or yaw dynamics (Healey & Lienard, 1993).

7.6.1 Sliding Mode Heading Controller Performance

The *RoboSalmon* is tested for heading tracking where the vehicle is commanded to steer into 60º, 0º, -60º and 0º heading as previously done by the PID controller. Comparing Figure 7.11 and Figure 7.12, similar vehicle responses have been observed for the sliding mode heading controller where it is able to achieve the desired heading with reasonable accuracy and the symmetrical vehicle response when operates on both heading direction. The heading errors converge to zero as the vehicle approaching the desired heading. It also has been noticed that the heading errors are corrected more quickly for the sliding mode than the PID controller. Moreover, the tail deflection angle required for the sliding mode is lower than the PID controller in order to acquire the same desired heading. Thus, it suggests that the Sliding Mode controller perform better and efficiently than the PID for the heading tracking manoeuvre.

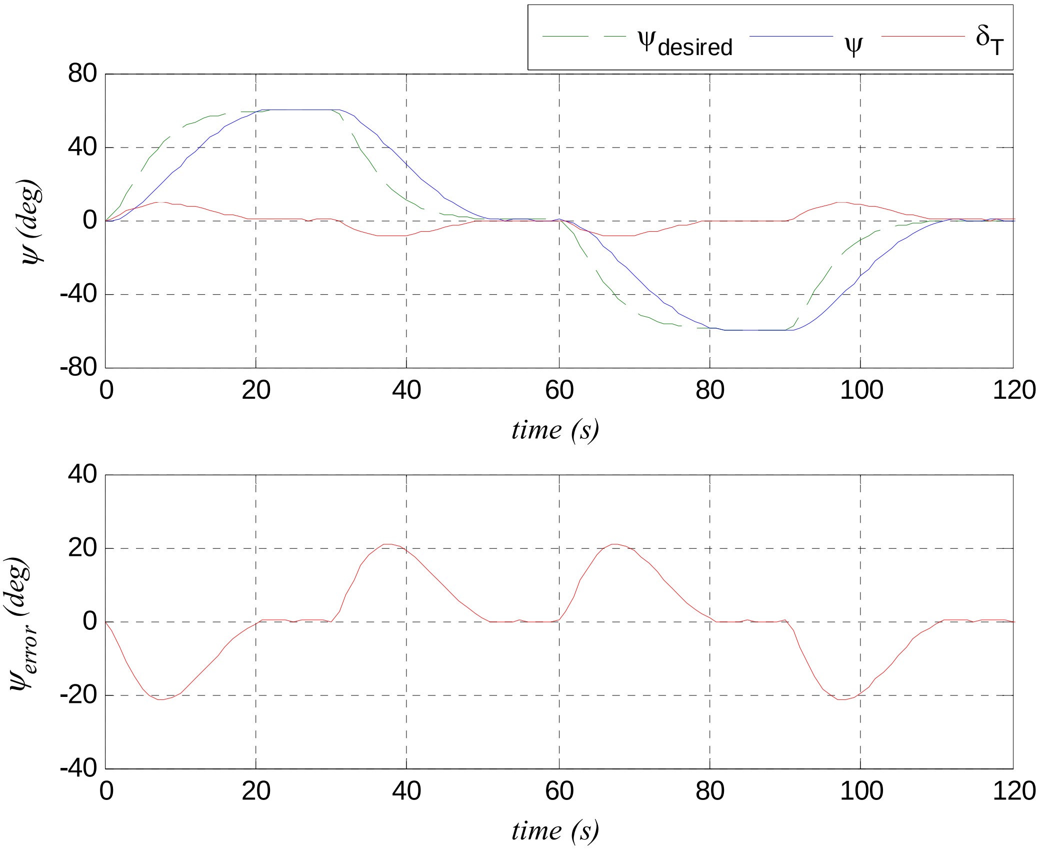

Figure 7.12: Vehicle heading motion based on change in tail centreline for sliding mode controller. The vehicle is commanded to 60º, 0º and 60º headings

7.7 Line of Sight (LOS)

One of the objectives in this study is to design an autonomous biomimetic underwater vehicle. In order to achieve this it is essential to have an efficient guidance system to guide the vehicle along a predetermined path. Several guidance regimes that been applied to AUVs have been reviewed by Naeem, et al. (2003) such as waypoint guidance using line of sight (LOS) principles, vision-based guidance, Lyapunov based guidance and guidance using chemical signals (e.g. sense chemical signal to locate the source of a chemical discharge (Consi, et al., 1994)), proportional navigation guidance and electro-magnetic guidance. It is found that the LOS guidance system is a popular choice for AUVs due to its simple and effective implementation (Healey & Lienard, 1993; McGookin, et al., 2000a; Fossen, et al., 2003).

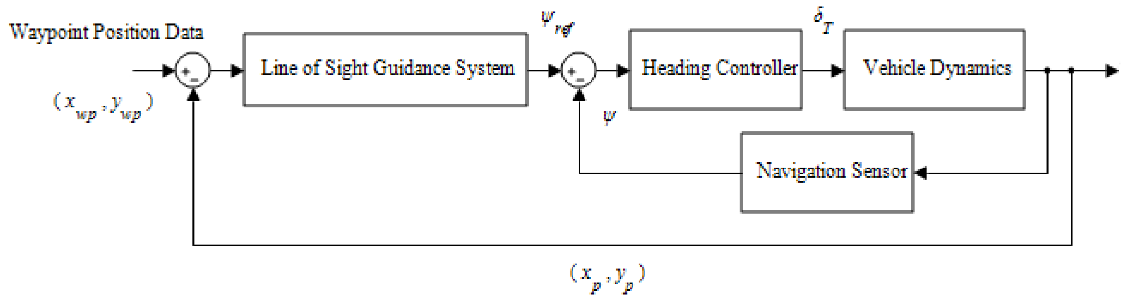

Figure 7.13. Autonomous guidance and heading control system

The LOS guidance system provides a heading command for the controller to follow, which in turn provides the centreline steering signal for the vehicle to follow. The figure above shows that the LOS guidance system is applied in series with the PID control system for navigation along the predetermined course which is set out prior to autopilot activation (McGookin, 1997). This course is made up of points known as waypoints. The vehicle is guided from one waypoint to another by calculating the reference heading angle between the vehicle current position and the waypoint position (Healey & Lienard, 1993; Fossen, 1994, 2011; Mazlan & McGookin, 2012) as shown in Figure 7.14 where Equation (7.20) is used to measure the heading angle, ψ_{ref}.

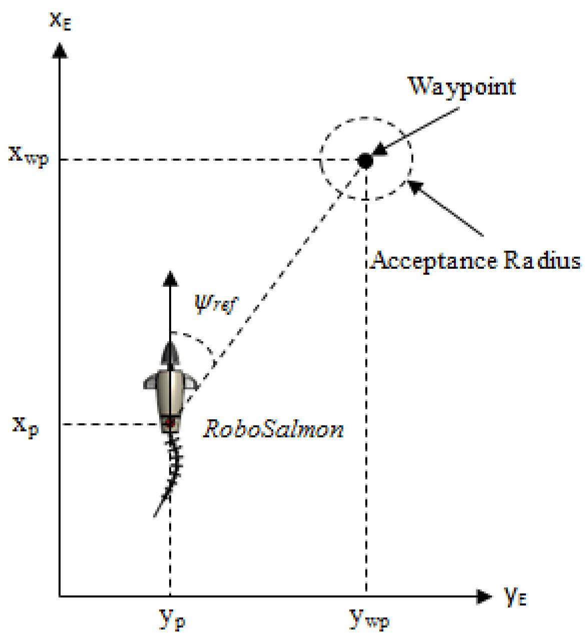

Figure 7.14: Waypoint and acceptance radius

$$\psi_{ref} = tan^{-1}\left(\frac{y_{wp} - y_p}{x_{wp} - x_p}\right) \qquad \text{where} \qquad -\pi \le \psi_{ref} \le \pi \tag{7.20}$$

It is noted that the ψ_{ref} range lies between $-\pi$ and π where there is a discontinuity at the $-\pi/\pi$. This could create a calculating error when measuring ψ_{ref} such as changing from negative to positive or positive to negative heading. This rapid change can be prevent by introducing reference heading so that ψ_{ref} can be varies from $-\infty$ to $+\infty$ (Breivik, 2003; Fossen, et al., 2003). This heading angle, ψ_{ref} is then compared to the current vehicle heading, ψ and serves as input for the steering controller. The controller used the difference to compute the required tail centreline deflection. The tail centreline signal steers the vehicle towards the specific target waypoint until it comes within range of the waypoint coordinates (x_{wp}, y_{wp}). This range, R_k, is called the radius of acceptance and it forms a circle of acceptance around the waypoint. Equation (7.21) shows the expression used to calculate the acquisition of a waypoint (Fossen, et al., 2003).

$$\left(x_{wp} - x_p\right)^2 + \left(y_{wp} - y_p\right)^2 \le R_k^2 \tag{7.21}$$

The (x_{wp} , y_{wp}) is waypoint stored in waypoint table, (x_p , y_p) is the current position of the vehicle and the radius for the circle of acceptance, R_k is defined as n times of vehicle length where typically, it is selected between one and three vehicle lengths (McGookin, et al., 2000b). In this study, the radius for the circle of acceptance is chosen to be equal to one vehicle length. Once the vehicle's position is within the circle of acceptance of the current waypoint, the next waypoint in the list is acquired and the vehicle starts to navigate towards it.

Table 7.2: Waypoints

Waypoint No.	Coordinate (x, y)
1	(3 , 3)
2	(-3 , 3)
3	(3 , -3)
4	(-3 , -3)

The PID controller applied in series with the LOS guidance system has been carried out in simulation where the vehicle is instructed to navigate through 4 waypoints in a 2D plane are listed in Table 7.2 with the radius of acceptance for all waypoints is set to one vehicle length (i.e. 0.90 m). These waypoints have been arranged in that manner so that the vehicle path trajectory will resemble '∞' shape while the distance between each waypoint is set approximately 6 m which appropriate to the *RoboSalmon* turning ability (i.e. over half of its body length) that has been analysed in Chapter 6.

The vehicle trajectory is shown in Figure 7.15 where it shows good performance of the PID heading controller and LOS guidance system. The controller has successfully demonstrated that it can guide the vehicle from one waypoint to another based on the LOS heading measurement. Once the vehicle within the circle of acceptance of the current desired waypoint, it updates to the next desired waypoint. This process is repeated until all waypoints are achieved. It took less than 300 seconds for vehicle to complete the navigation throughout the waypoints with the average surge velocity is measured at 0.0846 m/s.

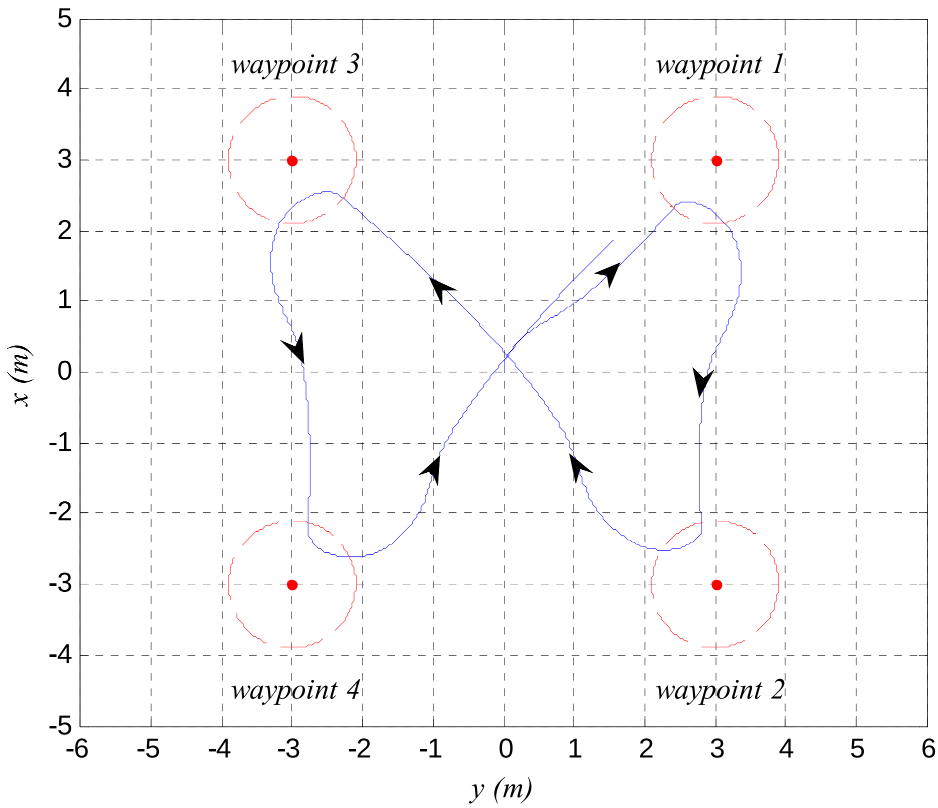

Figure 7.15: Line of sight guidance system for waypoint tracking with PID controller

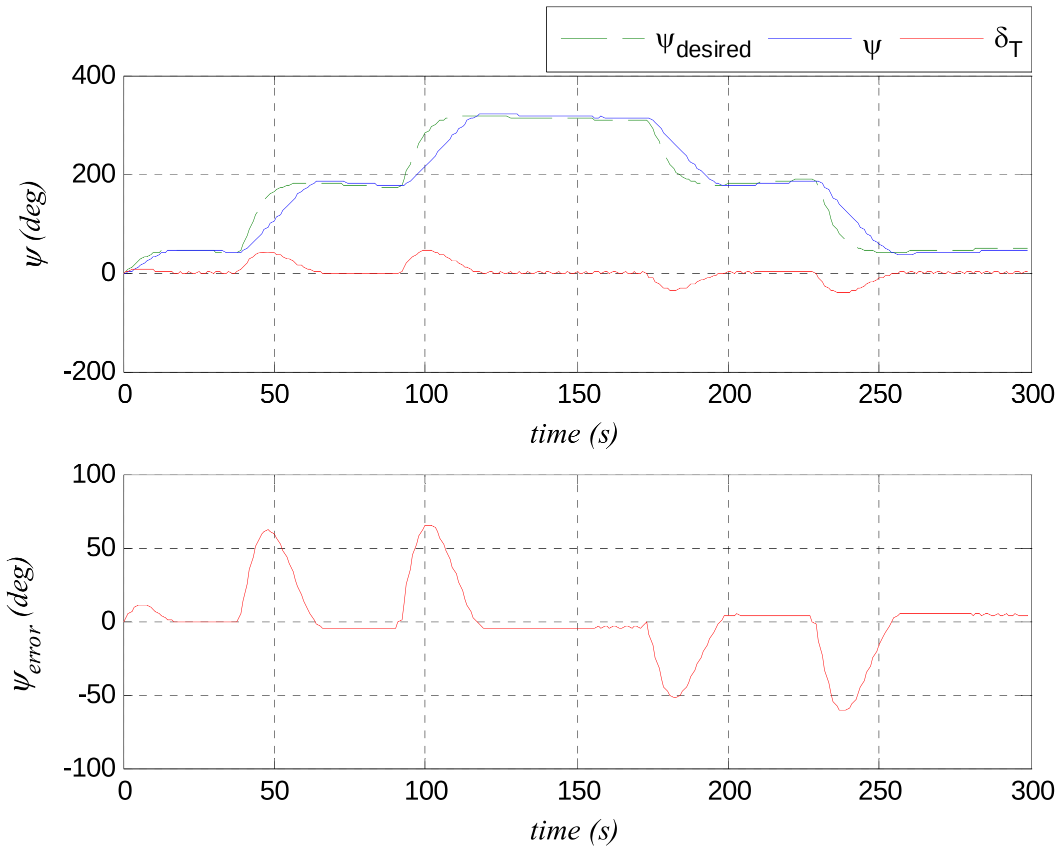

Figure 7.16: PID controller performance on vehicle tracking angle and tail centreline

Figure 7.17 illustrates the relationship between the change in tail centreline and motor (i.e. tail undulation) current. It can be seen that the change in tail centreline will results higher current demand by the motor in order to produce the require tail deflection angle. As consequence, it contributes to higher power consumption with an average power consumed by the vehicle is measured at 7.58 W.

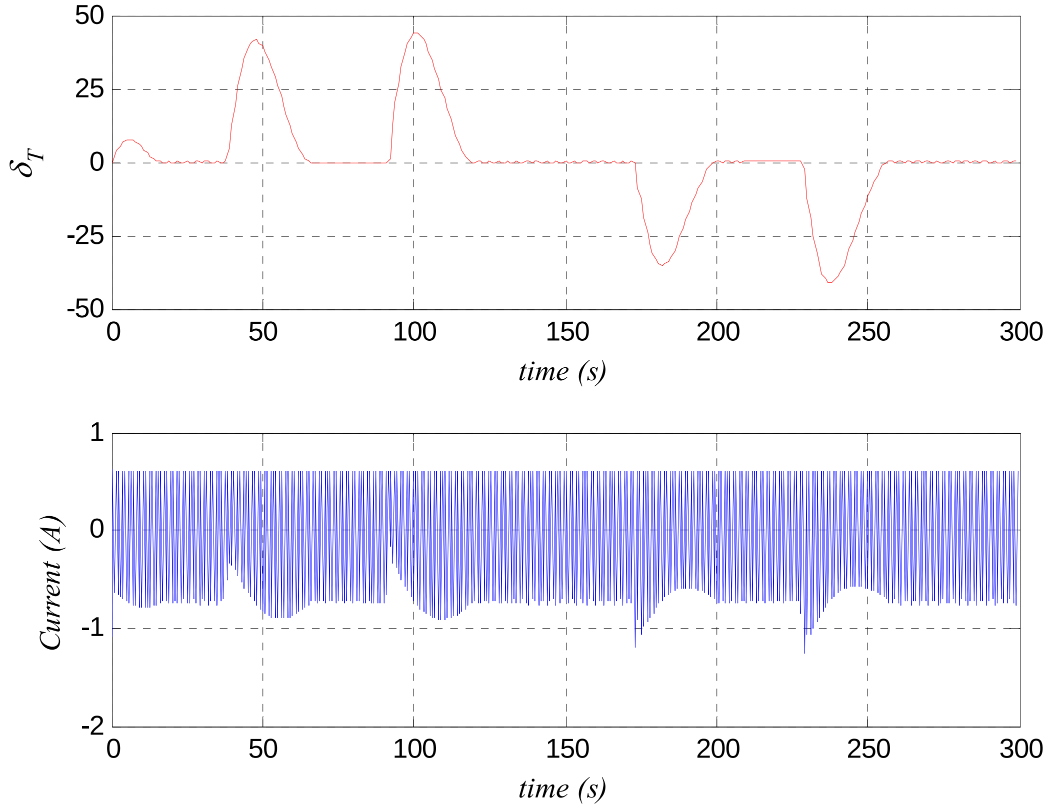

Figure 7.17: PID controller performance on the tail centreline relates to motor current

Next, the sliding mode controller was tested is series with the LOS guidance system and Figure 7.18 shows the vehicle path trajectory throughout the 4 waypoints. It has demonstrated that the sliding mode perform well with the LOS guidance. A similar analysis of PID controller performance can be made to the sliding mode controller such as the heading tracking error converges to zero as the vehicle approaches the waypoint (see Figure 7.19) and high current is consumed when altering the tail centreline (see Figure 7.20). The vehicle implemented with sliding mode controller has an average surge velocity of 0.0867 m/s and average power consumption of 7.57 W.

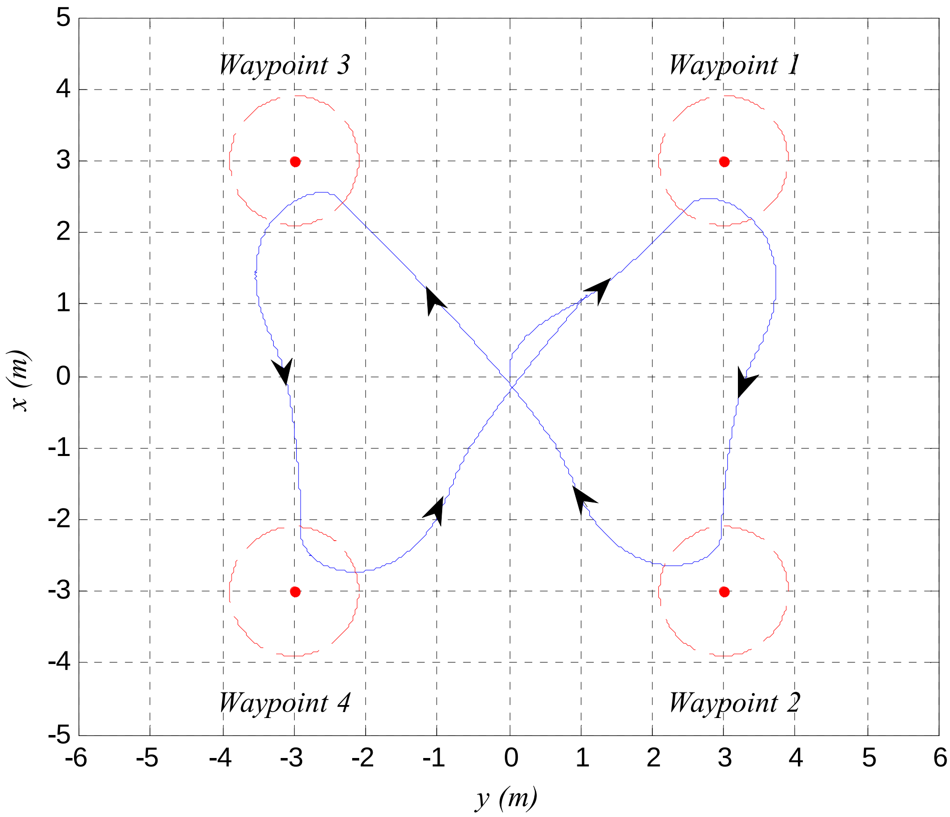

Figure 7.18: Line of sight guidance system for waypoint tracking with sliding mode controller

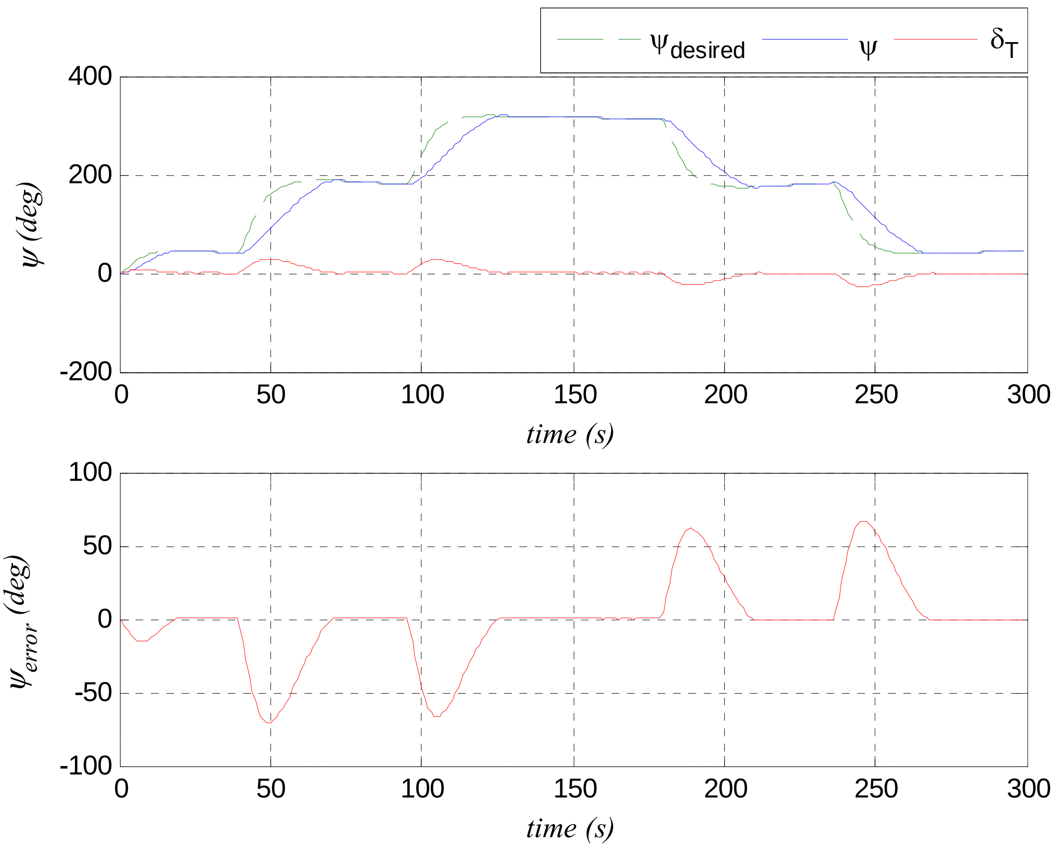

Figure 7.19: Sliding mode controller performance on vehicle tracking angle and tail centreline

The performance of these controllers are been compared and analysed, it can be observed the path trajectory generate by this two controllers are different (see Figure 7.15 and Figure 7.18). This is due to the difference alteration angle of vehicle tail centreline. The amplitude of tail deflection angle measured by the PID controller is higher than sliding mode controller (see Figure 7.16 and Figure 7.19). Therefore, the bigger tail deflection angle requires the vehicle to bend its body which then produce higher turning angle (i.e. sharp turning). This action decreases the vehicle surge velocity as most of generated thrust turn into sway velocity. Furthermore, much higher current and power is consumed to execute bigger tail deflection angle. Therefore, it can be conclude that the sliding mode perform slightly better than PID controller since it can efficiently guide the vehicle to manoeuvre throughout the waypoints without forcing bigger tail deflection angle and high current consumed.

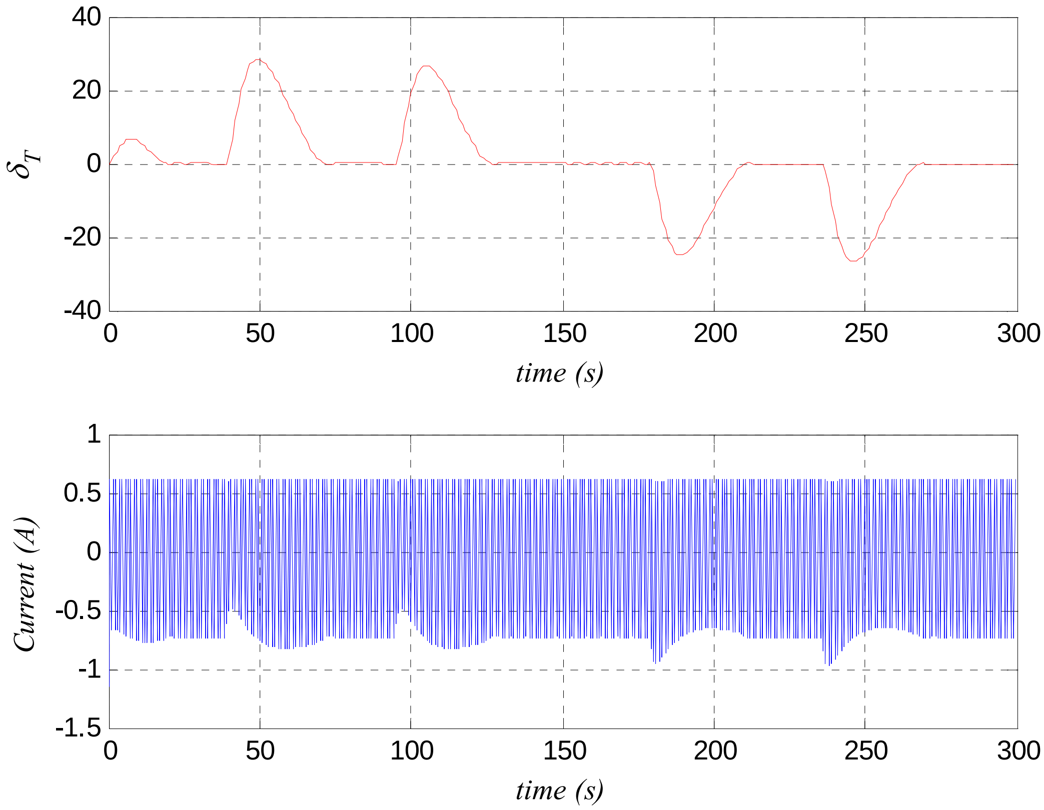

Figure 7.20: Sliding mode controller performance on the tail centreline relates to motor current

7.8 Summary

This chapter highlights a *RoboSalmon* navigation system that consists of a heading control system and a guidance system. Two sets of heading controller have been designed based on PID and sliding mode control theory. The heading controller has been implemented on the *RoboSalmon* to track the vehicle heading where the heading can be adjusted by manipulating the tail centreline. Both controller performances have been analysed and it can observed that both able to guide the vehicle to achieve the desired heading with reasonable accuracy with the heading errors converge to zero. Furthermore, it also can be seen that the symmetrical vehicle response when operates on both heading direction. From the results obtained, the sliding mode heading controller performed better and efficiently than the PID for the heading tracking manoeuvre since the heading errors are corrected more quickly. Moreover, the requirement of altering tail deflection angle is lower for the sliding mode than the PID controller in order to gain the same vehicle desired heading. Finally, a line of sight has been implemented where it used to guide the *RoboSalmon* through certain path made from several waypoints.

8

Discussion, Conclusions & Further Work

8.1 Discussion and Conclusions

The modelling, simulation, control and construction of a biomimetic underwater vehicle known as *RoboSalmon* have been presented in this thesis. The design of this vehicle is based on the physiology of an adult Atlantic salmon where approximately half of its body (i.e. the tail) performs an undulation motion in order to propel it forward. It has been designed with a multiple jointed fully actuated tail that is used to replicate the undulation tail gait of a real fish. The complexity of the design has been described in detailed in Chapter 3 which also includes the component configurations that are involved in the motion control of the multiple actuator motors, the motion detection by sensors, power system and data collection.

Chapter 4 discusses the development of a multi-variable mathematical model that describes the dynamics and electro-mechanics of this biomimetic underwater vehicle. This mathematical model is used to estimate the kinematic relationships for the tail, the vehicle's static hull and its head. In addition, the model contains expressions describing the rigid body dynamics and associated hydrodynamics of the vehicle. These aspects are modelled using conventional marine vessel techniques with several modifications made to incorporate the thrust production from the tail. In the model this is achieved by considering the undulatory motion of real fish tail as a travelling wave. Thus a simple gait has been developed to represent this undulation motion and the model of the tail itself is based on a multi-jointed robotic manipulator arm. The fusion of these modelled elements provides a very complex model that accurately represents the swimming performance for this biomimetic underwater vehicle.

In Chapter 5 experiments concerning the vehicle's forward swimming are presented. These involve the analysis of varying several tail beat parameters, amplitude and frequency. The results obtained showed the linear increase in the surge velocity related to these parameters. Even though actuator saturation occurred, it was observed the effect of increasing the tail beat frequency and keeping the amplitude constant at a value of 0.05 m where the vehicle's surge velocity is increasing. Similar observations have been made when varying the tail beat amplitude while maintaining a constant frequency. The highest surge velocity measured during these experiments was 0.143 ms^{-1} when the tail beat frequency and amplitude are set at 1 Hz and 0.15 m respectively.

Numbers of computer simulation studies have been carried out based on the mathematical model developed in Chapter 4. These computer simulations have been a powerful tool for predicting the vehicle performance when actuator saturation and other physical limitations prevented true experimental analysis to be performed. The result obtained from simulation model agreed with the experimental observation where the vehicle surge velocity increases based on the increase in tail beat amplitude and frequency. However, the ranges of forward speeds achieved by the physical vehicle are much lower than the estimated values for real salmon. This disparity is due to the mechanical limitations imposed by the tail actuators. Thus, an improvement in the operational specification of the motors used to actuate the tail sections would provide an increased range of achievable velocities. The required motor speed specification is suggested to be at least 160 rpm to meet the design of tail beat amplitude (i.e. 0.05 - 0.20 m) and frequency (i.e. 0.5 - 3.0 Hz).

In addition to swimming performance, the vehicle propulsion efficiency has been investigated and analysed. It has been found that the efficiency increased linearly with swimming speed up to a maximum measured efficiency value of 2.14%. Moreover, it is suggested that the efficiency improved when vehicle is operate at higher and larger tail beat frequency and amplitude. The reason for low efficiency values is due to the recoil motion experienced by the vehicle. This adverse motion is the reaction force from the tail which causes the vehicle to roll and pitch during each undulation cycle. The utilisation of an actuated head during forward swimming to counteract the recoil of the has been tested but the results indicated that it produces an even larger recoil motion, which in turn contributed to the decrease in the magnitude of the vehicle's surge velocity.

The manoeuvring experimentation and simulation studies were next analysed where the vehicle has been tested with cruise in turning and zig-zag swimming patterns. This involved varying the same tail parameters used for forward swimming (i.e. tail beat frequency f and tail beat amplitude A) with the addition of tail deflection angle, δ_T. This tail deflection angle is used to change the vehicle heading. The cruise in turn manoeuvring pattern is designed where the vehicle tail centreline is deflected to a predefined angle and holding it constant until circular path is obtained. Several sets of tail beat configurations have been tested with different values of tail deflection angle. Here, one of characteristics been measured is the vehicle turning radius. It has been observed that when the tail beat amplitude and frequency are keep constant, increases in tail deflection angle produces increase in vehicle roll and yaw angular velocities which in turn results in a decrease in the vehicle turning radius. The similar pattern has been observed when the tail beat frequency is set to increase but when the vehicle turning radius vehicle act oppositely when it is applied with larger tail beat amplitude. During manoeuvring, it can be noticed that the vehicle surge velocity decreases compared to surge velocity for forward motion. This is expected since some of the thrust propulsion is used to generate the turning motion and becomes sway velocity.

The smallest turning radius that the vehicle able to attain is 0.58 m which is just over half of its body length when operated at the largest tail deflection angle. This also demonstrated it has smaller turning radius than the conventional underwater vehicles that in general tend to have an average turn radius of 3 -15 times of the body length. The vehicle experimental manoeuvring performance also has been compared to the results obtained using computer simulation. It has been found that the simulation model is reasonably accurate to represent the actual system. Thus, it proves useful where this model can be used to estimate the vehicle performance for the tail deflection angles that have not been tested experimentally. The *RoboSalmon* has been simulated to turn in both directions (i.e. left/right) for varies tail deflection angles. The vehicle shows a symmetrical path trajectory and smaller tuning radius able to be produced when larger tail deflection angle been applied. The zig-zag manoeuvre is another pattern that been simulated to evaluate the vehicle manoeuvring capability. The vehicle tail deflection angle is commanded to be 20º from an initially straight course and this heading is maintained until the vehicle heading reached the desired heading. Then the tail centreline is deflected to the opposite direction. The vehicle exhibits a high manoeuvrability performance with the time to change its heading from the time tail centre being execute depends on the tail beat parameters. It was found that the time duration to complete one cycle is shorter when operated at larger tail beat amplitude and higher frequency.

Finally, *RoboSalmon* heading and guidance control system have been discussed in order to enable it to navigate without human intervention. Two types of heading controller have been designed based on PID and sliding mode control theory. These heading controllers were used to track the vehicle heading where the heading can be adjusted by altering the tail centreline. The results obtained from both controllers show satisfactory performance in the heading tracking. Both controllers were able to guide the vehicle to achieve the desired heading with reasonable accuracy and shown that the heading errors converge to zero. Moreover, it was suggested that the sliding mode heading controller performed better and efficiently than the PID heading the controller for the heading tracking manoeuvre. It can be observed that the heading error in sliding mode controller is corrected more quickly than in the PID controller. Furthermore, it required lower tail deflection angle to achieve the same vehicle desired heading.

A line of sight guidance system was introduced where it used to guide the *RoboSalmon* through certain path made by several waypoints. The vehicle will move from one waypoint to another once it reaches within the radius of acceptance acceptable that is situated around the waypoint. The results show that the vehicle capable to navigate through set of waypoints to form '∞' shape. It took less than 300 seconds simulation time for the vehicle to complete the shape. The PID controller measured an average surge velocity of 0.0846 m/s and average power consumption of 7.58 W while the sliding mode controller has an average surge velocity of 0.0867 m/s and average power consumption of 7.57 W.

In conclusion, the design work and control of an autonomous underwater vehicle that mimics a fish tail propulsion system has been investigated in this research. The work was to determine whether this system can be considered as an alternative option to the current AUV design. The approach of using multiple jointed fully actuated tail allows the replication of the undulation swimming gait of the real fish. The vehicle has exhibits experimentally that it capable to swim and perform basic manoeuvres. This work also involved developing a mathematical model which was used to validate the vehicle performance. The simulation data show that it reasonably agreed with the data obtainable from experimentation. Thus, it proved to be useful tool as it can also be used to predict the vehicle performance for several manoeuvres that been able to be tested experimentally that includes the autonomous navigation through waypoints. Another conclusion can be made is that the sinusoidal shape of undulation movement helps to reduce vehicle recoil motion when compared to the tendon drive system in Watts (2009) research. As consequences, this should contribute to a higher vehicle surge velocity. However due to under specified actuator selection, the vehicle surge velocity cannot be tested for a higher and larger tail beat frequency and amplitude respectively. Even at low speed, the vehicle tends to have a higher propulsion efficiency compared to propeller based model when operate at the same condition. According to the results obtained from the simulation model, there is potential for the vehicle's swimming speeds to be improved if the actuators are better specified.

This vehicle also demonstrates a higher manoeuvrability corresponding to the flexibility in multilink tail manipulation and the vehicle able to perform 180º turn with less than one body length. This proposes that the *RoboSalmon* has superior turning ability than conventional underwater vehicles. Although the experimental stage of this study encountered actuator limitation, it can be deduced that the *RoboSalmon* forward and manoeuvring capability may have advantages over the conventional AUVs. Thus, it suggests that the biomimetic fish tail system can be considered as a suitable alternative to the current AUVs propulsion system that generally based on propeller.

8.2 Further Work

It is very apparent that the design and construction of this biomimetic underwater vehicle incorporates multi-disciplinary subject areas such as naval, mechanical, computer, electrical and electronics engineering. Many lessons have been learned throughout this study and the work presented has the potential to be expanded further in order to improve the vehicle performance. Some ideas for further work to expand the scope of this research are outlined in the sections below.

8.2.1 Modelling and Simulation

The mathematical model has been validated in this research and it can be observed that it sufficiently represent the actual vehicle performance. Thus in the future, a control law can be introduced for vehicle speed and diving control. This includes diving and climbing manoeuvres where a 3D simulation can be generated. This computer simulation can also be extended in order to produce more realistic conditions. These include the presence of disturbance in physical environment such as ocean current and sensor noise. In addition, the vehicle navigation performance can be improved by implementing an obstacle avoidance algorithm into the simulation.

8.2.2 *RoboSalmon* System Improvement

As been mentioned in Chapter 3, a latex skin has been developed to contain the electronic components and one of the problems encountered during experimentation concern waterproofing the tail undulation part. There are cases that water flooding the undulation part due to improper seal and the degrading of latex skin condition over time. Even though the circuit board is well protected, the water still can cause damage to the actuator part and disturb the vehicle buoyancy force where the vehicle starts to sink. Thus, in order to prevent future electrical problem, individual actuator housing can be implemented in addition to provide extra precaution when reapplying seal toward the latex skin.

The design of printed circuit board (PCB) also can be improved where currently, all PCB are designed only for double sided layers. If a multilayer option is available, it can be a useful addition especially for the tail part controller since it will take less space and reduce wiring connections. This will also help to reduce the complexity in case of system troubleshooting and allow for additional sensors to be placed.

The mathematical model of vehicle with the fish like propulsion system has been designed in 6 degree of freedom, though only 5 parameters are available to be validated which are surge, sway, roll, pitch and yaw. Unfortunately, heave dynamics cannot be validated since the current prototype does not have the capability of changing its operational depth. A pair of pectoral fins is designed and mounted on each side of the body in order to allow vehicle depth control. However, the offset in pectoral fin alone not sufficient to cause the vehicle to dive. An alternative method needs to be introduced and it is known that fish are able to dive up and down as part of their routine of feeding and avoiding predators by changing the volume of the *swim bladder* (Bone, et al., 1995). Thus, a similar concept can be used for the underwater vehicle by employing artificial bladder or ballast tank. The vehicle vertical movement can then be control by alternately filled with water or air where filling it with air in order to float or water in order to submerge. Other further possible areas that can be expanded from this research include multiple vehicle coordination, implementing other types of control and guidance methodologies for autonomous swimming and integration of sensors for the purpose of obstacle avoidance.

References

Afolayan, M. O., Yawas, D. S., Folayan, C. O., & Aku, S. Y. (2012). Mechanical Description of a Hyper-Redundant Robot Joint Mechanism Used for a Design of a Biomimetic Robotic Fish. *Journal of Robotics, 2012*, 16.

Akcakaya, H., Yildiz, H. A., Saglam, G., & Gurleyen, F. (2009). *Sliding Mode Control of Autonomous Underwater Vehicle.* Proceedings of the International Conference on Electrical and Electronics Engineering, ELECO 2009, Bursa, Turkey, 332-336.

Allegro MicroSystems. (n.d.). Fully Integrated, Hall Effect-Based Linear Current Sensor IC with 2.1kVRMS Isolation and a Low-Resistance Current Conductor (pp. 15).

Allen, B., Vorus, W. S., & Prestero, T. (2000). *Propulsion System Performance Enhancements on REMUS AUVs.* Proceedings of the MTS/IEEE Conference and Exhibition, OCEANS 2000 Rhode Island, 1869-1873.

American Bureau of Shipping. (2006). Guide for Vessel Maneuverability (pp. 124). Houston, TX.

Analog Devices. (2013). ADXL345: 3-Axis, ±2 g/±4 g/±8 g/±16 g Digital Accelerometer Data Sheet (pp. 40). Norwood, MA, USA.

Anderson, J. M., & Chhabra, N. K. (2002). Maneuvering and Stability Performance of a Robotic Tuna. *Integr. Comp. Biol., 42*(1), 118-126.

Anderson, J. M., & Kerrebrock, P. A. (2002). Biomimetics in Action: Design and Performance of an Autonomous Robotic Fish. In J. Ayers, J. L. Davis & A. Rudolph (Eds.), *Neurotechnology for Biomimetic Robots* (pp. 297-308). London, England: MIT Press.

Apalkov, A., Fernández, R., Fontaine, J. G., Akinfiev, T., & Armada, M. (2012). Mechanical Actuator for Biomimetic Propulsion and the Effect of the Caudal Fin Elasticity on the Swimming Performance. *Sensors and Actuators A: Physical, 178*(0), 164-174.

Araujo, J., Sandberg, H., & Johansson, K. H. (2009). *Experimental Validation of a Localization System Based on a Heterogeneous Sensor Network.* Proceedings of the 7th Asian Control Conference Hong Kong, China, 465-470.

Arnold, M. (2007). Multi-Rate Time Integration for Large Scale Multibody System Models. In P. Eberhard (Ed.), *Proceedings of the IUTAM Symposium on Multiscale Problems in Multibody System Contacts* (Vol. 1, pp. 1-10): Springer Netherlands.

Åström, K. J. (2002). PID Control. *Control System Design* (pp. 36).

Atlas Elektronik GmbH. (2013). Atlas SeaOtter. AUV for Multi-Purpose Underwater Operations (pp. 1-4). Bremen, Germany.

Attaway, S. (2013). Sights and Sounds. In S. Attaway (Ed.), *Matlab* (3rd ed., pp. 419-460). Boston: Butterworth-Heinemann.

Bainbridge, R. (1957). The Speed of Swimming of Fish as Related to the Size and to the Frequency and Amplitude of Tail Beat. *Journal of Experimental Biology, 35*, 109-133.

Balci, O. (1994). *Validation, Verification, and Testing Techniques Throughout the Life Cycle of a Simulation Study.* Proceedings of the Winter Simulation Conference, Piscataway, New Jersey, 215-220.

Ballard, R. D. (1993). The JASON Remotely Operated Vehicle System: Woods Hole Oceanographic Institution

Bandyopadhyay, P. R. (2004). Guest Editorial: Biology-Inspired Science and Technology for Autonomous Underwater Vehicles. *IEEE Journal of Oceanic Engineering, 29*(3), 542-546.

Bandyopadhyay, P. R. (2005). Trends in Biorobotic Autonomous Undersea Vehicles. *IEEE Journal of Oceanic Engineering, 30*(1), 109-139.

Bar-Cohen, Y. (2006). Biomimetics - Using Nature to Inspire Human Innovation. *Bioinspiration & Biomimetics, 1*, 12.

Barrett, D., Grosenbaugh, M., & Triantafyllou, M. (1996). *The Optimal Control of a Flexible Hull Robotic Undersea Vehicle Propelled by an Oscillating Foil.* Proceedings of the 1996 Symposium on Autonomous Underwater Vehicle Technology. AUV '96, Monterey, CA, 1-9.

Barrett, D. (2002). Optimization of Swimming Locomotion by Genetic Algorithm. In J. Ayers, J. L. Davis & A. Rudolph (Eds.), *Neurotechnology for Biomimetic Robots* (pp. 207-221). London, England: MIT Press.

Barton, M. (2007). *Bond's Biology of Fishes* (3rd ed.). Belmont, CA: Thomas Brooks/Cole.

Bednar, R., & Crosbie, R. E. (2007). *Stability of Multi-rate Simulation Algorithms*. Paper presented at the 2007 Summer Computer Simulation Conference, San Diego, California.

Beem, H. R., & Triantafyllou, M. (2012). *Biomimetic Design of an Undulatory Stingray AUV Fin.* Proceedings of the International Society of Offshore and Polar Engineers (ISOPE), Rhodes, Greece, 1 - 5.

Bellingham, J. (2001). Autonomous Underwater Vehicles (AUVs). *Academic Press*, 212-216.

Bellingham, J. G., Goudey, C. A., Consi, T. R., Bales, J. W., Atwood, D. K., Leonard, J. J., & Chryssostomidis, C. (1994). *A Second Generation Survey AUV.* Proceedings of the 1994 Symposium on Autonomous Underwater Vehicle Technology, Cambridge, MA, 148-155.

Bende, V., Pathak, P. M., Dixit, K. S., & Harsha, S. (2012). Energy Optimal Trajectory Planning of an Underwater Robot using a Genetic Algorithm. *Proceedings of the Institution of Mechanical Engineers, Part I: Journal of Systems and Control Engineering, 226*(8), 1077-1087.

Bhandari, S. A., Rana, A. D., Bhandari, S. Z., Kalange, V. A., & Sanghvi, M. R. (2012). *Mathematical Model for Digital Video Watermarking based on 3D Wavelet Transform.* Proceedings of the International Conference in Computational Intelligence (ICCIA2012) New York, USA.

Blake, R. W. (1983). *Fish Locomotion*. New York: Cambridge University Press.

Blake, R. W. (2004). Fish Functional Design and Swimming Performance. *Journal of Fish Biology, 65*(5), 1193-1222.

Blidberg, D. R. (2001). *The Development of Autonomous Underwater Vehicles (AUV); A Brief Summary.* Proceedings of the IEEE International Conference on Robotics and Automation, Seoul, Korea.

Bluefin Robotics. (2014). Propulsion Retrieved Oct 7 2014, from http://www.bluefinrobotics.com/technology/propulsion/

Bohn, C., & Atherton, D. P. (1995). An Analysis Package Comparing PID Anti Windup Strategies. *IEEE Control Systems, 15*(2), 34-40.

Bolton, W. (2008). *Mechatronics: Electronic Control systems in Mechanical and Electrical Engineering* (4th ed.). Essex, England: Prentice Hall.

Bone, Q., Marshall, N. B., & Blaxter, J. H. S. (1995). *Biology of Fishes*: Chapman & Hall.

Bowen, A. D., Yoerger, D. R., Taylor, C., McCabe, R., Howland, J., Gomez-Ibanez, D., Kinsey, J. C., Heintz, M., McDonald, G., Peters, D. B., Fletcher, B., Young, C., Buescher, J., Whitcomb, L. L., Martin, S. C., Webster, S. E., & Jakuba, M. V. (2008). *The Nereus Hybrid Underwater Robotic Vehicle for Global Ocean Science Operations to 11,000 m Depth.* Proceedings of the OCEANS 2008, Quebec, 1-10.

Brege, E. D. (2011). *Design and Construction of a Low Cost, Modular Autonomous Underwater Vehicle.* Naval Engineer and Master of Science in Mechanical Engineering, Massachusetts Institute of Technology, USA.

Breivik, M. (2003). *Nonlinear Maneuvering Control of Underactuated Ships.* MSc, Norwegian University of Science and Technology, Trondheim, Norway.

Brun, L. (2012). ROV/AUV Trends. Market and Technology. *Marine Technology Reporter, 55,* 48 - 51.

Budiyono, A. (2009). Advances in Unmanned Underwater Vehicles Technologies: Modeling, Control and Guidance Perspectives *Indian Journal of Marine Sciences, 38*(3), 282-295.

Cau, A., Concas, G., Melis, M., & Turnu, I. (2005). Evaluate XP Effectiveness Using Simulation Modeling. In H. Baumeister, M. Marchesi & M. Holcombe (Eds.), *Extreme Programming and Agile Processes in Software Engineering* (Vol. 3556, pp. 48-56): Springer Berlin Heidelberg.

Cen, L., & Erturk, A. (2013). Bio-inspired Aquatic Robotics by Untethered Piezohydroelastic Actuation. *Bioinspiration & Biomimetics, 8*(1), 13.

Chadwick, B. (2010). Remotely Operated Vehicles (ROVs) and Autonomous Underwater Vehicles (AUVs) Retrieved 15th August, 2014, from http://oceanexplorer.noaa.gov/explorations/02fire/background/rovs_auvs/rov_auv.html

Chapra, S. C., & Canale, R. P. (2003). *Numerical Methods for Engineers with Software and Programming Applications* (4th ed.): McGraw-Hill.

Chen, Z., Shatara, S., & Tan, X. (2010). Modeling of Biomimetic Robotic Fish Propelled by An Ionic Polymer–Metal Composite Caudal Fin. *IEEE/ASME Transactions on Mechatronics, 15*(3), 448-459.

Chopra, M. G. (1976). Large Amplitude Lunate-tail Theory of Fish Locomotion. *Journal of Fluid Mechanics, 74*(01), 161-182.

Christ, R. D., & Wernli Sr, R. L. (2014). The ROV Business. In R. D. Christ & R. L. Wernli (Eds.), *The ROV Manual* (2nd ed., pp. 3-20). Oxford: Butterworth-Heinemann.

Chu, W.-S., Lee, K.-T., Song, S.-H., Han, M.-W., Lee, J.-Y., Kim, H.-S., Kim, M.-S., Park, Y.-J., Cho, K.-J., & Ahn, S.-H. (2012). Review of Biomimetic Underwater Robots using Smart Actuators. *International Journal of Precision Engineering and Manufacturing, 13*(7), 1281-1292.

Colgate, J. E., & Lynch, K. M. (2004). Mechanics and Control of Swimming: A Review. *IEEE Journal of Oceanic Engineering, 29*(3), 660-673.

Conry, M., Keefe, A., Ober, W., Rufo, M., & Shane, D. (2013). *BIOSwimmer: Enabling Technology for Port Security.* Proceedings of the IEEE International Conference on Technologies for Homeland Security (HST), 2013, Waltham, Massachusetts, USA, 364-368.

Conservation of Atlantic Salmon in Scotland Project. (2010). The Atlantic Salmon (Salmo Salar L) Retrieved 1st May, 2011, from http://www.snh.org.uk/salmonlifeproject

Consi, T. R., Atema, J., Goudey, C. A., Cho, J., & Chryssostomidis, C. (1994). *AUV Guidance with Chemical Signals.* Proceedings of the 1994 Symposium on Autonomous Underwater Vehicle Technology, Piscataway, New Jersey, USA, 450-455.

Corfield, S., & Hillenbrand, C. (2002). Defence Applications for Unmanned Underwater Vehicles. In G. Griffiths (Ed.), *Technology and Applications of Autonomous Underwater Vehicles* (pp. 161-178): CRC Press.

Danson, E. F. S. (2002). AUV Tasks in the Offshore Industry. In G. Griffiths (Ed.), *Technology and Applications of Autonomous Underwater Vehicles* (pp. 127-138): CRC Press.

Dart, F. (2009). Interfacing a USB Flash Drive to a PIC Microcontroller. Retrieved from http://www.newelectronics.co.uk/embedded-electronics-technology/interfacing-a-usb-flash-drive-to-a-pic-microcontroller/17222/

Davies, J. H. (2011, 6th October). *A Basic Introduction to Cadence OrCAD PCB Designer Version 16.3 [unpublished lecture notes]*. Glasgow University, 70.

DELTRON Enclosures. (n.d.). Aluminium Enclosure IP68 Plain, from http://www.dem-uk.com/deltron-enclosures/products/ip68_enclosures/aluminium_enclosure_ip68_plain/

Domenici, P., & Blake, R. W. (1997). The Kinematics and Performance of Fish Fast-Start Swimming. *Journal of Experimental Biology, 200*, 1165–1178.

Donley, J. M., Sepulveda, C. A., Konstantinidis, P., Gemballa, S., & Shadwick, R. E. (2004). Convergent Evolution in Mechanical Design of Lamnid Sharks and Tunas. [10.1038/nature02435]. *Nature, 429*(6987), 61-65.

Edwards, C., & Postlethwaite, I. (1999). An Anti-windup Scheme with Closed-loop Stability Considerations. *Automatica, 35*(4), 761-765.

Ellerby, D. J. (2010). How Efficient is a Fish? *Journal of Experimental Biology, 213*(22), 3765-3767.

Eloy, C. (2012). Optimal Strouhal Number for Swimming Animals. *Journal of Fluids and Structures, 30*(0), 205-218.

Elvander, J., & Hawkes, G. (2012). *ROVs and AUVs in Support of Marine Renewable Technologies.* Proceedings of the Oceans 2012, Hampton Roads, Virginia, 1-6.

Eng You, H., Hong Geok, S., & Chitre, M. (2010). *Depth Control of an Autonomous Underwater Vehicle, STARFISH.* Proceedings of the IEEE OCEANS 2010, Sydney, 1-6.

Engelhardtsen, Ø. (2007). *3D AUV Collision Avoidance.* MSc, Norwegian University of Science and Technology, Trondheim, Norway. Retrieved from http://urn.kb.se/resolve?urn=urn:nbn:no:ntnu:diva-9534

Eskesen, J., Owens, D., Soroka, M., Morash, J., Hover, F. S., & Chrysosstomidis, C. (2009). Design and Performance of ODYSSEY IV: A Deep Ocean Hover-Capable AUV (pp. 10). Cambridge, Massachusetts: MIT Sea Grant College Program.

Faltinsen, O. M. (2006). Maneuvering *Hydrodynamics of High-Speed Marine Vehicles* (pp. 390-434): Cambridge University Press.

Fiazza, C., Salumae, T., Listak, M., Kulikovskis, G., Templeton, R., Akanyeti, O., Megill, W., Fiorini, P., & Kruusmaa, M. (2010). *Biomimetic Mechanical Design for Soft-Bodied Underwater Vehicles.* Proceedings of the OCEANS 2010 IEEE, Sydney, 1-7.

Finnish Game and Fisheries Research Institute. (2008). Atlantic salmon (Salmo salar), from http://www.rktl.fi/english/fish/fish_atlas/atlantic_salmon/

Fish, F. E. (1997). *Biological Designs for Enhanced Maneuverability: Analysis of Marine Mammal Performance.* Proceedings of the 10th International Symposium on Unmanned Untethered Submersible Technology, Special Session on Bio-Engineering Research Related to Autonomous Underwater Vehicles, Durham, NH, 109 -117.

Fossen, T. I. (1994). *Guidance and Control of Ocean Vehicles*: John Wiley & Son, Ltd.

Fossen, T. I., Breivik, M., & Skjetne, R. (2003). *Line-Of-Sight Path Following Of Underactuated Marine Craft.* Proceedings of the 6th IFAC MCMC, Girona, Spain, 244-249.

Fossen, T. I., & Johansen, T. A. (2006). *A Survey of Control Allocation Methods for Ships and Underwater Vehicles.* Proceedings of the 14th Mediterranean Conference on Control and Automation, MED '06, Ancona, Italy, 1-6.

Fossen, T. I. (2011). *Handbook of Marine Craft Hydrodynamics and Motion Control*: John Wiley & Son, Ltd.

Fountain, H. (2010). ABE, Pioneering Robotic Undersea Explorer, Is Dead at 16. Retrieved Oct 7, 2014. Retrieved from http://www.nytimes.com/2010/03/16/science/16sub.html?_r=0

Freitag, L., Grund, M., von Alt, C., Stokey, R., & Austin, T. (2005). *A Shallow Water Acoustic Network for Mine Countermeasures Operations with Autonomous Underwater Vehicles.* Proceedings of the Underwater Defense Technology (UDT), Amsterdam, Netherlands.

From, P., Gravdahl, J., & Pettersen, K. (2014). Underwater Robotic Systems *Vehicle-Manipulator Systems* (pp. 307-324): Springer London.

Fukuda, T., Kawamoto, A., Arai, F., & Matsuura, H. (1994). *Mechanism and Swimming Experiment of Micro Mobile Robot in Water.* Proceedings of the 1994 IEEE Workshop on Micro Electro Mechanical Systems, MEMS '94, Oiso, Japan, 273-278.

Future Developments. (2002). Aqua Stop Technical Information.

Future Technology Devices International Limited (FTDI). (2010). VNC2-32Q Development Module Datasheet.

Geder, J. D., Ramamurti, R., Pruessner, M., & Palmisano, J. S. (2013). *Maneuvering Performance of a Four-Fin Bio-Inspired UUV.* Proceedings of the OCEANS '13, San Diego, CA.

German, C. R., Yoerger, D. R., Jakuba, M., Shank, T. M., Langmuir, C. H., & Nakamura, K.-i. (2008). Hydrothermal Exploration with the Autonomous Benthic Explorer. *Deep Sea Research Part I: Oceanographic Research Papers, 55*(2), 203-219.

Gockenbach, M. S. (1999). A Practical Introduction to MATLAB, from http://www.math.mtu.edu/~msgocken/intro/intro.html

Goldberg, D. (2011). *Huxley: A Flexible Robot Control Architecture for Autonomous Underwater Vehicles.* Proceedings of the IEEE OCEANS 2011, Spain, 1-10.

Gonzalez, R. C., Woods, R. E., & Eddins, S. L. (2004). *Digital Image Processing using MATLAB* (1st ed.): Prentice Hall.

Gray, G. J. (1992). *Development and Validation of Nonlinear Models for Helicopter Dynamics.* PhD, University of Glasgow.

Gray, G. J., Murray-Smith, D. J., Li, Y., Sharman, K. C., & Weinbrenner, T. (1998). Nonlinear Model Structure Identification using Genetic Programming. *Control Engineering Practice, 6*(11), 1341-1352.

Gray, J. (1968). *Animal locomotion*. London: Weidenfeld and Nicolson.

Griffiths, G. (1999). *Technological Needs for Autonomous Underwater Vehicles. A Requirements Driven Approach.* Proceedings of the EUROMAR Workshop: Technologies for Ocean and Coastal Survey, Brussels, Belgium.

Guo, C., & Wang, Z. (2008). Design and Simulations of a Virtual Fishlike Robot Actuated by a Muscle Model. In N. Kato & S. Kamimura (Eds.), *Bio-mechanisms of Swimming and Flying* (pp. 221-232): Springer Japan.

Guo, S., Fukuda, T., Kato, N., & Oguro, K. (1998). *Development of Underwater Microrobot using ICPF Actuator.* Proceedings of the 1998 IEEE International Conference on Robotics and Automation, Leuven, Belgium, 1829-1834.

Guo, S., Ge, Y., Li, L., & Liu, S. (2006). *Underwater Swimming Micro Robot Using IPMC Actuator.* Proceedings of the 2006 IEEE International Conference on Mechatronics and Automation, Luoyang, Henan, 249-254.

Hasvold, Ø., Størkersen, N. J., Forseth, S., & Lian, T. (2006). Power Sources for Autonomous Underwater Vehicles. *Journal of Power Sources, 162*(2), 935-942.

Healey, A. J., & Lienard, D. (1993). Multivariable Sliding-Mode Control for Autonomous Diving and Steering of Unmanned Underwater Vehicles. *IEEE Journal of Oceanic Engineering, 18*(3), 327-339.

Hirata, K. (2000). *Development of Experimental Fish Robot.* Proceedings of the 6th International Symposium on Marine Engineering, 711 -714.

Hirata, K., Takimoto, T., & Tamura, K. (2000). *Study on Turning Performance of a Fish Robot.* Proceedings of the 1st International Symposium on Aqua Bio-Mechanisms, ISABM, 287 -292.

Hirata, K. (2001, April 25, 2001). Prototype Fish Robot, PF-700, National Maritime Research Institute Retrieved May, 2012, from http://www.nmri.go.jp/eng/khirata/fish/experiment/pf700/pf700e.htm

Hirata, K., & Kawai, S. (2001, November 9, 2001). Prototype Fish Robot, UPF-2001, National Maritime Research Institute Retrieved June, 2013, from http://www.nmri.go.jp/eng/khirata/fish/experiment/upf2001/index_e.html

Hirata, K., & Aoki, D. (2003). Prototype Fish Robot, PF-200, National Maritime Research Institute Retrieved May, 2012, from http://www.nmri.go.jp/eng/khirata/fish/experiment/pf200/index_e.html

Hirata, K., & Sakurai, K. (2003). Prototype Fish Robot, PF-550, National Maritime Research Institute Retrieved Jan, 2013, from http://www.nmri.go.jp/eng/khirata/fish/experiment/pf550/index_e.html

Hoar, W. S., & Randall, D. J. (Eds.). (1970). *The Nervous System, Circulation, and Respiration* (Vol. IV). New York: Academic Press.

Hoar, W. S., & Randall, D. J. (Eds.). (1978). *Form, Function and Locomotory Habits in Fish* (Vol. VII). New York: Academic Press.

Hoerner, S. F. (1965). *Fluid-Dynamic Drag: Practical Information on Aerodynamic Drag and Hydrodynamic Resistance*. New Jersey.

Horner, D. P., Healey, A. J., & Kragelund, S. P. (2005). *AUV Experiments in Obstacle Avoidance.* Proceedings of the MTS/IEEE OCEANS, 2005, Washington, 1464-1470 Vol. 1462.

Hu, H. (2006). *Biologically Inspired Design of Autonomous Robotic Fish at Essex.* Proceedings of the IEEE SMC UK-RI Chapter Conference 2006 on Advances in Cybernetic Systems, Sheffield.

Hu, H., Liu, J., Dukes, I., & Francis, G. (2006). *Design of 3D Swim Patterns for Autonomous Robotic Fish.* Proceedings of the 2006 IEEE/RSJ International Conference on Intelligent Robots and Systems, Beijing, China, 2406-2411.

Ibrahim, D. (2008). Microcontroller and SD-Card based Multichannel Data Logger. *DATA LOGGER/MCU*. Retrieved from Electronics World website: www.electronicsworld.co.uk

Imlay, F. H. (1961). The Complete Expressions for Added Mass of a Rigid Body Moving in an Ideal Fluid (pp. 31). Washington DC: Department of the Navy David Taylor Model Basin.

InvenSense. (2010). ITG-3200 Product Specification Revision 1.4 (pp. 39). Sunnyvale, CA, USA.

Iosilevskii, G., & Weihs, D. (2008). Speed limits on Swimming of Fishes and Cetaceans. *Journal of The Royal Society Interface, 5*(20), 329-338.

Issac, M. T., Adams, S., Moqin, H., Bose, N., Williams, C. D., Bachmayer, R., & Crees, T. (2007). *Manoeuvring Experiments Using the MUN Explorer AUV.* Proceedings of the International Symposium on Underwater Technology, Tokyo, Japan, 256-262.

Jayne, B. C., & Lauder, G. V. (1994). How Swimming Fish Use Slow and Fast Muscle Fibers: Implications for Models of Vertebrate Muscle Recruitment. *Journal of Comparative Physiology A, 175*(1), 123-131.

Jobling, M. (1995). *Environmental Biology of Fishes*. London, UK: Chapman & Hall.

Journée, J. M. J., & Pinkster, J. (2002). *Introduction in Ship Hydromechanics*. MT519. Delft University of Technology.

Kang, D. S., Anderson, J. M., & Debitetto, P. A. (2000). Draper Unmanned Vehicle Systems. *Robotica, 18*(3), 263-272.

Kemp, M., Hobson, B., & Long, J. H. (2005). *MADELEINE: An Agile AUV Propelled by Flexible Fins.* Proceedings of the 14th International Symposium on Unmanned Untethered Submersible Technology (UUST). New Hampshire, USA, 1-6.

Kenaley, C. (2009). *Function: Locomotory Mechanisms, Modes of Swimming, Anguilliform Versus Carangiform Swimming, Undulation Versus Oscillation, and the Functions of Fins [unpublished lecture Notes]*. FISH/BIOL 311, Biology of Fishes. University of Washington.

Killingsworth, N. J., & Krstic, M. (2006). PID Tuning using Extremum Seeking: Online, Model-free Performance Optimization. *IEEE Control Systems, 26*(1), 70-79.

Korsmeyer, K. E., Steffensen, J. F., & Herskin, J. (2002). Energetics of Median and Paired Fin Swimming, Body and Caudal Fin Swimming, and Gait Transition in Parrotfish (Scarus Schlegeli) and Triggerfish (Rhinecanthus Aculeatus). *Journal of Experimental Biology, 205*(9), 1253-1263.

Kreith, F. (1999). *Fluid Mechanics*: CRC Press.

Kuhn, V. N., Drews, P. L. J. J., Gomes, S. C. P., Cunha, M. A. B., & Botelho, S. S. d. C. (2014). Automatic Control of a ROV for Inspection of Underwater Structures using a Low-cost Sensing. *Journal of the Brazilian Society of Mechanical Sciences and Engineering*, 1-14.

Kumph, J. M. (2000). *Maneuvering Robotic Pike.* MSc, Massachussetts Institute of Technology, USA.

Langdon, M. (2010). Huge Growth for AUV Technology. *5*(7), Retrieved Oct 26, 2014. Retrieved from http://eandt.theiet.org/magazine/2010/07/auv-market-growth.cfm

Lauder, G. V., & Tytell, E. D. (2005). Hydrodynamics of Undulatory Propulsion. In R. E. Shadwick & G. V. Lauder (Eds.), *Fish Biomechanics* (Vol. 23, pp. 425-468). Amsterdam: Elsevier, Inc.

Lauder, G. V., & Madden, P. G. A. (2006). Learning from Fish. Kinematics and Experimental Hydrodynamics for Roboticists. *International Journal of Automation and Computing, 3*(4), 325-335.

Lauder, G. V., Anderson, E. J., Tangorra, J., & Madden, P. G. A. (2007). Fish Biorobotics Kinematics and Hydrodynamics of Self Propulsion. *Journal of Experimental Biology, 210*(16), 2767-2780.

Lautrup, B. (2011). *Physics of Continuous Matter, Second Edition: Exotic and Everyday Phenomena in the Macroscopic World* (Vol. 2): CRC Press.

Law, A. M. (2009). *How to Build Valid and Credible Simulation Models.* Proceedings of the Winter Simulation Conference (WSC), Austin, TX, 24-33.

Lee, J. J. (2014). Deep-Sea Vehicle Nereus Lost 6 Miles Down. Retrieved Oct 5, 2014. Retrieved from http://news.nationalgeographic.com/news/2014/05/140512-nereus-deep-sea-vehicle-lost-ocean-technology-science/

Leonard, N. E. (1997). Stability of a Bottom-Heavy Underwater Vehicle. *Automatica, 33*(3), 331-346.

Leyendecker, S., & Ober-Blöbaum, S. (2013). A Variational Approach to Multirate Integration for Constrained Systems. In J.-C. Samin & P. Fisette (Eds.), *Multibody Dynamics* (Vol. 28, pp. 97-121): Springer Netherlands.

Liang, J., Wang, T., Wang, S., Zou, D., & Sun, J. (2005). *Experiment of Robofish Aided Underwater Archaeology.* Proceedings of the 2005 IEEE International Conference on Robotics and Biomimetics (ROBIO), Shatin, N.T., China, 499-504.

Liang, J., Wei, H., Wang, T., Wen, L., Wang, S., & Liu, M. (2009). Experimental Research on Biorobotic Autonomous Undersea Vehicle. In A. V. Inzartsev (Ed.), Underwater Vehicles (pp. 173-194). Vienna, Austria: In-Tech. Retrieved from http://www.intechopen.com/books/underwater_vehicles/experimental_research_on_biorobotic_autonomous_undersea_vehicle.

Liang, J., Wang, T., & Wen, L. (2011). Development of a Two-Joint Robotic Fish for Real-World Exploration. *Journal of Field Robotics, 28*(1), 70-79.

Licht, S. C., Polidoro, V., Flores, M., Hover, F. S., & Triantafyllou, M. S. (2004). Design and Projected Performance of a Flapping Foil AUV. *IEEE Journal of Oceanic Engineering, 29*(3), 786-794.

Licht, S. C. (2012). *Biomimetic Robots for Environmental Monitoring in the Surf Zone and in Very Shallow Water.* Proceedings of the IEEE/RSJ International Conference on Intelligent Robots and Systems (IROS), Vilamoura, Algarve, Portugal.

Lienard, D. E. (1990). *Autopilot Design for Autonomous Underwater Vehicles Based on Sliding Mode Control.* MSc, Naval Postgraduate School, Monterey, California.

Lighthill, M. J. (1960). Note on the Swimming of Slender Fish. *Journal of Fluid Mechanics, 1*, 305 - 317.

Lighthill, M. J. (1970). Aquatic Animal Propulsion of High Hydromechanical Efficiency. *Journal of Fluid Mechanics, 44*(02), 265-301.

Lighthill, M. J. (1971). Large-Amplitude Elongated-Body Theory of Fish Locomotion. *Proceedings of the Royal Society B: Biological Sciences, 179*(1055), 125-138.

Liu, H., Tang, Y., Zhu, Q., & Xie, G. (2014). Present Research Situations and Future Prospects on Biomimetic Robot Fish. *International Journal on Smart Sensing and Intelligent Systems, 7*(2).

Liu, J., & Hu, H. (2003). *Simulator Building and Parameter Optimization of an Autonomous Robotic Fish.* Proceedings of the Chinese Automation & Computing Society, CACSCUK, Luton, England, 317-322.

Liu, J., & Hu, H. (2004). A 3D Simulator for Autonomous Robotic Fish. *International Journal of Automation and Computing, 1*(1), 42-50.

Liu, J., Dukes, I., & Hu, H. (2005). *Novel Mechatronics Design for a Robotic Fish.* Proceedings of the 2005 IEEE/RSJ International Conference on Intelligent Robots and Systems (IROS 2005). , Edmonton, Alberta, Canada, 807-812.

Liu, J., & Hu, H. (2005). *Mimicry of Sharp Turning Behaviours in a Robotic Fish.* Proceedings of the 2005 IEEE International Conference on Robotics and Automation, Barcelona, Spain, 6.

Liu, J., & Hu, H. (2010). Biological Inspiration: From Carangiform Fish to Multi-Joint Robotic Fish. *Journal of Bionic Engineering, 7*(1), 35-48.

Liu, J., & Wang, X. (2011). Fuzzy Sliding Mode Control *Advanced Sliding Mode Control for Mechanical Systems* (pp. 233-279): Springer Berlin Heidelberg.

Loueipour, M., & Hadian, H. (2011). *Effect of Considering Sensors and Actuators Modeling on the Design of PID Controllers for an Autonomous Underwater Vehicle.* Proceedings of the 2nd International Conference on Control, Instrumentation and Automation (ICCIA), 2011, Shiraz, Iran, 582-587.

Low, K. H., Zhou, C., & Zhong, Y. (2009). Gait Planning for Steady Swimming Control of Biomimetic Fish Robots. *Advanced Robotics, 23*(7-8), 805-829.

Low, K. H., Chong, C. W., & Zhou, C. (2010). *Performance Study of a Fish Robot Propelled by a Flexible Caudal Fin.* Proceedings of the IEEE International Conference on Robotics and Automation, Alaska, USA.

Low, K. H. (2011). *Current and Future Trends of Biologically Inspired Underwater Vehicles.* Proceedings of the Defense Science Research Conference and Expo (DSR), Singapore 1-8.

Mandujano, R. A. (2002). *Design Study of Flapping Foil Propulsion for an Odysey Class Autonomous Underwater Vehicle.* BSc, Massachusetts Institute of Technology, USA.

Maria, A. (1997). *Introduction to Modeling and Simulation.* Proceedings of the 1997 Winter Simulation Conference, Atlanta, Georgia, USA.

Marthiniussen, R., Vestgard, K., Klepaker, R. A., & Storkersen, N. (2004). *HUGIN-AUV Concept and Operational Experiences to Date.* Proceedings of the MTTS/IEEE TECHNO-OCEAN '04, Kobe, Japan, 846-850.

Martono, W. (2006). *DC Servo Motor with PID Controller*. MCT 3210 Control Systems. Laboratory Manual. Department of Mechatronics Engineering. International Islamic University Malaysia.

Matko, D., Zupancic, B., & Karba, R. (1992). *Simulation and Modelling of Continuous Systems : A Case Study Approach*. New York: Prentice Hall.

Mazlan, A. N. A., & McGookin, E. W. (2012). *Modelling and Control of a Biomimetic Autonomous Underwater Vehicle.* Proceedings of the 12th International Conference on Control Automation Robotics & Vision (ICARCV), Guangzhou, China, 88-93.

McGookin, E. W. (1997). *Optimisation of Sliding Mode Controllers for Marine Applications: A Study of Method and Implementation Issues.* PhD, University of Glasgow.

McGookin, E. W., Murray-Smith, D. J., Li, Y., & Fossen, T. I. (2000a). Ship Steering Control System Optimisation using Genetic Algorithms. *Control Engineering Practice, 8*(4), 429-443.

McGookin, E. W., Murray-Smith, D. J., Li, Y., & Fossen, T. I. (2000b). The Optimization of a Tanker Autopilot Control System using Genetic Algorithms. *Transactions of the Institute of Measurement and Control, 22*(2), 141-178.

Melsaac, K. A., & Ostrowski, J. P. (1999). *A Geometric Approach to Anguilliform Locomotion: Modelling of an Underwater Eel Robot.* Proceedings of the 1999 IEEE International Conference on Robotics and Automation Detroit, MI 2843-2848.

Menciassi, A., Valdastri, P., Harada, K., & Dario, P. (2011). Single and Multiple Robotic Capsules for Endoluminal Diagnosis and Surgery. In J. Rosen, B. Hannaford & R. M. Satava (Eds.), *Surgical Robotics* (pp. 313-354): Springer US.

Microchip Technology Inc. (2009). Microchip PIC16F87/88 Data Sheet: 18/20/28-Pin Enhanced Flash Microcontrollers with nanoWatt Technology.

Microchip Technology Inc. (2010). Microchip dsPIC30F3014/4013 Data Sheet: High-Performance, 16-bit Digital Signal Controllers.

Millard, N., McPhail, S., Pebody, M., Perrett, J., Stevenson, P., & Webb, A. (1997). *Autosub-1. From Test-tank to Autonomy and the Science Beyond.* Proceedings of the 7th International Conference on Electronic Engineering in Oceanography, Southampton, UK, 1-8.

Mohd Aras, M. S. b., Abdullah, S. S. b., Shafei, S. S. b., Rashid, M. Z. A., & Jamali, A. (2012). Investigation and Evaluation of Low Cost Depth Sensor System Using Pressure Sensor for Unmanned Underwater Vehicle. *Majlesi Journal of Electrical Engineering, 6*(2), 1-12.

Molnar, L., Omerdic, E., & Toal, D. (2007). Guidance, Navigation and Control System for the Tethra Unmanned Underwater Vehicle. *International Journal of Control, 80*(7), 1050-1076.

Mora, C., Menozzi, D., & Merigo, A. (2011). *Exploring the Potential Competition in the Salmon Industry: A Scenario Analysis of Genetically Modified Fish Marketing.* Proceedings of the EAAE 2011 Congress Change and Uncertainty. Challenges for Agriculture, Food and Natural Resources, Zurich, Switzerland.

Morgansen, K. A., Triplett, B. I., & Klein, D. J. (2007). Geometric Methods for Modeling and Control of Free-Swimming Fin-Actuated Underwater Vehicles. *IEEE Transactions on Robotics, 23*(6), 1184-1199.

Moyle, P. B., & Cech Jr, J. J. (2004). *Fishes: An Introduction to Ichthyology* (5th ed.): Prentice Hall.

Murray-Smith, D. J. (1995). *Continuous System Simulation*: Chapman & Hall.

Naeem, W., Sutton, R., Ahmad, S. M., & Burns, R. S. (2003). A Review of Guidance Laws Applicable to Unmanned Underwater Vehicles. *Journal of Navigation, 56(1)*, 15-29.

Navarro-Serment, L. E., Grabowski, v., Paredis, C. J. J., & Khosla, P. K. (1999). *Modularity in Small Distributed Robots.* Proceedings of the SPIE conference on Sensor Fusion and Decentralized Control in Robotic Systems II, 297--306.

Nguyen, B., Hopkin, D., & Yip, H. (2008). Autonomous Underwater Vehicles: A Transformation in Mine Counter-Measure Operations. *Defense & Security Analysis, 24*(3), 247-266.

Nguyen, P. L., Do, V. P., & Lee, B. R. (2013). Dynamic Modeling and Experiment of a Fish Robot with a Flexible Tail Fin. *Journal of Bionic Engineering, 10*(1), 39-45.

Nguyen, T. T., Nguyen, N. P., & Dang, M. N. (2011). *Swimming of Robotic Fish based Biologically-Inspired Approach.* Proceedings of the 11th International Conference on Control, Automation and Systems (ICCAS), 2011, 625-630.

Niku, S. B. (2001). *Introduction to Robotics: Analysis, Systems, Applications*: Prentice Hall.

Niku, S. B. (2011). *Introduction to Robotics: Analysis, Systems, Applications* (2nd ed.). Hoboken, NJ: Wiley.

Oberschelp, O., & Vocking, H. (2004). *Multirate Simulation of Mechatronics Systems.* Proceedings of the IEEE International Conference on Mechatronics, ICM '04, Istanbul, Turkey, 404-409.

Otten, K. (2008). AN1145 Using a USB Flash Drive with an Embedded Host (pp. 14): Microchip Technology Inc.

Palmer, A., Hearn, G. E., & Stevenson, P. (2009). A Theoretical Approach to Facilitating Transition Phase Motion in a Positively Buoyant Autonomous Underwater Vehicle. *Transactions of RINA, Part A - International Journal of Maritime Engineering (IJME), 151*.

Panish, R. (2009). *Dynamic Control Capabilities and Developments of the Bluefin Robotics AUV Fleet.* Proceedings of the 16th International Symposium Unmanned Untethered Submersible Technology, Durham, NH.

Pascoal, A., Oliveira, P., Silvestre, C., Bjerrum, A., Ishoy, A., Pignon, J. P., Ayela, G., & Petzelt, C. (1997). MARIUS: An Autonomous Underwater Vehicle for Coastal Oceanography. *IEEE Robotics & Automation Magazine, 4*(4), 46-59.

Pearce, J. G., Crosbie, R. E., Zenor, J. J., Bednar, R., Word, D., & Hingorani, N. G. (2009). *Developments and Applications of Multi-rate Simulation.* Proceedings of the 11th International Conference on Computer Modelling and Simulation, UKSIM '09. , Cambridge, UK, 129-133.

Pekarek, S. D., Wasynczuk, O., Walters, E. A., Jatskevich, J. V., Lucas, C. E., Ning, W., & Lamm, P. T. (2004). An Efficient Multirate Simulation Technique for Power-Electronic-based Systems. *IEEE Transactions on Power Systems, 19*(1), 399-409.

Petersen, J. K. (2007). Sonar.Understanding Surveillance Technologies: Spy Devices, Privacy, History & Applications (2nd ed., pp. 223-294): CRC Press.

Pettersen, K. Y., & Egeland, O. (1999). Time-Varying Exponential Stabilization of the Position and Attitude of an Underactuated Autonomous Underwater Vehicle. *IEEE Transactions on Automatic Control, 44*(1), 112-115.

Pololu. (2005). Micro Serial Servo Controller User Guide.

Precision Microdrives. (n.d.). Precision Microdrives Technical Datasheet for 212-404, from https://catalog.precisionmicrodrives.com/order-parts/product/212-404-12mm-dc-gearmotor-24mm-type

Purcell, M., Gallo, D., Packard, G., Dennett, M., Rothenbeck, M., Sherrell, A., & Pascaud, S. (2011). *Use of REMUS 6000 AUVs in the search for the Air France Flight 447.* Proceedings of the OCEANS 2011, Waikoloa, HI, 1-7.

Robinson, S. (1997). *Simulation Model Verification and Validation: Increasing the Users' Confidence.* Proceedings of the 29th conference on Winter simulation, Atlanta, Georgia, USA, 53-59.

Rohr, J. J., & Fish, F. E. (2004). Strouhal Numbers and Optimization of Swimming by Odontocete Cetaceans. *Journal of Experimental Biology, 207*(Pt 10), 1633-1642.

Rome, L., Swank, D., & Corda, D. (1993). How Fish Power Swimming. *Science, 261*(5119), 340-343.

Roper, D. T., Sharma, S., Sutton, R., & Culverhouse, P. (2011). A Review of Developments Towards Biologically Inspired Propulsion Systems for Autonomous Underwater Vehicles. *Proceedings of the Institution of Mechanical Engineers, Part M: Journal of Engineering for the Maritime Environment, 225*(2), 77-96.

Rossi, C., Colorado, J., Coral, W., & Barrientos, A. (2011a). Bending Continuous Structures with SMAs: a Novel Robotic Fish Design. *Bioinspiration & Biomimetics, 6*(4), 045005.

Rossi, C., Coral, W., Colorado, J., & Barrientos, A. (2011b). *A Motor-less and Gear-less Bio-mimetic Robotic Fish Design.* Proceedings of the 2011 IEEE International Conference on Robotics and Automation (ICRA), Shanghai, China, 3646-3651.

Rowell, D. (2002). *State-Space Representation of LTI Systems*. 2.14 Analysis and Design of Feedback Control Systems. Massachusetts Institute of Technology, 1-18.

Rufo, M., & Smithers, M. (2011). GhostSwimmer™ AUV: Applying Biomimetics to Underwater Robotics for Achievement of Tactical Relevance. *Biomimetics and Marine Technology, 45,* 24-30.

Sanchez, H. A. (2014). The Search for the Flight MH370 Goes to the Next Stage: A Monumental Task. Retrieved Oct 6, 2014. Retrieved from http://gulfnews.com/multimedia/graphics/the-search-for-mh370-goes-to-next-stage-1.1329687

Sargent, R. G. (2010). *Verification and Validation of Simulation Models.* Proceedings of the 2010 Winter Simulation Conference (WSC), Baltimore, MD, 166-183.

Saunders, A., & Nahon, M. (2002). *The Effect of Forward Vehicle Velocity on Through-Body AUV Tunnel Thruster Performance.* Proceedings of the MTS/IEEE OCEANS '02, 250-259.

Sazawa, M., Yamada, T., Ohishi, K., & Katsura, S. (2010). Anti-Windup Algorithm with Priority to Proportional Control Output of Speed PI Controller for Precision Servo System. *Electrical Engineering in Japan, 170*(3), 57-64.

Schnoor, R. T. (2003). *Modularized Unmanned Vehicle Packages for the Littoral Combat Ship Mine Countermeasures Missions.* Proceedings of the OCEANS 2003, San Diego, CA, USA, 1437-1439.

Schultz, W. W., & Webb, P. W. (2002). Power Requirements of Swimming: Do New Methods Resolve Old Questions? *Integrative and Comparative Biology, 42*(5), 1018-1025.

Scottish Salmon Producers' Organisation. (2012). Salmon Facts. Retrieved Dec 1, 2014, from http://scottishsalmon.co.uk/facts-figures/

Sellers, W. (2010). A Titanic Tale: A Former Alvin Pilot Recalls His 1986 Dives on the Shipwreck. *Oceanus Magazine* Retrieved Sept 26, 2014, from http://www.whoi.edu/oceanus/feature/a-titanic-tale

Seto, M. L., Paull, L., & Saeedi, S. (2013). Introduction to Autonomy for Marine Robots. In M. L. Seto (Ed.), *Marine Robot Autonomy* (pp. 1-46): Springer New York.

Sfakiotakis, M., Lane, D. M., & Davies, J. B. C. (1999). Review of Fish Swimming Modes for Aquatic Locomotion. *IEEE Journal of Oceanic Engineering, 24*(2), 237-252.

Shatara, S. W. (2011). Development of Small Biomimetic Robotic Fish with Onboard Fine-Grained Localization

Shi, L., Guo, S., Mao, S., Li, M., & Asaka, K. (2013). Development of a Lobster-Inspired Underwater Microrobot. *International Journal of Advanced Robotic Systems, 10*(44).

Silva, J., & Sousa, J. (2008). Models for Simulation and Control of Underwater Vehicles H. Aschemann (Ed.) *New Approaches in Automation and Robotics* Retrieved from http://www.intechopen.com/books/new_approaches_in_automation_and_robotics/models_for_simulation_and_control_of_underwater_vehicles doi:10.5772/5395

Silva, J. d., Terra, B., Martins, R., & Sousa, J. a. B. d. (2007). *Modeling and Simulation of the LAUV Autonomous Underwater Vehicle.* Proceedings of the 13th IEEE IFAC International Conference on Methods and Models in Automation and Robotics (MMAR'07), Szczecin, Poland, 1-6.

Singh, H., Yoerger, D., & Bradley, A. (1997). *Issues in AUV Design and Deployment for Oceanographic Research.* Proceedings of the 1997 IEEE International Conference on Robotics and Automation Albuquerque, New Mexico, 1857-1862.

Smith, W. H. F., & Marks, K. M. (2014). Seafloor in the Malaysia Airlines Flight MH370 Search Area. *Eos, Transactions American Geophysical Union, 95*(21), 173-174.

Sonardyne. (2014). Exceptional Imagery Bluefin Robotics AUV with Sonardyne Solstice. *Marine Technology Reporter, 57,* 42 - 43.

Sparkfun Electronics. (n.d.). 9 Degrees of Freedom - Sensor Stick from http://www.sparkfun.com/products/10724

Standen, E. M., & Lauder, G. V. (2005). Dorsal and Anal Fin Function in Bluegill Sunfish Lepomis Macrochirus: Three-Dimensional Kinematics during Propulsion and Maneuvering. *Journal of Experimental Biology, 208*(14), 2753-2763.

Stead, S. M., & Laird, L. (2002). *The Handbook of Salmon Farming*: Praxis Publishing.

Steenson, L., Phillips, A., Rogers, E., Furlong, M., & Turnock, S. R. (2011). *The Performance of Vertical Tunnel Thrusters on an Autonomous Underwater Vehicle Operating Near the Free Surface in Waves.* Proceedings of the 2nd International Symposium on Marine Propulsors, SMP.

Steenson, L. V. (2011). *Preliminary Results of a Hover Capable AUV Attempting Transitional Flight.* Proceedings of the 17th International Unmanned Untethered Submersible Technology Conference, USA.

Stevenson, P., Furlong, M., & Dormer, D. (2007). *AUV Shapes - Combining the Practical and Hydrodynamic Considerations.* Proceedings of the OCEANS 2007, 1-6.

Stevenson, P., Furlong, M., & Dormer, D. (2009). *AUV Design: Shape, Drag and Practical Issues.* Proceedings of the Oceans '07, Piscataway, NJ, USA, 41–44.

Størkersen, N. J., & Hasvold, Ø. (2004). *Power sources for AUVs.* Proceedings of the Science and Defence Conference, Brest, France.

Strutt, J. E. (2006). *Report of the Inquiry into the Loss of Autosub2 under the Fimbulisen*. Tech. Rep., (12). National Oceanography Centre Southampton, Southampton, UK, 39.

Tan, C. S., Sutton, R., & Chudley, J. (2007). An Integrated Collision Avoidance System for Autonomous Underwater Vehicles. *International Journal of Control, 80*(7), 1027-1049.

Tang, J., & Wardle, C. S. (1992). Power Output of Two Sizes of Atlantic Salmon (Salmo Salar) at Their Maximum Sustained Swimming Speeds. *Journal of Experimental Biology, 166*(33-46).

Tao, T., Liang, Y.-C., & Taya, M. (2006). Bio-inspired Actuating System for Swimming using Shape Memory Alloy Composites. *International Journal of Automation and Computing, 3*(4), 366-373.

Techet, A., Hover, F., & Triantafyllou, M. (2003). Separation and Turbulence Control in Biomimetic Flows. *Flow, Turbulence and Combustion, 71*(1-4), 105-118.

Techet, A. H. (2008). Propulsive Performance of Biologically Inspired Flapping Foils at High Reynolds Numbers. *Journal of Experimental Biology, 211*(Pt 2), 274-279.

Texas Instruments. (1995). SN754410 Quadruple Half-H Driver.

The Mathworks Inc. (2014). Image Processing Toolbox Retrieved 2nd February, 2014, from http://uk.mathworks.com/help/images/functionlist.html

Tipsuwan, Y., & Mo-Yuen, C. (1999). *Fuzzy Logic Microcontroller Implementation for DC Motor Speed Control.* Proceedings of the 25th Annual Conference of the IEEE Industrial Electronics Society, San Jose, California, USA 1271-1276.

Triantafyllou, G. S., Triantafyllou, M. S., & Grosenbaugh, M. A. (1993). Optimal Thrust Development in Oscillating Foils with Application to Fish Propulsion. *Journal of Fluids and Structures, 7*(2), 205-224.

Triantafyllou, G. S., & Triantafyllou, M. S. (1995). An Efficient Swimming Machine. *Scientific American, 272*(3), 64.

Triantafyllou, M. S., Triantafyllou, G. S., & Yue, D. K. P. (2000). Hydrodynamics of Fishlike Swimming. *Annual Review of Fluid Mechanics, 32*, 33 – 53.

Triantafyllou, M. S., & Hover, F. S. (2003). Maneuvering and Control of Marine Vehicles Retrieved from http://ocw.mit.edu/courses/mechanical-engineering/2-154-maneuvering-and-control-of-surface-and-underwater-vehicles-13-49-fall-2004/lecture-notes/1349_notes.pdf

Triplett, B. (2008). *Multiple Vehicle Coordination and Cooperative Estimation for Target Tracking with Applications to Autonomous Underwater Vehicle Systems.* PhD, University of Washington, Ann Arbor. ProQuest Dissertations & Theses A&I database.

Tytell, E. D., & Lauder, G. V. (2004). The Hydrodynamics of Eel Swimming: I. Wake Structure. *Journal of Experimental Biology, 207*(Pt 11), 1825-1841.

Tytell, E. D. (2010). Do Trout Swim Better than Eels Challenges for Estimating Performance based on the Wake of Self-Propelled Bodies. In G. Taylor, M. S. Triantafyllou & C. Tropea (Eds.), *Animal Locomotion* (pp. 63-74): Springer.

Utkin, V. (2008). Sliding Mode Control: Mathematical Tools, Design and Applications. In P. Nistri & G. Stefani (Eds.), *Nonlinear and Optimal Control Theory* (Vol. 1932, pp. 289-347): Springer Berlin Heidelberg.

Verspoor, E., Stradmeyer, L., & Nielsen, J. L. (2007). *The Atlantic Salmon: Genetics, Conservation and Management*. Oxford: Blackwell Publishing Ltd.

Videler, J. J., & Weihs, D. (1982). Energetic Advantages of Burst-And-Coast Swimming of Fish at High Speeds. *Journal of Experimental Biology, 97*, 169-178.

Videler, J. J. (1993). *Fish Swimming*. London: Chapman & Hall.

von Alt, C., Allen, B., Austin, T., & Stokey, R. (1994). *Remote Environmental Measuring Units.* Proceedings of the 1994 Symposium on Autonomous Underwater Vehicle Technology, Cambridge, MA, 13-19.

von Alt, C., Allen, B., Austin, T., Forrester, N., Goldsborough, R., Purcell, M., & Stokey, R. (2001). *Hunting for Mines with REMUS: A High Performance, Affordable, Free Swimming Underwater Robot.* Proceedings of the MTS/IEEE Conference and Exhibition OCEANS, 2001, Honolulu, HI, 117-122.

von Alt, C. (2003). *REMUS 100 Transportable Mine Countermeasure Package.* Proceedings of the OCEANS 2003, San Diego, CA, USA, 1925-1930.

Waldron, K., & Schmiedeler, J. (2008). Kinematics. In B. Siciliano & O. Khatib (Eds.), *Springer Handbook of Robotics* (pp. 9-33): Springer Berlin Heidelberg.

Wang, J., Alequin-Ramos, F., & Xiaobo, T. (2011). *Dynamic Modeling of Robotic Fish and Its Experimental Validation.* Proceedings of the 2011 IEEE/RSJ International Conference on Intelligent Robots and Systems (IROS), San Francisco, CA, 588-594.

Wang, J., McKinley, P. K., & Tan, X. (2012). *Dynamic Modeling of Robotic Fish With a Flexible Caudal Fin.* Proceedings of the ASME 2012 5th Annual Dynamic Systems and Control Conference joint with the JSME 2012 11th Motion and Vibration Conference, Fort Lauderdale, Florida, USA, 203-212.

Wang, P., Song, B., Wang, Y., & Zhang, L. (2007). *Application of Concurrent Subspace Design to Shape Design of Autonomous Underwater Vehicle.* Proceedings of the 8th ACIS International Conference on Software Engineering, Artificial Intelligence, Networking, and Parallel/Distributed Computing, 2007, Qingdao, China, 1068-1071.

Wang, T., Liang, J., Shen, G., & Tan, G. (2005). *Stabilization Based Design and Experimental Research of a Fish Robot.* Proceedings of the 2005 IEEE/RSJ International Conference on Intelligent Robots and Systems, IROS, Edmonton, Alberta, Canada, 954-959.

Wang, W. H., Chen, X. Q., Marburg, A., Chase, J. G., & Hann, C. E. (2008a). *A Low-Cost Unmanned Underwater Vehicle Prototype for Shallow Water Tasks.* Proceedings of the IEEE/ASME International Conference on Mechtronic and Embedded Systems and Applications, MESA 2008, Beijing, China, 204-209.

Wang, Z., Hang, G., Li, J., Wang, Y., & Xiao, K. (2008b). A Micro-Robot Fish with Embedded SMA Wire Actuated Flexible Biomimetic Fin. *Sensors and Actuators A: Physical, 144*(2), 354-360.

Watts, C. M., McGookin, E. W., & Macauley, M. (2007). *Modelling and Control of a Biomimetic Underwater Vehicle with a Tendon Drive Propulsion System.* Proceedings of the OCEANS 2007, Aberdeen, UK, 1-6.

Watts, C. M., & McGookin, E. W. (2008). *Modeling and Simulation of a Biomimetic Underwater.* Proceedings of the Summer Simulation Multi-Conference 2008 - Grand Challenges in Modelling and Simulation, Edinburgh, UK.

Watts, C. M. (2009). *A Comparison Study of Biologically Inspired Propulsion Systems for an Autonomous Underwater Vehicle.* PhD, Glasgow University.

Watts, C. M., & McGookin, E. W. (2013). Surge Performance of an Underwater Vehicle with a Biomimetic Tendon Drive Propulsion System. *Proceedings of the Institution of Mechanical Engineers, Part M: Journal of Engineering for the Maritime Environment*.

Webb, A. P., Phillips, C. W. G., Hudson, D. A., & Turnock, S. R. (2012). *Can Lighthill's Elongated Body Theory Predict Hydrodynamic Forces in Underwater Undulatory Swimming?* Proceedings of the 9th Conference of the International Sports Engineering Association (ISEA), Lowell, Massachusetts, USA, 724-729.

Webb, P. W. (1984). Body Form, Locomotion and Foraging in Aquatic Vertebrates. *American Zoologist, 24*(1), 107-120.

Webb, P. W. (1988). 'Steady' Swimming Kinematics of Tiger Musky, an Esociform Accelerator, and Rainbow Trout, a Generalist Cruiser. *Journal of Experimental Biology, 138*, 51-69.

Webster, C. (2012). Action Analysis for Animators (pp. 408): Focal Press.

Weihs, D. (1993). Stability of Aquatic Animal Locomotion. *Contemporary Mathematics, 141*, 443–461.

Weihs, D. (2002). Stability Versus Maneuverability in Aquatic Locomotion. *Integr. Comp. Biol., 42*, 127–134.

Whitcomb, L. L., Jakuba, M. V., Kinsey, J. C., Martin, S. C., Webster, S. E., Howland, J. C., Taylor, C. L., Gomez-Ibanez, D., & Yoerger, D. R. (2010). *Navigation and Control of the Nereus Hybrid Underwater Vehicle for Global Ocean Science to 10,903 m Depth: Preliminary results.* Proceedings of the 2010 IEEE International Conference on Robotics and Automation (ICRA) Anchorage, Alaska, USA, 594-600.

Whitehead, P. J. P., Bauchot, M.-L., Hureau, J.-C., Nielsen, J., & Tortonese, E. (Eds.). (1989). *Fishes of the North-eastern Atlantic and the Mediterranean* (Vol. 1): Unesco.

Wise, J. (2011). How Air France 447's Missing Wreckage Was Found—and Why It Took So Long. Retrieved Sept 30, 2014. Retrieved from Popular Mechanics website: http://www.popularmechanics.com/technology/engineering/robots/how-air-france-447s-missing-wreckage-was-found-5583302

Witten, P. E., Gil-Martens, L., Hall, B. K., Huysseune, A., & Obach, A. (2005). Compressed Vertebrae in Atlantic Salmon Salmo Salar: Evidence for Metaplastic Chondrogenesis as a Skeletogenic Response Late in Ontogeny. *Diseases of Aquatic Organisms, 64*, 237–246.

Worrall, K. J. (2008). *Guidance and Search Algorithms for Mobile Robots: Application and Analysis within the Context of Urban Search and Rescue.* PhD, University of Glasgow.

Xu, J.-X., Ren, Q., Gao, W., & Niu, X.-L. (2012). *Mimicry of Fish Swimming Patterns in a Robotic Fish.* Proceedings of the IEEE International Symposium on Industrial Electronics (ISIE), 2012 1274-1279.

Yamamoto, I., Terada, Y., Nagamatu, T., & Imaizumi, Y. (1995). Propulsion System with Flexible Rigid Oscillating Fin. *IEEE Journal of Oceanic Engineering, 20*(1), 23-30.

Yoerger, D. R., & Slotine, J. J. E. (1991). *Adaptive Sliding Control of an Experimental Underwater Vehicle.* Proceedings of the 1991 IEEE International Conference on Robotics and Automation, Sacramento, California, 2746-2751 vol.2743.

Young, D. F., Munson, B. R., Okiishi, T. H., & Huebsch, W. W. (2007). *A Brief Introduction To Fluid Mechanics* (Vol. 4th): John Wiley & Sons.

Young, J. Z. (1962). *The Life of Vertebrates* (2nd ed.). New York: Oxford University Press.

Yu, J., Wang, L., & Tan, M. (2005a). *A Framework for Biomimetic Robot Fish's Design and its Realization.* Proceedings of the American Control Conference, Portland, Oregon, 1593-1598.

Yu, J., Wang, S., & Tan, M. (2005b). A Simplified Propulsive Model of Bio-mimetic Robot Fish and its Realization. *Robotica, 23*(1), 101-107.

Yu, J., Wang, L., & Tan, M. (2007). Geometric Optimization of Relative Link Lengths for Biomimetic Robotic Fish. *IEEE Transactions on Robotics, 23*(2), 382-386.

Yu, J., Liu, L., Wang, L., Tan, M., & Xu, D. (2008). Turning Control of a Multilink Biomimetic Robotic Fish. *IEEE Transactions on Robotics, 24*(1), 201-206.

Yu, J., Tan, M., & Zhang, J. (2010). *Fish-Inspired Swimming Simulation and Robotic Implementation.* Proceedings of the 41st International Symposium on Robotics (ISR) and 2010 6th German Conference on Robotics (ROBOTIK), Munich, Germany, 1-6.

Yuh, J. (2000). Design and Control of Autonomous Underwater Robots: A Survey. *Autonomous Robots, 8*(1), 7-24.

Yuh, J., Marani, G., & Blidberg, D. R. (2011). Applications of Marine Robotic Vehicles. *Intelligent Service Robotics, 4*(4), 221-231.

Zhu, D., & Sun, B. (2013). The Bio-Inspired Model Based Hybrid Sliding-Mode Tracking Control for Unmanned Underwater Vehicles. *Engineering Applications of Artificial Intelligence, 26*(10), 2260-2269.

Appendix A

RoboSalmon Circuit Schematics

Appendix A presents the circuit schematics for all electronic system within *RoboSalmon* vehicle. As been mentioned in Chapter 3, the body section contains 2 watertight enclosures (i.e. upper and lower) which are intended to be used for housing the electronic systems circuit board for the vehicle. In addition, the tail enclosure will consists of layers of circuit boards that responsible to generate the fish like undulation motion.

Upper enclosure

The *RoboSalmon* main microcontroller, dsPIC30F4013 is situated inside the upper enclosure among others electrical components such as current sensor, data logger and inertial measurement unit. This microcontroller is used to send commands to the microcontrollers placed in other enclosures via CAN bus. In other hand, it collects all sensors data via varies of communication modules and stores the date into USB drive by using vinculum device. The 12 V battery pack also has been positioned in this enclosure where it has been used to regulate to three different voltage level (3.3/5/12 V) to power *RoboSalmon* electrical components.

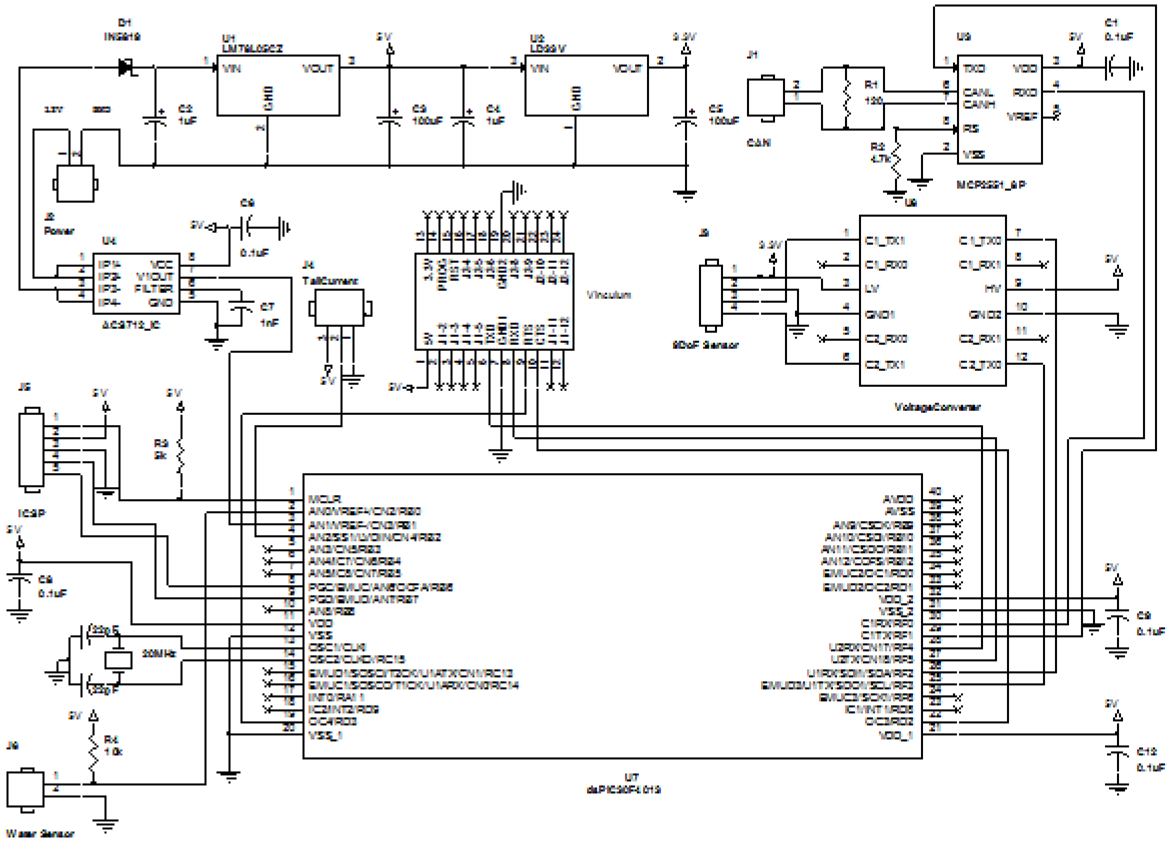

Figure A.1: Upper enclosure circuit schematic

Lower enclosure

The lower enclosure circuit schematic shown in Figure A.2 comprises of PIC18F2480 microcontroller, current and pressure sensor and servo controller. These components are powered by the battery in the upper enclosure. The current consumed by the components in the tail part is measured using the current sensor and *RoboSalmon* vehicle depth is calculated using the pressure sensor. This lower enclosure microcontroller received commands from the upper enclosure thru the CAN bus and send it to the servo controller where it is used to control the head and pectoral fins angles independently.

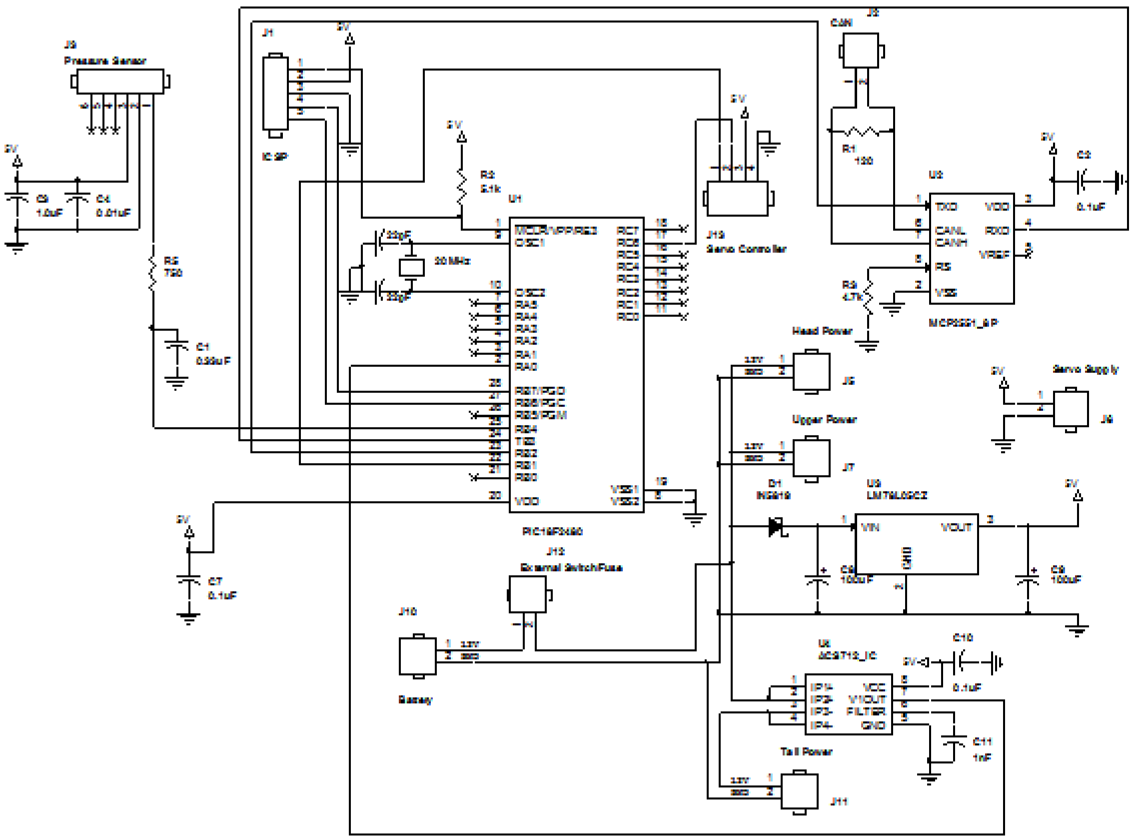

Figure A.2: Lower enclosure circuit schematic

Tail Enclosure

The tail design circuit schematics are divided into five layers due to size constraint (see Table 3.2) where the microcontrollers communicate thru RS485 serial interface. All circuits in tail enclosure are powered by the battery in the upper enclosure where two different voltage levels (5/12 V) are used to operate the electrical components and motors. The first layer known as tail main circuit schematic is shown in Figure A.3 consists of PIC18F25K80, CAN and RS485 transceiver. This circuit receives commands (i.e. tail beat amplitude, tail beat frequency and tail deflection angle) from the circuit in the upper enclosure thru the CAN bus.

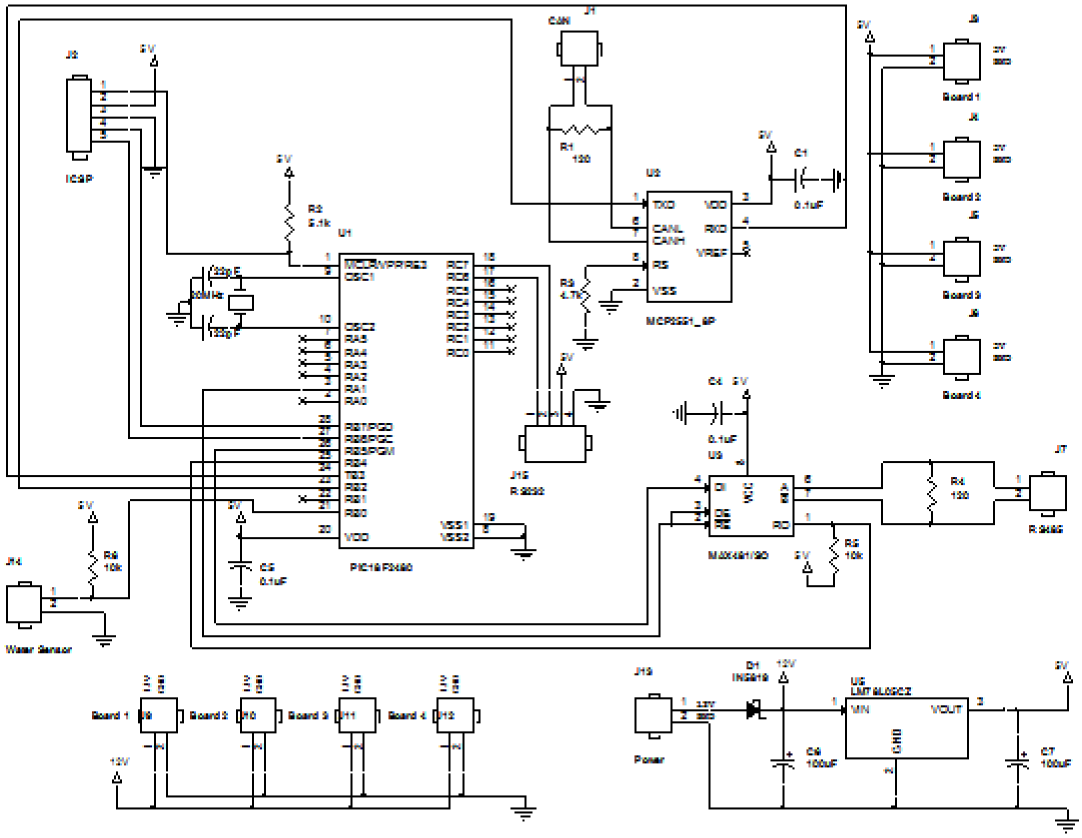

Figure A.3: Tail main circuit schematic

Then, it passed this information to microcontrollers in in the other layers illustrated in Figure A.4 and Figure A.5 thru the RS485 communication. The circuit schematic in Figure A.4 has been designed for layer 2, 3 and 4 while circuit schematic in Figure A.5 has been designed for layer 5. The difference between these two circuit schematic is the termination resistor at the end node. The microcontrollers in layer 2, 3, 4 and 5 are used to drive the motor to perform the undulation motion

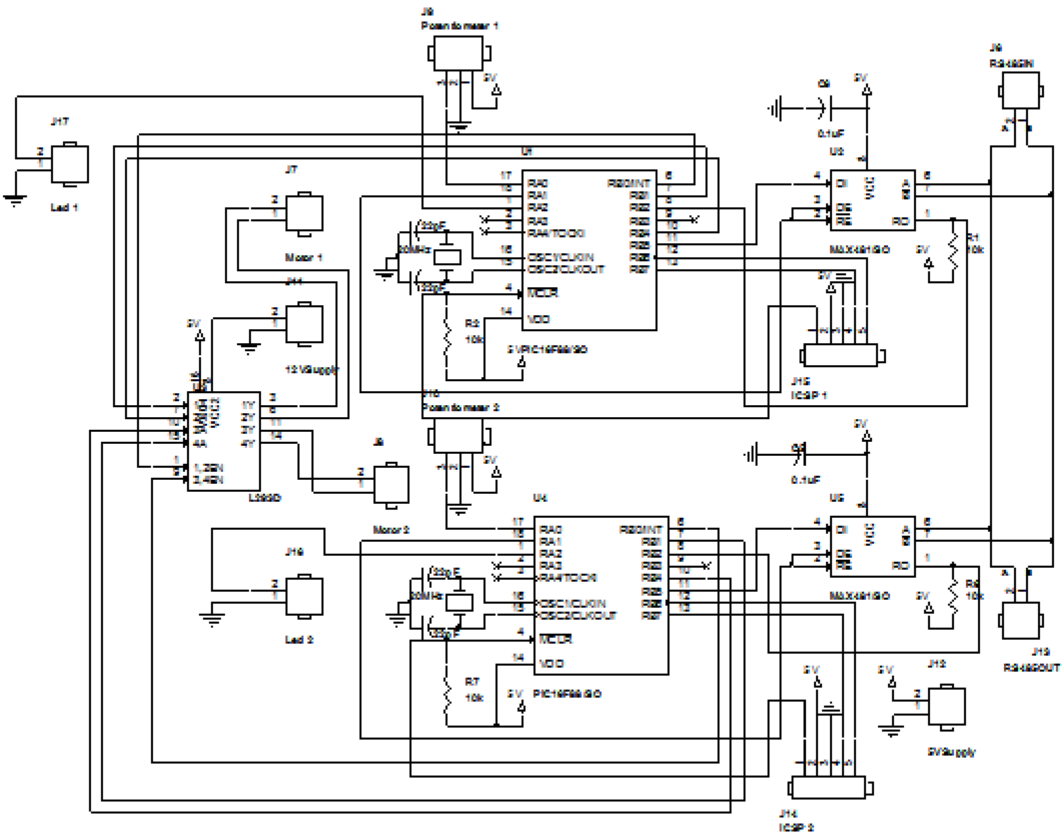

Figure A.4: Tail layer 1, 2, 3 circuit schematic

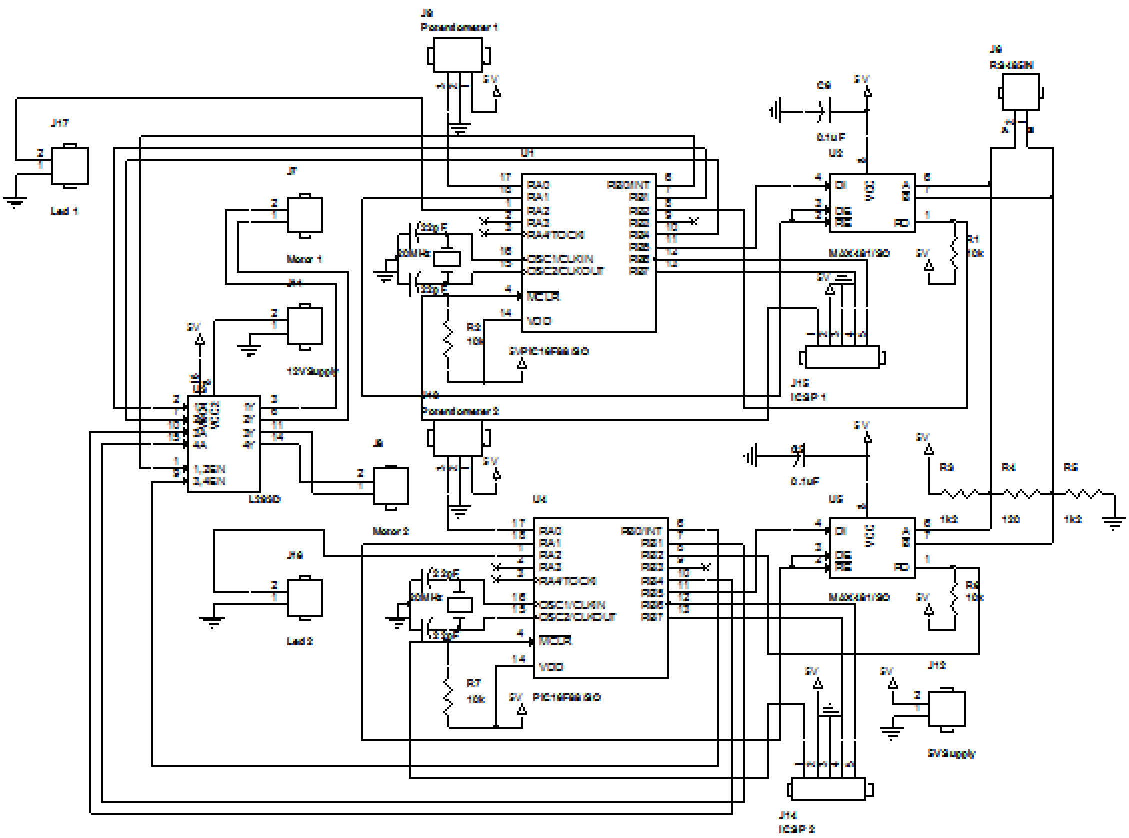

Figure A.5: Tail layer 4 circuit schematic

Appendix B

RoboSalmon dimensions and specifications

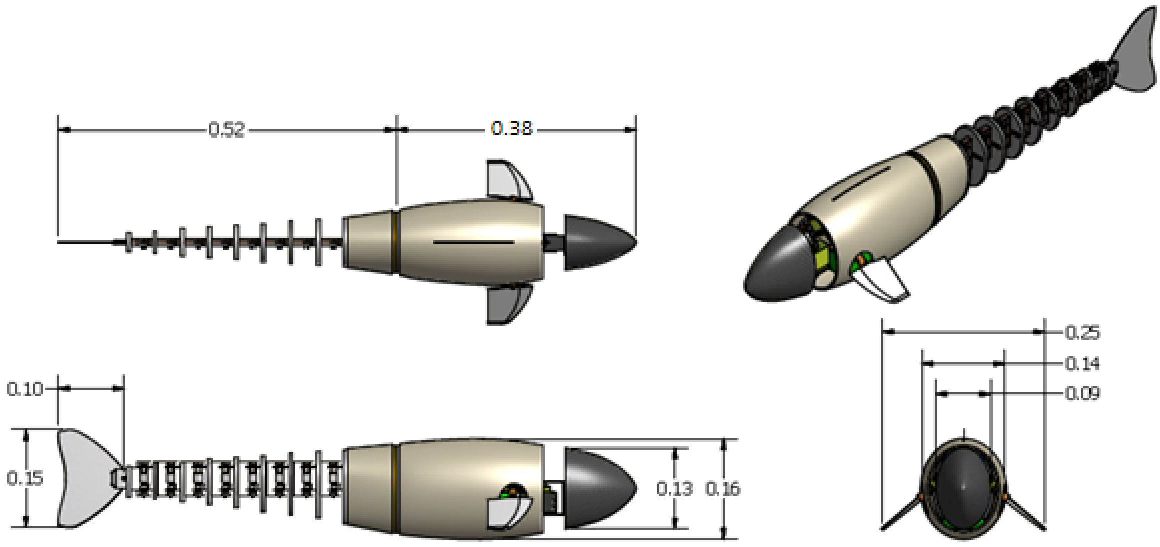

Figure B.1: *RoboSalmon* Dimensions

Table B.1: *RoboSalmon* Specifications

Vehicle specification	
Total Mass	4.3 Kg
Tail Mass	1.66 Kg
Body Mass	2.64 Kg
Power Source	12V 2600 mAh NiMH battery pack

Appendix C

Mathematical Model Equations

This appendix includes the equations used within the mathematical model of the *RoboSalmon*. The state equation for each of the 6 degrees of freedom is shown in Equations (C.1) to (C.6).

Surge: $$\dot{u} = \frac{mvr - mwq + X_t + X_d - Y_{\dot{v}}vr + Z_{\dot{w}}wq}{m - X_{\dot{u}}} \tag{C.1}$$

Sway: $$\dot{v} = \frac{-mur + mwp + Y_t + Y_d + X_{\dot{u}}ur - Z_{\dot{w}}pw}{m - Y_{\dot{v}}} \tag{C.2}$$

Heave: $$\dot{w} = \frac{-muq + mvp + Z_d - X_{\dot{u}}uq + Y_{\dot{v}}vp}{m - Z_{\dot{w}}} \tag{C.3}$$

Roll: $$\dot{p} = \frac{K_t + K_d - I_z qr + I_y qr - Y_{\dot{v}}vw + Z_{\dot{w}}vw - M_{\dot{q}}qr + N_{\dot{r}}qr}{I_x - K_{\dot{p}}} \tag{C.4}$$

Pitch: $$\dot{q} = \frac{M_t + M_d - I_x rp + I_z rp - Z_{\dot{w}}wu + X_{\dot{u}}wu + K_{\dot{p}}rp - N_{\dot{r}}rp}{I_y - M_{\dot{q}}} \tag{C.5}$$

Yaw: $$\dot{r} = \frac{N_t + N_d - I_y pq + I_x pq - X_{\dot{u}}uv + Y_{\dot{v}}uv - K_{\dot{p}}pq + M_{\dot{q}}pq}{I_z - N_{\dot{r}}} \tag{C.6}$$

The kinematic relationships used to translate these body-fixed linear and angular velocities to linear and angular velocities in the Earth-fixed frame were shown in matrix form in Equations 4.5 and 4.6 in Chapter 4. Expanding this relationship for each degree of freedom produces Equations (C.7) to (C.12).

$$\begin{aligned}\dot{X}_E &= u\,cos\,\psi\,cos\,\theta + v\left(cos\,\psi\,sin\,\theta\,sin\,\phi - sin\,\psi\,cos\,\phi\right)\\ &\quad + w\left(sin\,\psi\,sin\,\phi + cos\,\psi\,cos\,\phi\,sin\,\theta\right)\end{aligned} \tag{C.7}$$

$$\begin{aligned}\dot{Y}_E &= u\,sin\,\psi\,cos\,\theta + v\left(cos\,\psi\,cos\,\phi + sin\,\phi\,sin\,\phi\,sin\,\psi\right)\\ &\quad + w\left(sin\,\theta\,sin\,\psi\,cos\,\phi - cos\,\psi\,sin\,\phi\right)\end{aligned} \tag{C.8}$$

$$\dot{Z}_E = -u\,sin\,\theta + v\,cos\,\theta\,sin\,\phi + w\,cos\,\theta\,cos\,\phi \tag{C.9}$$

$$\dot{\theta} = p + q\,sin\,\psi\,tan\,\theta + r\,cos\,\phi\,tan\,\theta \tag{C.10}$$

$$\dot{\phi} = q\cos\phi - r\sin\phi \tag{C.11}$$

$$\dot{\psi} = q\frac{\sin\phi}{\cos\theta} + r\frac{\cos\phi}{\cos\theta}, \qquad \theta \neq \pm 90^o \tag{C.12}$$

From Section 4.3, the mathematical model can be written in the form

$$\dot{\boldsymbol{x}} = \boldsymbol{Ax} + \boldsymbol{Bu}$$

Where $\boldsymbol{x}$ is the state vector, $\boldsymbol{u}$ is the control vector, $\boldsymbol{A}$ is the system matrix, and $\boldsymbol{B}$ is the control matrix. In this case, the state vector is given by

$$\boldsymbol{x} = \begin{bmatrix} u & v & w & p & q & r & X_E & Y_E & Z_E & \varphi & \theta & \psi \end{bmatrix}^T$$

The first six terms represent surge, sway, heave, roll, pitch, yaw velocities expressed in body fixed reference while the other six terms describe the vehicle position and orientation expressed in Earth-fixed reference. Here the control vector is given by τ.

$$\begin{bmatrix} \dot{\boldsymbol{v}} \\ \dot{\boldsymbol{\eta}} \end{bmatrix} = \begin{bmatrix} \boldsymbol{M}^{-1}\left(-\left(\boldsymbol{C}(\boldsymbol{v}) + \boldsymbol{D}(\boldsymbol{v}) + \boldsymbol{g}(\boldsymbol{\eta})\boldsymbol{v}^{-1}\right)\right) \\ \boldsymbol{J}(\boldsymbol{\eta}) \end{bmatrix} \begin{bmatrix} \boldsymbol{v} \\ \boldsymbol{\eta} \end{bmatrix} + \begin{bmatrix} \boldsymbol{M}^{-1} \\ \boldsymbol{0} \end{bmatrix} \tau$$

$$\nu = \left[\nu_1^T, \nu_2^T\right]^T; \quad \nu_1 = [u, v, w]^T; \qquad \nu_2 = [p, q, r]^T$$
$$\eta = \left[\eta_1^T, \eta_2^T\right]^T; \quad \eta_1 = [X_E, Y_E, Z_E]^T; \quad \eta_2 = [\phi, \theta, \psi]^T$$

The constants used within the model are defined as follow:

Mass	m	4.3 Kg
Length	l	0.90 m
Semi axis of prolate ellipsoid	a	0.45 m
	b	0.08 m
	c	0.07 m
Caudal fin height	h	0.15 m
Caudal fin length	l_{Fin}	0.10 m

Moments of inertia	I_x	0.0097 kgm^3
	I_y	0.1784 kgm^3
	I_z	0.1797 kgm^3
Added mass derivatives	$X_{\dot{u}}$	-0.3495
	$Y_{\dot{v}}$	-3.5554
	$Z_{\dot{w}}$	-3.7321
	$K_{\dot{p}}$	0
	$M_{\dot{q}}$	-0.1123
	$N_{\dot{r}}$	-0.1123

Appendix D

Model Validation

The mathematical model need to be evaluate to determine whether it represent the real system. This process is known as validation where the analogue matching and integral least squares method which have previously discussed in Chapter 4 are used in this research. The validation results for several configuration and types of swimming are shown in this section. These consist of forward and turning manoeuvring swimming where two types of graph are plotted for each configuration; simulation model denotes by red colour and the experiment data denotes by blue colour.

Eight variables consist of surge, sway, roll, pitch, yaw, tail current, x and y position are used for comparison. These variables have been chosen based on the data availability collected from experiment and produced from simulation model. Figure D.1 indicates the vehicle sensor orientation relates to body fixed frame.

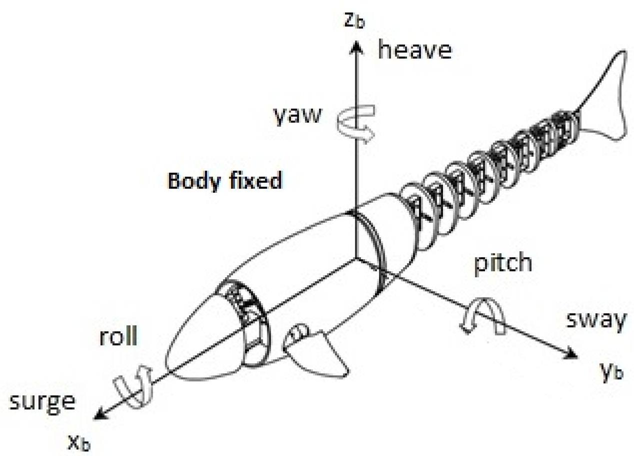

Figure D.1: vehicle sensor orientation

Forward swimming validation (1)

The forward swimming validation is been carried out for four configuration. The first configuration with the tail beat amplitude and frequency set at 0.05 m and 0.5 Hz respectively. The analogue matching results are shown in Figure D.2.

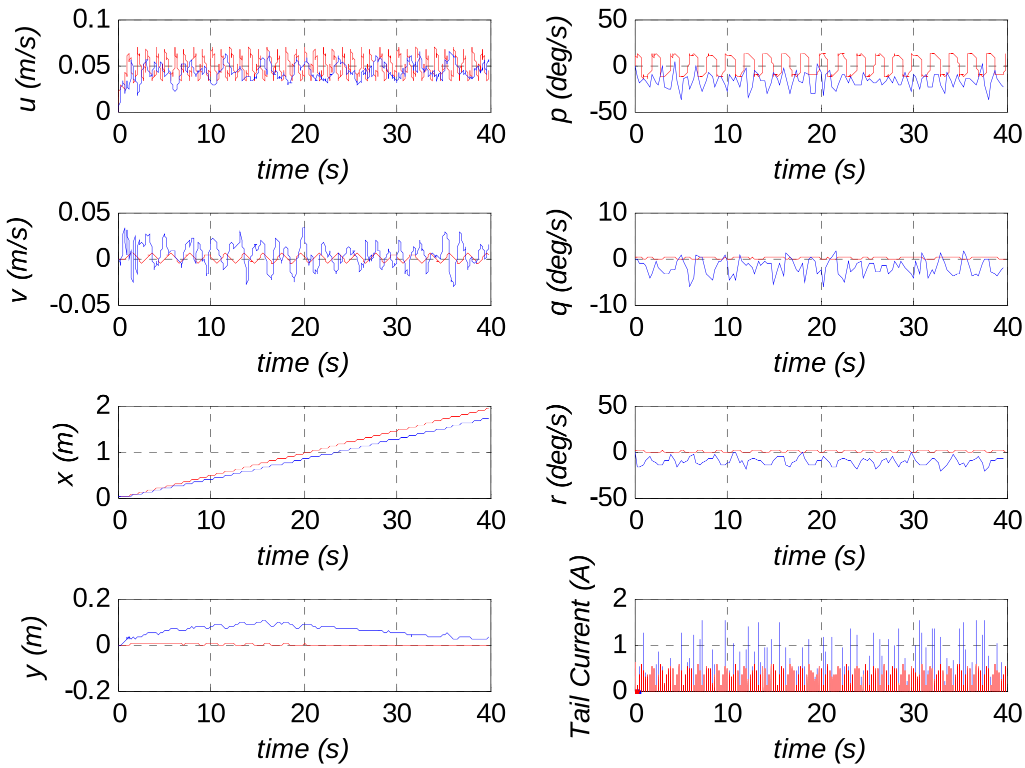

Figure D.2: Analogue matching validation for forward swimming (0.05 m, 0.5 Hz). Blue indicates experiment data and red for simulation data

Table D.1: Integral Least Square Method for forward swimming with tail beat amplitude and frequency of 0.05 m and 0.5 Hz

Variable	Integral Least Square
u (m/s)	0.23
v (m/s)	0.17
p (deg/s)	55757.23
q (deg/s)	854.13
r (deg/s)	16647.58
x (m)	19.14
y (m)	4.42
Tail Current (A)	79.96

Forward swimming validation (2)

In this experiment, the tail beat amplitude and frequency is set at 0.05 m and 1.0 Hz. The analogue matching results are shown in Figure D.3.

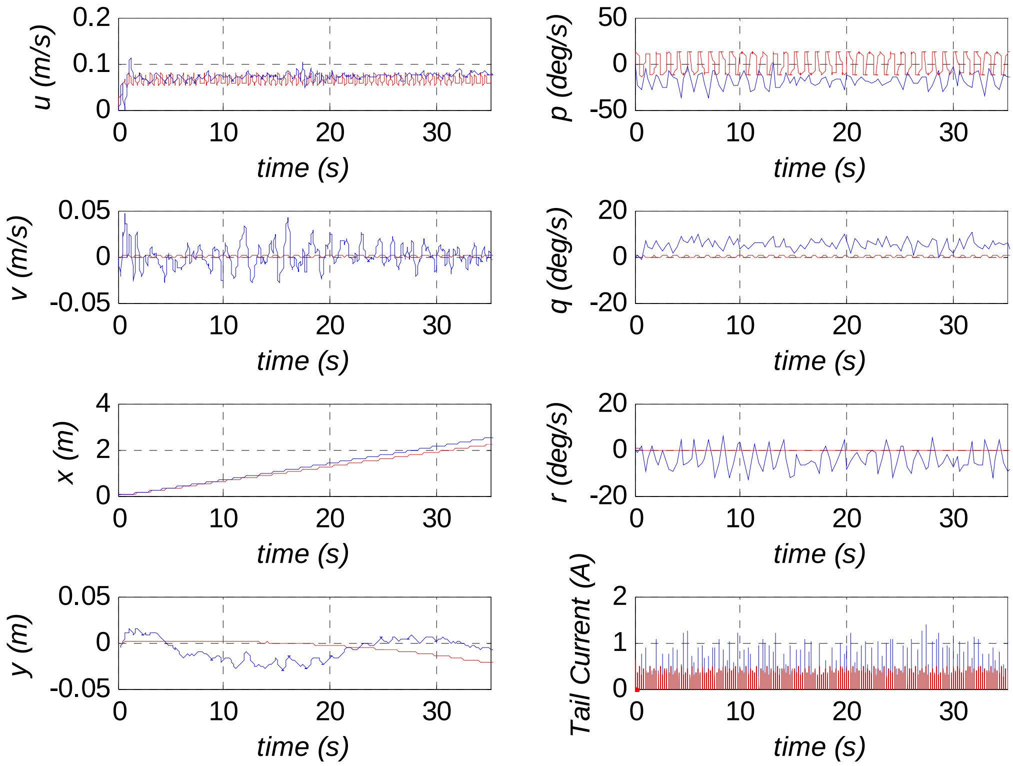

Figure D.3: Analogue matching validation for forward swimming (0.05 m, 1 Hz). Blue indicates experiment data and red for simulation data

Table D.2: Integral Least Square Method for forward swimming with tail beat amplitude and frequency of 0.05 m and 1.0 Hz

Variable	Integral Least Square
u (m/s)	0.23
v (m/s)	0.15
p (deg/s)	60092.35
q (deg/s)	3909.18
r (deg/s)	4785.18
x (m)	28.34
y (m)	0.25
Tail Current (A)	88.24

Forward swimming validation (3)

Next, the tail beat amplitude and frequency is set at 0.10 m and 1.0 Hz. The analogue matching results are shown in Figure D.4.

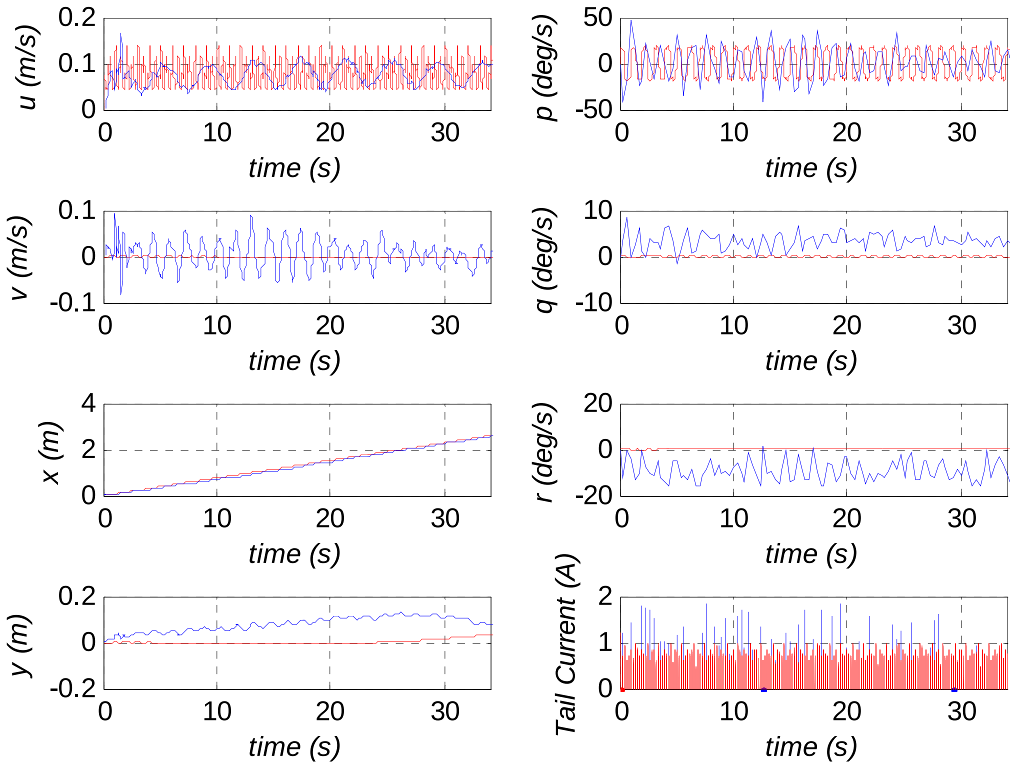

Figure D.4: Analogue matching validation for forward swimming (0.10 m, 1 Hz). Blue indicates experiment data and red for simulation data

Table D.3: Integral Least Square Method for forward swimming with tail beat amplitude and frequency of 0.10 m and 1.0 Hz

Variable	Integral Least Square
u (m/s)	1.01
v (m/s)	0.74
p (deg/s)	55507.82
q (deg/s)	1459.25
r (deg/s)	11475.44
x (m)	3.04
y (m)	5.87
Tail Current (A)	119.87

Forward swimming validation (4)

Finally, the tail beat amplitude and frequency is set at 0.15 m and 1.0 Hz. The analogue matching results are shown in Figure D.5.

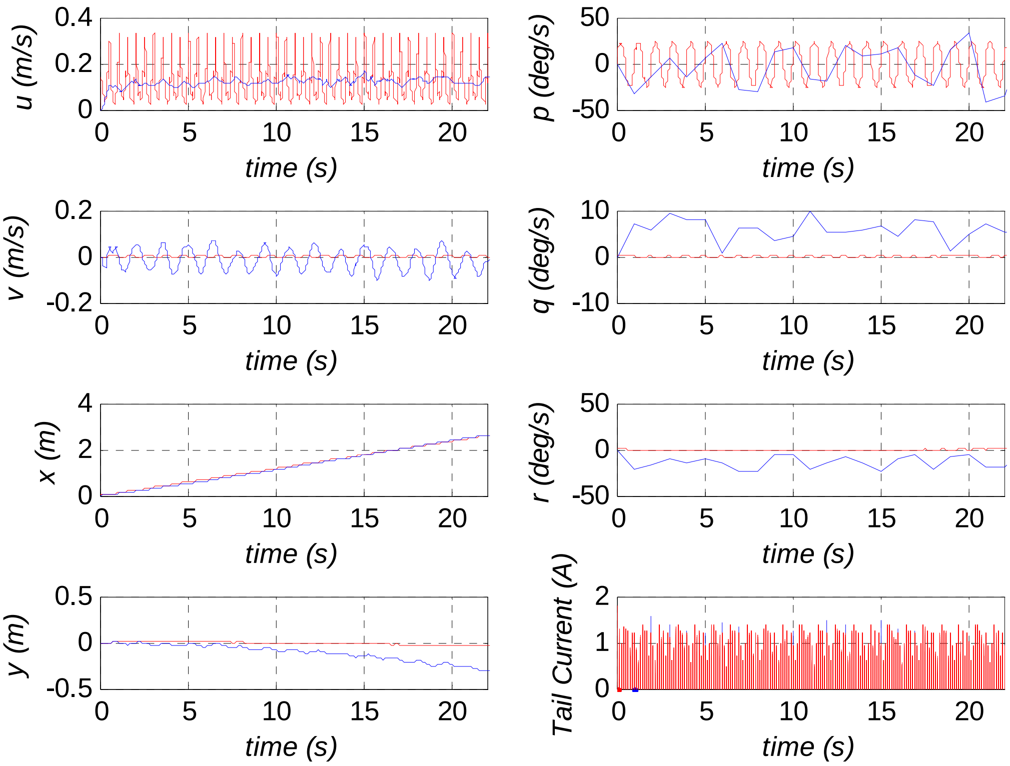

Figure D.5: Analogue matching validation for forward swimming (0.15 m, 1 Hz). Blue indicates experiment data and red for simulation data

Table D.4: Integral Least Square Method for forward swimming with tail beat amplitude and frequency of 0.15 m and 1.0 Hz

Variable	Integral Least Square
u (m/s)	3.48
v (m/s)	1.37
p (deg/s)	22796.06
q (deg/s)	1424.99
r (deg/s)	8634.28
x (m)	1.17
y (m)	11.15
Tail Current (A)	91.80

Manoeuvring swimming validation (1)

The tail beat amplitude and frequency is set at 0.10 m and 1.0 Hz with 10º tail deflection angle. The analogue matching results are shown in Figure D.6.

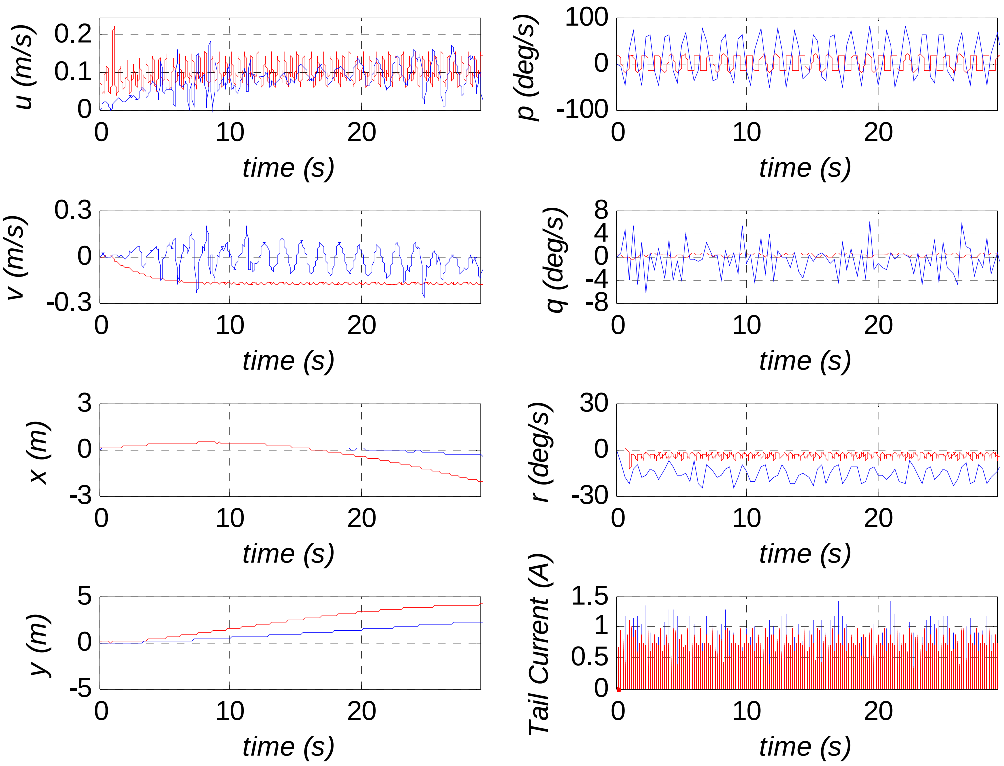

Figure D.6: Analogue matching validation for manoeuvring swimming (0.10 m, 1 Hz, 10º tail deflection angle). Blue indicates experiment data and red for simulation data

Table D.5: Integral Least Square Method for manoeuvring with 10º tail deflection angle

Variable	Integral Least Square
u (m/s)	1.71
v (m/s)	20.66
p (deg/s)	213748.60
q (deg/s)	718.43
r (deg/s)	15793.30
x (m)	2924.28
y (m)	5505.12
Tail Current (A)	113.42

Manoeuvring swimming validation (2)

The tail beat amplitude and frequency is set at 0.10 m and 1.0 Hz with 50º tail deflection angle. The analogue matching results are shown in Figure D.7.

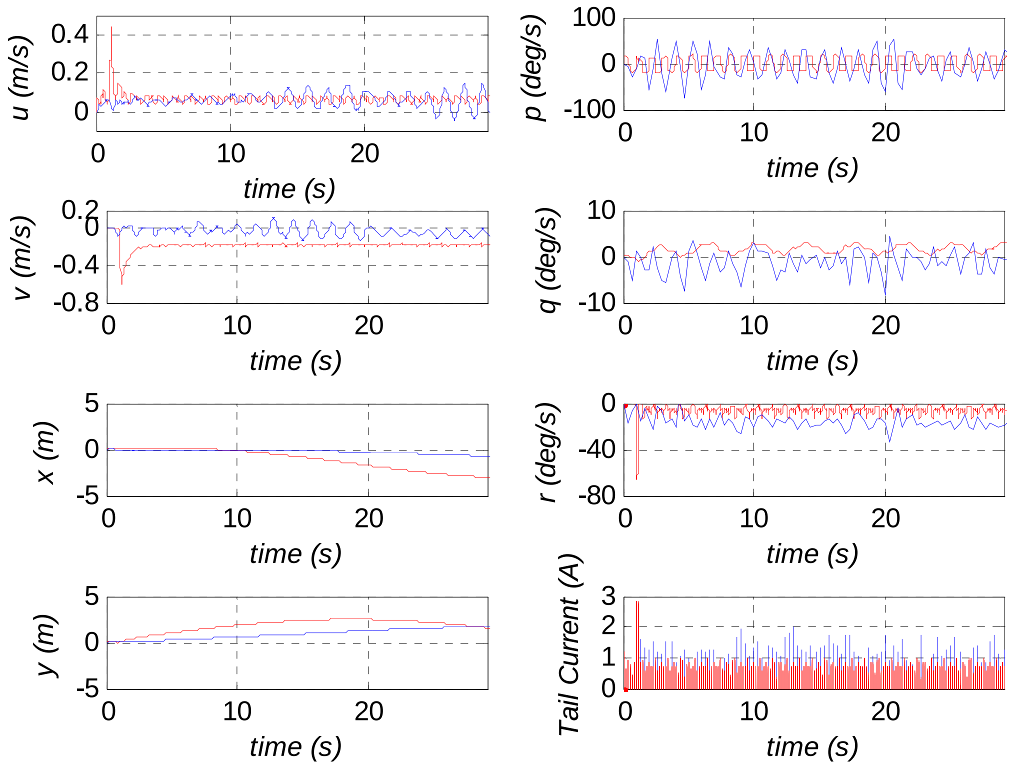

Figure D.7: Analogue matching validation for manoeuvring swimming (0.10 m, 1 Hz, 50º tail deflection angle). Blue indicates experiment data and red for simulation data

Table D.6: Integral Least Square Method for manoeuvring with 50º tail deflection angle

Variable	Integral Least Square
u (m/s)	1.85
v (m/s)	21.93
p (deg/s)	110411.82
q (deg/s)	1366.03
r (deg/s)	13652.50
x (m)	5173.86
y (m)	3631.64
Tail Current (A)	176.97

Manoeuvring swimming validation (3)

The tail beat amplitude and frequency is set at 0.10 m and 1.0 Hz with 90º tail deflection angle. The analogue matching results are shown in Figure D.8.

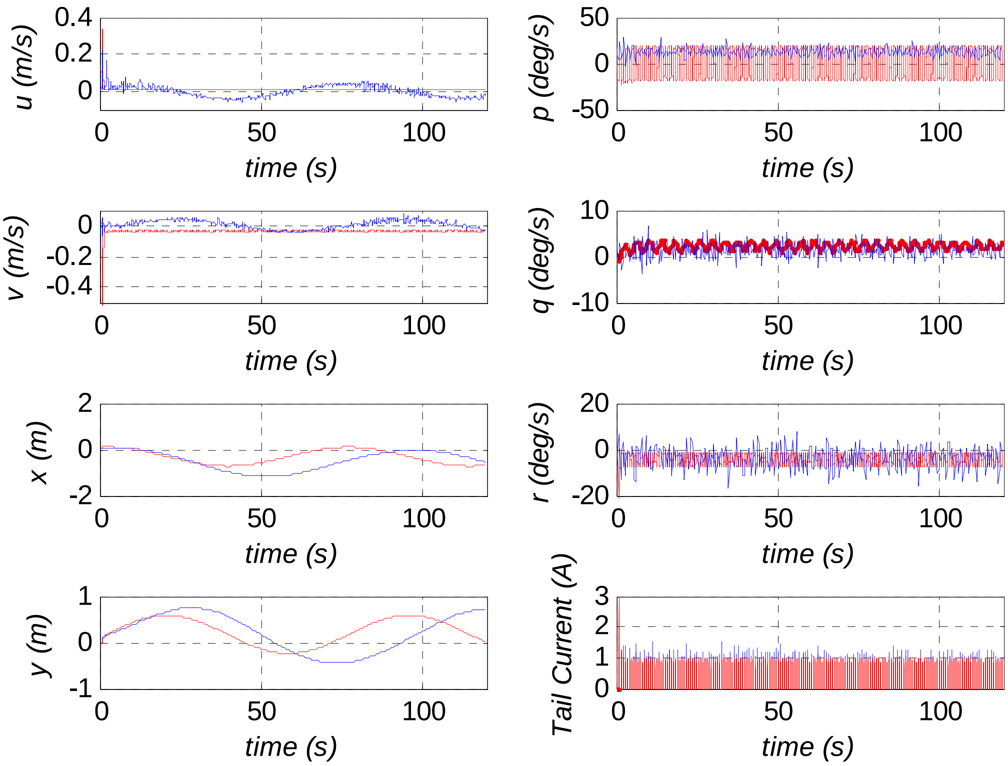

Figure D.8: Analogue matching validation for manoeuvring swimming (0.10 m, 1 Hz, 90º tail deflection angle). Blue indicates experiment data and red for simulation data

Table D.7: Integral Least Square Method for manoeuvring with 90º tail deflection angle

Variable	Integral Least Square
u (m/s)	3.32
v (m/s)	9.30
p (deg/s)	159445.25
q (deg/s)	1343.05
r (deg/s)	9563.17
x (m)	285.77
y (m)	1428.83
Tail Current (A)	424.44